Friedrich-Alexander-Universität
Faculty of Sciences

Doctoral thesis

2025

Paul Philipp Fadler

Quantum and classical light-matter coupling of Mott insulators

Quantum and classical light-matter coupling of Mott insulators

Klassische und quantisierte Licht-Materie Kopplung von Mott-Isolatoren

Der Naturwissenschaftlichen Fakultät
der Friedrich-Alexander-Universität
Erlangen-Nürnberg

zur
Erlangung des Doktorgrades Dr.-rer.nat.

vorgelegt von

Paul Philipp Fadler

Als Dissertation genehmigt
von der Naturwissenschaftlichen Fakultät
der Friedrich-Alexander-Universität Erlangen-Nürnberg

Tag der mündlichen Prüfung:	9.5.2025
Gutachter:	Prof. Dr. Martin Eckstein & Prof. Dr. Kai Phillip Schmidt
	Prof. Dr. Michael Sentef

Preface

Zusammenfassung

Diese Arbeit beschäftigt sich mit Licht-Materie gekoppelten korrelierten Elektronensystemen. In diesen Systemen dient das Licht als Werkzeug um die Dynamik der Materie zu messen und ihre Eigenschaften zu beeinflussen.
Im ersten Teil dieser Arbeit geht es um die ultra-schnelle Dynamik von optisch gepumptem Titanoxychlorid (TiOCl). Dabei handelt es sich um ein Spin-Peierls Material mit optisch aktiven *d*-*d*-Übergängen bei 0.7 eV und 1.5 eV. Wir erstellen ein tight-binding Modell für Elektronen in diesem Material basierend auf ab-initio Rechnungen. In diesem Modell berechnen wir die Nichtgleichgewichts optische Leitfähigkeit der Mott-Anregungen auf der Fermtosekunden Zeitskala unmittelbar nach einer optischen Anregung einer der beiden Übergänge. Das sich ergebende Spektrum korrespondiert zu dem Nichtgleichgewichts Transmissionsspektrum, das von unseren experimentellen Kollaboratoren gemessen wurde indem zunächst einen dieser beiden Übergänge angeregt wurde und nach einem kurzen Zeitversatz die Transmission gemessen wurde. Wir berechnen die Spektren auf kleinen Clustern durch eine iterative Eigenzerlegung der gepumpten Zustände basierend auf deren Spektralfunktion. Da nur kleine Cluster numerisch auswertbar sind, ist die Übereinstimmung zwischen Rechnung und Experiment nur qualitativ.
Die Abhängigkeit der Nichtlinearität eines Doppel-Anregungsexperimentes vom Zeitversatz zwischen den beiden Anregungen erlaubt uns Rückschlüsse auf die Zeitskala in der das Material zurück ins Gleichgewicht kommt zu ziehen. Unter der Annahme, dass diese Zeitskala von ca. 300 fs durch die Lebensdauer der orbitalen Anregungen gegeben ist, berechnen wir diese Lebensdauern mit Hilfe von Fermis goldener Regel. Wir werten diese auf großen Clustern durch Lanczos Methoden aus. Um eine größere Clustergröße zu erreichen verwenden wir ein effektives Spin-Orbit Modell, das aus dem tight-binding Modell durch eine Reihenentwicklung in zweiter Ordnung bestimmt wird. In dieser Beschreibung sind die angeregten Zustände Orbitonen. Dies sind Quasiteilchen, die man als orbitale Anregung mit einer an sich gebundenen Magnon-Wolke verstehen kann. Wir vergleichen die Zerfallsbreite der Spin-Orbit-Zerfallskanäle in unserer Beschreibung mit den experimentell bestimmten Lebensdauern. Dies lässt uns folgern, dass die Lebensdauer der 0.7 eV-Anregung zum Großteil durch diese Prozesse beschrieben wird. Für die 1.5 eV-Anregung gibt es dagegen keine Kanäle, die der gemessenen Lebensdauer nahe kommen. Es ist deshalb wahrscheinlich, dass die Berücksichtigung zusätzlicher Prozesse wie beispielsweise phononische Zerfälle oder anderer Nichtlinearitäten des Experiments relevant sind.
Im letzten Teil dieser Arbeit beschäftigen wir uns mit langreichweitigen Spinwechselwirkungen, die ein quantisiertes elektromagnetisches Feld in Mott-Isolatoren induzieren kann. Da die Spins nur über virtuelle Ladungsanregungen mit dem elektromagnetischen Feld wechselwirken, sind Wechselwirkungen zwischen Spins und Licht inhärent nicht-linear. Wir untersuchen die langreichweitigen Wechselwirkungen in zwei verschiedenen Situationen: Einer isolierten optischen Kavität und einer getriebenen optischen Kavität mit dem zusätzlichen Feld eines externen Lasers. Im isolierten Fall findet die Wechselwirkung durch den Austausch von zwei virtuellen Photonen statt. Wir zeigen, dass selbst der Austausch durch Vakuumfluktuationen genügt um für materialrealistische Parameter Wechselwirkungen zu erhalten, die in mesoskopischen Systemen kollektiv genauso stark beitragen können, wie der lokale Heisenberg-Austausch. Im getriebenen Fall kann der Austausch auch durch hybride Prozesse der Photonen aus dem Laser und der Kavität stattfinden. Diese hybriden Prozesse

können sogar im thermodynamischen Limes beitragen, was das System zu einer interessanten Plattform für Floquet-Engineering von langreichweitigen Wechselwirkungen in makroskopischen Systemen macht. Bei der Herleitung dieser Wechselwirkungen muss allerdings darauf geachtet werden, dass dies basierend auf dem Streuvertex zwischen Licht und Spins, wie er beispielsweise durch eine Reihenentwicklung des elektronischen Modells oder durch Raman-Streuung bestimmt werden kann, außerhalb eines schmalen nahresonanten Fensters nicht möglich ist. Stattdessen bedarf es einer Reihenentwicklung in vierter Ordnung innerhalb des elektronischen Modelles. Wir führen diese für das Hubbard Modell bei halber Füllung durch.

Abstract

In this thesis we study light-matter coupled correlated electron systems. Light therein serves as a tool to measure and manipulate the properties of the matter systems.
The first part of this thesis is centered around the ultrafast dynamics of optically pumped titaniumoxychloride (TiOCl). This material is a spin-Peierls compound with optically active d-d-transitions at 0.7 eV and 1.5 eV. We construct a tight-binding model from ab-initio calculations to model the non-equilibrium optical conductivity of the Mott gap of this system on the femtosecond time-scale following an optical pump of either of these excitations. This observable corresponds to the spectra measured using optical pump-probe transmission spectroscopy performed by our experimental collaborators. We compute the non-equilibrium spectra using a spectral function based iterative eigendecomposition scheme on small clusters. Limitations on the evaluable cluster sizes only allow for a qualitative agreement between our computed and the experimental spectra.
The dependence of the non-linear signal in a double-pump-probe spectroscopy experiment on the pump-pump delay gives us additional information on the timescale on which the pumped sample returns to equilibrium. Assuming this timescale of around 300 fs to be dominated by the lifetime of either orbital excitation, we compute the lifetimes using Fermi's golden rule evaluated on large clusters using Lanczos techniques. To achieve larger cluster sizes we make use of an effective spin-orbital Hamiltonian derived from the tight-binding model via a second-order series expansion. Within this description the pumped excitations are orbitons, i.e., hybrid spin-orbital quasiparticles, that can be understood as orbital excitations surrounded by a bound magnon cloud. Comparing the theoretical predictions for all resulting spin-orbital decay channels to the decay times as obtained by the double-pump experiment we conclude that these channels are likely the dominant decay processes for the 0.7 eV excitation. For the 1.5 eV excitation there is no such match and other types of processes, such as phonon-assisted decay processes or non-linearities in the double-pump scheme, should be taken into account.
In the last part of this thesis we investigate the potential to induce long-range spin interactions in Mott insulators through the coupling to the quantized electromagnetic field of a cavity. Since it requires an intermediate charge excitation, interactions between light and spins are inherently non-linear. We investigate an undriven setting and one where the cavity field is supplemented by the field of a laser. In the former the interaction is mediated by the exchange of two virtual cavity photons. We show that for material realistic parameters the vacuum-mediated interactions can collectively compete with local Heisenberg exchange up to mesoscopic system sizes. In the later case the sign and amplitude of the interactions can be controlled via the drive. This control is possible through hybrid processes involving photons from both the drive and the cavity. These can even contribute in the thermodynamic limit. The driven setting therefore offers a versatile pathway for Floquet engineering of long-range interactions in macroscopic systems. The derivation of these interactions has to be done with special care: A derivation based on the spin-photon scattering vertex, that can be obtained from the electronic model through a second-order series expansion or experimentally through e.g. Raman-scattering, is not sufficient to compute these interactions outside of a narrow resonantly driven regime. It instead requires a fourth-order series expansion within the underlying electronic model, which we perform for the half-filled Hubbard model.

Contents

List of Figures

List of Tables

1 Introduction

1.1 Motivation

Correlated electron systems are materials, in which an understanding of its properties and electronic dynamics is not possible in a single-particle picture. Instead one has to track the intricate collective dynamics of all 10^{23} particles in the thermodynamic limit in order to compute thermodynamic quantities, such as conductivity, heat capacities or phase transitions.

This property makes them a blessing and a curse at the same time:

On one hand this class of materials is much more difficult to describe. In uncorrelated materials the wavefunctions of electrons factorize, such that the dynamics of a macroscopic number of electrons separates. Bands or orbitals used as basis states are still coupled, but the associated eigenvalue problem is identical for all particles and its complexity therefore scales linearly with the size of the basis employed. There are powerful techniques available to treat these systems, even in an ab-initio context, such as density functional theory (DFT) [1, 2]. They have proven invaluable to quantum chemistry and condensed matter systems [3]. It can treat weakly correlated settings or, as we present in this thesis, be used as starting point for an explicit treatment of interacting electrons within some bands or orbitals. In correlated electron systems there is no such factorization. Without any additional approximations the complexity of a full diagonalization for the wavefunctions is factorial, i.e., super-exponential. Complete solutions are therefore usually not possible in an ab-initio context, but only within cleverly chosen small subspaces.

On the other hand, electronic correlations allow for much richer dynamics. They can lead to highly intricate ground states and excitations such as magnetic states beyond mean-field descriptions [4, 5], superconducting states [6] or compound quasiparticles as in a Fermi liquid [7–9]. The materials and toy models we consider in this thesis are Mott insulators [10]. They have partially filled valence bands which in conventional single-particle band theory would lead to mobile charge carriers. They are nevertheless insulating due to strong repulsive electron-electron interactions. This leads to highly correlated ground states and excitations.

One such Mott insulating material, that we encounter in Chapters 3 and 4, is TiOCl. It is a quasi two dimensional $3d^1$ transition metal oxyhalide which hosts correlated electrons due to the bandwidth of the valence band being narrow compared to electron-electron interactions. This class of materials is of special interest due to their similarity to the high-T_c superconducting cuprates [11] hosting a $3d^9$ configuration. There are however two key differences between such cuprates and TiOCl: The cuprates are charge transfer insulators [12, 13] while TiOCl is Mott insulating [14]. Furthermore, the low temperature dynamics of the cuprates remains two dimensional while TiOCl becomes one dimensional even undergoing a spin-Peierls transition [14, 15]. This is due to the crystal field lifting all orbital degeneracies and a subsequent alignment of the energetically lowest orbital with the crystallographic b-axis. Since the d-d-transitions in TiOCl are furthermore infrared active [16], it is an advantageous experimental platform to optically pump and probe the entanglement between spin, orbital and charge degrees of freedom.

In this thesis we model Mott insulators using the Hubbard model [5, 17, 18]. Depending on the choice of its parameters, it captures metallic or Mott insulating behavior, as well as the corresponding metal-to-insulator transition between these phases. It is defined for electrons

tightly-bound on a lattice. They can hop from site to site while strongly repelling each other when on the same lattice site. Despite being a seemingly simple model, it already contains many of the interesting phases and phenomena. Its solution is straightforward in two limiting cases: If there is no repulsion between the electrons, it can be understood in the single particle picture of band electrons. If on the contrary the electrons are immobile, we can solve it as many isolated atomic systems. Since these two solutions use mutually exclusive basis sets (momentum space and real space respectively), a general solution in between those limiting cases is difficult to formulate. Beyond exact solutions for one-dimensional lattices [19] and infinite dimensional lattices [20], there exist only approximate techniques, such as dynamical mean-field theories [21–24], series expansions [25–27] or density matrix renormalization group based approaches [28].

Diametrically opposed to this complicated condensed matter setting lies the field of quantum optics: Instead of complexity emerging from a simple starting point bottom-up, complex optical components are linked and used in concert to create simple states of light[1]. In practice this allows constructing highly sophisticated optical setups to engineer pulses and/or bound states of light in optical cavities. In this thesis we use light as a tool to manipulate and measure the properties of correlated electron systems. The coupling between light and matter is therefore a central pillar of this thesis, that stands at the intersection between both fields.

We want to use light to control materials with two different purposes in mind:
(i) We want to enhance the information a measurement is able to obtain. Equilibrium spectroscopy is only able to probe equilibrium states of matter. Photodoping specific excitations allows pump-probe spectroscopy [29] to shine light on their non-equilibrium properties as well [30]. We utilize a pump resonant to an orbital transition in this thesis to investigate the exchange coupling between spin and orbital degrees of freedom (different from the relativistic spin-orbit coupling) in Chapters 3 and 4.
(ii) We want to engineer material (quasi-) equilibrium properties [31]. In addition to photodoping, we can continuously drive Mott insulators for Floquet engineering [32] or couple them to quantized electromagnetic modes for cavity material engineering [33]. In Chapter 5 we use both of these to derive long-range magnetic interactions.

1.2 Outline of this thesis

This thesis divides in three major parts.

The first one consisting of Chapter 2, introduces concepts and techniques relevant for the remaining parts of this thesis. Its focus lies on the derivation of light-matter coupling for condensed matter systems. From Maxwell's equations for the Schroedinger field we derive the minimal coupling action and Hamiltonian (Section 2.2), linear response theory (Section 2.3.3) and the dipolar representation of the light-matter coupling (Section 2.4.3). We additionally provide a short primer on the Hubbard model (Section 2.1), series expansion in terms of the Schrieffer-Wolff transformation (Section 2.5) and Floquet theory (Section 2.6).

Chapters 3 and 4 are focused on the non-equilibrium dynamics of optically pumped TiOCl. In Chapter 3 we compute the non-equilibrium optical conductivity of the Mott gap in TiOCl. This corresponds to the measured transmission spectra of an experiment of our experimental collaborators briefly outlined in Section 3.2.2. We start with an ab-initio derivation of an

[1] Or at least states that are simple to describe

effective few-band model for TiOCl (Section 3.3) using density functional theory. For this tight-binding model we derive an effective spin-orbital exchange Hamiltonian (for the derivation see Section 3.4, for a discussion of its matrix elements see Section 4.2), which we use to fix the remaining free parameters of our tight-binding Hamiltonian by fitting the magnetic exchange and to simplify the numerical complexity in Chapter 4. In Section 3.5 we evaluate the time-dependent non-equilibrium optical conductivity of our tight-binding Hamiltonian on small clusters for optically pumped states using an iterative eigendecomposition scheme. In Chapter 4 we compute the lifetime of the pumped excitations. We accomplish this by evaluating Fermi's golden rule as spectral function (Section 4.3) using the effective spin-orbital Hamiltonian evaluated on large clusters.

Lastly, in Chapter 5 we derive long-range cavity-mediated four-spin interactions for a cavity-coupled Hubbard model. Their derivation (see Section 5.3) using a second order approach based on the spin-cavity scattering does not properly reproduce it and a fourth order expansion is necessary instead. We show that an additional Floquet-drive can be used to control these interactions and allows these interactions to contribute even in the thermodynamic limit.

2 Models and Methods

In this chapter we will give a brief overview over the models and methods relevant for this thesis. We start out with a brief introduction to the Hubbard model in Section 2.1. Sections 2.2 to 2.4 form the biggest part of this chapter. Starting from Maxwell's equations and the action of the Schroedinger field we derive the light-matter coupling relevant to the main parts of this thesis. Series expansions are also a recurring aspect and therefore introduced in terms of the Schrieffer-Wolff transformation in Section 2.5. Lastly we derive the Floquet-block Hamiltonian as obtained from Floquet-theory applicable to time-periodic systems in Section 2.6.

2.1 Hubbard model

Condensed matter systems usually combine a macroscopic number of negatively charged electrons with positively charge ions. Since the latter are usually orders of magnitude heavier than the former, a common tool to simplify the treatment is the Born-Oppenheimer approximation [34]: Instead of simultaneously treating the slow movement of the ionic cores and the fast electrons, we can separate the dynamics based on their timescales.

To describe the dynamics of the electrons, it is therefore often times helpful to project the continuum theory to a discrete set of basis states. In this thesis, we focus on electrons tightly bound to ionic cores forming a periodic potential landscape. the spacing between electrons is usually short enough for the bare Coulomb repulsion of electrons to be of a similar order of magnitude as the strength of the periodic potential[1]. This long-range ($\propto r^{-1}$) interaction is in most materials strongly screened by their polarizability. This screening described by the materials dielectric function often leads to an effective short-range ($\propto \exp(-\alpha r)$) electron-electron interaction. The length scale therein can vary greatly between materials. The limit of strong screening is described by the Hubbard model [5, 17, 18]

$$H = -\sum_{\langle i,j\rangle}\sum_{\sigma} t_{ij} c^{\dagger}_{i\sigma} c_{j\sigma} + U \sum_{i} n_{i\uparrow} n_{i\downarrow}\,, \tag{2.1}$$

where $n_{i\sigma} = c^{\dagger}_{i\sigma} c_{i\sigma}$ and the sum $\langle i,j\rangle$ runs over all nearest neighbors. Apart from a kinetic hopping term, that allows electrons of spin σ to move from one Wannier orbital to another one with the hopping amplitude t_{ij} [2], there is an on-site repulsion proportional to the Hubbard interaction U. It was originally introduced to describe the emergent magnetism of interacting itinerant electrons. E.g., for small values of $U \ll t$ under the Hartree-Fock approximation, it hosts Stoner band ferromagnetism [17, 35], while in the opposite Mott-insulating limit $t \ll U$, exchange interactions lead to Heisenberg-antiferromagnetism [4, 25].

Beyond being applicable for some types of materials, the Hubbard model remains a basis for paradigmatic descriptions of correlated electrons even after 60 years [36–38]: While the kinetic term is diagonal in the delocalized Bloch basis, the interaction term is diagonalized by the incompatible localized Wannier basis. To this day, exact solutions only exist in one

[1] After all, in a neutral solid each unit cell of the periodic lattice has to contain equal ionic and electronic charges.

[2] The sign of t_{ij} is up to convention. Most often it is chosen positive with an overall negative prefactor in the kinetic term to produce the band minimum at $k = 0$.

dimension [19, 39], while for other cases approximative methods, such as series expansions [25–27] or (dynamical-) mean-field theories [17, 21], or numerical methods, such as density-matrix renormalization techniques [40] or Lanczos-based cluster diagonalizations [41], are necessary.

While sometimes it may be possible to reduce the relevant degrees of freedom to a single band close to the Fermi energy, this is not always the case. E.g., for transition metal oxides, such as TiOCl, a material we will encounter in Chapters 3 and 4, an explicit description of multiple bands near the Fermi energy may be necessary. Since the hopping amplitudes t_{ij} depend on the overlap integrals between neighboring Wannier orbitals $w_{\mathbf{R},\alpha}(\mathbf{r})$, a generalization to multiple orbitals per site leads to a hopping matrix

$$t_{ij}^{\alpha\beta} = \int d\mathbf{r}\, w^*_{\mathbf{R}_i,\alpha}(\mathbf{r}) w_{\mathbf{R}_j,\beta}(\mathbf{r})\,. \tag{2.2}$$

It is similarly possible to evaluate the on-site Coulomb repulsion by considering all combinations of orbitals on the same site:

$$U_{\alpha\beta\gamma\delta} = \iint d^3\mathbf{r} d^3\mathbf{r}' w^*_\alpha(\mathbf{r}) w^*_\beta(\mathbf{r}') W(|\mathbf{r}-\mathbf{r}'|) w_\gamma(\mathbf{r}') w_\delta(\mathbf{r}), \tag{2.3}$$

where $W(|\mathbf{r}-\mathbf{r}'|)$ is the screened Coulomb operator. Since electrons and nuclei surrounding these orbitals can lead to complicated screenings, these integrals are usually evaluated numerically using constrained random phase approximation (cRPA) within density functional theory [42] (DFT) or fit to experimental data as we will do for TiOCl in Section 3.3. Having found these integrals, in second quantization we obtain

$$H_{\text{int}} = \sum_{\alpha\beta\gamma\delta} \sum_{\sigma\sigma'} U_{\alpha\beta\gamma\delta} c^\dagger_{\alpha\sigma} c^\dagger_{\beta\sigma'} c_{\gamma\sigma} c_{\delta\sigma'}\,. \tag{2.4}$$

If we expand our Wannier functions in terms of atomic wavefunctions, i.e., as a radial part and spherical harmonics, there exists a particularly compact parametrization of these matrix elements in the form of Slater integrals [43]. These make use of the fact, that the angular part of the above integrals can be solved analytically for spherical harmonics. The radial part of the integration has to be evaluated numerically [44]. For orbitals with angular momentum principle quantum number l, the matrix elements $U_{\alpha\beta\gamma\delta}$ are then fully parametrized by $l+1$ parameters, usually denoted as $F_0, F_2, \ldots, F_{2l}$. E.g. for two electrons in a p-shell, F_0 governs the strength of the interaction independent on the magnetic quantum number m, whereas F_2 parametrizes its dependence on m and leads to Hund's rule [45]. In practice due to the spatial extent of the Wannier functions beyond the atomic case, F_0 is difficult to compute, since it strongly depends on the radial part of the Wannier functions and the crystal field and screening processes. The other contributions $F_2, \ldots$ are effected relatively weakly by their surroundings, such that it is usually sufficient to use literature values computed e.g. within the Hartree-Fock approximation [44].

2.2 Light-matter coupling for classical fields

In the main part of this thesis, we want to investigate correlated electrons coupled to an external classical and/or quantum electromagnetic field. We therefore want to use this section to properly introduce the corresponding fields and how they couple to tight-binding models, such as the Hubbard model introduced in Section 2.1. The content reported in this section and the following two Sections 2.3, 2.4 does therefore not constitute new scientific

results, but summarizes, combines and applies well known results and formulation from literature. It is intended as a starting point for readers with a condensed matter background new to the field of light-matter coupled condensed matter systems. For more experienced readers it acts as compendium of the different formulations of light-matter coupling for matter described by the Schroedinger equation from classical field theory all the way to quantized fields, that in this form to the authors knowledge is not found elsewhere in literature. The same (and for the particular details these works specify in an even better) understanding of these subjects can be achieved by consulting the literature referenced in this chapter, such as, e.g., the books of Abrikosov *et al.* [9], Altland and Simons [46], Cohen-Tannoudji *et al.* [47], Năstase [48], or Srednicki [49], directly.

We start from Maxwell's equations, which we formulate in terms of a classical field theory for the potentials $\phi, \mathbf{A}$. We then show how and why gauge invariance of these potentials constrains the light-matter coupling for matter described by the Schroedinger equation to the minimal coupling formulation. Upon quantization of the matter, we show how the light-matter coupling can be used to measure matter properties within linear response theory. Next we consider the quantization of the electromagnetic field either subject to boundary conditions or a dielectric environment. Lastly we derive the dipolar representation of the light-matter coupling due to its importance for descriptions within a reduced matter Hilbert space.

2.2.1 Maxwell's equations

There are two common formulations of classical electrodynamics: a microscopic and a macroscopic one. The microscopic one using the fields $\mathbf{E}$, $\mathbf{B}$ aims to capture the full dynamics of the fields generated by the charges and currents ρ, $\mathbf{j}$. The macroscopic formulation uses the fields $\mathbf{D}$, $\mathbf{H}$ and is obtained by separating the charges and currents into free ρ_{free}, $\mathbf{j}_{\text{free}}$ and bound contributions ρ_{bound}, $\mathbf{j}_{\text{bound}}$. This can often times make their treatment easier, e.g., when the bound charges form the polarization of some dielectric material. If the microscopic details of this polarization is not important it can be spatially averaged [50, 51]. This smoothens the microscopic structure of bound charges and currents hosted in some material and allows for an effective macroscopic description of the fields produced by the free charges and currents in the dielectric environment of the material hosting the bound charges and currents.

$$\nabla \cdot \mathbf{B} = 0 \tag{2.5a}$$

$$\nabla \times \mathbf{E} = -\frac{\partial \mathbf{B}}{\partial t} \tag{2.5b}$$

$$\nabla \cdot \mathbf{E} = \rho/\epsilon_0 \tag{2.5c}$$

$$\nabla \times \mathbf{B} = \mu_0 \mathbf{j} + \frac{1}{c^2}\frac{\partial \mathbf{E}}{\partial t} \tag{2.5d}$$

$$\nabla \cdot \mathbf{D} = \rho_{\text{free}} \tag{2.5e}$$

$$\nabla \times \mathbf{H} = \mathbf{j}_{\text{free}} + \frac{\partial \mathbf{D}}{\partial t}\,, \tag{2.5f}$$

In leading order of a microscopic multipolar expansion [51], the fields are linearly related

through the material-dependent dielectric function ϵ and diamagnetic function μ, which are complex tensor fields in the most general setting.

$$\mathbf{D} = \epsilon_0 \mathbf{E} + \mathbf{P} = \underline{\underline{\epsilon}}(\mathbf{r})\mathbf{E} \tag{2.6}$$

$$\mathbf{H} = \frac{1}{\mu_0}\mathbf{B} - \mathbf{M} = \underline{\underline{\mu}}^{-1}(\mathbf{r})\mathbf{B}\,, \tag{2.7}$$

where $\mathbf{P}$ is the polarization and $\mathbf{M}$ the magnetization due to bound charges and currents. If we want to characterize how materials react to outside fields, it therefore suffices to compute ϵ and μ to fully characterize the resulting polarization, magnetization and wave propagation[3].

For the remainder of this thesis, we will neglect magnetization effects by setting $\mu = \mu_0$ leading to $\mathbf{M} = 0$. This is valid for a wide class of materials, as in the multipolar expansion used to derive the macroscopic fields the electric dipolar coupling is usually much stronger than the magnetic one [50].

Maxwell's equations for the $\mathbf{E}$ and $\mathbf{B}$ fields are overcomplete (eight equations for six field components). It is therefore usually helpful to parametrize the fields in terms of a scalar potential $\phi(\mathbf{r})$ and a vector potential $\mathbf{A}(\mathbf{r})$ such that

$$\mathbf{E}(\mathbf{r}, t) = -\nabla\phi(\mathbf{r}, t) - \frac{\partial \mathbf{A}(\mathbf{r}, t)}{\partial t} \tag{2.8}$$

$$\mathbf{B}(\mathbf{r}, t) = \nabla \times \mathbf{A}(\mathbf{r}, t)\,. \tag{2.9}$$

For a homogeneous isotropic material $\underline{\underline{\epsilon}}(\mathbf{r}) = \epsilon$, we obtain four equations for four components

$$-\nabla^2\phi - \frac{\partial}{\partial t}\left(\nabla \cdot \mathbf{A}\right) = \rho/\epsilon \tag{2.10}$$

$$-\nabla^2\mathbf{A} + \epsilon\mu_0\frac{\partial^2 \mathbf{A}}{\partial t^2} + \nabla\left(\nabla \cdot \mathbf{A} + \epsilon\mu_0\frac{\partial \phi}{\partial t}\right) = \mu_0 \mathbf{j}\,. \tag{2.11}$$

In this parametrization $(\phi, \mathbf{A})$ form a local gauge theory, since for every solution $(\phi, \mathbf{A})$, the potentials

$$\mathbf{A}' = \mathbf{A} - \nabla\Lambda(\mathbf{r}, t) \tag{2.12}$$

$$\phi' = \phi + \frac{\partial \Lambda(\mathbf{r}, t)}{\partial t} \tag{2.13}$$

are a solution as well for any arbitrary smooth scalar gauge function $\Lambda(\mathbf{r}, t)$ [50]. In the following, we drop the arguments of the gauge function $\Lambda = \Lambda(\mathbf{r}, t)$ for ease of notation.

This gauge invariance constrains light-matter coupling to certain forms. To clarify this aspect, we will at first derive how the electromagnetic field obeying Maxwell's equations can couple to a charged matter field.

[3] This holds true as long as the averaging of the microscopic matter structure is still valid. E.g. when considering x-ray scattering on condensed matter systems this is no longer the case, since the wavelength of the scattered light and characteristic matter length scales do not separate.

2.2.2 Classical action formulation

Since we want to utilize Noether's theorem in the following, a formulation in terms of the action is best suited. We choose the conventions $\eta_{\mu\nu} = \mathrm{diag}(-1,1,1,1)$, $\partial_\mu = (c^{-1}\partial_t, \nabla)^T$, $j^\mu = (c\rho, \mathbf{j})^T$, $A^\mu = (\phi/c, \mathbf{A})^T$.

For the Lagrangian density

$$\mathcal{L}_{\text{field}} = \frac{1}{2}(\epsilon_0 \mathbf{E}^2 - \mu_0^{-1}\mathbf{B}^2) + A_\mu j^\mu \tag{2.14}$$

$$= -\frac{1}{4\mu_0} F_{\mu\nu}F^{\mu\nu} + A_\mu j^\mu\,, \tag{2.15}$$

where $F^{\mu\nu} = \partial^\mu A^\nu - \partial^\nu A^\mu$ is the electromagnetic field tensor, the Euler-Lagrange equations produce Maxwell's equations:

$$\frac{\partial \mathcal{L}_{\text{field}}}{\partial A_\mu} = \partial_\nu \left(\frac{\partial \mathcal{L}_{\text{field}}}{\partial(\partial_\nu A_\mu)} \right)$$

$$\mu_0 j^\mu = \partial_\nu F^{\mu\nu}, \tag{2.16a}$$

which component-wise yields

$$\mu_0 j^0 = -c^{-1}\partial_t(\nabla \cdot \mathbf{A}) - \nabla^2 A^0 \tag{2.16b}$$

$$\mu_0 j^i = \partial^i(c^{-1}\partial_t A^0 + \nabla \cdot \mathbf{A}) + c^{-2}\partial_t^2 A^i - \nabla^2 A^i\,. \tag{2.16c}$$

In this compact form, it is straightforwardly shown, that (i) the current j^μ has to follow the continuity equation for charge and current

$$\partial_\mu j^\mu = \partial_\mu \partial_\nu F^{\mu\nu} = -\partial_\nu \partial_\mu F^{\nu\mu} = 0 \tag{2.17}$$

even without having imposed the equations of motion and that (ii) the action is invariant under the gauge transformation of equations 2.12, 2.13. It changes the vector potential as $\delta A_\mu = -\partial_\mu \Lambda$. In the absence of source currents j^μ, the Lagrangian density is directly invariant as $\delta(F_{\mu\nu}F^{\mu\nu}) = 0$. If source currents provide an inhomogenous contribution the Lagrangian is no longer necessarily invariant under the gauge transformation. If the current is sufficiently well-behaved at the boundaries of the region we are solving the field for, the action $S = \int d^4x^\mu\, \mathcal{L}(x^\mu)$ and therefore the equations of motion are still invariant [49]. As we will see in Section 2.2.3, statements (i) and (ii) are equivalent and connected via Noether's second theorem.

We do, however, not want to impose some current j^μ and compute the fields. Rather, the current should be a charged dynamic matter field. In the condensed matter context non-relativistic descriptions generally suffice. We therefore want to neglect direct coupling between spin and field such that the matter field can be described by the Schrödinger action [47, 52, 53]

$$\mathcal{L}_{\text{matter}} = i\bar{\psi}\partial_t\psi - \frac{1}{2m}(\nabla\bar{\psi})(\nabla\psi) - V\bar{\psi}\psi\,. \tag{2.18}$$

$\psi, \bar{\psi}$ are complex-valued classical fields with the Euler-Lagrange equations

$$\frac{\partial \mathcal{L}_{\text{matter}}}{\partial \psi} - \nabla\left(\frac{\partial \mathcal{L}_{\text{matter}}}{\partial(\nabla\psi)}\right) - \partial_t\left(\frac{\partial \mathcal{L}_{\text{matter}}}{\partial(\partial_t\psi)}\right) = 0 \tag{2.19a}$$

$$-V\bar{\psi} + \frac{1}{2m}\nabla^2\bar{\psi} - i\partial_t\bar{\psi} = 0 \tag{2.19b}$$

$$\frac{\partial \mathcal{L}_{\text{matter}}}{\partial \bar{\psi}} - \nabla\left(\frac{\partial \mathcal{L}_{\text{matter}}}{\partial(\nabla\bar{\psi})}\right) - \partial_t\left(\frac{\partial \mathcal{L}_{\text{matter}}}{\partial(\partial_t\bar{\psi})}\right) = 0 \tag{2.19c}$$

$$i\partial_t\psi - V\psi + \frac{1}{2m}\nabla^2\psi = 0 \tag{2.19d}$$

producing the Schrödinger equation for $\hbar = 1$. Since the Lagrangian density is left invariant under the global gauge transformation $\psi' = e^{-i\alpha}\psi$, $\bar{\psi}' = e^{i\alpha}\bar{\psi}$ leading to the variations $\delta\psi = -i\alpha\psi$, $\delta\bar{\psi} = i\alpha\bar{\psi}$, the action is invariant as well. According to Noether's first theorem [54] this leads to an associated conserved current

$$j_S^\mu = \frac{\partial \mathcal{L}_{\text{matter}}}{\partial(\partial_\mu\psi)}\frac{\delta\psi}{\alpha} + \frac{\partial \mathcal{L}_{\text{matter}}}{\partial(\partial_\mu\bar{\psi})}\frac{\delta\bar{\psi}}{\alpha}$$

$$j_S^0 = c\bar{\psi}\psi \tag{2.20a}$$

$$\mathbf{j}_S = \frac{i}{2m}\left((\nabla\bar{\psi})\psi - (\nabla\psi)\bar{\psi}\right), \tag{2.20b}$$

that is a conserved quantity 'on-shell'[4], which means

$$\partial_\mu j_S^\mu = \partial_t(\bar{\psi}\psi) + \nabla\mathbf{j}_S = 0\,, \tag{2.21}$$

if the fields $\psi, \bar{\psi}$ fulfill the equations of motion. We can interpret j_S^0 as probability density and the $\mathbf{j}_S$ probability current[5]. Equipping this density with a charge q, we want it to produce the charge density and current density of Maxwell's equations.

2.2.3 Gauge invariant coupling

If our previous assertions on Maxwell's equations are supposed to hold true, there are two problems with the combined Lagrangian density for the fields $A^\mu, \bar{\psi}, \psi$

$$\mathcal{L}_{\text{trial}} = -\frac{1}{4\mu_0}F_{\mu\nu}F^{\mu\nu} + qA_\mu j_S^\mu + i\bar{\psi}\partial_t\psi - \frac{1}{2m}(\nabla\bar{\psi})(\nabla\psi) - V\bar{\psi}\psi\,. \tag{2.22}$$

Imagine a setting, where we have solved for the fields $A^\mu, \psi, \bar{\psi}$. From $\psi, \bar{\psi}$, we can compute the current j_S^μ, which provides the inhomogeneity for the Maxwell action, that is solved by the field A^μ. If A^μ is a solution of Maxwell's equations with j_S^μ imposed as inhomogeneity,

[4] In this thesis we will denote conserved quantities 'on-shell', if they are only conserved when the corresponding field fulfill the equations of motion. In contrast, 'off-shell' conserved quantities are fulfilled, even if the equations of motion are not imposed. These terms originate from relativistic theories, where the shell refers to the energy-mass shell.

[5] The factor c in the probability density is due to our choice of parametrization. Since we want the four component vector potential to have the same units as the vector potential, the derivative ∂_0 has to carry an extra factor c^{-1}, which cancels the factor c in the probability density.

so is $A'^{\mu} = \delta A^{\mu} + A^{\mu}$ under the gauge transformation $\delta A^{\mu} = -\partial^{\mu}\Lambda$. For this set of infinite additional solutions, there are two possibilities:

(i) There are A'^{μ} differing from A^{μ} by gauge transformation, that are not solutions of the coupled system $A'^{\mu}, \psi', \bar{\psi}'$. As a consequence, we could measure the gauge function Λ by measuring the physical fields $\psi, \bar{\psi}, \mathbf{E}, \mathbf{B}$ and inferring it from the Lagrangian (2.22). The gauge of the electromagnetic field Λ and the absolute values of the potentials would therefore be a physical, measurable quantity.

(ii) All A'^{μ} are solutions of the coupled system of equations as well. This preserves the local gauge invariance but necessitates some changes to our gauge transformation by also affecting the matter fields $\psi' = \psi'(\psi, \Lambda)$, $\bar{\psi}' = \bar{\psi}'(\bar{\psi}, \Lambda)$ and requiring an additional term in our action as we will show below. The gauge invariance of the coupled system is ensured irrespective of boundary conditions if the coupled Lagrangian is already invariant under the gauge transformation.

A second issue with the Lagrangian (2.22) is that the conservation of the Schroedinger probability current j_S^{μ} is a result of a global gauge symmetry and thereby Noether's first theorem. It therefore requires the fields $\bar{\psi}, \psi$ to fulfill the classical equations of motion [55]. The field A^{μ} does however carry a local gauge symmetry and its current therefore has to be conserved even 'off-shell'. Since in the classical case the fields follow the equations of motion, this distinction might seem to be superfluous, but it becomes important when considering quantum fields: Generalized Takahashi-Ward identities between field propagators are the equivalent to conserved currents for quantum field theories [56, 57]. For a local gauge symmetry these have to be fulfilled even for the 'off-shell' propagators describing the quantum fluctuations.

Consider for example a double well potential in which a charged particle is placed. The time translational invariance leads to a global U(1) symmetry. It ensures that the only non-vanishing propagators are the ones where all external ends are on the energy shell, i.e. describing energy conserving processes. There is however no need for these propagators to conserve energy for internal virtual states allowing for instanton contributions [46]. The local U(1) gauge symmetry from the electromagnetic field constrains the propagators stronger. Even internal 'off-shell' contributions have to conserve the current and fulfill the Takahashi-Ward identities [57].

Promoting the global gauge symmetry of the matter field to a local gauge symmetry circumvents this issue, as due to Noether's second theorem the electric current and thereby electric charge become conserved quantities even in 'off-shell' fluctuations.

We should therefore construct a locally gauge-invariant coupled Lagrangian. This is possible by means of the Noether construction [48]. Since we know

$$\delta \mathcal{L}_{\text{field}} = -q(\partial_{\mu}\Lambda) j^{\mu} + q A_{\mu}(\delta j^{\mu}) \,, \tag{2.23}$$

we can cancel the first term, if the matter fields transform as $\delta\psi = -iq\Lambda\psi$ and $\delta\bar{\psi} = iq\Lambda\bar{\psi}$ corresponding to the local unitary transformation $\psi' = e^{-iq\Lambda}\psi$, $\bar{\psi}' = e^{iq\Lambda}\bar{\psi}$. We obtain

$$\delta \mathcal{L}_{\text{matter}} = i\delta(\bar{\psi}\partial_t\psi) - \frac{1}{2m}\delta\left((\nabla\bar{\psi})(\nabla\psi)\right) - V\delta(\bar{\psi}\psi) \tag{2.24}$$

$$= q(c^{-1}\partial_t\Lambda) j^0 + q(\nabla\Lambda)\mathbf{j} = q(\partial_{\mu}\Lambda) j^{\mu} \,. \tag{2.25}$$

Under this transformation of the fields the current is affected as well:

$$qA_\mu(\delta j^\mu) = q\frac{i\mathbf{A}}{2m}\delta((\nabla\bar{\psi})\psi - (\nabla\psi)\bar{\psi}) \tag{2.26}$$

$$= -q^2(\nabla\Lambda)\frac{\mathbf{A}}{m}\bar{\psi}\psi\,. \tag{2.27}$$

We can counteract the currents contribution by adding an $\mathbf{A}^2$-term to the action:

$$\delta\left(-\frac{q^2\mathbf{A}\cdot\mathbf{A}}{2m}\bar{\psi}\psi\right) = -q^2(\delta\mathbf{A})\frac{\mathbf{A}}{m}\bar{\psi}\psi = q^2(\nabla\Lambda)\frac{\mathbf{A}}{m}\bar{\psi}\psi \tag{2.28}$$

The A^2-term we have to add does not involve the scalar potential ϕ due to our starting point only having one time derivative. If we had we used the Klein-Gordon instead of the Schroedinger action, our construction would produce the scalar quantum electrodynamics with a Lorentz invariant $A_\mu A^\mu$-term [48, 49]. In contrast, the Dirac action does not need an A^2-term to be gauge invariant [56, 58]. Taking its non-relativistic limit and reducing the description from the four component spinor to the two matter spin components, the minimally coupled Schroedinger including its A^2-term is recovered [59].

The proper gauge-invariant action is therefore the minimally coupled Schroedinger action

$$\begin{aligned}\mathcal{L}_{\text{coupled}} &= -\frac{1}{4\mu_0}F_{\mu\nu}F^{\mu\nu} + qA_\mu j^\mu - \frac{q^2\mathbf{A}\cdot\mathbf{A}}{2m}\bar{\psi}\psi \\ &\quad + i\bar{\psi}\partial_t\psi - \frac{1}{2m}(\nabla\bar{\psi})(\nabla\psi) - V\bar{\psi}\psi \qquad (2.29)\\ &= -\frac{1}{4\mu_0}F_{\mu\nu}F^{\mu\nu} + i\bar{\psi}\partial_t\psi - \frac{1}{2m}(\bar{\nabla}\bar{\psi})(\nabla\psi) - \tilde{V}\bar{\psi}\psi, \qquad (2.30)\end{aligned}$$

where in the last step we have used the shorthand $\bar{\nabla} = \nabla + iq\mathbf{A}$, $\nabla = \nabla - iq\mathbf{A}$ and $\tilde{V} = V + q\phi$.

The conserved current of this Lagrangian is now a hybrid of the light and matter fields, that we can write as the functional derivative of the matter fields $\mathcal{L}_{\text{matter,coupled}} = \mathcal{L}_{\text{coupled}} - \mathcal{L}_{\text{field}}$ [53]:

$$j^\mu = \frac{\delta\mathcal{L}_{\text{matter,coupled}}}{\delta A_\mu} \tag{2.31}$$

$$j^0 = qc\bar{\psi}\psi \tag{2.32}$$

$$\mathbf{j} = \frac{iq}{2m}\left((\bar{\nabla}\bar{\psi})\psi - \bar{\psi}(\nabla\psi)\right)\,. \tag{2.33}$$

2.2.4 Hamiltonian formulation

Since we want to use a Hamiltonian formulation for the rest of this thesis, let us perform a Legendre transform replacing the time derivatives of the fields using the canonical momentum densities.

$$\pi = \frac{\partial\mathcal{L}}{\partial(\partial_t\psi)} = i\bar{\psi} \tag{2.34}$$

$$\Pi^\nu = \frac{\partial\mathcal{L}}{\partial(\partial_t A_\nu)} = -c\epsilon_0 F^{0\nu}, \tag{2.35}$$

where importantly, we find $\Pi^0 = 0$ and subsequently $\Pi^\nu = \Pi_\nu$. We can identify the other components as $\mathbf{\Pi} = -\epsilon_0 \mathbf{E}$. The lack of canonical momentum Π^0 is an artifact of the local gauge symmetry. Fixing the gauge and thereby removing redundancies in our description is required for the proper canonical commutation relations [60]. To keep a more familiar form for the field operators, we will continue parametrizing the canonical matter momentum density using the field $\bar{\psi} = -i\pi$. We obtain the Hamiltonian density

$$\begin{aligned}\mathcal{H} &= i\bar{\psi}(\partial_t \psi) + \Pi^\nu(\partial_t A_\nu) - \mathcal{L}_{\text{coupled}} && (2.36)\\ &\overset{P.I.}{=} \frac{1}{2}\left(\epsilon_0^{-1}\mathbf{\Pi}^2 + \mu_0^{-1}(\nabla \times \mathbf{A})^2\right) + \frac{1}{2m}(\not{\nabla}\bar{\psi})(\not{\nabla}\psi) + V\bar{\psi}\psi \\ &\quad + A^0(c\nabla\mathbf{\Pi} + qc\bar{\psi}\psi), && (2.37)\end{aligned}$$

where we have used $\mathbf{\Pi}(\nabla A^0) \overset{P.I.}{=} -(\nabla\mathbf{\Pi})A^0$, which holds true under integration by parts with vanishing boundary terms, and $F_{ij}F^{ij} = 2\mathbf{B}^2$. In this form, A^0 can be identified as Lagrange multiplier, that ensures the electric field follows Gauss's law. Using the functional derivative, which in our case works out as

$$\frac{\delta f(\phi, \nabla\phi)}{\delta\phi} = \frac{\partial f}{\partial\phi} - \nabla\frac{\partial f}{\partial(\nabla\phi)} \tag{2.38}$$

we can derive the Hamiltonian equations of motion:

$$i\frac{d}{dt}\psi = \left(\tilde{V} - \frac{1}{2m}\not{\nabla}^2\right)\psi \tag{2.39a}$$

$$-i\frac{d}{dt}\bar{\psi} = \left(\tilde{V} - \frac{1}{2m}\not{\nabla}^2\right)\bar{\psi} \tag{2.39b}$$

$$\frac{d}{dt}A^i = \epsilon_0^{-1}\Pi^i - c\partial^i A^0 \tag{2.39c}$$

$$\frac{d}{dt}\Pi^i = j^i + \mu_0^{-1}\nabla^2 A^i - \mu_0^{-1}\partial^i(\nabla\mathbf{A}) \tag{2.39d}$$

$$\frac{d}{dt}\Pi^0 = c\nabla\mathbf{\Pi} + qc\bar{\psi}\psi = 0 \tag{2.39e}$$

These form a familiar set of equations: Equations (2.39a) and (2.39b) are the minimally coupled Schroedinger equation and its conjugate. The boundary condition imposed by the Lagrange multiplier A_0 provides equation (2.39e), which is equivalent to equation (2.10). Lastly, taking the time derivative of equation (2.39c) in conjunction with equation (2.39d) produces equation (2.11).

2.3 Working with quantized matter

2.3.1 Canonical quantization of the matter fields

Since the matter field does not come with any constraints and all canonical momenta are well defined, we can canonically quantize it by replacing the classical Poisson brackets of the fields

$$\{f, g\} = \int d^3\mathbf{r}\left(\frac{\delta f}{\delta\psi(\mathbf{r}, t)}\frac{\delta g}{\delta\pi(\mathbf{r}, t)} - \frac{\delta f}{\delta\pi(\mathbf{r}, t)}\frac{\delta g}{\delta\psi(\mathbf{r}, t)}\right), \tag{2.40}$$

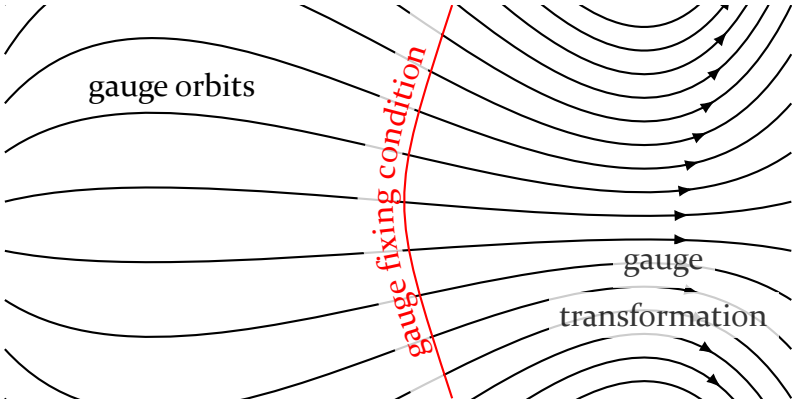

Figure 2.1: Map of all field configurations A_μ; Configurations connected via gauge transformation $A'_\mu = A_\mu + \partial_\mu \Lambda$ (arrows) lie on the same gauge orbit indicated by the black lines. A gauge fixing condition indicated by the red line cuts through every gauge orbit exactly once, such that the mapping between physical fields and gauge fields is bijective under the gauge condition.

with canonical commutators of the field operators:

$$\{\psi(\mathbf{r},t),\pi(\mathbf{r}',t)\} = \delta(\mathbf{r}-\mathbf{r}') \tag{2.41a}$$
$$\{\psi(\mathbf{r},t),\psi(\mathbf{r}',t)\} = 0 \tag{2.41b}$$
$$\{\pi(\mathbf{r},t),\pi(\mathbf{r}',t)\} = 0 \tag{2.41c}$$
$$\{O,H\} + \partial_t O = \dot{O} \tag{2.41d}$$
$$\left[\hat{\psi}(\mathbf{r},t),\hat{\psi}^\dagger(\mathbf{r}',t)\right] = \delta(\mathbf{r}-\mathbf{r}') \tag{2.41e}$$
$$\left[\hat{\psi}(\mathbf{r},t),\hat{\psi}(\mathbf{r}',t)\right] = 0 \tag{2.41f}$$
$$\left[\hat{\psi}^\dagger(\mathbf{r},t),\hat{\psi}^\dagger(\mathbf{r}',t)\right] = 0 \tag{2.41g}$$
$$-i[\hat{O},\hat{H}] + \partial_t \hat{O} = \dot{\hat{O}} \tag{2.41h}$$

By choosing the commutator, the quantized field will have a bosonic many-particle statistic. The quantization of the classical Schroedinger field is however also possible when imposing the anti-commutator on the quantized field operators. In this case the quantized field carries the fermionic anti-commutation relations [47]. Since we do not rely on the exchange statistics in the following derivations, we explicitly show the derivation for a bosonic field, but will use the fermionic version for the electrons in the main part of this thesis. We will furthermore from now on only consider quantized matter fields and therefore drop the hat superscript of all matter field operators.

To write the Hamiltonian density in terms of the field operators and a single differential operator acting on $\psi(\mathbf{r},t)$, we can integrate by parts while keeping the order of operators:

$$(\nabla\psi^\dagger)(\nabla\psi) \overset{P.I.}{=} \psi^\dagger(i\nabla + q\mathbf{A})^2\psi = \psi^\dagger(\mathbf{p} - q\mathbf{A})^2\psi \tag{2.42}$$

using the differential operator $\mathbf{p} = -i\nabla$. The above outlined quantization generalizes for the many-particle case, where we consider multiple fields ψ_i with corresponding commutation relations with the conjugate and among each other.

2.3.2 Gauge fixing to the Coulomb gauge

As a last simplifying step before we turn to linear response theory and a quantization of the electromagnetic fields, we will fix the gauge of our description. Since the crystal lattice already breaks the Lorentz invariance, we do not lose any generality by choosing a gauge condition that also lacks Lorentz invariance. The common choice is the Coulomb gauge where the gauge fixing condition

$$\nabla \cdot \mathbf{A} = 0 \tag{2.43}$$

holds. For the gauge to be properly fixed, this condition has to pick a single field configuration from each gauge orbit, which are gauge field configurations connected via gauge transformation leading to the same physical fields. This is illustrated in Figure 2.1 and fulfilled for the Coulomb gauge [48, 56].

This gauge has three advantages:
(i) It separates the equations of motion for the scalar and vector potential. Since the vector potential becomes fully transverse, the boundary condition imposed on our Hamiltonian simplifies to the Poisson equation for the scalar potential:

$$0 = \nabla\mathbf{\Pi} + q\psi^\dagger\psi \tag{2.44}$$
$$-\nabla^2\phi = q\psi^\dagger\psi/\epsilon_0 \tag{2.45}$$

We can solve it using the Green's function of the Laplace operator:

$$\phi(\mathbf{r},t) = \int d^3\mathbf{r}' \frac{q\psi^\dagger(\mathbf{r}',t)\psi(\mathbf{r}',t)}{4\pi\epsilon_0|\mathbf{r}-\mathbf{r}'|} \tag{2.46}$$

Using this relation, we can simplify the kinetic term of the electromagnetic field by separating transverse and longitudinal components [47, 49, 56] as

$$\epsilon_0^{-1}\mathbf{\Pi}^2 = \epsilon_0^{-1}(\epsilon_0\partial_t\mathbf{A} + \epsilon_0\nabla\phi)^2 \tag{2.47}$$
$$\overset{P.I.}{=} \epsilon_0(\partial_t\mathbf{A})^2 - 2\epsilon_0(\partial_t\nabla\mathbf{A})\phi - \epsilon_0\phi(\nabla^2\phi) \tag{2.48}$$
$$= \epsilon_0(\partial_t\mathbf{A})^2 + \underbrace{\frac{q^2}{4\pi\epsilon_0}\int d^3\mathbf{r}' \frac{\psi^\dagger(\mathbf{r}',t)\psi(\mathbf{r}',t)\psi^\dagger(\mathbf{r},t)\psi(\mathbf{r},t)}{|\mathbf{r}-\mathbf{r}'|}}_{H_{\text{int}}} . \tag{2.49}$$

We can identify two contributions: The square of the transverse electric field (since $\mathbf{E}^\perp = -\partial_t\mathbf{A}$) and an instantaneous electrostatic density-density interaction from the longitudinal contribution[6]. The latter is usually used to include the electrostatic interaction between charged particles. We can therefore use existing solutions containing this type of electrostatic interaction as an appropriate sparse basis for our fields. E.g. in quantum optics the orbitals of the Hydrogen atom are commonly used, whereas in condensed matter context Bloch bands or Wannier orbitals are often times useful. Since the treatment of electrostatic interaction remains classical and reliant on equation (2.46), this approach is not exact. For the classical case, it can miss out on modifications of equation (2.46) through deliberate screening via Coulomb engineering [62, 63]. Quantum effects renormalizing the electrostatic interaction, such as the Lamb shift, are absent as well. The projection to few states or bands for an effective low-energy description usually does not preserve the gauge invariance of our gauge-fixed continuum model. If there is no clear separation of energy scales to justify this truncation, observables can become dependent on the truncation and the chosen gauge. In Section 2.4.3 we will show a basis that somewhat alleviates the impact of matter Hilbert space truncations.

(ii) The remaining equations of motion are no longer singular and allow for the canonical quantization of the electromagnetic field. Since the scalar potential is implicitly linked to the matter degrees of freedom, it is no longer an independent dynamic degree of freedom. The remaining ones are the transverse vector potential $\mathbf{A}$ and its conjugate momentum $\mathbf{\Pi}^\perp$. The

[6] The lack of retardation in this formulation of the electrostatic potential is an artifact of evaluating Maxwell's equations in Coulomb gauge. When the equations of motion are evaluated, the retardation effects are recovered when both the longitudinal field of electrostatics and the transverse radiation field are combined [61].

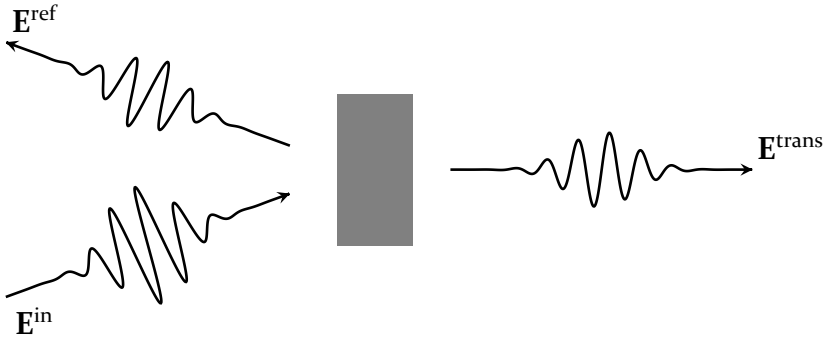

Figure 2.2: Sketch of the experimental setup. Incoming radiation described by the electric field $E^{\text{in}}(\omega)$ is reflected (E^{ref}) and transmitted E^{trans}. Depending on the experimental setup either of these fields is measured to provide the retarded Green's function of equation 2.52, as $\omega^{-1}E^{\text{in}}(\omega) = A^{\text{in}}$ and $\omega^{-1}E^{\text{ref/trans}} = A^{\text{out}}$.

quantization can further be simplified by a normal mode expansion [64, 65] of the resulting wave equation

$$\frac{1}{c^2}\frac{\partial^2 \mathbf{A}}{\partial t^2} - \nabla^2 \mathbf{A} = \mu_0 \mathbf{j}^{\perp}, \tag{2.50}$$

where we have decomposed the current into a transverse and longitudinal part $\mathbf{j} = \mathbf{j}^{\perp} + \mathbf{j}^{L}$ with $\nabla \cdot \mathbf{j}^{\perp} = 0$ and $\nabla \times \mathbf{j}^{L} = 0$.

(iii) The Coulomb condition leads to $[\mathbf{p}, \mathbf{A}] = 0$, which simplifies some computations.

We obtain the Hamiltonian

$$\begin{aligned} H = &\int d^3\mathbf{r} \frac{1}{2}\left(\epsilon_0^{-1}\left(\mathbf{\Pi}^{\perp}\right)^2 + \mu_0^{-1}(\nabla \times \mathbf{A})^2\right) \\ &+ \frac{1}{2m}\psi^{\dagger}(\mathbf{p} - q\mathbf{A})^2\psi + \psi^{\dagger}V\psi + H_{\text{int}}, \end{aligned} \tag{2.51}$$

where $\mathbf{A}$ denotes the transverse vector potential obeying the Coulomb gauge condition (2.43) and the transverse electric field $\mathbf{\Pi}^{\perp} = \epsilon_0 \partial_t \mathbf{A}$ is its conjugate momentum.

2.3.3 Linear response in interacting matter

In Chapter 3 we want to compute the optical properties of an interacting correlated material as they are probed by a spectroscopy measurement [66, 67]. Such measurements can be accomplished by either measuring the reflected or transmitted field (see Figure 2.2). As we will see, both setups can provide the same information. For the optical frequency range we are interested in, the wavelength and characteristic length scales of the material are still separated by multiple orders of magnitude. It is therefore valid to utilize the macroscopic Maxwell equations and coarse grain the dynamics of the sample. The free charges and currents are the ones creating and measuring the probe field, while all charges and currents in the material are bound and therefore incorporated using the materials dielectric function ϵ. We can describe the experimental observable as the expectation value

$$\left\langle \mathbf{A}^{\text{out}}(\mathbf{r}_2, t_2)\mathbf{A}^{\text{in}}(\mathbf{r}_1, t_1)\right\rangle \theta(t_2 - t_1) = G^R(2,1), \tag{2.52}$$

which is a retarded Green's function. Since it is difficult to solve the Hamiltonian generating the time evolution from t_1 to t_2 fully, we want to employ an expansion for $G^R(2,1)$ in the interaction

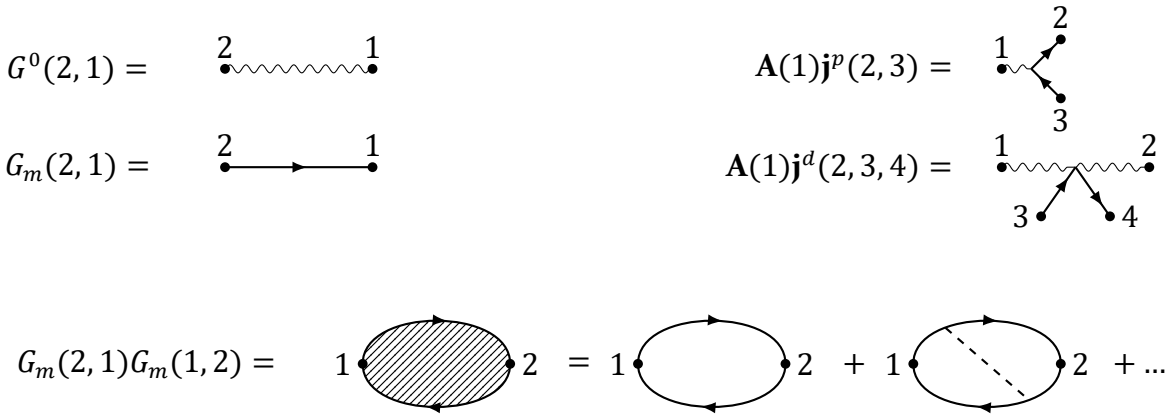

Figure 2.3: Building blocks of a diagrammatic expansion of the Hamiltonian (2.53). Top left: Propagators of H_0; the non-interacting electromagnetic field propagator is G^0 and the fully longitudinally interacting matter propagator is G_m. Top right: Vertices allowed by H_1; they are to be understood as without the attached propagators and are equivalent to those found in literature for scalar electrodynamics [49]. Bottom: Fully longitudinally interacting fermionic bubble; just like the matter propagators matter bubbles contain the full longitudinal Coulomb interaction, i.e. all vertex corrections through H_{int} indicated by the dashed line.

picture following Abrikosov, Gorkov and Dzyaloshinski [9]. We split the Hamiltonian density as

$$\begin{aligned} H_0(\mathbf{r}) &= \frac{1}{2}\left(\epsilon_0(\partial_t\mathbf{A})^2 + \mu_0^{-1}(\nabla\times\mathbf{A})^2\right) + \frac{1}{2m}\psi^\dagger\mathbf{p}^2\psi + V\psi^\dagger\psi + H_{\text{int}} \\ H_1(\mathbf{r}) &= \mathbf{A}\cdot\mathbf{j}^\perp \end{aligned} \tag{2.53}$$

with $\mathbf{j}^\perp = -\delta H/\delta\mathbf{A}$ (see equation (2.31)). We can split the current into a diamagnetic contribution $\mathbf{j}^d(\mathbf{A})$ and a paramagnetic contribution $\mathbf{j}^p$ as

$$\mathbf{j}^d(\mathbf{r}) = \frac{q^2}{m}\mathbf{A}(\mathbf{r})\psi^\dagger(\mathbf{r})\psi(\mathbf{r}) \tag{2.54}$$

$$\mathbf{j}^p(\mathbf{r}) = \frac{q}{m}\psi^\dagger(\mathbf{r})\mathbf{p}\psi(\mathbf{r})\,. \tag{2.55}$$

This allows us to write the interacting Green's function as a series of the interaction H_1. We can represent this series by Feynman diagrams, whose building blocks shown in Figure 2.3. In H_0 the classical field does not interact with the matter. We denote the resulting classical Green's function of the first summand of H_0 describing its propagation as $G_0(2,1)$.

The second half of H_0 describes a longitudinally (but not transversally) interacting matter field. In this section we will show, that from the dynamics of H_0 and its fully (longitudinally) interacting propagator G_m we only need the current-current correlation function (see equation (2.81)). We therefore perform the diagrammatic expansion of G^R in terms of the light-matter coupling and postpone all computation involving only matter to Chapter 3, where we explicitly perform this for a microscopic model of the material TiOCl using exact diagonalization.

The expansion is simplified if we assume temporal and spatial translational invariance and transform the equations of motion of the transverse vector potential (2.50) to momentum and frequency domain. These approximations are valid if the material is in an equilibrium

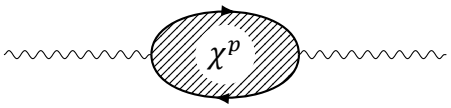

(a) $\mathbf{j}^p$-bubble diagram

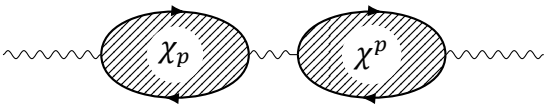

(b) $\mathbf{j}^p$-two bubble diagram

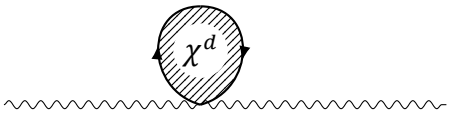

(c) $\mathbf{j}^d$-bubble diagram

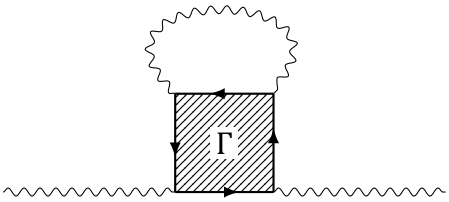

(d) Non-linear diagram 1

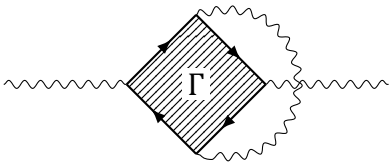

(e) Non-linear diagram 2

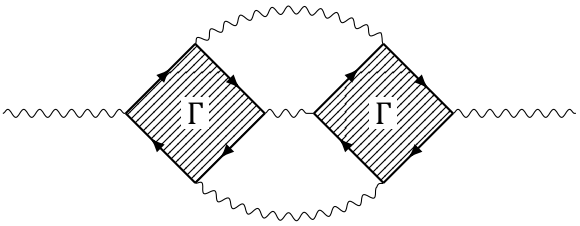

(f) Non-linear diagram 3

Figure 2.4: A selection of diagrams contributing to the series of propagators for the fully interacting light propagator G^R in parts adapted from Abrikosov *et al.* [9]. χ^p describes the matter propagator due to twice coupling with the paramagnetic current, which can be computed as the retarded current-current correlation function (see equation(2.78)). χ^d describes the matter propagator due to the diamagnetic coupling, which is the matter density (see equation (2.70)). Γ denotes a higher order four-current propagator.

state and we solely consider long wavelengths $\lambda \gg a$, where a is some characteristic matter length scale, such as the lattice constant. The defining equation for $\underline{\underline{G}}^0(\omega, \mathbf{k})$ is therefore

$$(c^{-2}\omega_2^2 - \mathbf{k}_2^2)G_{ij}^0(\omega_2, \omega_1, \mathbf{k}_2, \mathbf{k}_1) = \delta(\omega_2 - \omega_1)\delta(\mathbf{k}_2 - \mathbf{k}_1)\delta_{ij}^{\perp}, \tag{2.56}$$

such that

$$\mathbf{A}(\omega_2, \mathbf{k}_2) = -\mu_0 \int\int d\omega_1 d^3\mathbf{k}_1 \underline{\underline{G}}^0(\omega_2, \omega_1, \mathbf{k}_2, \mathbf{k}_1)\mathbf{j}(\omega_1, \mathbf{k}_1). \tag{2.57}$$

Therein $\delta_{ij}^{\perp} = \delta_{ij} - k_{2,i}k_{2,j}/k_2^2$ projects the current $\mathbf{j}(\omega_1, \mathbf{k}_1)$ on its transverse component $\mathbf{j}^{\perp}(\omega_1, \mathbf{k}_1)$. Solving for the Green's function we find

$$G_{ij}^0(\omega_2, \omega_1, \mathbf{k}_2, \mathbf{k}_1) = \frac{\delta(\omega_2 - \omega_1)\delta^3(\mathbf{k}_2 - \mathbf{k}_1)\delta_{ij}^{\perp}}{c^{-2}\omega_2^2 - \mathbf{k}_1^2}. \tag{2.58}$$

Due to the identities enforced by the numerator we can drop one set of indices. Our goal now is to use a diagramatic expansion of the interacting electromagnetic field propagator G^R using G^0, G_m and H_1. Therein H_0 defines the edges G^0, G_m of our diagrams (see top left in Figure 2.3) and H_1 dictates the types of vertices in the diagrams (see top right Figure 2.3). We denote G^0 by wavy lines and G_m by the thick lines with incoming and outgoing arrows corresponding to the fermionic field operators $\psi, \psi^{\dagger}$. Fermionic loops are shaded to indicate, that we do not only account for the matter propagators G_m forming the loop to be fully interacting but the loop itself also containing all vertex corrections due to the (screened) instantaneous Coulomb interaction of H_{int} between the propagators (see bottom of Figure 2.3). As G^R describes the propagator of some incoming field on its journey to become some outgoing field, all of the diagrams we have to consider have two wavy lines as open ends. To obtain G, we have to

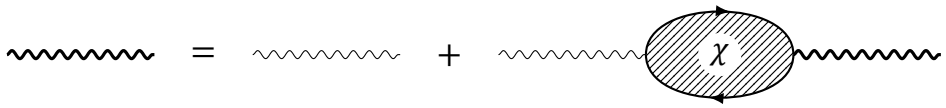

Figure 2.5: Self similarity of the fully interacting electromagnetic field propagator G indicated by a thick wavy line in terms of the non-interaction propagator G^0 and the combined paramagnetic and diagmagnetic susceptibility $\chi = \chi^p + \chi^d$.

sketch all diagrams, translate them to the corresponding product of Green's functions and integrate over all internal degrees of freedom. Figure 2.4 contains some of the infinite series of diagrams.

Without making additional assumptions about the material such as a sample thickness, there is no clear perturbative order at which we can truncate the series. The long wavelength approximation does justify neglecting many diagrams: In momentum space it limits the range of momenta we allow for radiation to some cutoff $k_0 \ll a^{-1}$. Due to conservation of momentum at each vertex, these bounds also limit the momentum range over which other connected propagators are integrated. Since these would usually be integrated over a much larger momentum range of the order of a^{-1}, diagrams scale as $k_0/a \ll 1$ for every such integration they contain. Of all diagrams we can construct, there is only a small subset which does not contain such integrations. Only where the momentum and energy of all electromagnetic field propagators are fully constrained by energy and momentum conservation to the external ends of the diagrams, no matter integration is limited by the cutoff. This is the case, when the diagram fully narrows down to these propagators, such that they have to carry the energy and momentum of the external edges. Looking at the sample diagrams in Figure 2.4, we can see that this is only the case for Diagrams 2.4a, 2.4b and 2.4c. Diagrams 2.4d, 2.4e contain one such constrained integration and Diagram 2.4f two.

Translating this argument to real space, we can obtain a more physical intuition on these scaling relations between diagrams: The electromagnetic propagator has only a very coarse-grained view of the matter system as $\lambda \gg a$. For a closed electromagnetic loop to appear, the propagating field has to interact twice with the same matter quasiparticle (see Diagram 2.4d) or a coherently scattered quasiparticle connected to its original emitter via some other propagators (see Diagrams 2.4e, 2.4f). Due to the coarse graining, there are however of the order $\lambda/a \gg 1$ other particles present, that are not yet involved in the diagram. Scattering with these is incoherent as all involved phases are random. Repeated incoherent scattering with random particles is therefore much more likely than repeated coherent scattering. The dominant diagrams are therefore bubble diagrams connected by the electromagnetic field propagator. The same approximation is usually used in the treatment of the longitudinal field to renormalize the two particle vertex, which describes the two particle interaction, and known as random-phase approximation (RPA) [46, 68].

In order to avoid having to truncate our series, we can leverage the self-similarity of the fully interacting propagator, that consists of the sum of all bubble diagrams, diagrammatically represented in Figure 2.5: The fully interacting propagator G^R represented by a thick wavy line is the infinite series of all bubble diagrams. The series we obtain by attaching a susceptibility χ-bubble and a non-interacting propagator G^0 to G^R is G^R with the leading term G^0 missing as all diagrams have at least one χ-bubble. Analytically, this self-similarity leads to the Dyson equation

$$G(2,1) = G^0(2,1) + \iint d3d4 G^0(2,3)\chi(3,4)G(4,1)\,, \tag{2.59}$$

where the integration over the internal degrees of freedom 3, 4 are simplified trivially, since all quantities are diagonal in frequency and momentum. If $H_0 - \chi$ is not singular[7], we can rephrase the fully interacting propagator in terms of the non interacting one and the susceptibility:

$$G = \frac{G^0}{1 - G^0 \chi}\,. \tag{2.60}$$

Since the assumptions, that we used to compute G are the same as the ones underlying the macroscopic Maxwell equations, we can find a relation between χ and the dielectric function ϵ. Using equation (2.5f)

$$\mathbf{D}(\omega) = \epsilon(\omega)\mathbf{E}(\omega)\,, \tag{2.61}$$

we find the macroscopic wave equation for the **A**-field:

$$(\mu_0 \epsilon(\omega)\omega^2 - \mathbf{k}^2)\mathbf{A} = -\mu_0 \mathbf{j}_{\text{free}}\,. \tag{2.62}$$

It similarly gives rise to a Green's function

$$G^\epsilon(\omega, \mathbf{k}) = \frac{1}{\mu_0 \epsilon(\omega)\omega^2 - \mathbf{k}^2}\,. \tag{2.63}$$

Equating these Green's functions, we obtain

$$\chi = \mu_0 \omega^2 (\epsilon_0 - \epsilon(\omega)) \tag{2.64}$$

$$\epsilon(\omega) = \epsilon_0 - \frac{\chi}{\mu_0 \omega^2}. \tag{2.65}$$

Furthermore, we can relate these quantities to the bound current:

$$\mathbf{j}_{\text{bound}} = \mathbf{j} - \mathbf{j}_{\text{free}} \tag{2.66}$$

$$= \partial_t (\mathbf{D} - \epsilon_0 \mathbf{E}) \tag{2.67}$$

$$= i\frac{\chi}{\mu_0 \omega}\mathbf{E} = \sigma \mathbf{E} \tag{2.68}$$

The imaginary part of χ/ω is therefore often called the optical conductivity[8] of the system.

Since the susceptibility χ does not contain any entanglement between the transverse electromagnetic field and matter fields, we can compute it solely from the matter part of H_0. It describes how an incoming field $A_j(1)$ is scattered to a single outgoing field $A_i(2)$ and is therefore the linear response kernel of our material [46][9]

$$A_i(t_2, r_2) = \int_{-\infty}^{\infty} dt_1 \chi_{ij}(t_2, t_1, r_2, r_1) A_j(t_2, r_2) + \mathcal{O}(A^2)\,. \tag{2.69}$$

[7] This would indicate an instability of the singular mode.

[8] Since it carries the full frequency dependence and not only the static part recovered as $\sigma_{\text{static}} = \lim_{\omega \to 0} \sigma(\omega)$.

[9] The non-linear response kernel would map e.g. three incoming fields to one outgoing field via the four-current correlation function Γ or two diamagnetic processes.

Since the diamagnetic current is directly proportional to $\mathbf{A}$, we obtain its linear response susceptibility taking the expectation value of the matter fields

$$\chi^d_{ij}(t_2, t_1, \mathbf{r}_2, \mathbf{r}_1) = \frac{q^2}{m} \langle n(t_2, \mathbf{r}_2) \rangle \, \delta(t_2 - t_1) \delta^3(\mathbf{r}_2 - \mathbf{r}_1) \delta_{ij} \tag{2.70}$$

with the density operator $n = \psi^\dagger \psi$.

The paramagnetic current couples indirectly. We therefore have to take into account that the paramagnetic current perturbs the state of the matter with this perturbation then being the origin of the outgoing radiation. We can account for this either by utilizing functional derivatives of the partition function [46] or by again employing the interaction picture [35, 46, 68] to linear order:

Given some matter Hamiltonian H_0 with equilibrium density operator ρ_0, we want to compute the deviation of some observable A from its equilibrium expectation value due to some generalized force $f(t)$, that couples to the operator B. Following the derivation of Czycholl [35] we use

$$H(t) = H_0 + f(t) B \,. \tag{2.71}$$

In the interaction picture, the time evolution of the density operator is governed by

$$\frac{d}{dt} \rho_I(t) = -i [B_I(t), \rho_I(t)] f(t) \,. \tag{2.72}$$

If the force is absent for $t \to -\infty$, we know $\rho(-\infty) = \rho_0$ allowing us to integrate the time evolution. Since equation (2.72) relates $\dot{\rho}(t)$ to $\rho(t)$, solving for $\rho(t)$ produces a series of infinitely nested commutators, which we truncate in linear order to

$$\rho_I(t) = \rho_0 - i \int_{-\infty}^{t} dt' [B_I(t'), \rho_0] f(t') + \mathcal{O}(f^2) \,. \tag{2.73}$$

Using this approximation for the density operator, we can evaluate the expectation value of A:

$$\langle A \rangle (t) = \mathrm{tr} \left(A_I(t) \rho(t) \right) \tag{2.74}$$

$$= \langle A \rangle - i \int_{-\infty}^{t} dt' \mathrm{tr} \left(A_I(t) [B_I(t'), \rho_0] f(t') \right) \tag{2.75}$$

$$= \langle A \rangle - i \int_{-\infty}^{\infty} dt' \mathrm{tr} \left(\rho_0 [A_I(t), B_I(t')] \right) \theta(t - t') f(t'), \tag{2.76}$$

where in the last step we have used the cyclic property of the trace. Comparing equation (2.76) and equation (2.69), we can identify Kubo's formula [69] for the susceptibility of A with respect to B as the retarded correlation function of A and B

$$\chi_{AB}(t, t') = -i \left\langle [A(t), B(t')] \right\rangle \theta(t - t') \,. \tag{2.77}$$

For the paramagnetic susceptibility, the incoming field acts as the generalized force $f(t') = \mathbf{A}(t')$ that couples via the paramagnetic current $B(t') = \mathbf{j}^p(t')$. The observable of interest is the paramagnetic current as well $A(t) = \mathbf{j}^p(t)$ since it acts as source for the outgoing field. We find

$$\chi^p_{ij}(t_2, t_1, \mathbf{r}_2, \mathbf{r}_1) = -i \left\langle [j_i(t_2, \mathbf{r}_2), j_j(t_1, \mathbf{r}_1)] \right\rangle \theta(t_2 - t_1) \,. \tag{2.78}$$

Lastly, if the material is translationally invariant and in equilibrium, $\chi(t_2, t_1, \mathbf{r}_2, \mathbf{r}_1) = \chi(t_2 - t_1, \mathbf{r}_2 - \mathbf{r}_1)$ allowing us to transform the response function to frequency and momentum space. These invariances lead to

$$\chi(\omega_2, \omega_1, \mathbf{q}_2, \mathbf{q}_1) = \chi(\omega_2, \mathbf{q}_2)\delta(\omega_2 + \omega_1)\delta^3(\mathbf{q}_2 + \mathbf{q}_1) \tag{2.79}$$

such that

$$\left\langle j_i(\omega, \mathbf{q}) \right\rangle = \chi_{ij}(\omega, \mathbf{q}) A_j(\omega, \mathbf{q}) \,. \tag{2.80}$$

Within linear response, the response is therefore at the same frequency as the generalized force[10]. For our susceptibility we obtain

$$\chi_{ab}(\omega, \mathbf{q}) = \frac{q^2}{m} \langle n \rangle \, \delta(\omega)\delta^3(\mathbf{q}) - i \int_0^\infty dt e^{i\omega t - \Gamma t} \left\langle [j_a(t, \mathbf{q}), j_b(0, -\mathbf{q})] \right\rangle \,, \tag{2.81}$$

where the broadening factor Γ ensures convergence of the Fourier transform and shifts the poles from the real axis to the lower half plane, such that $\chi_{ab}(\omega, \mathbf{q})$ is analytic in the complex upper half plane $\mathrm{Im}(\omega) \geq 0$. Since the analytic properties of the diamagnetic contribution is clear, let us check the paramagnetic contribution. We can employ the Lehmann representation, that expands χ in a complete eigenbasis $|\alpha\rangle, |\beta\rangle$ of H_0:

$$\chi^p_{ab}(\omega, \mathbf{q}) = Z^{-1} \sum_{\alpha,\beta} \frac{X_{a,\alpha\beta}(\mathbf{q}) X_{b,\beta\alpha}(-\mathbf{q})}{\omega + i\Gamma + E_\alpha - E_\beta} \left(e^{-\beta E_\alpha} - e^{-\beta E_\beta} \right) \tag{2.82}$$

with $X_{a,\alpha\beta}(\mathbf{q}) = \langle \alpha | \, j_a(\mathbf{q}) \, | \beta \rangle$ and $X_{b,\beta\alpha}(-\mathbf{q}) = \langle \beta | \, j_b(-\mathbf{q}) \, | \alpha \rangle$. Using

$$\mathrm{Im}\left(\frac{1}{x + i\Gamma} \right) = \frac{-\Gamma}{x^2 + \Gamma^2}, \tag{2.83}$$

we can understand the imaginary part $\chi_{aa}(\omega)$ as sum of Lorentz oscillators with its broadened poles at $\omega = E_\beta - E_\alpha$. At positive frequencies we therefore find $E_\beta > E_\alpha$ and therefore $e^{-\beta E_\alpha} - e^{-\beta E_\beta} > 0$. The weight of the poles at positive frequencies is therefore negative and flips its sign at $\omega = 0$.[11] The real part of the optical conductivity $\sigma(\omega)$ is therefore positive.

Going back to the experimental setting, we can conclude, that the real part of χ is accessible, by means of measuring the frequency-dependent reflectivity, which is related to $\mathrm{Re}(\epsilon(\omega))$ via the Fresnel equations [50]. In contrast, the optical conductivity $\sigma(\omega)$ describes the extinction of a beam in the material. It can therefore be measured via frequency-dependent transmission measurements allowing access to the imaginary part of $\chi(\omega)$. It is not necessary to perform

[10] Responses at different frequency therefore have their origin in some non-linear response, such as the processes outlined in the previous footnote.

[11] While we have made use of the thermal ensemble for this derivation, this relation extends to the non-equilibrium case as long as there is no population inversion: The weights of poles are determined by the difference in their occupation. Without any inversion, high energy states always have less population leading to a positive weight. If there is an inversion, the corresponding transition obtains a negative peak at the inversions frequency. This indicates lasing at that frequency, as incoming radiation is amplified.

both types of measurements to fully obtain χ, as it is an analytic function in the upper complex plane and its real and imaginary part are therefore connected via the Kramers-Kronig relations

$$\mathrm{Re}(\chi(\omega)) = \frac{1}{\pi}\mathcal{P}\int_{-\infty}^{\infty} d\omega' \frac{\mathrm{Im}(\omega')}{\omega' - \omega} \tag{2.84}$$

$$\mathrm{Im}(\chi(\omega)) = -\frac{1}{\pi}\mathcal{P}\int_{-\infty}^{\infty} d\omega' \frac{\mathrm{Re}(\omega')}{\omega' - \omega}, \tag{2.85}$$

where $\mathcal{P}$ denotes the Cauchy principal value of the integral.

2.4 Quantization of the electromagnetic field

2.4.1 Normal mode expansion with boundary conditions

Since the gauge-fixing condition removes the gauge ambiguity of our description, it is possible to quantize the electromagnetic field. The gauge condition leaves two linearly independent modes for each point in space for the three components of $\mathbf{A}$. These amount to the two transverse directions of polarization. In free space, we find

$$\begin{aligned} H(\mathbf{r}) = &\frac{1}{2}\left(\epsilon_0^{-1}(\mathbf{\Pi}^{\perp})^2 + \mu_0^{-1}(\nabla \times \mathbf{A})^2\right) \\ &+ \frac{1}{2m}\psi^{\dagger}(\mathbf{p} - q\mathbf{A})^2\psi + \psi^{\dagger}V\psi + H_{\mathrm{int}} \end{aligned} \tag{2.86}$$

with

$$[\psi(\mathbf{r}), \psi^{\dagger}(\mathbf{r}')] = \delta(\mathbf{r} - \mathbf{r}') \tag{2.87}$$

$$[A_i(\mathbf{r}), \mathbf{\Pi}_j^{\perp}(\mathbf{r}')] = i\delta^{\perp}(\mathbf{r} - \mathbf{r}')\delta_{ij}\,. \tag{2.88}$$

This free space Hamiltonian is able to describe the constrained electromagnetic field, e.g. of cavity or plasmonic settings, as long as the setting can be phrased as a boundary value problem for the free field.

We can expand the Hamiltonian in the solutions of the free electromagnetic field subject to these boundary conditions in a mode expansion using the modes μ. We can represent the field operator $\mathbf{A}(\mathbf{r}, t)$ through the operator A_μ:

$$A_\mu = \int d^3\mathbf{r}\mathbf{f}_\mu(\mathbf{r})\mathbf{A}(\mathbf{r}) \tag{2.89}$$

$$\mathbf{A}(\mathbf{r}) = \sum_\mu A_\mu \mathbf{f}_\mu^*(\mathbf{r})\,. \tag{2.90}$$

The transverse mode functions $\mathbf{f}_\mu(\mathbf{r})$ fulfill

$$\nabla \cdot \mathbf{f}_\mu(\mathbf{r}) = 0 \tag{2.91}$$

$$\frac{\omega_\mu^2}{c^2}\mathbf{f}_\mu(\mathbf{r}) = \nabla \times \left(\nabla \times \mathbf{f}_\mu(\mathbf{r})\right) \tag{2.92}$$

in addition to our imposed boundary conditions on the field. This can be understood as eigenvalue problem on the space of transverse functions, where we look for the eigenvectors $\mathbf{f}_\mu$ to the eigenvalues ω_μ. The mode functions form a complete orthonormal basis of the

transverse functions on the domain of $\mathbf{A}(\mathbf{r}, t)$ suitable for the expansion of our transverse fields:

$$\int d^3\mathbf{r}\mathbf{f}_\mu^*(\mathbf{r}) \cdot \mathbf{f}_\nu(\mathbf{r}) = \delta_{\mu\nu} \tag{2.93}$$

$$\sum_\mu \mathbf{f}_\mu^*(\mathbf{r}) \cdot \mathbf{f}_\mu(\mathbf{r}') = \delta^\perp(\mathbf{r} - \mathbf{r}')\,. \tag{2.94}$$

Since $\mathbf{A}(\mathbf{r}) = \mathbf{A}^\dagger(\mathbf{r})$ is selfadjoint, we find

$$\sum_\mu A_\mu \mathbf{f}_\mu^*(\mathbf{r}) = \sum_\mu A_\mu^\dagger \mathbf{f}_\mu(\mathbf{r})\,, \tag{2.95}$$

which we can alternatively express as

$$A_\mu^\dagger = \sum_\nu U_{\mu\nu}^* A_\nu = \sum_\nu \int d^3\mathbf{r}\mathbf{f}_\mu^*(\mathbf{r})\mathbf{f}_\nu^*(\mathbf{r})A_\nu\,. \tag{2.96}$$

$U_{\mu\nu}$ vanishes for $\omega_\mu \neq \omega_\nu$. If the mode functions are fully real, its definition furthermore reduces to the orthogonality between mode functions leading to $U_{\mu\nu} = \delta_{\mu\nu}$. From the orthogonality relations (2.93) (2.94) we furthermore see that U is unitary, i.e. $\sum_\nu U_{\mu\nu}U_{\nu\lambda}^* = \delta_{\mu\lambda}$.

Integrating the vector potentials contribution in the Hamiltonian by parts

$$(\nabla \times \mathbf{A}(\mathbf{r}))^2 \overset{\text{P.I.}}{=} \mathbf{A}(\mathbf{r}) \cdot (\nabla \times (\nabla \times \mathbf{A}(\mathbf{r}))) \tag{2.97}$$

allows us to rewrite equation (2.92) as

$$\int d^3\mathbf{r}(\nabla \times \mathbf{A}(\mathbf{r}))^2 = c^{-2} \sum_\mu \omega_\mu^2 A_\mu^\dagger A_\mu\,. \tag{2.98}$$

We want to perform the same expansion for $\mathbf{\Pi}^\perp(\mathbf{r})$. In order to obtain the canonical commutation relations $[A_\mu, \Pi_\nu] = i\delta_{\mu\nu}$, we use

$$\mathbf{\Pi}^\perp(\mathbf{r}) = \sum_\mu \Pi_\mu \mathbf{f}_\mu^*(\mathbf{r}) \tag{2.99}$$

$$\Pi_\mu = \int d^3\mathbf{r}\mathbf{f}_\mu(\mathbf{r})\mathbf{\Pi}^\perp(\mathbf{r}) \tag{2.100}$$

$$\Pi_\mu^\dagger = \sum_\nu U_{\mu\nu}\Pi_\nu\,. \tag{2.101}$$

The kinetic term similarly becomes

$$\int d^3\mathbf{r}(\mathbf{\Pi}^\perp(\mathbf{r}))^2 = \sum_\mu \Pi_\mu^\dagger \Pi_\mu\,. \tag{2.102}$$

Put together we find

$$\frac{1}{2}\left(\epsilon_0^{-1}(\mathbf{\Pi}^\perp(\mathbf{r}))^2 + \mu_0^{-1}(\nabla \times \mathbf{A}(\mathbf{r}))^2\right) = \sum_\mu \frac{\Pi_\mu^\dagger \Pi_\mu}{2\epsilon_0} + \frac{1}{2}\epsilon_0\omega_\mu^2 A_\mu^\dagger A_\mu\,, \tag{2.103}$$

which is the quantum harmonic oscillator of mass ϵ_0 and frequency ω_μ for each mode μ. Expressing the Hamiltonian in terms of mode ladder operators $a_\mu, a_\mu^\dagger$ as

$$\Pi_\mu = i\sqrt{\frac{\epsilon_0\omega_\mu}{2}}\left(a_\mu - \sum_\nu U_{\mu\nu}^* a_\nu^\dagger\right) \tag{2.104}$$

$$A_\mu = \sqrt{\frac{1}{2\epsilon_0\omega_\mu}}\left(a_\mu^\dagger + \sum_\nu U_{\mu\nu} a_\nu\right), \tag{2.105}$$

we obtain

$$\sum_\mu \frac{\Pi_\mu^\dagger \Pi_\mu}{2\epsilon_0} + \sum_\mu \frac{\epsilon_0\omega_\mu^2 A_\mu^\dagger A_\mu}{2} = \sum_\mu \frac{\omega_\mu}{2}(a_\mu^\dagger a_\mu + a_\mu a_\mu^\dagger) \tag{2.106}$$

$$= \sum_\mu \omega_\mu a_\mu^\dagger a_\mu + C\,, \tag{2.107}$$

where the constant C is some formally infinite offset. While its derivatives can encode physical effects, such as Casimir forces [64, 70], we will neglect it throughout this thesis as the electromagnetic environment is kept constant.

To properly phrase the complete Hamiltonian in the mode expansion, we still need the field amplitude. We find

$$\mathbf{A}(\mathbf{r}) = \sum_\mu \sqrt{\frac{1}{2\epsilon_0\omega_\mu}}\left(a_\mu \mathbf{f}_\mu(\mathbf{r}) + a_\mu^\dagger \mathbf{f}_\mu^*(\mathbf{r})\right), \tag{2.108}$$

which leads to the mode-expanded minimally coupled Hamiltonian

$$H = \sum_\mu \omega_\mu a_\mu^\dagger a_\mu + \int d^3\mathbf{r}\psi^\dagger(\mathbf{r})V(\mathbf{r})\psi(\mathbf{r}) + H_{\text{int}}$$
$$+ \frac{1}{2m}\int d^3\mathbf{r}\psi^\dagger(\mathbf{r})\left(\mathbf{p} - \sum_\mu g_\mu\left(a_\mu \mathbf{f}_\mu(\mathbf{r}) + a_\mu^\dagger \mathbf{f}_\mu^*(\mathbf{r})\right)\right)^2 \psi(\mathbf{r})\,, \tag{2.109}$$

with $g_\mu = q\sqrt{1/2\epsilon_0\omega_\mu}$.

For a given set of boundary conditions this coupling constant is therefore fixed. There exists a peculiarity when considering bound electromagnetic modes in the condensed matter thermodynamic limit. If we just add additional matter fields to equation (2.109) while keeping the electromagnetic setting unchanged the combined energy of the coupled system is super-extensive. This is unsurprising as the coupling not only relies on g_μ, but also the mode function $\mathbf{f}_\mu(\mathbf{r})$. In any bound state it has to be normalized over its mode volume V_μ such that

$$1 = \int_{V_\mu} d^3\mathbf{r}\mathbf{f}_\mu^*(\mathbf{r})\mathbf{f}_\mu(\mathbf{r})\,. \tag{2.110}$$

Naively taking the thermodynamic limit fills this finite volume with an infinite number of matter fields leading to the unphysical super-extensive behavior. We should instead keep the matter density N/V_μ constant and increase the mode volume in the thermodynamic limit

accordingly. The mode function and thereby the light matter coupling therefore scale as $1/\sqrt{N}$ in the thermodynamic limit.

2.4.2 Normal mode expansion in a dielectric environment

In the previously outlined technique there are only two possible ways to modify the electromagnetic field: We can either impose boundaries or place matter fields. If we want to compute matter placed in the vicinity of optical components, both avenues have difficulties describing this setting. The former approach requires optical components with an infinite conductivity for sharp boundary conditions while the latter requires an explicit microscopic description of the matter fields of the optical components making computations infeasible. We can again resort to the macroscopic formulation of Maxwell's equations, which allows us to make a distinction between matter whose interactions with the fields is explicitly described and matter dressing the electromagnetic field through its polarizability. This, additionally, has the advantage that for a particular setting the renormalization of matter properties through the light-matter coupling can be continuously tracked from the vacuum setting all the way to a cavity setting [71], where the cavity acts as electromagnetic environment redistributing spectral density of the transverse electromagnetic field.

Instead of optical components imposing additional matter fields or boundary conditions, they impose a dielectric environment $\epsilon(\mathbf{r})$[12]. The most general description would furthermore include non-local and retardation effects in the dielectric function as $\epsilon = \epsilon(\mathbf{r}, \mathbf{r}', t, t')$ (see Section 2.3.3). If the length scales of the electromagnetic field and the dielectric separate we can however neglect this non locality. There are settings, such as the plasmonic near-field [72], where this is no longer guaranteed. In equilibrium the retardation leads to the frequency dependence of the dielectric function $\epsilon(\mathbf{r}, \omega)$. We will ignore this frequency dependency in the following derivation and assume the dielectric function to be constant over the frequency range we consider.

The explicitly described matter fields then act as source fields for the free charge and free current. In order to contain this distinction, we have to modify our classical field theory. Formulating equations (2.5e) and (2.5f) in terms of the scalar and vector potential, we obtain

$$-\nabla(\epsilon\nabla\phi) - \nabla(\epsilon\partial_t\mathbf{A}) = \rho_{\text{free}} \tag{2.111}$$

$$-\nabla^2\mathbf{A} + \nabla(\nabla\mathbf{A}) + \mu_0\partial_t(\epsilon\nabla\phi) + \mu_0\partial_t(\epsilon\partial_t\mathbf{A}) = \mu_0\mathbf{j}_{\text{free}}\,. \tag{2.112}$$

In covariant notation we can write this set of equations as

$$j^\mu_{\text{free}} = \partial_\nu G^{\mu\nu}\,, \tag{2.113}$$

with the macroscopic field tensor $G^{\mu\nu}$. It is componentwise equivalent to the microscopic field tensor $F^{\mu\nu}$ with the microscopic fields $\mathbf{E}, \mathbf{B}$ replaced by the macroscopic fields $\mathbf{D}$ and $\mathbf{H}$

[12] For ease of notation, we will drop the double underscore. In this section $\epsilon(\mathbf{r})$ does however denote a matrix-valued field.

according to equations (2.6),(2.7). This linear transformation of $\mathbf{E}$ and $\mathbf{B}$ by $\epsilon(\mathbf{r})$ and $\mu(\mathbf{r})$[13] can be phrased as a linear transformation of $F^{\mu\nu}$ using some fourth rank tensor $\epsilon^{\gamma\delta}_{\alpha\beta}$

$$G^{\mu\nu} = \epsilon^{\mu\nu}_{\alpha\beta} F^{\alpha\beta} \tag{2.114}$$
$$\epsilon^{ij}_{kl} = \mu_0^{-1} \delta^i_k \delta^j_l \tag{2.115}$$
$$\epsilon^{0i}_{0j} = c^2 \epsilon^i_j(\mathbf{r}) = \epsilon^{i0}_{j0} \tag{2.116}$$
$$\epsilon^{00}_{\mu\nu} = \epsilon^{0i}_{j0} = \epsilon^{i0}_{0j} = 0\,. \tag{2.117}$$

Using this tensor, the equations of motion are generated by the Lagrangian

$$\mathcal{L} = -\frac{1}{4} F_{\alpha\beta} \epsilon^{\alpha\beta}_{\gamma\delta} F^{\gamma\delta} + A_\mu j^\mu_{\text{free}} \tag{2.118}$$
$$= \frac{1}{2} (\mathbf{E} \cdot \mathbf{D} - \mathbf{B} \cdot \mathbf{H}) + A_\mu j^\mu_{\text{free}}\,. \tag{2.119}$$

Since the considerations of Section 2.2.3 still hold true for the dielectrically rescaled Lagrangian, the gauge-invariant light-matter coupled action also requires the presence of an $\mathbf{A}^2$-term.

If we perform the Legendre transformation to obtain the Hamiltonian density, we find the conjugate momentum of the vector potential to be the negative displacement field

$$\mathbf{\Pi} = \frac{\partial \mathcal{L}}{\partial(\partial_t A_\nu)} = -\epsilon \mathbf{E} = -\mathbf{D}. \tag{2.120}$$

The Hamiltonian density is therefore given by

$$\mathcal{H} = \frac{1}{2} (\mathbf{\Pi} \epsilon^{-1} \mathbf{\Pi} + \mu_0^{-1} (\nabla \times \mathbf{A})^2) + \frac{1}{2m} \bar{\psi} (\mathbf{p} - q\mathbf{A})^2 \psi + \bar{\psi} V \psi + A^0 (c \nabla \mathbf{\Pi} + q c \bar{\psi} \psi)\,, \tag{2.121}$$

where we have again used integration by parts to simplify the kinetic matter contribution and to identify A^0 as Lagrange multiplier that ensures our equations of motion produce the correct electrostatics. It furthermore necessitates that the dielectric tensor ϵ is invertible at every point of space.

We can again straightforwardly quantize the matter fields $\bar{\psi}, \psi$, while for A_μ the lack of canonical momentum Π^0 requires fixing the gauge. If we want the equation of motion for the scalar potential (see equation (2.111)) to again decouple from the vector potential, we can use the generalized Coulomb gauge [64, 65]

$$\nabla(\epsilon \mathbf{A}) = 0\,. \tag{2.122}$$

As a consequence, the vector potential is no longer fully transverse (but $\epsilon\mathbf{A}$ is). The generalized Poisson equation for the scalar potential is

$$-\nabla(\epsilon \nabla \phi) = \rho_{\text{free}}\,. \tag{2.123}$$

We can see that the scalar potential does no longer generate a gradient field and can in general contain a transverse component. A separation of $\mathbf{\Pi}$ in a transverse and longitudinal part is therefore no longer helpful, but we instead separate in the scalar potential part $\mathbf{\Pi}^\phi = \epsilon \nabla \phi$ and

[13] For simplicity, we continue assuming $\mu(\mathbf{r}) = \mu_0^{-1}$.

the vector potential part $\mathbf{\Pi}^A = \epsilon \partial_t \mathbf{A}$. It is straightforward to see, that for a spatially uniform scalar dielectric function, this reduces to longitudinal and transverse parts. Assuming, that we are able to solve equation (2.123) for some charge configuration, we can again simplify the Hamiltonian density

$$\begin{aligned} \mathbf{\Pi}\epsilon^{-1}\mathbf{\Pi} &= (\mathbf{\Pi}^\phi + \mathbf{\Pi}^A)\epsilon^{-1}(\mathbf{\Pi}^\phi + \mathbf{\Pi}^A) && (2.124)\\ &\overset{\text{P.I.}}{=} -\nabla(\epsilon\nabla\phi)\phi - \nabla(\epsilon\partial_t\mathbf{A})\phi - \phi(\nabla\epsilon\partial_t\mathbf{A}) + \mathbf{\Pi}^A\epsilon^{-1}\mathbf{\Pi}^A && (2.125)\\ &= \rho_{\text{free}}\phi + \mathbf{\Pi}^A\epsilon^{-1}\mathbf{\Pi}^A\,, && (2.126) \end{aligned}$$

where we have used integration by parts, that ϵ is symmetric, and ϕ solves the generalized Poisson equation.

This makes it again helpful to expand in solutions of the dielectrically screened electrostatic problem of $\psi, \psi^\dagger, \phi$, such as Bloch bands or Wannier orbitals obtained by density functional theory. Expanded in these orthonormal basis sets we just have to keep track of their electrostatic energy $H_{\text{static}} = \rho_{\text{free}}\phi$ manifesting as, e.g. energies of atomic orbitals, crystal field splitting and electron-electron interactions.

$\mathbf{\Pi}^A$ is still a dynamic degree of freedom. It is again helpful to expand the vector potential in $\bar{\epsilon}$-normal modes.

$$\nabla \cdot (\bar{\epsilon}(\mathbf{r})\mathbf{f}_\mu(\mathbf{r})) = 0\,, \tag{2.127}$$

where we use $\bar{\epsilon}(\mathbf{r}) = \epsilon(\mathbf{r})\epsilon_0^{-1}$ to make sure that the expansion in these modes does not change units. These modes $\mathbf{f}_\mu(\mathbf{r})$ are the solutions of the generalized eigenvalue problem

$$\nabla \times \big(\nabla \times \mathbf{f}_\mu(\mathbf{r})\big) = \frac{\omega_\mu^2}{c^2}\bar{\epsilon}(\mathbf{r})\mathbf{f}_\mu(\mathbf{r}) \tag{2.128}$$

and form a complete basis of the $\bar{\epsilon}$-normal subspace, i.e.[14]

$$\begin{aligned} \int d^3\mathbf{r}\mathbf{f}_\mu(\mathbf{r})\bar{\epsilon}(\mathbf{r})\mathbf{f}_\nu^*(\mathbf{r}) &= \delta_{\mu\nu} && (2.129)\\ \sum_\mu \mathbf{f}_\mu^*(\mathbf{r})\mathbf{f}_\mu(\mathbf{r}') &= \delta^\epsilon(\mathbf{r}-\mathbf{r}') && (2.130)\\ \mathbf{A}(\mathbf{r}) &= \int d^3\mathbf{r}'\bar{\epsilon}(\mathbf{r}')\delta^\epsilon(\mathbf{r}-\mathbf{r}')\mathbf{A}(\mathbf{r}')\,. && (2.131) \end{aligned}$$

$\delta^\epsilon(\mathbf{r}-\mathbf{r}')$ therein furthermore denotes the identity on the subspace of $\bar{\epsilon}$-normal functions $\mathbf{A}(\mathbf{r})$ and acts as generalization to the transverse $\delta^\perp(\mathbf{r}-\mathbf{r}')$ of the free space setting (see equation (2.94)).

We find $\mathbf{A}(\mathbf{r})$ and $\mathbf{\Pi}^A(\mathbf{r})$ in terms of these modes as

$$\begin{aligned} A_\mu &= \int d^3\mathbf{r}\bar{\epsilon}(\mathbf{r})\mathbf{f}_\mu(\mathbf{r})\mathbf{A}(\mathbf{r}) && (2.132)\\ \mathbf{A}(\mathbf{r}) &= \sum_\mu A_\mu \mathbf{f}_\mu^*(\mathbf{r}) && (2.133) \end{aligned}$$

[14] We require this strange normalization in order for the mode expansion to simplify our Hamiltonian density. It can however be shown, that for $\mathbf{g}_\mu(\mathbf{r}) = \sqrt{\bar{\epsilon}(\mathbf{r})}\mathbf{f}_\mu(\mathbf{r})$, this reduces to finding orthonormal modes in the usual sense [64]. Since $\epsilon(\mathbf{r})$ is diagonalizable, such $\mathbf{g}_\mu(\mathbf{r})$ can also be found.

and

$$\Pi_\mu = \int d^3\mathbf{r}\mathbf{f}_\mu(\mathbf{r})\mathbf{\Pi}^A(\mathbf{r}) \tag{2.134}$$

$$\mathbf{\Pi}^A(\mathbf{r}) = \sum_\mu \Pi_\mu \bar{\epsilon}(\mathbf{r})\mathbf{f}^*_\mu(\mathbf{r})\,. \tag{2.135}$$

Since both $\mathbf{\Pi}^A$ and $\mathbf{A}$ are real, we again find

$$\sum_\mu A_\mu \mathbf{f}^*_\mu(\mathbf{r}) = \sum_\mu A^\dagger_\mu \mathbf{f}_\mu(\mathbf{r}) \tag{2.136}$$

$$\sum_\mu \Pi_\mu \bar{\epsilon}(\mathbf{r})\mathbf{f}^*_\mu(\mathbf{r}) = \sum_\mu \Pi^\dagger_\mu \bar{\epsilon}(\mathbf{r})\mathbf{f}_\mu(\mathbf{r})\,. \tag{2.137}$$

Expanding both terms in the Hamiltonian in these modes, we obtain

$$\frac{1}{2\mu_0}\int d^3\mathbf{r}(\nabla\times\mathbf{A}(\mathbf{r}))^2 \overset{\text{P.I.}}{=} \frac{1}{2\mu_0}\int d^3\mathbf{r}\mathbf{A}(\mathbf{r})\,(\nabla\times(\nabla\times\mathbf{A}(\mathbf{r}))) \tag{2.138}$$

$$= \frac{1}{2}\epsilon_0 \sum_\mu \omega^2_\mu A^\dagger_\mu A_\mu \tag{2.139}$$

and

$$\int d^3\mathbf{r}\frac{1}{2}\mathbf{\Pi}^A(\mathbf{r})\epsilon^{-1}(\mathbf{r})\mathbf{\Pi}^A(\mathbf{r}) = \frac{1}{2\epsilon_0}\sum_\mu \Pi^\dagger_\mu \Pi_\mu\,. \tag{2.140}$$

Apart from having to solve for a more complicated set of mode functions $\mathbf{f}_\mu(\mathbf{r})$, the dielectric case leads to the same form of the Hamiltonian, i.e. a sum over harmonic oscillators. Using $U_{\mu\nu} = \int d^3\mathbf{r}\mathbf{f}_\mu(\mathbf{r})\bar{\epsilon}(\mathbf{r})\mathbf{f}_\nu(\mathbf{r})$, we can again express H in terms of the ladder operators (see equations (2.104)-(2.107))[15]. For the vector potential $\mathbf{A}(\mathbf{r})$ we obtain

$$\mathbf{A}(\mathbf{r}) = \sum_\mu \sqrt{\frac{1}{2\epsilon_0\omega_\mu}}\left(a^\dagger_\mu \mathbf{f}^*_\mu(\mathbf{r}) + a_\mu \mathbf{f}_\mu(\mathbf{r})\right), \tag{2.141}$$

where we have again used $\forall\mu,\nu : U_{\mu\nu} \neq 0 \Rightarrow \omega_\mu = \omega_\nu$.

The mode-expanded minimal-coupling Hamiltonian in a dielectric environment is therefore

$$H = \sum_\mu \omega_\mu a^\dagger a + \int d^3\mathbf{r}\psi^\dagger(\mathbf{r})V(\mathbf{r})\psi(\mathbf{r}) + H_{\text{static}}$$

$$+ \frac{1}{2m}\int d^3\mathbf{r}\psi^\dagger(\mathbf{r})\left(\mathbf{p} - \sum_\mu g_\mu\left(a_\mu \mathbf{f}_\mu(\mathbf{r}) + a^\dagger_\mu \mathbf{f}^*_\mu(\mathbf{r})\right)\right)^2 \psi(\mathbf{r}) \tag{2.142}$$

[15] We will again drop the constant C describing the vacuum energy. One should however pay attention to the fact that in taking the vacuum limit in which our dielectric environment vanishes $\epsilon(\mathbf{r}) \to \epsilon_0$, it is modified.

with

$$g_\mu = q\sqrt{\frac{1}{2\epsilon_0\omega_\mu}}\,. \tag{2.143}$$

If we assume that $\epsilon(\mathbf{r})$ is constant throughout the volume, where the material is located, the generalized Coulomb gauge and the Coulomb gauge are equivalent in that volume and we can use $[\mathbf{A}, \mathbf{p}] = 0$. This allows us to simplify the square and we find

$$\begin{aligned} H = &\int d^3\mathbf{r}\psi^\dagger(\mathbf{r})\left(\frac{\mathbf{p}^2}{2m} + V(\mathbf{r})\right)\psi(\mathbf{r}) + H_{\text{static}} + \sum_\mu \omega_\mu a_\mu^\dagger a_\mu \\ &- \sum_\mu \frac{g_\mu}{m}\int d^3\mathbf{r}\psi^\dagger(\mathbf{r})\left(a_\mu \mathbf{f}_\mu(\mathbf{r}) + a_\mu^\dagger \mathbf{f}_\mu^*(\mathbf{r})\right)\mathbf{p}\psi(\mathbf{r}) \\ &+ \frac{1}{2m}\int d^3\mathbf{r}\psi^\dagger(\mathbf{r})\psi(\mathbf{r})\left(\sum_\mu g_\mu\left(a_\mu \mathbf{f}(\mathbf{r}) + a_\mu^\dagger \mathbf{f}_\mu^*(\mathbf{r})\right)\right)^2 . \end{aligned} \tag{2.144}$$

We can identify the first line as the Hamiltonian of the (transversally-) uncoupled system H_0. The second line describes the paramagnetic coupling between the momentum and field, which we denote by $H_{\mathbf{A}\cdot\mathbf{p}}$, and the third line the diamagnetic coupling $H_{\mathbf{A}^2}$ between the square of the field and the density.

Although the interpretation of the mode volume is not straightforward as in Section 2.4.1, the consideration for the scaling of g_μ it introduces in the thermodynamic limit holds here as well.

2.4.3 Dipolar representation

While the minimal-coupling Hamiltonian (equations (2.109) and (2.142)) is exact (in the non-relativistic limit), it is for most settings infeasible to fully solve. Expanding the minimal-coupling Hamiltonian in the uncoupled solutions of the (longitudinally-) interacting matter problem $|m, \mu\rangle$, where m denotes the matter quantum numbers and μ those of the light, we find

$$\langle m, \mu| H_0 |n, \nu\rangle = (E_m + E_\mu)\delta_{mn}\delta_{\mu\nu}\,. \tag{2.145}$$

Based on these energies it is usually possible to devise a truncation scheme[16]. In quantum optical settings, this is usually accomplished by making use of narrow resonances. The light and matter degrees of freedom can therein safely be reduced to few-level emitters and the corresponding resonant light modes.

In the condensed matter context this is generally not possible. Matter excitations are usually quasiparticles broadened by their dispersion and interactions. One can, however, often make use of low-temperature expansions. Instead of leveraging resonances, the temperature determines the size of the active Hilbert space around its ground state allowing us to truncate high-energy states m as $k_\mathrm{B}T \ll |E_m - E_{\text{gs}}|$. This allows us to truncate bands far away from the Fermi energy. Many common phenomena in condensed matter physics are already well

[16] It is however important to note, that in strongly driven settings, where modes a_μ are highly occupied or in the ultra strong coupling limit of cavity QED, where $g_\mu \cdot d/\sqrt{V}$ becomes comparable to ω_μ for some mode with mode volume V and a dipole transition with dipole moment $q \cdot d$, this can require more careful consideration as H_0 no longer necessarily provides the dominant energy scale.

captured with very few bands, e.g., the conductivity of metals [35] or BCS-superconductivity [6] are captured within a single band. There are special cases, where such truncations have to be taken carefully. In Chapter 3 and Chapter 4 we will for example encounter low-temperature condensed matter settings that are optically pumped. Our description therefore requires the inclusion of the low-energy subspace in addition to the high-energy states connected to it via the pump. Depending on the pump, these can be valence bands for optical pumps or core levels for x-ray spectroscopy.

Throughout this thesis, we will furthermore work with correlated electron systems. These can be notoriously difficult to solve even without considering any light-matter interactions. Since in our setting the light is described as non-interacting bosons (since there are no optical non-linearities), we should focus our truncation effort on the matter part of the Hilbert space and truncate it as much as possible.

When examining the structure of the minimally coupled Hamiltonian, the paramagnetic coupling $H_{\mathbf{A}\cdot\mathbf{p}}$ does unfortunately not lend itself to exhaustive truncations in the matter Hilbert space, since the momentum operator $\mathbf{p}$ has in general many offdiagonal contributions if expanded in the bands or orbitals $\langle n|\,\mathbf{p}\,|m\rangle$. Since these are removed by the truncation of the corresponding bands, observables in our truncated Hilbert space converge slowly to those in the full Hilbert space [65, 73]. It is possible to improve this convergence by applying a canonical/unitary transformation of the classical/quantum Hamiltonian prior to the truncation. For the appropriate choice of this transformation we mainly follow the arguments of Li *et al.* [65] in this section.

Since the paramagnetic $\mathbf{A}\cdot\mathbf{p}$ coupling comes from expanding the square $(\mathbf{p}-q\mathbf{A})^2$ in the minimal-coupling Hamiltonian, a displacement transformation mapping

$$\mathbf{p}' = \mathbf{p} + q\mathbf{A} \tag{2.146}$$

removes it. This necessitates a generating function F, that depends linearly on the vector potential, such as

$$F = \int d^3\mathbf{r}\mathbf{P}(\psi,\psi^\dagger,\mathbf{r})\cdot\mathbf{A}(\mathbf{r})\,. \tag{2.147}$$

The matter momentum is not the only momentum changed by the resulting transformation e^{iF}, as it also constitutes a displacement transformation for the momentum of the electromagnetic field

$$U^\dagger\mathbf{\Pi}^\perp U = \mathbf{\Pi}^\perp + \mathbf{P}^\perp(\psi,\psi^\dagger,\mathbf{r})\,. \tag{2.148}$$

Since we identified the momentum before the transformation as the transverse displacement field $\mathbf{\Pi}^\perp = -\mathbf{D}^\perp$, we can identify $\mathbf{P}^\perp$ as the transverse polarization (see equation (2.6)). Through our choice of the polarization field $\mathbf{P}(\psi,\psi^\dagger,\mathbf{r})$, we therefore choose which charges we want to consider as bound charges.

The Power-Zienau-Woolley (PZW) transformation [74–76] is a particular choice of this transformation. Each bound charge contributes to the polarization by adding a string of polarization from the point in space to which it is bound to its position [47]. E.g. for charge density bound to the origin, we find

$$\mathbf{P}(\mathbf{r}) = \int d^3\mathbf{r}' q\psi^\dagger(\mathbf{r}')\psi(\mathbf{r}')\int_0^{\mathbf{r}'} d\mathbf{r}''\delta^3(\mathbf{r}-\mathbf{r}'')\,. \tag{2.149}$$

Computing its sources, we find

$$\nabla \cdot \mathbf{P}(\mathbf{r}) = -q\psi^\dagger(\mathbf{r})\psi(\mathbf{r}) + \rho_0(\mathbf{r})\,, \tag{2.150}$$

where $\rho_0(\mathbf{r}) = \int d^3\mathbf{r}' q\psi^\dagger(\mathbf{r}')\psi(\mathbf{r}')\delta^3(\mathbf{r})$ is the charge opposing our charge density keeping it bound at the origin.

The transformed Hamiltonian becomes

$$\begin{aligned} H = &\int d^3\mathbf{r} \frac{1}{2\epsilon_0}\left((\mathbf{\Pi}^\perp)^2 - 2\mathbf{\Pi}^\perp\mathbf{P}^\perp + (\mathbf{P}^\perp)^2\right) + \frac{1}{2\mu_0}\left(\nabla\times\mathbf{A}\right)^2 \\ &+ \frac{1}{2m}\psi^\dagger\mathbf{p}^2\psi + \psi^\dagger V\psi + H_{\text{int}}\,. \end{aligned} \tag{2.151}$$

The paramagnetic and diamagnetic coupling $H_{\mathbf{A}\cdot\mathbf{p}}$ and $H_{\mathbf{A}^2}$ are therefore replaced by a dipolar coupling $H_{\mathbf{E}\cdot\mathbf{P}}$ and self polarization $H_{\mathbf{P}^2}$.

Charge(s) bound to the origin is a suitable approach for many quantum optical settings, where the objects of interest are usually electrons bound to an atom or molecule. Since the excitations of these are at optical frequencies, the electric field varies little on the length scale on which the electrons are bound. This allows us to make use of the dipole approximation $\mathbf{E}(\mathbf{r}) \approx \mathbf{E}$ on the length scale at which the electron is bound. We find

$$H_{\mathbf{E}\cdot\mathbf{P}} = \int d^3\mathbf{r} q\psi^\dagger(\mathbf{r})\psi(\mathbf{r}) \int_0^{\mathbf{r}} d\mathbf{r}'\mathbf{E}(\mathbf{r}') \tag{2.152}$$

$$\approx \int d^3\mathbf{r} q\psi^\dagger(\mathbf{r})\psi(\mathbf{r})\left(\mathbf{r}\cdot\mathbf{E}\right). \tag{2.153}$$

This is the common starting point for many paradigmatic quantum optical models, such as the Rabi or Jaynes-Cummings models [77, 78], where resonance conditions often allow neglecting $H_{\mathbf{P}^2}$. The integral over the electric field can also be expanded to higher orders for a multipolar expansion.

This form of the polarization is not suited to condensed matter systems, that we want to describe throughout this thesis. It treats the origin special and thereby does not carry the discrete translational symmetry of the lattice.

For a many-particle state, we instead want to allow for different charges q_i described by the fields $\psi_i, \psi_i^\dagger$ bound to the centers $\mathbf{R}_i$ as

$$\mathbf{P}(\mathbf{r}) = \sum_i \int d^3\mathbf{r}' q_i\psi_i^\dagger(\mathbf{r}')\psi_i(\mathbf{r}') \int_{\mathbf{R}_i}^{\mathbf{r}'} d\mathbf{r}''\delta^3(\mathbf{r}-\mathbf{r}'')\,. \tag{2.154}$$

If the fields are sufficiently localized around their corresponding centers, this again allows for the dipole approximation leading to e.g. the Dicke [79] or Tavis-Cummings models [80]. The dipole approximation therein only requires the field to vary little on the length scale on which the charges are bound and not on the complete extent of the system. If the field is described via a mode expansion as in Section 2.4.1 and Section 2.4.2 and the mode functions $\mathbf{f}_\mu(\mathbf{r})$ vary over the complete material, but still slow enough for the dipole approximation on each center to hold, we obtain the beforementioned quantum optical models with a spatially dependent coupling constant.

For condensed matter systems, there is however another complication. Electrons are generally not fully localized on some lattice site. They instead have some mobility allowing them to move from center to center. For our notion of bound electrons to still be applicable, we should limit ourselves to systems, where the electrons are tightly bound. In these cases a helpful basis to expand the field operators in is the Wannier basis, that we already encountered in Section 2.1.

$$\delta_{\alpha\beta} = \int d^3\mathbf{r} w_\alpha^*(\mathbf{r}) w_\beta(\mathbf{r}) \tag{2.155}$$

$$c_\alpha = \int d^3\mathbf{r} w_\alpha(\mathbf{r}) \psi(\mathbf{r}) \tag{2.156}$$

$$\psi(\mathbf{r}) = \sum_\alpha w_\alpha^*(\mathbf{r}) c_\alpha \,, \tag{2.157}$$

wherein the Wannier functions $w_\alpha(\mathbf{r})$ are real and exponentially localized around their centers $\mathbf{R}_\alpha$. Since the field operator of an electron bound to $\mathbf{R}_i$ transforms as

$$U^\dagger \psi_i(\mathbf{r}) U = \psi_i(\mathbf{r}) e^{-iq\int_{\mathbf{R}_i}^{\mathbf{r}} d\mathbf{r}' \mathbf{A}(\mathbf{r}')} \,, \tag{2.158}$$

the Wannier orbitals transform as

$$U^\dagger c_\alpha U = \int d^3\mathbf{r} w_\alpha^*(\mathbf{r}) e^{-iq\int_{\mathbf{R}_\alpha}^{\mathbf{r}} d\mathbf{r}' \mathbf{A}(\mathbf{r}')} \psi(\mathbf{r}) \,. \tag{2.159}$$

Instead of the field operators being dressed, we can interpret this as dressing the Wannier functions by the Peierl's phase [81] $\chi(\mathbf{r}, \mathbf{r}') = \int_{\mathbf{r}}^{\mathbf{r}'} d\mathbf{r}'' \mathbf{A}(\mathbf{r}'')$

$$\tilde{w}_\alpha(\mathbf{r}) = w_\alpha(\mathbf{r}) e^{iq\chi(\mathbf{R}_\alpha, \mathbf{r})} \,. \tag{2.160}$$

These are unfortunately no longer orthogonal [65] as

$$\int d^3\mathbf{r} \tilde{w}_\alpha^*(\mathbf{r}) \tilde{w}_\beta(\mathbf{r}) = e^{-iq\chi(\mathbf{R}_\alpha, \mathbf{R}_\beta)} \int d^3\mathbf{r} e^{iq\oint_{\partial\Delta} d^3\mathbf{r}\mathbf{A}(\mathbf{r})} w_\alpha^*(\mathbf{r}) w_\beta(\mathbf{r}) \tag{2.161}$$

Using Stokes theorem, we can interpret the integral along the boundary of the oriented triangle Δ spanned by $\mathbf{R}_\beta, \mathbf{r}, \mathbf{R}_\alpha$ as the magnetic flux through it

$$\oint_{\partial\Delta} d\mathbf{r}\mathbf{A}(\mathbf{r}) = \iint_\Delta d^2\mathbf{r}\mathbf{B}(\mathbf{r}) \,. \tag{2.162}$$

We therefore recover the orthogonality if this flux vanishes. If both Wannier functions are localized around the same center, it vanishes trivially since the triangle has zero surface. If Wannier functions of different centers are considered, the deviation from orthogonality is still small, as the functions are exponentially localized around their centers. An estimation of the order or magnitude of this deviation from orthogonality shows that it is safe to neglect even for large field strengths (of the order MV/cm) equivalent to neglecting magnetic dipolar interactions [65].

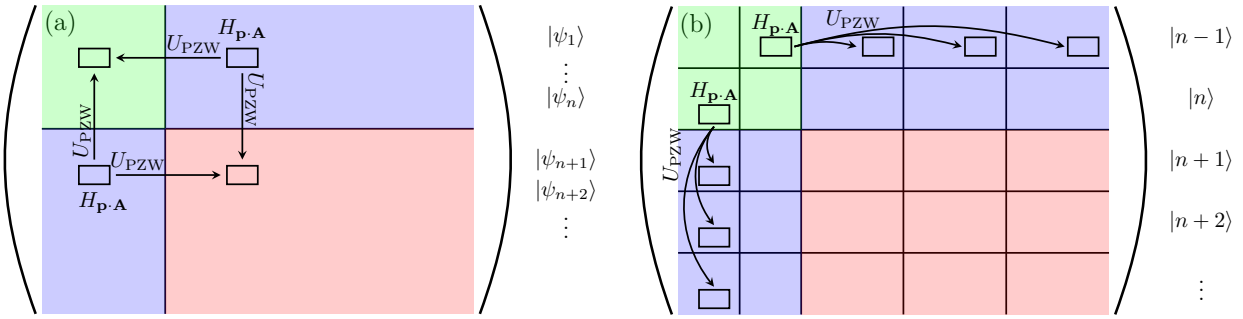

Figure 2.6: Influence of truncations to the matter (a) and electromagnetic (b) Hilbert spaces.
(a) The PZW transformation maps some of the paramagnetic matrix elements, that are lost due to the truncation of the matter space (blue) to the active subspace (green), into the active Hilbert space. (b) For truncations in the photonic Hilbert space, the PZW transformation maps matrix elements linear in the photonic operators to highly non linear ones. In the truncation to a small photonic Hilbert space (green), these non linear contributions are cut off by the truncation.

As already realized by Luttinger [82], under this approximation it is straightforwardly possible to express the matrix elements of the light-matter hybrid Wannier orbitals through those of the untransformed orbitals as

$$t = \langle w_\alpha | H | w_\beta \rangle \Leftrightarrow \langle \tilde{w}_\alpha | H | \tilde{w}_\beta \rangle = t e^{iq\chi(\mathbf{R}_\alpha, \mathbf{R}_\beta)} . \tag{2.163}$$

We can pictorially understand this phase as correction of the polarization string of the electron initially bound at $\mathbf{R}_\beta$ moving to $\mathbf{R}_\alpha$. We can again employ the dipole approximation as $\chi(\mathbf{R}_\alpha, \mathbf{R}_\beta) \approx \mathbf{A}(\mathbf{R}_{\alpha/\beta})(\mathbf{R}_\beta - \mathbf{R}_\alpha)$. In this form, we can again identify the field as momentum displacement. If it is constant throughout the complete system and the single-particle Hamiltonian in the original formulation is solved by the dispersion $\epsilon_{\mathbf{k}}$, the transformed model will produce the dispersion $\epsilon_{\mathbf{k}-q\mathbf{A}}$.

The dipolar Hamiltonian is also sometimes called dipolar gauge, as going from the minimal-coupling Hamiltonian to the dipolar Hamiltonian with all charges bound to the same center can also be phrased as a gauge transformation. This gauge transformation maps from the Coulomb gauge to the Poincaré gauge with the gauge condition [47]

$$\mathbf{r} \cdot \mathbf{A}(\mathbf{r}) = 0 . \tag{2.164}$$

Since the multi-center version can no longer be represented as a gauge transformation [47], the multi-center version should not be referred to as a gauge. The dipolar Hamiltonian nevertheless has a gauge-invariant structure even after the projection on a low-energy matter subspace [65, 73]. As the gauge invariance is related to the conservation of current without having to impose the equations of motion (see Section 2.2.3), this is an advantage of this formulation.

In a direct comparison between the two formulations, we can see, that the dipolar representation is more suited to truncations in the matter Hilbert space. Since this comes at the cost of being highly non linear in the vector potential it is much more sensitive to truncations in the electromagnetic Hilbert space. This is illustrated in figure 2.6. For a more quantitative analysis of this convergence, see Li *et al.* [65] and Dmytruk, Schiró [73]. If our goal is a minimal matter Hilbert space, we should therefore use the dipolar Hamiltonian while keeping a moderate size of the electromagnetic Hilbert space to ensure convergence.

2.5 Series expansion by means of the Schrieffer-Wolff transformation

The goal of series expansions is usually approximating a complicated and generally degenerate system around some perturbative limit [25, 83–88]. We want to phrase this expansion based on the Hamiltonian of some system, which we split in an unperturbed part H_0 and the perturbation αV, where α is a small scalar parameter.

$$H = H_0 + \alpha V \tag{2.165}$$

If the unperturbed part H_0 has special properties, different techniques for this expansion can be utilized. E.g., if it is quadratic the Wick theorem [89] allows for diagrammatic expansions or if it has an equidistant ladder spectrum the coefficients of a linked cluster expansion can be precomputed [86].

Throughout this thesis, we want to utilize series expansions to map an interacting fermion problem to a hardcore boson spin system. Such expansions are valid around the atomic limit, i.e., for the Hubbard model $t/U \ll 1$ at half filling [25–27, 90]. As such the unperturbed Hamiltonian is quartic and not quadratic making diagrammatic techniques unsuitable. Since the cavity mode we will encounter in Chapter 5 furthermore couples to all electrons, linked cluster expansions do not provide us any advantage.

We therefore utilize a low level technique in the form of the Schrieffer-Wolff transformation [84]. It requires the unperturbed Hamiltonian H_0 to be gapped with respect to two subspaces $\mathcal{P}_0, \mathcal{P}_1$. For such systems it provides the minimal unitary transformation $U = e^S$ generated by the antihermitian generator S, that decouples the two blocks up to some perturbative order in α. After this decoupling the system can be projected in either of these subspaces for a dimensionality reduced effective description, where the degrees of freedom in $\mathcal{P}_1$ have been perturbatively eliminated[17].

This transformation is most commonly formulated as two-block scheme [84, 91], but multi-block schemes [92, 93] are possible as well, when the subspaces $\mathcal{P}_0, \mathcal{P}_1$ consist of many blocks with all of them still gapped between each other. It can be shown that the two-block version of the transformation is equivalent to multiple other series expansions [88], such as the one derived by Takahashi [25].

We can construct this transformation in successive orders by writing the generator as series $S = \sum_{n=1} \alpha^n S_n$. The zeroth order vanishes under the condition, that our transformation is supposed to be minimal [91], i.e., it does not contain any rotation inside the subspaces. Using the projectors P_0, $P_1 = 1 - P_0$ we can expand the transformed Hamiltonian and solve for the generator order by order, such that the transformed Hamiltonian is block diagonal.

We find

$$\begin{aligned} H_{\text{eff}} &= e^{-S}(H_0 + \alpha V)e^S && (2.166)\\ &= H_0 + \alpha V + [\alpha S_1, H_0] \\ &\quad + [\alpha^2 S_2, H_0] + \frac{1}{2}[\alpha S_1, [\alpha S_1, H_0]] + [\alpha S_1, \alpha V] + \mathcal{O}(\alpha^3)\,, && (2.167) \end{aligned}$$

[17] This elimination is sometimes also referred to as 'integrating out degrees of freedom'. This name comes from a path integral formulation, where such elimination are performed by evaluating the integral over these degrees of freedom. This produces an effective action for the remaining system, where the other degrees of freedom are integrated out and thereby contained only implicitly.

where we have expanded the transformation as sum over n-fold nested commutators

$$e^{-S}Xe^{S} = \sum_{n=0}^{\infty} \frac{1}{n!} \underbrace{[S,[S,[S,\dots}_{n} H_0]]] \tag{2.168}$$

and for simplicity truncated in second order of α. If we project the linear order of equation (2.167) on one of its block offdiagonal component, its linear order allows us to solve for S_1:

$$0 \overset{!}{=} P_0 H_{\text{eff}} P_1 = P_0 V P_1 + P_0[S_1, H_0]P_1 \tag{2.169}$$

$$P_0 S_1 P_1 = \sum_{i\in\mathcal{P}_0, j\in\mathcal{P}_1} \frac{|i\rangle\langle i| V |j\rangle\langle j|}{E_i - E_j}, \tag{2.170}$$

where $\{i\},\{j\}$ form a complete eigenbasis of H_0 in their appropriate subspaces. Since S is antihermitian, all of its Taylor coefficients S_n also have to be antihermitian. Projecting the effective Hamiltonian on the other offdiagonal block $P_1 H_{\text{eff}} P_0$ therefore leads to the same equation up to taking the antihermitian conjugate. Keeping the transformation minimal, the diagonal components of S vanish as $S_{\text{d}} = 0$.

The notation is simplified if we introduce the resolvent superoperator $\mathcal{L}$ [91], that maps a block offdiagonal operator to

$$\mathcal{L}(X_{\text{od}}) = \sum_{i,j} \frac{|i\rangle\langle i| X_{\text{od}} |j\rangle\langle j|}{E_i - E_j}. \tag{2.171}$$

It acts as the inverse of the commutator with the unperturbed Hamiltonian $[H_0, \mathcal{L}(X_{\text{od}})] = X_{\text{od}}$ as long as the blocks are gapped.

Plugging $S_1 = \mathcal{L}(V_{\text{od}})$ back in equation(2.167), we obtain a second order correction to the block diagonal part of H_{eff}, that stems from the block offdiagonal part of the perturbation V_{od}.

$$P_0 H_{\text{eff}} P_0 = P_0 H_0 P_0 + \alpha P_0 V_{\text{d}} P_0 + \frac{\alpha^2}{2}[S_1, V_{\text{od}}] + \mathcal{O}(\alpha^3) \tag{2.172}$$

The same procedure can be carried to higher orders. The sequence of operators and superoperators one has to evaluate for an arbitrary problem can be precomputed using a diagram technique [91]. In this thesis we will require this expansion up to fourth order in α. We find [91]

$$\begin{aligned} P_0 H_{\text{eff}} P_0 = {} & P_0 H_0 P_0 + \frac{1}{2} P_0[S_1, V_{\text{od}}]P_0 + \frac{1}{2} P_0[V_{\text{od}}, \mathcal{L}([V_{\text{d}}, S_1])]P_0 \\ & - \frac{1}{2} P_0[V_{\text{od}}, \mathcal{L}([V_{\text{d}}, \mathcal{L}([V_{\text{d}}, S_1])])]P_0 \\ & - \frac{1}{6} P_0[V_{\text{od}}, \mathcal{L}([S_1, [S_1, V_{\text{od}}]])]P_0 - \frac{1}{24} P_0[S_1, [S_1, [S_1, V_{\text{od}}]]]P_0 \,. \end{aligned} \tag{2.173}$$

Applied to a specific problem, the following steps are necessary:
(i) Identify H_0 and V.
(ii) Define the low-energy subspace $\mathcal{P}_0$ of H_0 and its projector P_0, such that the $\mathcal{P}_0$ and its complement $\mathcal{P}_1$ are properly gapped.
(iii) Evaluate equation (2.173) as operator product using the resolvent superoperator $\mathcal{L}$, which

requires an eigendecomposition of H_0 in all participating intermediate states.
Altogether this yields an effective Hamiltonian in the low-energy subspace if projected to $\mathcal{P}_0$.

2.6 Floquet theory

Floquet theory can be used when dealing with differential equations with time-periodic coefficients. For our case this requires a time-periodic Hamiltonian ($H(t+T) = H(t)$). Much like for discrete spatial translations of a lattice in Bloch theory a common eigenbasis of the Hamiltonian and the stroboscopic time-evolution operator $U(t_0+T, t_0)$ can be found. We can therefore write the eigenstates $\psi_\alpha(t)$ as the product of a phase factor using the quasi-energy ϵ_α and a function, that is invariant under the discrete time-translation $\phi_\alpha(t_0+T) = \phi_\alpha(t_0)$ [32, 94, 95]:

$$\psi_\alpha(t) = e^{-i\epsilon_\alpha t}\phi_\alpha(t)\,. \tag{2.174}$$

Inserting this expansion in the Schroedinger equation yields

$$\epsilon_\alpha\phi_\alpha(t) = (H - i\partial_t)\phi_\alpha(t)\,. \tag{2.175}$$

This lends itself to a expansion in terms of Fourier coefficients, where one finds

$$\phi_\alpha(t) = \sum_{m=-\infty}^{\infty} e^{im\Omega t}\phi_{\alpha,m} \tag{2.176}$$

$$\phi_{\alpha,m} = \frac{1}{T}\int_{-T/2}^{T/2} dt e^{-im\Omega t}\phi_\alpha(t) \tag{2.177}$$

with the frequency $\Omega = 2\pi/T$. This expansion can be equivalently be performed substituting $t \to t + t_0$ for $-T/2 \leq t_0 < T/2$. This choice in t_0 is often referred to as Floquet-gauge and can be used to yield a particularly convenient expansion [32, 95]. In Bloch theory this corresponds to finding a particularly convenient choice of the unit cell.

Inserted in the Schroedinger equation, we find a coupled set of equations for these coefficients:

$$\epsilon_\alpha\phi_{\alpha,n} = \sum_{m=-\infty}^{\infty}\frac{1}{T}\int_{-T/2}^{T/2} dt e^{-in\Omega t}(H + m\Omega)e^{im\Omega t}\phi_{\alpha,m}\,. \tag{2.178}$$

We can interpret this coupled set of equations as eigenvalue problem in terms of the extended Floquet-Hilbert space

$$\epsilon_\alpha\phi_{\alpha,n} = \sum_{m=-\infty}^{\infty} H^{nm}\phi_{\alpha,m}\,. \tag{2.179}$$

Instead of through the time-dependent Hamiltonian, it is defined by the Floquet-block matrix

$$H^{nm} = \frac{1}{T}\int_{-T/2}^{T/2} dt e^{i(m-n)\Omega t}(H(t) + m\Omega)\,. \tag{2.180}$$

Since m, n run from $-\infty$ to ∞, we can understand the domain of this eigenvalue problem as an infinite number of copies of the original Hilbert space. Offdiagonal elements $m \neq n$ in H^{nm} hybridize these bands. Since the eigenvalue problem is translationally invariant in the indices m, n, i.e., $H^{nm} = H^{n-m}$, it suffices to find $\phi_{\alpha,m}$ for one particular choice of m. This is

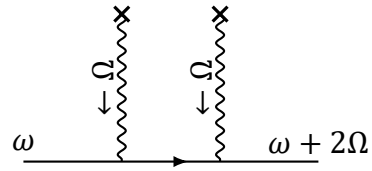

(a) Diagrammatic representation of the Floquet-Green's function $G_{02}(\omega)$; Adapted from reference [94]

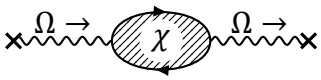

(b) Linear response in Floquet theory

(c) Raman scattering with a second mode ω_R

Figure 2.7: Diagrammatic representation for various processes in terms of Floquet-Green's functions. (a) A fermionic Floquet-Green's function, that under the absorbtion of two photon changes its energy from ω to $\omega + 2\Omega$, which in terms of Floquet-Green's functions corresponds to $G_{02}(\omega)$ (see reference [94]); (b) The bubble diagram determining the linear response (see Section 2.3.3) can be understood in terms of second order Floquet process; (c) Upon the inclusion of a second mode ω_R, Raman-type processes can also be unterstood in terms of Floquet theory. For details see Section 5.2.3 and Appendix E.

usually accomplished for the band $\phi_{\alpha,0}$ from which the hybridization with all other sidebands $\phi_{\alpha,m\neq 0}$ is eliminated through e.g. a series expansion.

For this eigenvalue problem we can also find Floquet-Green's functions. These can also be understood as a particularly convenient representation of general Green's functions on the Keldysh contour for the periodically driven non-equilibrium steady state [94, 96]. How this steady state emerges and stabilizes is however still subject of current research [97].

Much like we can understand he usual Green's functions as matrix elements of the time-evolution operator, Floquet-Green's functions additionally carry the sideband indices of the extended Floquet Hilbert space. For these Floquet-Green's functions we can understand expansions in terms of diagrammatics. In Figure 2.7a, we show the Floquet-Green's function $G_{02}(\omega)$ in leading order of the light-matter interaction[18], the linear response in terms of Floquet-Green's functions (see Figure 2.7b) and Raman-type processes[19] (see Figure 2.7c) possible, if an additional mode ω_R is included, which we will do in Section 5.2.3.

[18] Higher orders correspond to an equal number of additional absorptions and emissions.

[19] The formulation generalizes to Hyper-Raman type processes, if multiple photons are emitted and or absorbed.

3 Pump-probe spectroscopy of TiOCl

In this chapter we want to outline the computation of the time-dependent optical conductivity as reported in the currently unpublished work [P1]. As such, it follows [P1] in notation, terminology and phrasings. In this work, we report on the single and double pump-probe spectroscopy of the compound TiOCl. The authors contribution to this work was the development of an effective low-energy description, that is able to capture the non-equilibrium spectroscopy and dynamics observed in the experiment. In this effective model the author computed the non-equilibrium optical conductivity as well as decay lifetimes of orbital excitations. In this chapter we treat the former, while the later is subject of Chapter 4. Explicit contributions of the coauthors of [P1] will be mentioned throughout this chapter, wherever applicable.

3.1 Motivation

Transition metal oxides are versatile compounds to explore the spin, orbital and charge dynamics of correlated electrons [98, 99] with the most famous of these being the $3d^9$ high-T_c cuprates [11]. In this chapter we investigate the $3d^1$-halide TiOCl, which also hosts an unpaired spin 1/2 in the valence band. Due to its optically active [16] non-degenerate [100] orbitals it is a suitable platform to explore the non-equilbrium dynamics of these three degrees of freedom using time-resolved pump-probe spectroscopy [66] (see Figure 3.1): At the probed energies, the electromagnetic field couples to charge excitations across the Mott gap. The optical pumps are resonant to orbital excitations and the low-temperature phase is characterized by antiferromagnetic order in a spin-Peierls phase.

For this purpose we first give a brief overview over the material TiOCl and the experimental platform on which our experimental collaborators performed their measurements (see Section 3.2). We then derive a tight-binding Hamiltonian, which is able to capture all of the dynamics above, using ab-initio techniques (see Section 3.3). Next we describe how this model can be used to compute the non-equilbrium optical conductivity on small clusters (see Section 3.5), which is the corresponding theoretical quantity corresponding to the transmission measurements of the experiment. Finally, we compare our results to the experimental data, where we find, that the evaluable cluster sizes are too small for a quantitative agreement.

3.2 Overviews

3.2.1 Spin-Peierls material TiOCl

Titanium oxychloride is a layered transition metal oxide with the titanium ions in the $3d^1$ configuration [101]. The bilayers are therein stacked in the crystallographic c-direction with van-der-Waals interactions between the chloride ions connecting them [14] (see Figure 3.2).

The orthorhombic structure of the compound fully lifts the orbital degeneracy of the d-shell. The unpaired electron on each titanium side therefore resides in lowest orbital such that the orbital degree of freedom is fully quenched in equilibrium [100, 102]. The alignment of the lobes of this lowest orbital along the b-axis combined with strong electronic correlations [14] lead to the low temperature behavior of this material being that of antiferromagnetic spin-1/2

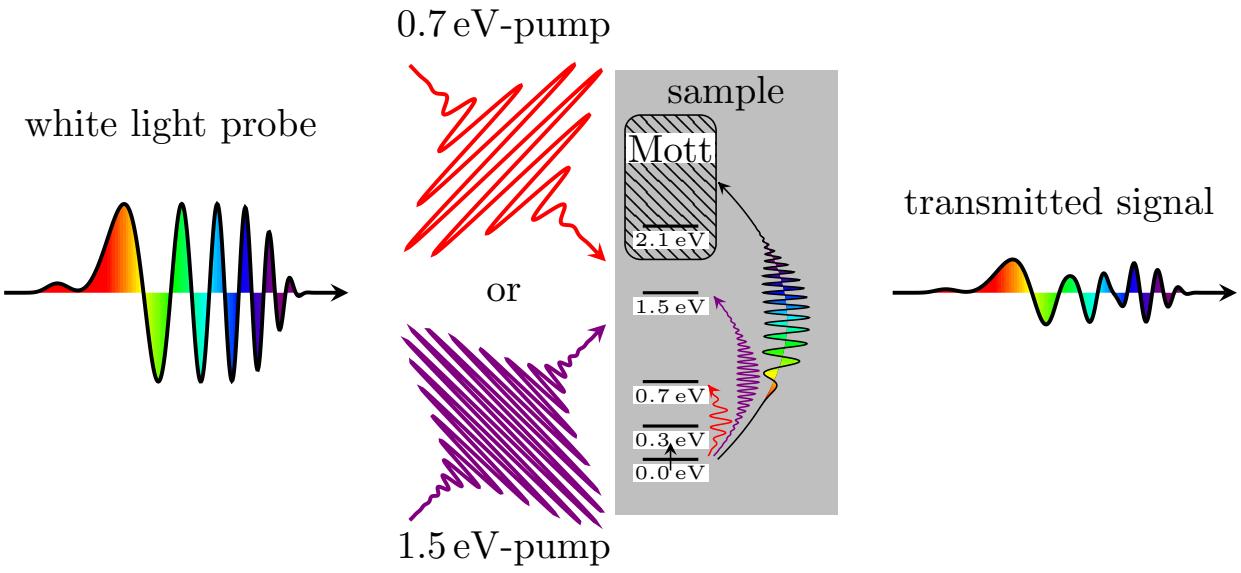

Figure 3.1: Sketch of the single pump-probe experimental setting described in reference [66]. The sample is first photo-doped by either a 0.7 eV-pump or a 1.5 eV-pump and after some time-delay probed using a chirped white light probe beam. Indicated on the sample is the crystal field splitting to which the pumps are resonantly tuned and the Mott gap, which in large parts covers the energy range of the white-light probe beam. The measured spectrum is the transmitted beam, where the effect of the chirping is removed in post-processing the data.

Heisenberg chains oriented along the b-axis [14, 100, 103–106]. Starting from a high symmetry high temperature phase the material undergoes a spin-Peierls transition with dimerization along the b-axis at 67 K [14, 15, 104, 107] via some intermediate incommensurate phase at 92 K [15, 104, 108, 109].

The spin-Peierls transition is result of an instability of spin-1/2 Heisenberg chains with respect to coupled phonons and leads to a doubling of the unit cell [110]. This results in gapped spin excitations [100, 111, 112], which are captured within a dimerized Heisenberg model with an exchange coupling of $J = 90$ meV on the short/strong and $J = 68$ meV on the long/weak bond [100].

Due to the broken inversion symmetry around the titanium ions there are optically active d-d-excitations [16, 105]. Measurements of the optical conductivity [16, 105] and resonant inelastic x-ray scattering [100] place the energies of the orbital excitations at 0.34 eV, 0.62 eV, 1.48 eV and 2.05 eV [100]. The second and third of these excitations are optically active if the polarization of the incident field is tuned in the crystallographic a- or b-axis respectively [16, 67, 105]. Beyond 2 eV the absorption spectrum is dominated by charge excitations [16, 67, 105].

3.2.2 The experimental platform

In this chapter and Chapter 4, we provide the theoretical complement to measurements performed by our experimental collaborators [P1]. The experimental platform used therein is described in detail by Montanaro *et al.* [66] and a sketch abstracted to the essentials relevant for our theoretical considerations shown in Figure 3.1. A report on the measurement process and the measured data can be found in the PhD thesis of A. Montanaro [67].

On this platform our experimental collaborators are able to measure the optical conductivity of a thin TiOCl crystal by means of a transmission measurement of a broad band probe

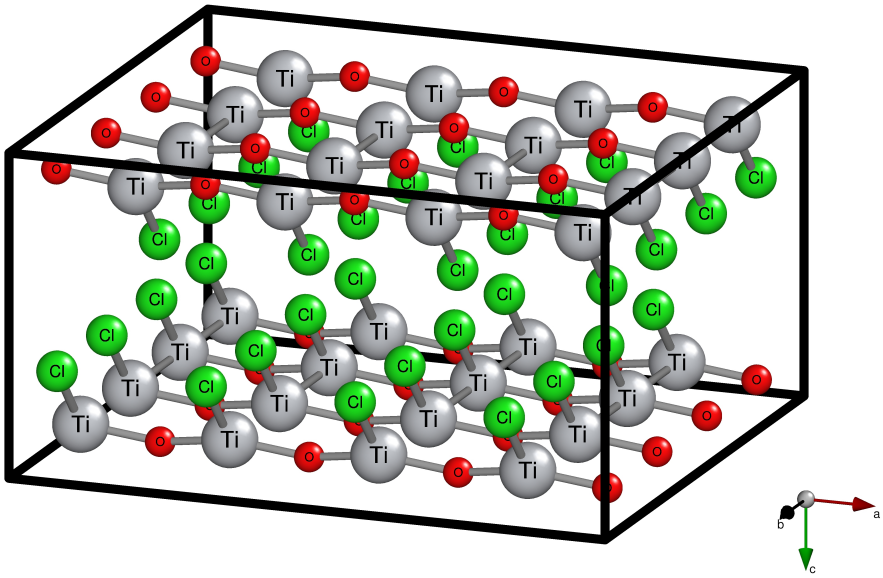

Figure 3.2: Lattice structure of TiOCl [113] the dimerization due to the spin-Peierls transition is along the b-axis. To reproduce the materials magnetic properties we have rescaled its magnitude to one fifth of the reported value [113]. It therefore amounts to a difference in bond length of around 1% and is therefore not clearly visible in this figure.

polarized along the a- and b-axis. The wavelength of the probe beam is in the optical range from 500 nm to 800 nm. This amounts to a photon energy of $\hbar\omega = 1.5\,\text{eV}$ to $2.5\,\text{eV}$, which covers the Mott gap in TiOCl. Due to the way it is generated, it is a chirped pulse with a duration of 1.5 ps. Time and frequency resolving the transmitted signal does, however, allow for time resolutions better than this duration [114]. On this particular experimental platform this is accomplished by postprocessing the signal, which allows for a time resolution of less than 20 fs [66].

The frequency of the narrow pump beams is adjusted to be resonant to the TiOCl d-d-transitions at 0.7 eV and 1.5 eV. The temporal pump envelopes are approximately 50 fs and 30 fs respectively. Their polarization is adjusted such that they align to the selection rules observed by Rückamp et al. [16], i.e. for the 0.7 eV transition with the beam polarization aligned to the a-axis, for the 1.5 eV transition with the polarization aligned to the b-axis.

Since we are interested in the non equilibrium signature, the equilibrium transmissivity is subtracted from the transient transmissivity [66, 67]. The pumps operator in a regime, where the signature ΔT is linear in the pumps fluence, i.e., where only few excitations are photodoped [67]. In this regime, ΔT is proportional to the difference in optical conductivity $\Delta\sigma$ between the pumped and equilibrium state to leading order in the effciency of the photodoping. The measurments were performed at 10 K, such that the sample is well within the spin-Peierls phase.

3.3 Derivation of an effective few band model for TiOCl

Since the key observable in the experiment is the transmission of a probe beam, our model should compute the samples non equilibrium optical conductivity. In Section 2.3.3 we show, that this can be accomplished using the retarded current-current correlation function. Since we are interested in the response at large frequencies, we can furthermore drop the diamagnetic contribution. Experiments on this compound [16, 100] and ab-initio computations [115] showed both to the partially occupied d-band the other four d-bands are flat and gapped from the ligands. A tight-binding formulation of the Hamiltonian should therefore be suited for this compound. Electronic correlations play a strong role in this material with estimations of the onsite interaction $U = 2\,\mathrm{eV}$ to $4\,\mathrm{eV}$ [67, 105, 115, 116]. In order for our model to capture the experimentally probed energy range we should therefore model TiOCl as five-band Hubbard model:

$$H = \sum_{i,j}\sum_{\alpha,\beta}\sum_{\sigma} t_{i\alpha,j\beta} c^\dagger_{i\alpha\sigma} c_{j\beta\sigma} + \sum_{i}\sum_{\alpha,\beta,\gamma,\delta}\sum_{\sigma,\sigma'} U_{\alpha\beta\gamma\delta} c^\dagger_{i\alpha\sigma} c^\dagger_{i\beta\sigma'} c_{i\gamma\sigma'} c_{i\delta\sigma}\,. \tag{3.1}$$

This allows us to on the one hand capture the magnetic low energy behavior, since a leading order expansion in t/U for the lowest orbital yields the spin-1/2 Heisenberg model [25–27, 35, 46, 117]. On the other hand we explicitly describe the pumped orbital excitations as well as the probed Mott-gap. We want to derive the parameters $t_{i\alpha,j\beta}$ and $U_{\alpha\beta\gamma\delta,\sigma\sigma'}$ of this model through ab-initio computations where possible. As outlined below, the overlap integrals $t_{i\alpha,j\beta}$ can be obtained from the bands as obtained by density functional theory and $U_{\alpha\beta\gamma\delta,\sigma\sigma'}$ in parts from literature [44] and in parts by fitting to the experiment [100, 111].

3.3.1 Density functional theory

We obtain the single particle contribution of the Hamiltonian using density functional theory (DFT). The crystalline structure used as input was provided by S. van Smaalen, who utilized x-ray diffraction to construct it [113]. The spin gap is highly sensitive to the strength of the dimerization [112]. In order for our model to have the proper dimerization in the magnetic exchange $J'/J = 0.75$ [100, 111], we found that we have to rescale the magnitude of the dimerization in the real space structure to 1/5 of the provided value. We accomplished this by (i) linearly interpolating the lattice structure with its symmetrized version, (ii) carrying out the complete derivation of the resulting tight binding Hamiltonian outlined below and (iii) performing a second order series expansion for the magnetic exchange parameters J, J' (see Section 2.5)[1].

The DFT computation was performed by P. Hansmann using the FPLO software package [118–120]. It uses a full-potential localized orbitals approach[2] suited to this class of material in which the electrons are strongly localized. We utilize the generalized gradient approximation as exchange functional [121], since the resulting crystal field splitting most closely resembled the RIXS results [100]. The resulting band structure is shown as black lines in Figure 3.3. Their hybridization with the surrounding bands on the other side of the gaps can be removed using a unitary transformation, which in this context is usually referred to as downfolding. For the downfolded hybrid titanium-ligand bands the active Hilbert space can then be truncated to

[1] We utilize a similar approach to determine the magnitude of the onsite interaction U necessary to perform the series expansion. Since the dimerization effects the ratio J'/J and the onsite interaction U effects the magnitude of J, J', we can use the series expansion to deduce both of them.

[2] Hence its name

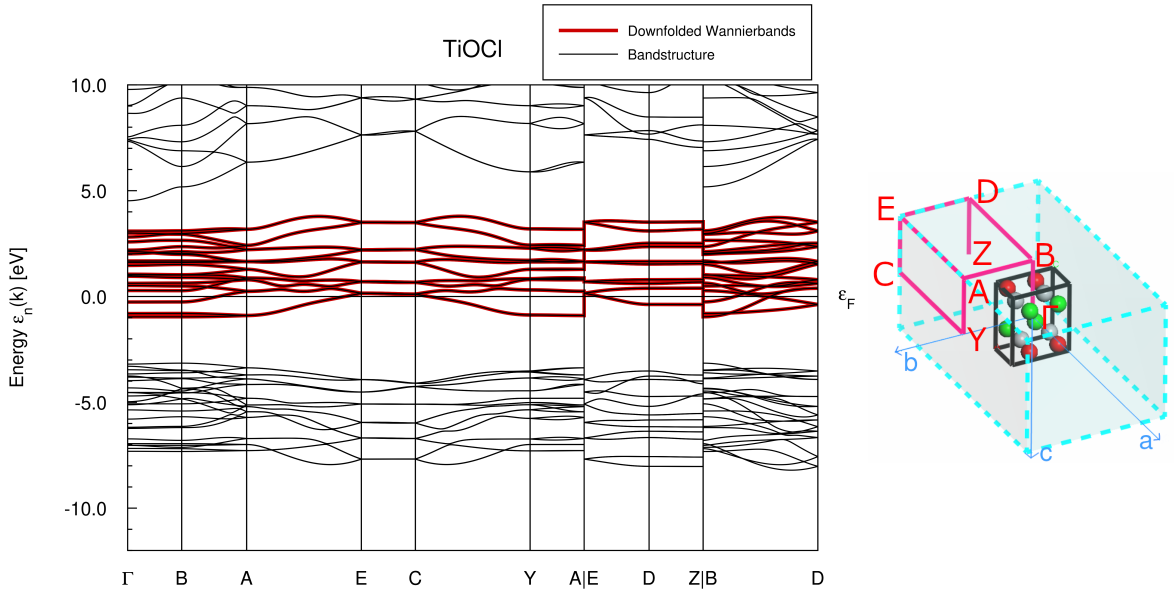

Figure 3.3: Black: Bandstructure of TiOCl as computed using FPLO with GGA. Around the Fermi energy ϵ_F, there are the titanium d-bands. Isolated from them below lie the ligand oxygen and chlorine bands. Red: Titanium bands as obtained by a downfolding of the complete bandstructure to the titanium bands only. The right side shows the Brilloin zone with its high symmetry points and the path it for the band structure on the left indicated in red.

these five bands only without distorting them. These are shown in red in Figure 3.3 and lie on top of the corresponding bands of the full bandstructure.

A subsequent Wannierization [122] utilizing cubic harmonics yields a set of basis orbitals which we use to construct the tight-binding Hamiltonian. These orbitals are visualized in Figure 3.4. The downfolding causes these to have some density on the ligand sites. For each unit cell we obtain 20 of these orbitals amounting to the four titanium sites in a unit cell. Since we only want to model the dynamics within the a-b-plane, it is sufficient to use only the corresponding 10 single particle orbitals. The site local energies and hybridizations lead to the crystal field splitting in the single particle Hamiltonian, while the overlaps with neighboring sites lead to the single particle hopping [34].

3.3.2 Coulomb repulsion

When considering the electron-electron interactions, we only want to consider site local two particle interactions. Since our Wannier basis carries the symmetry of a d-shell and they are localized strongly enough, that deviations from atomic wavefunctions are small, the local Coulomb interaction between electrons is sufficiently parametrized by the three Slater integrals F^0, F^2 and F^4 [43]. They quantify a spin and configuration agnostic Hubbard part of the interaction, the Hund's coupling [45] and pair-hopping [5] terms of the Coulomb repulsion expanded in our Wannier basis. Limiting our active many particle Hilbert space to the $3d^0$, $3d^1$ and $3d^2$ configurations, we can take the values for F^2 and F^4 from a Hartree-Fock calculation by M. Haverkort [44], i.e. $F^2 = 8.243\,\text{eV}$ and $F^4 = 5.132\,\text{eV}$. We account for the screening due to the ligand orbitals by introducing a phenomenological screening factor of 0.8 [16].

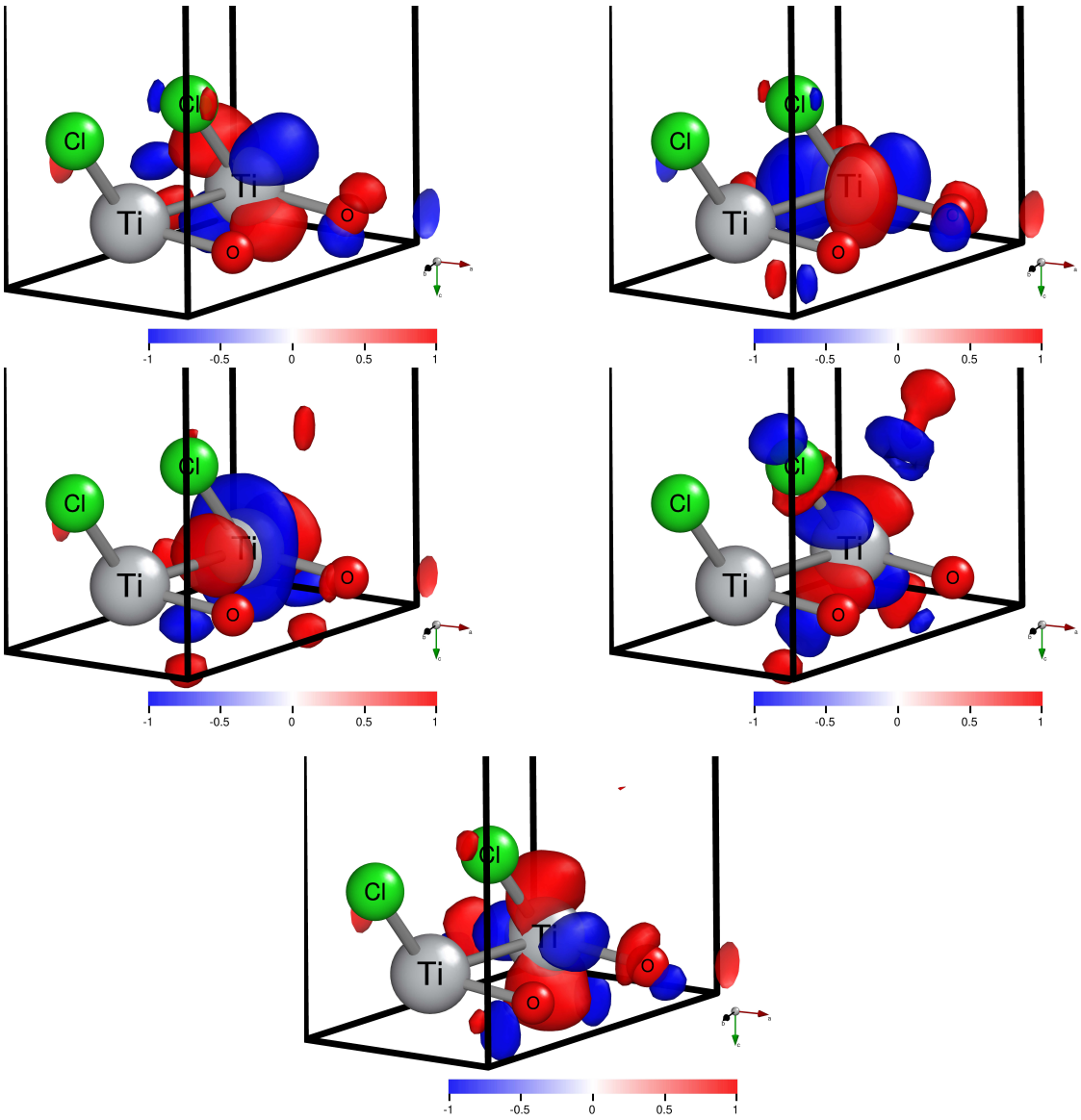

Figure 3.4: Densities of the Wannier orbitals constructed through a downfolding and Wannierization of the bandstructure shown in Figure 3.3.

F^0 is however more difficult to compute, since it sensitively depends on the radial component of our hybrid titantium ligand Wannier orbitals. It parametrizes the center of the upper Hubbard band U as

$$F^0 = U + 2/63 \cdot (F^2 + F^4)\,. \tag{3.2}$$

While it is generally possible to compute it within some DFT frameworks, e.g., using the constraint random phase approximation [123, 124], we instead use it as free parameter to fix the amplitude of the magnetic exchange. Much like for the dimerization, we use a second order series expansion to map the five band Hubbard model to an effective spin-orbital model. A Heisenberg spin exchange of $J = 90\,\mathrm{meV}$ on the strong bond [100] requires a Hubbard interaction of $U = 2.527\,\mathrm{eV}$.

We implement the Hamiltonian within the 'Quanty' many body scripting language [125]. It is a framework for ligand-field theory [126], which we use to implement our tight-binding Hamiltonian on small clusters. It contains helpful definitions for common ligand field objects, such as the Coulomb interaction as operator in second quantization parametrized via the Slater integrals or common spectroscopic operators in second quantization. It furthermore provides Krylov subspace routines for diagonalizations and spectral functions [127].

3.4 Deriving a spin orbital description by series expansion

As described in Section 3.3, we have to compute the magnetic Heisenberg exchanges J, J' on the short and the long bond to fix the magnitude of the dimerization and Hubbard U. This can either be accomplished by an exact diagonalization of a two site cluster and comparison of the energies of the singlet and triplet eigenstates of the cluster or utilizing a series expansion which we perform here. This has the advantage of keeping orbital and spin degrees of freedom disentangled. Following Section 2.5, we split the Hamiltonian into an unperturbed part and a perturbation

$$H = H_0 + \alpha V\,. \tag{3.3}$$

For the expansion around the atomic limit, the hybridization between sites acts as perturbative parameter, such that we find

$$H_0 = \sum_i \sum_{\alpha,\beta} \sum_\sigma t_{i\alpha,i\beta} c^\dagger_{i\alpha\sigma} c_{i\beta\sigma} + \sum_i \sum_{\alpha,\beta,\gamma,\delta} \sum_{\sigma,\sigma'} U_{\alpha\beta\gamma\delta,\sigma\sigma'} c^\dagger_{i\alpha\sigma} c^\dagger_{i\beta\sigma'} c_{i\gamma\sigma'} c_{i\delta\sigma} \tag{3.4}$$

$$\alpha V = \sum_{i,j\neq i} \sum_{\alpha,\beta} \sum_{\sigma,\sigma'} t_{i\alpha,j\beta} c^\dagger_{i\alpha\sigma} c_{j\beta\sigma}\,, \tag{3.5}$$

i.e., the crystalfield splitting and onsite interactions as unperturbed part and the hopping terms as perturbation. Upon proper definition of the subspace projectors P_0, P_1 and the resolvent superoperator $\mathcal{L}$ (see equation (2.171)), both of which we will do in the following, in second order the series expansion yields

$$H_{2,\mathrm{eff}} = \frac{\alpha^2}{2} P_0 \left[\mathcal{L}(V_{\mathrm{od}}), V_{\mathrm{od}}\right] P_0\,, \tag{3.6}$$

where $V_{\mathrm{od}} = P_0 V P_1 + P_1 V P_0$ denotes the offdiagonal part of the perturbation.

We want to perturbatively eliminate the charge excitations. $\mathcal{P}_0$ therefore has to be the charge excitation free subspace and $\mathcal{P}_1$ its complement. As the electronic filling provides one electron per titanium site, $\mathcal{P}_0$ is equivalent to the $3d^1$ configuration for every titanium ion. Keeping

our expansion to second order, the only part of $\mathcal{P}_1$ accessible via the perturbation are states, where two titanium ions are in the $3d^0$ and $3d^2$ configuration with all other titanium ions still hosting a $3d^1$ configuration. We therefore do not have to treat the full $\mathcal{P}_1$ subspace, but only the part, that contains a single double occupation (doublon) and a single hole.

Evaluating equation (2.172) requires a complete eigenbasis of $\mathcal{P}_0$ and $\mathcal{P}_1$. Applied to our specific system, we can simplify this task:

(i) Our perturbation V can only act on the system in four ways. Either it creates a charge excitation, moves a charge excitation, moves a hole or recombines a charge excitation with a hole. As there are no holes or charge excitations in $\mathcal{P}_0$, the only type of process that can appear in second order is the creation of a doublon hole pair with a subsequent recombination. The entire process is therefore contained on a two-site cluster and (since H_0 is local) acts trivially on the rest of the system.

(ii) The locality of H_0 furthermore allows us writing its eigenstates as product states. In $\mathcal{P}_0$ the local Hilbert space for each site is 10 dimensional as the spin quantum number σ can take two values and the orbital quantum number of the crystal field orbtials α can take five values. The dimensionality of the two-site cluster we have to consider is therefore 100 dimensional. Similarly, the local subspace of $\mathcal{P}_1$ we have to consider is 180 dimensional, as it is spanned by all states of the $3d^0 \otimes 3d^2$ and $3d^2 \otimes 3d^0$ configurations, each of which is 90 dimensional[3].

There is, however, one complication: The convergence of the Schrieffer-Wolff transformation requires the perturbation to be smaller than the magnitude of the gap. In the $\mathcal{P}_0$ subspace there are however states with orbital configurations, whose combined energy is of a similar magnitude as the Mott gap, e.g. one 2.05 eV excitation or a 1.48 eV excitation on one site and a 0.62 eV excitation on the other site. Mathematically speaking we should therefore exclude such states from $\mathcal{P}_0$ and instead contain them in $\mathcal{P}_1$. In second order this does however have no impact on the effective Hamiltonian for the low energy states in $\mathcal{P}_0$, as the intermediate states in $\mathcal{P}_1$ accessible via V are only those with a double occupation. Starting in fourth order, this choice in $\mathcal{P}_0$ and $\mathcal{P}_1$ would lead to a different effective Hamiltonian for the low energy states. Since we only compute the second order we ignore this peculiarity keeping in mind that matrix elements of the effective Hamiltonian mapping from, to and between high energy states are not converged.

Making use of (i) and (ii), we find the eigenbasis of $P_0 H_0 P_0$ and $P_1 H_0 P_1$ by exact diagonalization of the corresponding subspaces using the 'Eigensystem' routine provided by Quanty [126]. It allows for diagonalizations via a Krylov subspace routine whose Hilbert space can be restricted. In order to avoid issues in constructing this subspace with iterative Lanczos routines, we manually span the accessible 180 dimensional part of the $\mathcal{P}_1$ subspace using the crystal field basis and use the 'Eigensystem' routine to converge this basis to an eigenbasis. Using this basis, we evaluate $P_1 V P_0$ as 180×100 matrix and $P_0 V P_1$ as 100×180 matrix. In the eigenbasis the resolvent superoperator $\mathcal{L}$ (see equation (2.171)) is straightforwardly implemented:

$$(P_0 S_1 P_1)_{ij} = (\mathcal{L}(P_0 V P_1))_{ij} = \frac{(P_0 V P_1)_{ij}}{E_i - E_j} \tag{3.7}$$

[3] Due to the hermiticity of H and H_{eff} using either of these configurations would have sufficed. Since it is numerically still easily feasible and allows us to use the hermiticity of our results as check, we decided on using the complete subspace.

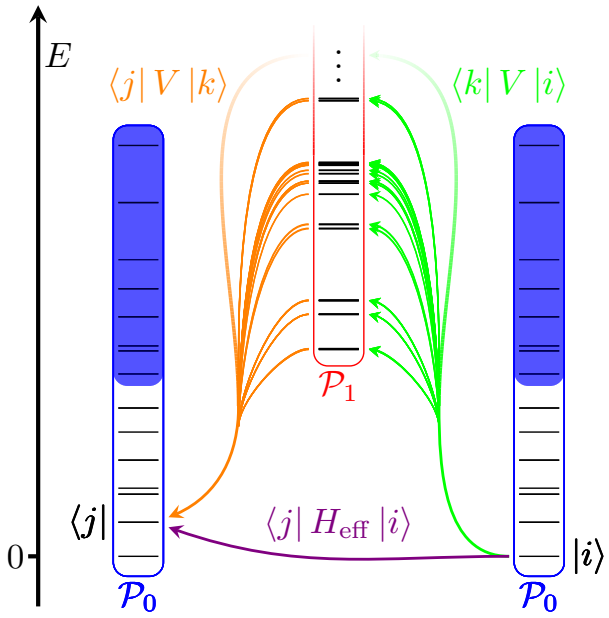

Figure 3.5: Sketch of the types of matrix elements we evaluate in order to obtain the matrix element mapping the low energy state $|i\rangle$ on the low energy state $|j\rangle$ in the effective Hamiltonian. The blue shaded region indicates the part of the low energy Hilbertspace $\mathcal{P}_0$ for which this series expansion is not properly converged due to the small gap between E_i/E_j in $\mathcal{P}_0$ and E_k in $\mathcal{P}_1$. Evaluated on a two site cluster $|i\rangle, |j\rangle$ are crystalfield product states and $|k\rangle$ are all doublon holon product states on this cluster.

with $(P_1S_1P_0)_{ij}$ similarly. With all four operators represented as matrices, equation (2.172) becomes the sum of two matrix products

$$(H_{\text{eff}})_{ij} = \frac{1}{2}\left(\sum_{k=1}^{180}(P_0S_1P_1)_{ik}(P_1VP_0)_{kj} - (P_0VP_1)_{ik}(P_1S_1P_0)_{kj}\right). \tag{3.8}$$

We illustrate this in Figure 3.5. For each two site cluster this produces a 100×100 matrix, whose entries we can interpret as the spin and orbital exchange. We postpone a detailed analysis of these exchanges to Chapter 4, where the intermixing of these degrees of freedom through this exchange is the key ingredient allowing for a fast decay of the pumped excitations. For this chapter the relevant matrix elements are choosing $|i\rangle, |j\rangle$ as the states with no orbital excitations, i.e., the crystal field groundstate, and all four possible spin configurations. The resulting 4×4 matrix has the structure of the spin 1/2 Heisenberg Hamiltonian. Considering nearest neighbor exchange only, we perform this series expansion on the two-site cluster containing the strong dimerized bond along the b-axis and the weak inter-dimer bond along the b-axis to extract J and J'. As described in Section 3.3, we use $J'/J = 0.75$ to adjust the crystal structure with respect to the dimerization in real space and the absolute value $J = 90$ meV to fix the Mott gap, i.e. F^0.

3.5 Non-equilibrium spectral functions

In Section 2.3.3 we showed, that the observable measured in a transmission experiment is the optical conductivity. We can compute via the retarded current-current correlation function. In the present context, this is somewhat complicated by the optical pumping producing a non-equilibrium state. A general description requires evaluating a spatially resolved four-point current correlation function, where two current operators describe the pump and the

other two the probe. To get a coarse understanding on the orbital sensitivity of this pump probe scheme, we use multiple simplifications, that make this correlation function accessible on small clusters.

3.5.1 Simplified out-of-equilibrium setting

Firstly, we want to assume, that the sample is always pumped before it is probed. This allows us describing the time ordered four-point correlation function as a two-time current-current correlation function $\chi(t, t')$, that we have to evaluate on a pumped non-equilbrium state. A similar reduction of observables usually corresponding to four-point correlation functions to two-point non-equilibrium correlation functions is also common in other settings, e.g. for spectra of resonant inelastic x-ray scattering (RIXS) via exact diagonalization [128] or dynamical mean field theory [129, 130] or for computing the optical conductivity within other Krylov subspace approaches [131].

Next, we want to neglect all retardation effects caused by the thickness of the sample, the pump envelope and probe envelope. This allows us describing the transmission via a sample homogeneous non-equilbrium optical conductivity. This approximation does not necessarily equate to treating the sample as infinitely thin. If the pump is weak enough[4], such that the pumped refractive index is approximately unchanged, each point in the sample is probed with the same pump-probe delay. It is only through the interplay of a finite sample thickness and finite pump and probe envelopes, that retardation effects become important.

Since our model does not contain a microscopic description of the pumped transition, we employ a phenomenological model: The selection rules of equilibrium transmission measurements hint towards local d-d-transitions being the dominant mechanism at orbital resonance. We therefore construct a pump operator, that couples locally and only to the orbital degree of freedom:

$$P_n = p_n \sum_i \sum_\sigma c^\dagger_{in\sigma} c_{i0\sigma} + \text{h.c.} \tag{3.9}$$

Therein n denotes the pumped orbital and p_n the transition probability. As we have no microscopic description of the pump, we can not make any predictions on the magnitude of p_n, which will depend on the exact form of the breaking of the point symmetry on the titanium sites [16]. Since the wavelength is much larger than the lattice spacing the pumping occurs homogeneously on all sites.

Under these approximations and without loss of generality setting the time at which the pump occurs to zero, we find that the susceptibility we have to compute is

$$\chi^R(t, t') = \langle\psi_0|\, P_n[j(t), j(t')] P_n \,|\psi_0\rangle\, \theta(t - t')\theta(t')\,, \tag{3.10}$$

where j is the current along the crystallographic b-axis corresponding to the polarization of the probe beam.

For direct correspondence to the experiment, we are not interested in two-time correlation functions, but the pump-probe delay dependent frequency resolved response. We again

[4] This is given in our setting, since the pump only changes the transmission by a few percent.

achieve this by a Fourier transform, where here we have to transform the probe-response time difference $\tilde{t} = t - t'$. If we leverage the eigendecomposition of the pumped state

$$P_n |\psi_0\rangle = \sum_E c_E |\psi_E\rangle , \tag{3.11}$$

where $H |\psi_E\rangle = E |\psi_E\rangle$, we can again phrase this Fourier transformed response function as spectral function:

$$\begin{aligned} \chi(\omega, t') &= \int_{-\infty}^{\infty} d\tilde{t} e^{i\omega\tilde{t} - \Gamma\tilde{t}} \chi(\tilde{t} + t', t') && (3.12) \\ &= \sum_{E,E'} c^*_{E'} c_E e^{i(E'-E)t'} \theta(t') \Bigg(\langle \psi_{E'} | j \frac{1}{\omega - H + E' + i\Gamma} j |\psi_E\rangle \\ &\qquad - \langle \psi_{E'} | j \frac{1}{\omega + H - E \ + i\Gamma} j |\psi_E\rangle \Bigg) . && (3.13) \end{aligned}$$

As outlined for the Lagrangian density in Section 2.2.3, we can compute the current in our tight binding Hamiltonian as the functional derivative of the Hamiltonian. Since we are only interested in the linear response A, both the minimal coupling and dipolar representation yield

$$j = \frac{\delta H}{\delta A_b}\bigg|_{A_b=0} = ie \sum_{i,j} d_{ij} \sum_{\alpha\beta} \sum_{\sigma} t_{i\alpha,j\beta} c^\dagger_{i\alpha\sigma} c_{j\beta\sigma} , \tag{3.14}$$

where $d_{ij} = -d_{ji}$ is the directed distance between sites i and j.

3.5.2 Eigendecomposition of the pumped states

If we know the eigendecomposition of the pumped states, we can evaluate the non equilibrium optical conductivity using offdiagonal spectral functions within Quanty [127]. Since spectral functions can be efficiently evaluated using Lanczos techniques [132–134][5], the eigendecomposition is the bottleneck, if the clusters exceed a trivial, fully diagonalizable size. Below, we outline a procedure, that iteratively finds the eigendecomposition of some state in the order of their importance utilizing the pumped states spectral function and auxiliary eigenvalue problems. It is as such similar to a method suggested by Ericsson and Ruhe in which they iteratively solve auxiliary eigenvalue problems to find all eigenvalues and vectors in a fixed spectral range [135]. We instead use the spectral function to create our auxiliary eigenvalue problems. Our strategy, outlined below, is summarized in Figure 3.6.

In large systems it is helpful, if the eigenvalues and eigenvectors we are interested in are extremal. This allows for the usage of iterative Lanczos techniques, which are able to converge extremal eigenvalues and eigenvectors quickly and efficiently. We can map a given eigenvalue problem on an auxiliary eigenvalue problem with the same eigenvectors but different eigenvalues associated to them using spectral transforms, such as a shift-and-invert or a Cayley transformation [136, 137]. Through a clever choice of these transforms we can therefore choose which eigenvectors in the original problem have extremal eigenvalues in the auxiliary problem. If we know at which energies the eigenvectors in the eigendecomposition of our pumped states

[5] We postpone a detailed discussion of the evaluation of such spectral functions to Chapter 4, where a manual implementation this kind of spectral function was necessary.

lie, we can therefore efficiently find these eigenvectors through these auxiliary eigenvalue problems.

In order to determine these energies, we can use the retarded spectral function of the pump operator. Formulated using the Lehmann representation it reads

$$A_n(\omega) = -\frac{1}{\pi}\lim_{\Gamma\to 0^+}\mathrm{Im}\left(\langle\psi_0|\, P_n \frac{1}{\omega - H + E_0 + \mathrm{i}\Gamma} P_n\, |\psi_0\rangle\right) \tag{3.15}$$

$$= \sum_E |\,\langle\psi_E|\, P_n\, |\psi_0\rangle\,|^2 \delta(\omega - (E - E_0))\,, \tag{3.16}$$

where the states $|\psi_E\rangle$ form a complete energy eigenbasis with energy E. It is a sum over the spectrum of H with a peak[6] at every energy in the pumped states eigendecomposition. Eigenstates of H not in the pumped states decomposition do not contribute as for them the matrix element $|\,\langle\psi_E|\, P_n\, |\psi_0\rangle\,|^2$ vanishes. Equation (3.15) can efficiently be approximated using a Lanczos Krylov subspace routine provided by Quanty via the 'CreateSpectra' function [127] for some finite broadening Γ. We can take the spectral function as probability distribution from which we randomly sample an energy E_{aux}. If the broadening is chosen appropriately and the spectral function properly converged, E_{aux} will likely lie in the vicinity of an eigenvalue whose eigenvector has a large overlap with the pumped state. We can therefore use it to construct an auxiliary eigenvalue problem with a spectral transform making the vicinity of E_{aux} extremal.

It would be possible to speed up the convergence by extracting the positions of the Lorentz peaks in the spectral function and using their centers as E_{aux}. Since we do not know the exact spectral function this can however create cases, where our iterative procedure becomes stuck sampling a dense region closeby to a relevant eigenvector. Randomly sampling avoids this issue. Furthermore iterating until a sufficient convergence is achieved does remove the influence on these random choices.

Within the Quanty framework there is no routine for spectral transforms and its diagonalization routine 'Eigensystem' searches iteratively for the smallest eigenvalues. We therefore manually implement a spectral transform using a shift and backfold, such that the Hamiltonian of the auxiliary eigenvalue problem is defined as

$$H_{\mathrm{aux}} = (H - E_{\mathrm{aux}})^2\,. \tag{3.17}$$

It is clear to see, that eigenvectors of H with eigenvalue E are also eigenvectors of H_{aux} and have the eigenvalue $(E - E_{\mathrm{aux}})^2$. Searching for the smallest eigenvalues of H_{aux} therefore searches in the vicinity of E_{aux} in H. In contrast to shift-and-invert or Cayley transformations our spectral transformation does however introduce two drawbacks:
(i) It introduces artificial (near-) degeneracies. The space spanned by the eigenvectors corresponding to the eigenvalues $E_{\mathrm{aux}} \pm \epsilon$ in H span a degenerate subspace in H_{aux} with the eigenvalue ϵ^2. Eigenvectors of H_{aux} are therefore not necessarily eigenvectors of H.
(ii) The square in our transform decreases the distance in energy between eigenvalues in the vicinity of E_{aux}. This worsens numerical precission and can slow down convergence. We counteract these drawbacks by postprocessing of our converged eigenvectors H_{aux}: We fully diagonalize H in the small space spanned by the converged eigenvectors. This removes any

[6] In the case of a finite broadening Γ, these infinitely sharp peaks become Lorentz curves with their center at the corresponding energy.

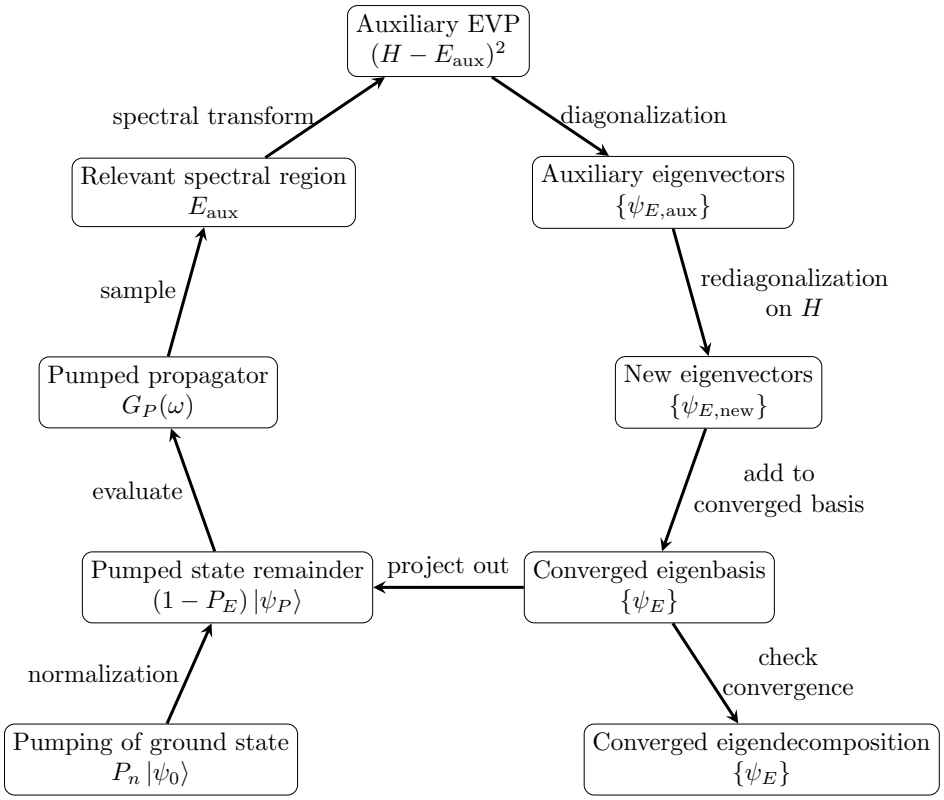

Figure 3.6: Schematic for the iterative eigendecomposition procedure. Convergence is achieved once the norm of the difference of the pumped state and its eigendecomposition is smaller than a threshold $\|(1 - P_E)\,|\psi_P\rangle\|_2 < \epsilon$.

degeneracies introduced by our spectral transform and returns us to numerical precission used throughout.

Having found one or more eigenvectors $|\psi_E\rangle$ in the pumped states eigendecomposition we can remove their contribution to the spectral function of the pump operator. This can be accomplished by using a projected pump operator $P_{\{E\}} \cdot P_n$, where $P_{\{E\}} = \prod_E (1 - |\psi_E\rangle\langle\psi_E|)$. Due to the restictions of Quanty we instead use the propagator[7] of the pumped state with all contributions of converged eigenstates removed. With this spectral function we can again find new eigenvectors via an auxiliary eigenvalue problem running through this loop until we are satisfied with the representation of our pumped state in terms of the converged eigenvectors. We determine this convergence by computing the difference in norms.

A summary of this procedure is sketched in Figure 3.6. Since we are using Krylov subspace routines for the spectral function and eigendecomposition steps, a comparison to a straightforward full diagonalization in a large Krylov subspace [131] is warranted. Our procedure has three advantages:
(i) Each eigenvectors is obtained through a diagonalization of the full operator H and not necessarily its projection on a small Krylov subspace.
(ii) The order in which we find converged eigenstates is controlled by their overlap with the pumped state and not its eigenvalue with respect to H.
(iii) The impact the accumulation of numerical imprecision in spanning the Krylov space is smaller, since we avoid spanning a single huge Krylov space, but instead span small once many times. These do however come at the cost of a much bigger computational effort, since

[7] Since Quanty only knows about spectral functions of operators evaluated on some state, we implement this as spectral function of the identity operator acting on our pumped state.

each iteration requires a computationally expensive diagonalization and the computation of a comparatively computationally cheap spectral function.

3.6 Results

Within the previously outlined procedure we are able to compute the optical conductivity for two site clusters with open boundary conditions and a four site cluster with periodic boundary conditions. In order for the resulting spectral functions to contain peaks at the experimentally measured center, it is however not sufficient to consider the pumped ground state alone. Excited states on the cluster prior to the pump are, however, energetically far removed from thermally accessible energies. In addition to this discrepancy, the results for the two and four site cluster differ. For TiOCl the optical conductivity of the Mott gap is therefore not converged with respect to cluster size for a four site cluster. We can nevertheless learn something about the accessible states and the spin-orbital configurations accessible to the current operator, that generate the spectra. Below we first discuss the two-site cluster, where we can distinguish between the contributions from the singlet and the triplet configurations on the cluster. We then briefly outline the differences found in the four site cluster.

3.6.1 Two-site cluster

On the two site cluster the highly entangled groundstate of the Heisenberg model cannot be represented: Written in terms of bond operators [138], the spin-1/2 Heisenberg Hamiltonian becomes the sum over projectors on the singlet state on each bond plus a global offset[8]. On a two site cluster the groundstate will therefore be a singlet. Projecting the lattice groundstate to the two site cluster does however also produce triplet admixture. As the current operator preserves the total spin (see equation (3.14)), we consider the measurement of the optical conductivity on a two site cluster as a projective measurement of the spin of the cluster. In the absence of dimerization the groundstate energy per bond in the spin-1/2 Heisenberg model is known to be $J(\ln 2 + 1/4)$ [139, 140]. Interpreted as projective measurement we should therefore find a singlet with probability $\ln 2$ and a triplet with probability $1 - \ln 2$. Averaged over all two site clusters these probabilities become the weights with which we have to average the corresponding optical conductivities.

In the dimerized system we furthermore have to distinguish between two site clusters on the strong and on the weak bonds. The magnetic ground state in the dimerized setting is changed with the weak bonds more likely to host triplets while the strong bonds are more likely to host a the singlets. The approximate singlet and triplet weights for given dimerization can be obtained using exact diagonalization of large spin systems [141] or series expansions [112]. Since this is beyond the scope of this thesis, we ignore the impact of the dimerization on the magnetic states when combining the conductivities of the two site clusters in Figure 3.7a. The corresponding spectra resolved by cluster and configuration can be found in Appendix A.

In Figure 3.7a we show the time resolved optical conductivity from the two site clusters and the experimentally measured non-equilibrium transmissivity difference. Comparing both pumps to the experimental data, we find that both spectra we computed are missing the long lived feature visible in the experimental data at 1.5 eV. It originates from resonant d-d-excitations by the probe beam. They are absent since our model contains the necessary transition matrix

[8] This offset depends on the choice of the Heisenberg Hamiltonian. Here we use $H_{\mathrm{Hb}} = J \sum_{\langle i,j \rangle} \vec{S}_i \cdot \vec{S}_j$. If we instead use $J \sum_{\langle i,j \rangle} (\vec{S}_i \cdot \vec{S}_j - 1/4)$, this offset vanishes (see Chapter 5).

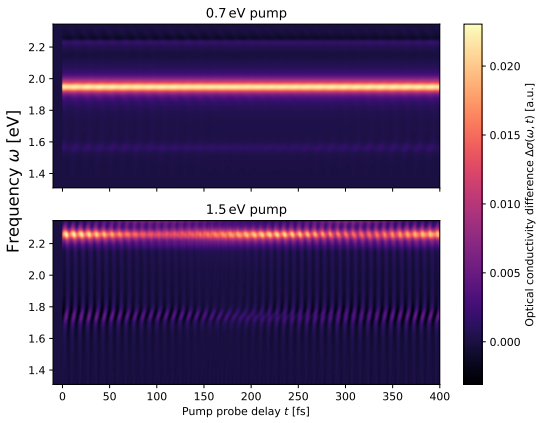

(a) Two site cluster

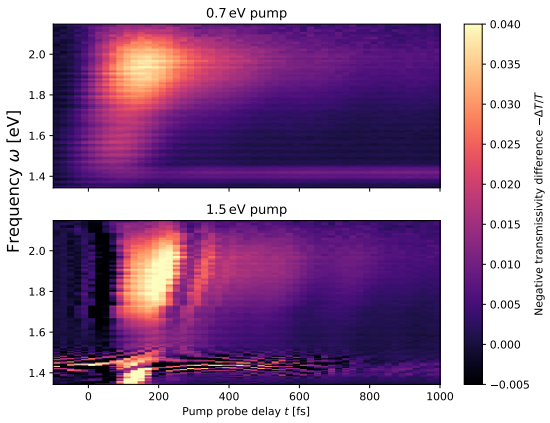

(b) Experimental data

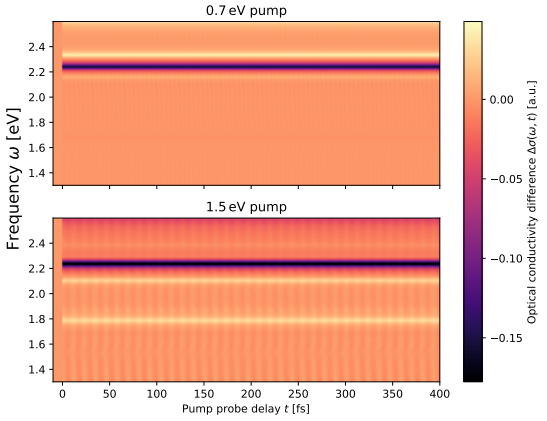

(c) Four site cluster groundstate

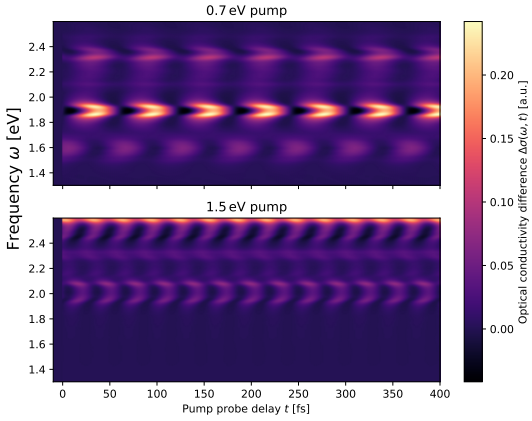

(d) Four site cluster first excited state

Figure 3.7: Computed conductivity differences (a),(c),(d) $\Delta\sigma(\omega, t)$ and experimental negative transmissivity difference (b) $-\Delta T/T$. (a) shows the conductivity as evaluated on the two site cluster with all four contributions (weak/strong bond, singlet/triplet state) averaged as outlined in the main text; (b) shows the corresponding experimentally measured transmissivity difference [67] provided by A. Montanaro; (c), (d) show the conductivity as evaluated on the four site cluster, where (c) shows the pumped ground state and (d) the pumped first excited state of the cluster. In Appendix A we additionally show the two site results of (a) resolved by bond type and configuration (see Figure A.3) as well as the spectral functions obtained in the eigendecomposition loop (see Figure A.1 for the two site cluster and Figure A.2 for the four site cluster).

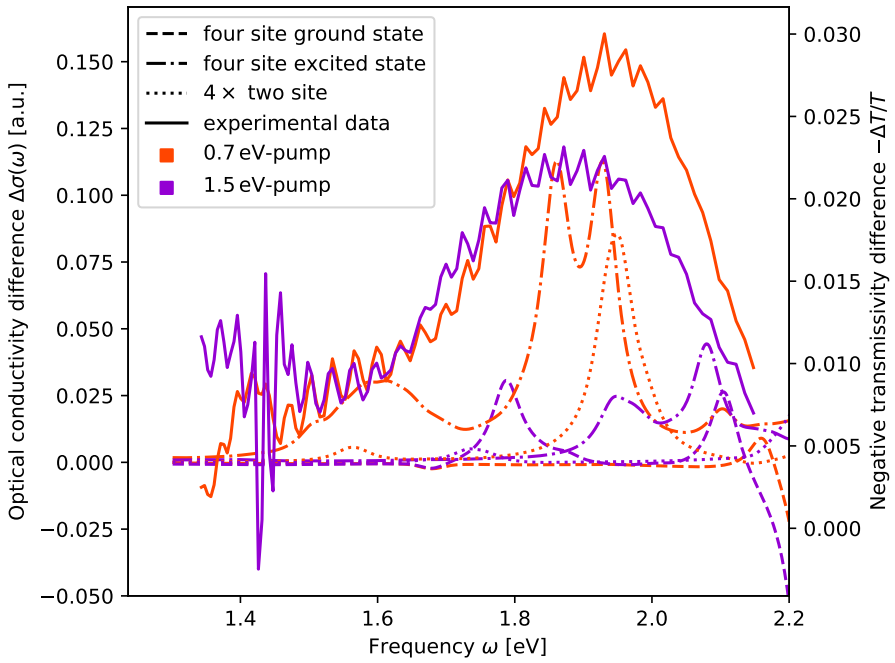

Figure 3.8: Time-averaged conductivity difference $\langle \Delta\sigma(\omega) \rangle_t$ (left axis) for the first 400 fs evaluated on the two and four site clusters. As with Figure 3.7, the four bond configuration combinations of the two site cluster are combined into a single conductivity. Since the four site cluster contains four times as many nearest neighbor bonds as the two site cluster, we scale the two site cluster results by a factor of 4. The experimental negative transmissivity difference (right axis) provided by A. Montanaro [67] is averaged over the first 400 fs as well.

elements neither for the equilibrium probe nor for the pump-probe spectra. Our current operator j only takes into account the dipole moment of electrons hopping between sites (see equation (3.14)). If we were to add local quadrupolar [142] currents or the dipole allowed d-d currents [16] to our description, we should be able recover this contribution as well.

Since our description neglects the envelopes of the pump and the probe, the build up of the spectral response at short times in the experimental data is not captured within our computations either. Instead the change in orbital configuration is instant at $t = 0$.

Figure 3.8 shows the spectra averaged over the first 400 fs after the pump. The 0.7 eV-pump spectrum is dominated by a peak at $\hbar\omega \approx 1.95$ eV. This corresponds approximately to the center of the Mott-gap in the experimental measurement. Resolving the clusters and states on the clusters separately (see Figure A.3), we find that this peak is only present, if the two site clusters are in a triplet configuration. It is therefore reliant on the Hund's coupling in the probed state. In the spectrum of the 1.5 eV-pump this peak is absent. We instead find one at much higher frequencies at $\hbar\omega \approx 2.25$ eV and one at lower frequencies $\hbar\omega \approx 1.75$ eV. Whether or not the low energy peak is responsible for shifting the experimentally measured Mott response to lower energies can however not conclusively stated without checking the convergence of these peaks with respect to cluster size.

All oscillations visible in the computed spectra are caused by multiple eigenstates in the pumped eigendecomposition contributing: If the offdiagonal current-current correlation function has spectral weight at some frequency ω between eigenstates $|\psi_E\rangle, |\psi_{E'}\rangle$, the exponential in equation (3.13) leads to an oscillation with angular frequency $\omega = (E - E')/\hbar$. Since

our energy resolution scales inversely with the cluster size, we are generally limited to being able to resolve fast oscillations[9].

3.6.2 Four-site cluster

Employing the same procedure for the four site cluster we again find few strongly contributing eigenstates in the pumped states eigendecomposition (see Figure A.2 in the appendix). The prominent triplet feature at 1.9 eV for the 0.7 eV-pump is however absent if we consider the cluster ground state only for our pump-probe formalism, despite it containing some triplet admixture. We recover it when we pump the first excited state of the cluster. Since we cannot evaluate larger clusters, it is unclear if the lack of this peak is an artifact of the small cluster size or physical. Without employing some other embedding technique, it is not directly clear how the ground and excited states of the cluster should be combined for a single spectra consistent with our treatment of the two site cluster. We therefore show both of them separately.

Compared to the two site cluster (see Figure 3.8), we expect the conductivity to be larger by a factor of $\gtrsim 4$, since the two site cluster was evaluated with open boundary conditions and therefore only contains one bond, while the four site cluster has four nearest neighbors and two next-nearest neighbor bonds on which the current operator can act.

3.7 Conclusion and Outlook

Our results hint show the potential for probing the Mott-gap being sensitive to the orbital occupation. Since we can only evaluate the two site cluster and the four site cluster numerically our results are not yet converged with respect to the cluster size, such that quantitative predictions are not possible and the qualitative link is not conclusively proven.

This can be the result of the cluster not being able to contain the processes contributing to the lattice current-current correlation function properly or the pumped state not being contained properly on the reduced cluster Hilbert space. The former could be checked by comparing against a different more local observable, that is more directly sensitive to orbital occupations. This could among other methods be accomplished using the linear dichroism of time-resolved x-ray absorption (tr-XAS). If the different crystalfield orbitals have different transition matrix elements, it should be able to resolve orbital occupancy using the titanium L-edge at around 450 eV [143]. Similarly, time-resolved resonant inelastic x-ray scattering (tr-RIXS) could provide direct access to the difference in orbital occupation by either resolving anti-Stokes peaks [144] or changed spectral weight of the Stokes peaks.

In order to better describe the optical transmission experiment, there are two possibilities: We can either try to increase the cluster size on which we evaluate the optical conductivity. This could be accomplished by reducing the Hilbert space. As currently implemented the local Hilbert space on each site has five orbital and two spin degrees of freedom. In a manual implementation tailored to this setting it would be possible to make use of these to increase the cluster size to more sites. Furthermore, the Quanty framework, with which we evaluate our spectra, is written for small local cluster computations for e.g. x-ray absorption spectra. It

[9] Since the clusters spectral density is not evenly distributed, we can also find slower oscillations, if by chance the pumped state contains multiple eigenstates from the same dense spectral region. This is visible e.g. in the spectrum of the 1.5 eV-pump at $\hbar\omega = 2.3$ eV, where two eigenstates with an energy difference of ca. 20 meV contribute. The frequency of their oscillation is therefore $f \approx 200$ fs.

and its routines are therefore not optimized for the kinds of computations, i.e., the eigendecompositions on large clusters. We are currently working on writing a custom configuration interaction solver, that allows for more control of internal subroutines and importantly uses neural network to find the minimal basis necessary to treat large clusters [145, 146]. In its current state this is possible for the computation of cluster ground states [147], while spectral functions and eigendecompositions are under development.

To improve the results it would also be beneficial to account for the embedding of the cluster in the lattice. It would e.g. be possible to compute the lattice ground state in the thermodynamic limit [112] and project it to the cluster for a better approximation than just using the cluster ground state. Additionally, it is not only possible to use an embedded starting state, but include an effective embedding for dynamical quantities using dynamical mean field theory (DMFT) [20, 21, 148]. Within DMFT it is also possible to evaluate explicitly time-dependent correlation functions accounting for a pump with a given envelope [149]. The large local Hilbert space of TiOCl and non-local magnetic correlations might, however, make an evaluation of $\sigma(t, \omega)$ difficult within DMFT. These embeddings also allow for open dynamics on the cluster, which are currently absent in our description. In the following Chapter 4, we derive the building blocks for an effective open description of the setting. By evaluating the lifetime of orbital excitations due to the decay into other types of orbital excitations and magnons, a master equation [150], that describes an effective open theory for our cluster coupled to a spin-orbital bath, could be constructed [151]. In this thesis we present the computation of this lifetime using Fermi's golden rule. Setting up the master equation and solving for its dynamics is beyond the scope of this thesis.

4 Lifetime of orbital excitations in TiOCl

In this chapter we continue the theoretical description from Chapter 3, that supports the experimentally obtained time-dependent transmission spectra as reported in the as of yet unpublished work [P1]. As such, it follows [P1] in notation, terminology and phrasings. As outlined in Chapter 3, the authors contribution to this work was the derivation of the effective low energy Hamiltonian from DFT computations done by P. Hansmann (see Sections 3.3 and 3.4), the computation of the non-equilibrium optical conductivity (see Sections 3.5 3.6) and the orbiton lifetime due to decay into magnons, which is the subject of this chapter.

4.1 Motivation

The time-dependent spectra computed in Chapter 3 neglected the open dissipative dynamics. This is due to us only considering small clusters and the unitary dynamics therein. In the experimental pump-probe spectra (see Figure 3.7b) we could however identify, that on a timescale of few hundred fs the spectral features of the pump vanish. Assuming that, as we conjecture in Chapter 3, the spectra are orbitally sensitive, the lifetime of the pumped excitation can therefore be estimated from the experimental data. This estimation is, however, more accurately possible by a non-linear measurement: In Chapter 3 we showed the time-resolved spectra our experimental collaborators obtained by pumping the sample with either a 0.7 eV-pump or a 1.5 eV-pump. Their setup [66] does additionally allow subjecting the sample to both pumps with time delays between the pumps controllable. We sketch this setting in Figure 4.1. This give rise to a non-linear signature, that is obtained by subtracting the equilibrium and single-pump spectra from the measured double pump-spectrum. This non-linear signature shows an asymmetry with respect to the order and time delay of both pumps (see Figure 4.2). It can be quantified by the time-constants of the exponential decays with respect to the pump-pump delay. While other origins of and influences on this asymmetry are possible, the lifetimes of the pumped excitations definitely influences these time-constants: Pumping a short-lived excitation should produce a non-linear signature only for short pump-pump delays, while a long-lived excitation can produce this signature also for long delays.

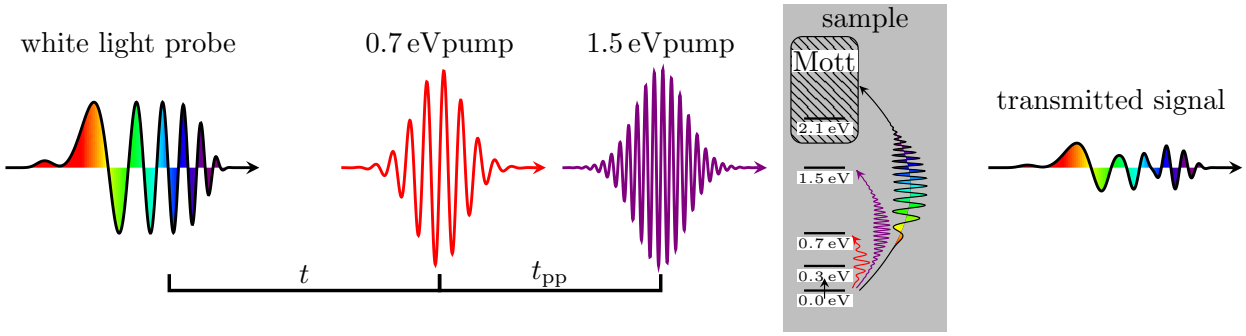

Figure 4.1: Sketch of the double-pump-probe spectroscopy experimental setting: The system is first pumped using the 1.5 eV-pump; After a time-delay t_{pp} it is pumped using the second pump at 0.7 eV (for negative t_{pp} the order is reversed). Indicated on the sample are the crystal field transitions to which the pump beams are resonant and the Mott gap, which in large parts covers the energy range of the white-light probe beam. The transmission of the probe beam is measured. To obtain the non-linear signature shown in Figure 4.2, the static and transient linear pump signatures are subtracted from the transmitted signal.

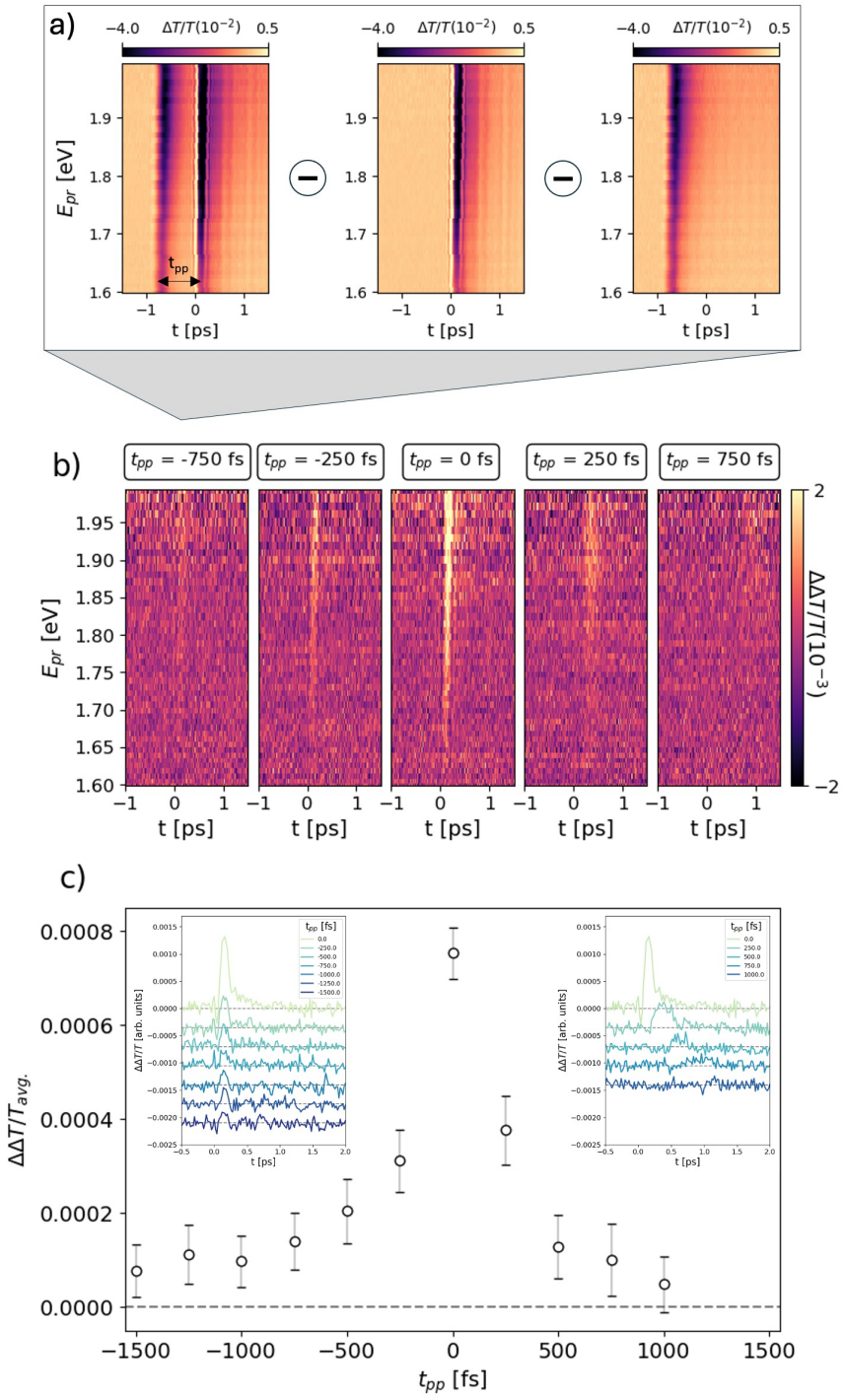

Figure 4.2: Experimental double pump signature as measured by our experimental collaborators. a) Double pump spectra from which the subtraction of the single pump-spectra is indicated to produce the non-linear double pump feature; b) Time-resolved non-linear double pump spectra $\Delta\Delta T/T$ for various pump-pump delays; c) Non-linear double pump spectra averaged over the relevant energy range against the pump-pump delay. Figure taken from [P1].

As hinted to at the end of Chapter 3, open dynamics requires an embedding of the cluster on the lattice. In systems of interacting fermions dynamical mean-field theory (DMFT) [20, 21, 148] is a sophisticated approach that generally can accomplishing this. For our setting it is however difficult to use: Keeping track of the magnetic non-local correlation requires either cluster extensions [152–156] or diagrammatic extensions [22, 23]. For non-equilibrium states it not sufficient to track Green's functions on the Matsubara frequencies, but the complete Keldysh contour [46, 157] has to be considered [24, 149]. Combining both approaches is possible [94, 158] but computationally unfeasible due to the large necessary local Hilbert space for our magnetically ordered five-band model.

In its simplest formulation, the embedding does however not need any self-consistency. If the matrix elements coupling different orbital configurations are small, we can use the leading order of a weak coupling expansion, i.e., Fermi's golden rule [34, 46, 159], to compute the transition rate between these configurations. In order to compute the lifetime of an orbital excitation we therefore have to sum over all transition rates to other configurations. Since we still keep track of the orbital configuration this amounts to tracing out the spin configuration. It can be shown that the lifetime we obtain thereby is equivalent to that of a master equation [46, 150] in the space of orbital configurations. In this master equation the spins are contained as a Markovian bath whose coupling strength is determined by the transition rates we compute using Fermi's golden rule [151, 160]. Formulating this master equation and solving it is left for future work.

We evaluate Fermi's golden rule as spectral function on a cluster using a Lanczos approach. Since the gap between orbital excitations is much larger than the energy of single magnons, decays can only be facilitated by multi-magnon processes, which in turn require large clusters to evaluate[1]. In Chapter 3 we were limited to small clusters by the quickly growing size of the Hilbert space. Since in this chapter we no longer need an explicit description of the charge excitations, we can work within the effective spin-orbital Hamiltonian derived in Section 3.4 allowing for much larger cluster sizes.

4.2 Form of the effective spin-orbital-Hamiltonian

The time evolution of low energy excitations well below the Mott-gap is properly captured within the effective spin-orbital Hamiltonian (3.8) we derived in Section 3.4. It maps transitions to the upper Hubbard band to spin- and orbital exchange allowing for the truncation of all charge excitations. Our Hamiltonian is therefore an ab-initio version without any orbital degeneracies of the spin and orbital pseudo-spin model suggest by Kugel and Khomskii [161].

The transformation mapping the tight-binding model to the spin-orbital description does not produce a block diagonal current operator. We were therefore not able to utilize the reduced spin-orbital basis in Chapter 3 to compute optical conductivities. Since we found some sensitive of the optical conductivity at the Mott-gap to the orbital occupation, even on small clusters, we will not compute any direct observables in this chapter but instead limit ourselves to computing the decay of a initially prepared states.

As mentioned in Section 3.4, the series expansion is only converged for states well gapped from the Mott-gap. Since orbital excitations provide the dominant energy scale, we limit orbital

[1] We can also formulate this argument in terms of the master equation: The density of states of the spin bath is given by the spectrum of all spin configurations. If we choose our clusters too small there is no density of states at the high energies of the orbital gap required for the decay.

configurations allowed on our large cluster. We therefore consider only the subspace, where there is at most 1.5 eV in the orbital excitation determined by the bare crystal field splitting. Throughout this chapter we will refer to orbital excitations by their approximate crystal field energies (0.0 eV, 0.4 eV, 0.7 eV, 1.5 eV) or by an index $o \in \{0, 1, 2, 3\}$[2] corresponding to the energetic order. In preparation for again using the interaction picture we split the spin-orbital Hamiltonian

$$H_{\text{sp-orb}} = H_0 + V \tag{4.1}$$

in an orbital configuration preserving contribution H_0 and one that changes it V.

4.2.1 Orbital configuration preserving terms

We find

$$\begin{aligned} H_0 = &\sum_i H_{i,\text{crystal field}} \\ &+ \sum_{\langle i,j \rangle} \sum_{d=s,w,k} |\hat{e}_{ij}\hat{e}_d| \left(H^d_{ij,\text{int}} + H^d_{ij,\text{disp}} + (H^d_{ij,\text{Hb}} + H^d_{ij,\text{Hb-disp}})\vec{S}_i \cdot \vec{S}_j \right), \end{aligned} \tag{4.2}$$

where $H_{i,\text{crystal field}}$ is the energy due to the crystal field splitting. Since decay widths strongly depend on gaps between the different orbital excitations, we use the crystal field splitting as measured by Glawion et al. [100] using RIXS instead of the values obtained by our ab-initio calculation. This amounts to $E_0 = 0\,\text{meV}$, $E_1 = 340\,\text{meV}$ $E_2 = 620\,\text{meV}$ $E_3 = 1480\,\text{meV}$[3]. Furthermore,

$$H^{0,d}_{ij,\text{int}} = \sum_{o,o'} I^d_{o,o'} \cdot |o_i \otimes o'_j\rangle \langle o_i \otimes o'_j| \tag{4.3}$$

denotes the interaction on the bond ij oriented in direction d diagonal in spin and orbital configuration,

$$H^{0,d}_{ij,\text{disp}} = \sum_{o,o'} D^d_{o,o'} \cdot |o_i \otimes o'_j\rangle \langle o'_i \otimes o_j| \tag{4.4}$$

the exchange of orbital configurations on sites i, j,

$$H^{0,d}_{ij,\text{Hb}} = \sum_{o,o'} J^d_{o,o'} \cdot |o_i \otimes o'_j\rangle \langle o_i \otimes o'_j| \tag{4.5}$$

the orbitally dressed Heisenberg exchange and

$$H^{0,d}_{ij,\text{Hb-disp}} = \sum_{o,o'} K^d_{o,o'} \cdot |o'_i \otimes o_j\rangle \langle o_i \otimes o'_j| \tag{4.6}$$

simultaneous Heisenberg and orbital configuration exchange. $I^d_{o,o'}, D^d_{o,o'}, J^d_{o,o'}$ and $K^d_{o,o'}$ are the amplitudes of these terms as obtained by the series expansion (see equation (3.8)). We list the

[2] We drop the $o = 4$ excitation, since it is outside of the converged region of the Hilbert space and redundant for the decay of $o = 3$ and $o = 2$ excitations.

[3] Note that there is some discrepancy between rounding these values and the energetic names we associate with them. This is due our naming being based on a different measurement [16].

ones used in this chapter in Table 1. Of these, we want to put emphasis on a few of them: $J^s_{0,0}$ and $J^w_{0,0}$ are the ground state Heisenberg exchange, that we utilize to fix the onsite interaction and the dimerization. The low energy description as one-dimensional Heisenberg chains is possible, since $J^p_{0,0}$ is much smaller than those two. In a multi-orbital Hubbard model the series expansion renormalizes the energy of the singlet and triplet states. The Heisenberg exchange denotes the difference between those two. For the singlet configuration, there are more exchange processes possible (since there is no Pauli exclusion), while for the triplet configurations the energy of the intermediate state is lowered by the Hund's coupling. Due to this competition, we find configurations for which the Heisenberg exchange favors the singlet configuration $J^d_{o,o'} > 0$ and ones where the triplet configuration is favored $J^d_{o,o'} < 0$.

In the electronic picture an orbital excitation has a hole in the valence band and an electron in the conduction band. We can therefore consider it as a tightly-bound Frenkel-exciton [34]. Since all $I^d_{o,o'}$ are positive, orbital excitations repel each other on short ranges[4]. $D^d_{o,o'}$ and $K^d_{o,o'}$ allow the orbital excitations to move between sites. They therefore determine the bandwidth of these excitations, which is much smaller than the electronic single-particle bandwidths.

Lastly the amplitudes for spin exchange drastically differ depending on the orbital configuration. Similarly the orbital exchange is influenced by the spin configuration. In contrast to e.g. Sr_2CuO_3, where spin of an excitation is approximately conserved by exchange processes [162], both sectors are strongly intertwined. We therefore call a quasiparticle consisting of an excitation of the orbital sector with a magnon cloud according to the Hamiltonian $H_{\mathrm{Sp-Orb}}$ equation (4.2) an orbiton. For the remainder of this chapter we will refer to excitations as orbitons, when including the magnon cloud, and as orbital excitation, if this cloud is absent.

This quasiparticle nature can have a big impact on the lifetime: If the spin and orbital sectors were decoupled in H_0, such that the orbiton would just be an orbital excitation without any magnon cloud, the only way for decay to emit magnons would be via the decay operator. To bridge the gaps between the orbital excitations we require many magnons. A multi-magnon decay operator would require extending the second order expansion we have performed in Section 3.4 to much higher orders or remaining in the electronic Hilbert space altogether [163]. Since both sectors in our case are coupled, there is a mismatch between the magnon cloud of the decaying orbiton and the decayed states [163]. We sketch this in Figure 4.3. An orbiton does therefore not straightforwardly decay into different kinds of orbitons but additionally excites the magnetic sector through the formation of a new magnon cloud and potentially emitting free magnons in this formation[5,6].

[4] Since they hybridize with the local magnetic environment, we can however not exclude the possibility, that on longer length scales, there can be a spin-mediated attraction.

[5] If both orbitons renormalize the magnetic exchange equally, we return to the decoupled case. Consulting Table 1 for the different $J^d_{o,o'}$, we can see that for TiOCl this is not the case for any decay process.

[6] Since we treat the whole decay using exact diagonalization, distinguishing between the bound and free magnons is not straightforward. If this is desired decoupled toy models should be considered or the decay process formulated in an effective quasiparticle description, e.g., using a series expansion as in Reference [112].

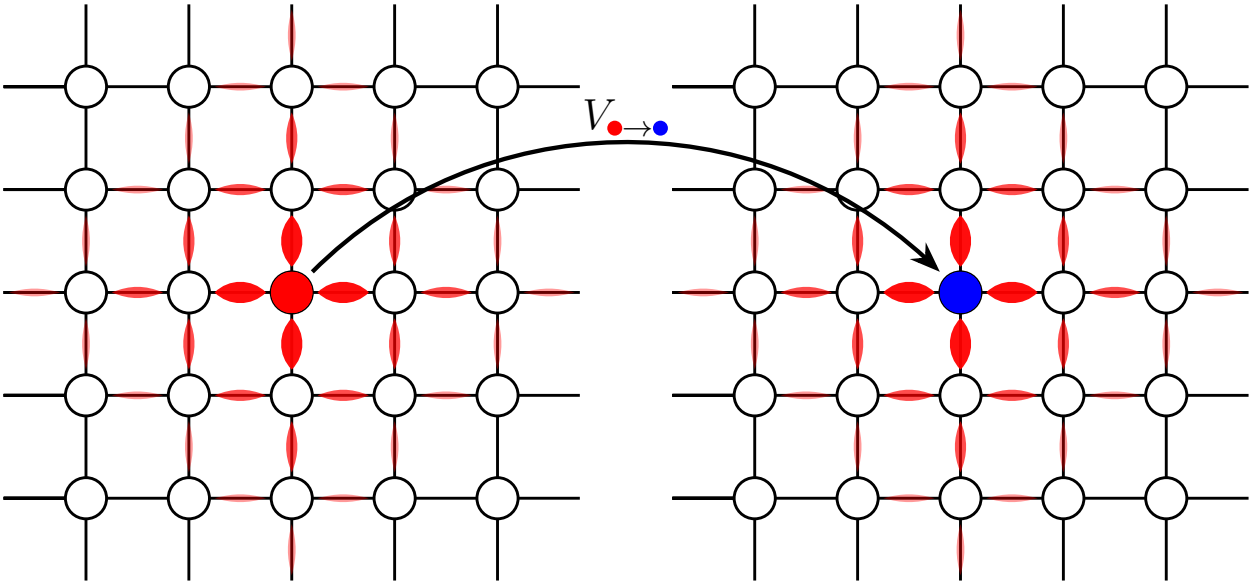

Figure 4.3: Sketch of the role of the magnon cloud for an orbiton decay process: In the decaying state the presence of a localized orbital excitation (red circle) strains the magnetic surrounding (red bonds with size indicating the strength of the distortion) if compared to no orbital excitations present. If the decay operator $V_{\bullet\to\bullet}$, that describes the decay of the red to the blue orbital excitation, acts on this state, the resulting differing orbital excitation (blue circle) is surrounded by the wrong kind of magnon cloud. This mismatch decomposes into a new bound blue magnon cloud and free magnons. The formation of both of these can take on a part of the energy to facilitate the decay.

$I^d_{o,o'}$[meV]		direction d		
		s	w	p
(o,o')	$(1,1)$	92.4	74.4	50.9
	$(1,2)$	85.8	68.4	9.0
	$(2,2)$	84.6	67.0	26.9

$D^d_{o,o'}$[meV]		direction d		
		s	w	p
(o,o')	$(0,1)$	6.0	3.5	4.1
	$(0,2)$	−19.7	−16.9	0.3
	$(0,3)$	−8.6	−4.1	−0.4
	$(1,2)$	2.3	1.5	−25.7

$J^d_{o,o'}$[meV]		direction d		
		s	w	p
(o,o')	$(0,0)$	90.0	68.0	−1.6
	$(0,1)$	−21.2	−17.0	−15.0
	$(0,2)$	−16.5	−13.2	−13.2
	$(0,3)$	−12.5	−10.2	−6.3
	$(1,1)$	0.7	0.0	74.4
	$(1,2)$	−1.9	−1.5	−25.7
	$(2,2)$	15.8	15.5	8.4

$K^d_{o,o'}$[meV]		direction d		
		s	w	p
(o,o')	$(0,1)$	15.7	9.1	9.4
	$(0,2)$	−54.8	−47.3	1.3
	$(0,3)$	−26.1	−12.6	−0.7
	$(1,2)$	6.5	4.3	−57.0

Table 1: Amplitudes of the different contributions to the spin-orbital Hamiltonian (4.2). The operators for each of these amplitudes are shown in equations (4.3)-(4.6). The symmetry $(o,o') \leftrightarrow (o',o)$ is implied.

(2,0) to (0,0)	direction d		
	s	w	p
L	0.0	0.0	−8.2
M	0.0	0.0	−1.6

(2,0) to (1,1)	direction d		
	s	w	p
L	0.0	0.0	1.1
M	0.0	0.0	−2.8

(2,0) to (1,0)	direction d		
	s	w	p
L	−6.1	5.8	0.0
M	−16.3	15.6	0.0
B	−1.2	1.4	0.0
N	−0.4	0.5	0.0

Table 2: Amplitudes $L^d_{2;o'o''}, M^d_{2;o'o''}, B^d_{2;o'o''}, N^d_{2;o'o''}$ describing the decay of an $o = 2$ orbiton. For $(o', o'') \in \{(0,0),(1,1)\}$ $B^d_{2;o'o''}$ and $N^d_{2;o'o''}$ vanish as the associated processes are already described using $L^d_{2;o'o''}$ and $M_{2;o'o''}$.

4.2.2 Decay channels

We limit our discussion of V to the contributions, that are relevant for the decay of the $o = 3$ orbiton at $\approx 1.5\,\mathrm{eV}$ and the $o = 2$ orbiton at $\approx 0.7\,\mathrm{eV}$.

$$V = \sum_{\langle i,j\rangle} \sum_{d=s,w,k} |\hat{e}_{ij}\hat{e}_d| \left(V^d_{ij,\mathrm{loc}} + V^d_{ij,\mathrm{disp}} + \left(V^d_{ij,\mathrm{Hb}} + V^d_{ij,\mathrm{Hb-disp}} \right) \vec{S}_i \cdot \vec{S}_j \right) \tag{4.7}$$

We can split these four contributions into different decay channels depending on the orbital configurations between which they map:

$$V^d_{ij,\mathrm{loc}} = \sum_{o;o',o''} L^d_{o;o_1,o_2} \, |o'_i \otimes o''_j\rangle \langle o_i \otimes 0_j| \tag{4.8}$$

denotes the in-place decay of an o-orbiton to an o'-orbiton on the same site and an o''-orbiton on the neighboring site. $V^d_{ij,\mathrm{Hb}}$ denotes the same process with the additional spin exchange of $\vec{S}_i \cdot \vec{S}_j$. We label its amplitude $M^d_{o;o_1,o_2}$. $V^d_{ij,\mathrm{disp}}$ and $V_{ij,\mathrm{Hb-disp}}$ denote the same kind of processes with the orbital configuration in the final state swapped, i.e,

$$V^d_{ij,\mathrm{disp}} = \sum_{o;o',o''} B^d_{o;o_1,o_2} \, |o''_i \otimes o'_j\rangle \langle o_i \otimes 0_j| \ . \tag{4.9}$$

We label their amplitudes by $B^d_{o;o',o''}$ and $N^d_{o;o',o''}$. For decay channels to symmetric configurations $o' = o''$, we treat them as in-place processes such that $\forall o, o' : B^d_{o;o'o'} = N^d_{o;o'o'} = 0$. We list the amplitudes of these decay channels in Table 2 for those starting with an $o = 2$ orbiton. Those for the $o = 3$ orbiton are listed in Table 3. For the decay channels it is helpful to group them by orbital occupations instead of spin and orbital configurations as done in Table 1, since we will later on implement them simultaneously.

Energetics tells us, that the $o = 2$ orbiton can decay either into magnons only ($(2,0) \to (0,0)$), into one $o = 1$ orbiton and magnons ($(2,0) \to (1,0)$) or to two $o = 1$ orbitons and magnons

(3,0) to (0,0)	direction d		
	s	w	p
L	4.6	−5.0	0.2
M	4.7	−6.8	0.1

(3,0) to (1,0)	direction d		
	s	w	p
L	0.0	0.0	17.1
M	0.0	0.0	14.2
B	0.0	0.0	−1.0
N	0.0	0.0	−1.9

(3,0) to (2,0)	direction d		
	s	w	p
L	0.0	0.0	−0.5
M	0.0	0.0	−0.5
B	0.0	0.0	0.0
N	0.0	0.0	0.0

(3,0) to (1,1)	direction d		
	s	w	p
L	1.1	−1.0	0.0
M	−1.0	−1.5	0.0

(3,0) to (2,1)	direction d		
	s	w	p
L	−1.7	−1.0	4.5
M	−2.2	−1.3	9.1
B	3.7	3.1	4.5
N	5.2	4.4	9.1

(3,0) to (2,2)	direction d		
	s	w	p
L	1.2	−1.0	0.0
M	−1.0	−2.1	0.0

Table 3: Amplitudes $L^d_{3;o'o''}, M^d_{3;o'o''}, B^d_{3;o'o''}, N^d_{3;o'o''}$ describing the decay of an $o = 3$ orbiton. For $(o', o'') \in \{(0,0),(1,1),(2,2)\}$ $B^d_{2;o'o''}$ and $N^d_{2;o'o''}$ vanish as the associated processes are already described using $L^d_{2;o'o''}$ and $M_{2;o'o''}$.

$((2,0) \to (1,1))$. The gaps due to the crystal field Hamiltonian for these decay channels are 620 meV, 280 meV and –60 meV respectively.

Since the $o = 3$ orbiton has a higher energy there are more target states for the decay channels. We find the decay into magnons only $((3,0) \to (0,0))$, into a single $o = 1$ orbiton and magnons $((3,0) \to (1,0))$, a single $o = 2$ orbiton and magnons $((3,0) \to (2,0))$, two $o = 1$ orbitons and magnons $((3,0) \to (1,1))$, an $o = 2$ and an $o = 1$ orbiton and magnons $((3,0) \to (2,1))$ or two $o = 2$ orbitons and magnons $((3,0) \to (2,2))$. The gaps due to the crystal field Hamiltonian for these decay channels are 1480 meV, 1140 meV, 860 meV, 800 meV, 520 meV and 240 meV respectively.

4.3 Fermi's golden rule

Since we have a Hamiltonian with well defined orbital excitations $|i\rangle$ of H_0 with $H_0 |i\rangle = E_i |i\rangle$ and some perturbation V acting on it, the interaction picture can be used to compute the transition rate to some other orbital excitation $|f\rangle$ with $H_0 |f\rangle = E_f |f\rangle$. Truncating the transition rate in leading order of V produces Fermi's golden rule [34, 46]

$$\Gamma_{i\to f} = \frac{2\pi}{\hbar} |\langle f| V |i\rangle|^2 \delta(E_f - E_i)\,. \tag{4.10}$$

We can interpret both halfs of this equation physically: The matrix element $|\langle f|V|i\rangle|^2$ is the matrix element of the transition and tells us how strong the decaying and decayed states are connected via the operator of the decay channel. The Dirac delta furthermore ensures that only those transitions are contributing, which conserve the energy of the system.

Since $|i\rangle, |f\rangle$ are eigenstates of H_0, a direct evaluation of equation (4.10) is numerically very expensive for large clusters. In Section 2.3.3 we used the Lehmann representation to write a spectral function as a sum over matrix elements in the systems eigenbasis. Here we can do the same in reverse using

$$\delta(\omega + E_f - E_i) = -\frac{1}{\pi} \lim_{\Gamma \to 0} \mathrm{Im}\left(\frac{1}{\omega - E_f + E_i + \mathrm{i}\Gamma}\right) \tag{4.11}$$

to write Fermi's golden rule as a spectral function [163]

$$A(\omega) = -\frac{2}{\hbar}\mathrm{Im}\left(\langle i|V^\dagger \frac{1}{\omega - H_0 + E_i + \mathrm{i}\Gamma} V|i\rangle\right), \tag{4.12}$$

where Γ is some phenomenological broadening. To recover equation (4.10) we have to send $\Gamma \to 0^+$. Since we want to evaluate equation (4.12) on a large cluster, Γ allows us to broaden all excitations of the discrete spectrum as approximation for the infinite system, where the spectrum is continuous. While this representation of Fermi's golden rule seems more complicated, it can be evaluated very efficiently [133, 134, 164]:

Given the decaying state $|i\rangle$ as vector, we can compute the state $\mathcal{N}|\phi_0\rangle = V|i\rangle$ as matrix vector product, where $\mathcal{N}$ denotes the normalization of the state. The spectral function of equation (4.12) is then just the diagonal matrix element of the operator $(\omega - H_0 + E_i + \mathrm{i}\Gamma)^{-1}$ with respect to the state $V|i\rangle$.

Since H_0 is in general not a diagonal operator with respect to $|\phi_0\rangle$ we find

$$\left(\langle\phi_0|\left(\omega - H_0 + E_i + \mathrm{i}\Gamma\right)|\phi_0\rangle\right)^{-1} \neq \langle\phi_0|\left(\omega - H_0 + E_i + \mathrm{i}\Gamma\right)^{-1}|\phi_0\rangle\,. \tag{4.13}$$

We can however consider its diagonal and its offdiagonal contributions separately. Since $\omega - E_i + i\Gamma$ is proportional to the identity, we limit our treatment to H_0. Following the notation of Lanczos [165], we find

$$\alpha_0 = \langle\phi_0|H_0|\phi_0\rangle \tag{4.14}$$
$$\beta_1|\phi_1\rangle = H_0|\phi_0\rangle - \alpha_1|\phi_0\rangle \tag{4.15}$$

where we choose β_1 real such that $\langle\phi_1|\phi_1\rangle = 1$ is normalized. It is clear, that $|\phi_1\rangle$ is again not an eigenvector of H_0. We can therefore use equations (4.14) (4.15) recursively for $n > 0$

$$\alpha_n = \langle\phi_n|H_0|\phi_n\rangle \tag{4.16}$$
$$\beta_{n+1}|\phi_{n+1}\rangle = H_0|\phi_n\rangle - \alpha_n|\phi_n\rangle - \beta_n|\phi_{n-1}\rangle \tag{4.17}$$

to iteratively span a Krylov space until it either terminates[7] as $\beta_k = 0$ or we manually truncate by setting it as such.

[7] Our construction terminates, if we perform more iterations than there are eigenvectors in the eigendecomposition of $|\phi_0\rangle$.

This basis has two distinct advantages:
(i) the first basis vector $|\phi_0\rangle$ is the basis vector whose matrix element $C(z) = ((z - H_0)^{-1})_{00}$ we want to compute for $z = \omega + E_i + i\Gamma$.
(ii) H_0 is tridiagonal in this basis. We find

$$z - H_0 = \begin{pmatrix} z-\alpha_0 & \beta_1 & 0 & \cdots & 0 \\ \beta_1 & z-\alpha_1 & \beta_2 & \cdots & 0 \\ 0 & \beta_2 & z-\alpha_2 & \cdots & 0 \\ \vdots & \vdots & \vdots & \ddots & \vdots \\ 0 & 0 & 0 & \cdots & z-\alpha_k \end{pmatrix} \tag{4.18}$$

This structure allows us to iteratively invert $z - H_0$. Consider the matrix M_1 obtained by removing the first row and column from $z - H$. If we know the first entry of its inverse $(M_1^{-1})_{00}$, we find

$$C(z) = \frac{1}{z - \alpha_0 - \frac{\beta_1^2}{(M_1^{-1})_{00}}}. \tag{4.19}$$

With the same line of argument we can obtain $(M_1^{-1})_{00}$ from $(M_2^{-1})_{00}$, where M_2 is $z - H_0$ with the first two rows and columns removed. Since $(M_{k-1}^{-1})_{00} = (z - \alpha_k)^{-1}$, we obtain

$$C(z) = \cfrac{1}{z - \alpha_0 - \cfrac{\beta_1^2}{z-\alpha_1 - \cfrac{\beta_2^2}{z-\alpha_2 - \cfrac{\beta_3^2}{z-\alpha_3-\ldots}}}} \tag{4.20}$$

as $k - 1$-fold nested fraction. Combined these steps allow us to approximate the spectral function (4.12) iteratively by computing $k + 1$ matrix-vector-products and $k + 2$ vector-vector-products instead of having to fully diagonalize the decayed subspace. Since the inverse only relies on the coefficients α, β, it is not necessary to keep more than three vectors $|\phi\rangle$ in memory to generate new coefficients.

As we increase the depth of our Krylov space k, $C(z)$ slowly converges to the true spectral function, that we would obtain by fully diagonalizing H_0. It can be shown the distribution $-\mathrm{Im}(C(z))$ has the correct moments up to order k [133, 164].

Going to arbitrarily large k is however numerically not feasible. At some point numerical precision will lead to a loss of orthogonality of our basis vectors $\{\phi_0, \ldots, \phi_k\}$. While this can in general be remedied, it is more expensive than the iterations themselves and requires keeping all of them in memory [166]. We heuristically use 100 iterations, which according to literature is usually the point, where orthogonality issues within double-precision floating-point numbers should start to occur [164, 166], but should still have little impact on the spectral function.

We can furthermore leverage the structure of the Hamiltonian H_0 and decay operator V to simplify computing the total decay rate. Since H_0 preserves orbital occupations we can separate V into different channels V_c by the orbital occupations to which they map. Instead of treating all decay channels at once we can separate their computation. This drastically reduces the key bottleneck, as we do not have to keep H_0 within the complete Hilbert space in memory for the creation of the Krylov space, but only within the orbital occupation subspace of the decay channel.

Taking all of this together we are able to compute the life-time of an excitation using the following steps:
(i) Diagonalize the occupation preserving Hamiltonian H_0 to obtain starting states $|i\rangle$ with $H_0 |i\rangle = E_i |i\rangle$.
(ii) Compute the decayed state $V_c |i\rangle$, its magnitude $|\mathcal{M}|^2 = \langle i| V_c^\dagger V_c |i\rangle$ and normalized form $|\phi_0\rangle = V_c |i\rangle / \sqrt{|\mathcal{M}|^2}$
(iii) Span the Krylov space using the Lanczos procedure for H_0 in terms of the coefficients α, β.
(iv) Compute the phase space element for the channel c as the spectral function $A_c(\omega) = \langle \phi_0 | (\omega - H_0)^{-1} |\phi_0\rangle$ using the coefficients α, β as well as the initial states energy E_i and the broadening Γ. (v) Combine the decay matrix element and the phase space spectral function to obtain the decay width $\Gamma = |\mathcal{M}|^2 A_c(\omega)$.

4.4 Implementational details

Since the orbital energy gap between the decaying and decayed sector (up to 1480 meV) spans the characteristic energy of a magnon (68 meV to 90 meV) many times, we need large clusters if we want to compute the lifetime using the previously outlined Lanczos techniques. To treat these clusters in a timely fashion and to have enough memory accessible to keep the Hamiltonian in memory we want to implement our computation MPI parallel. Once we have cast the Hamiltonian into a matrix representation steps (i)-(iii) are linear algebra, which can be parallelized highly efficiently.

Since an efficient parallelization has to avoid many pitfalls, it is common to use existing established implementations of fundamental linear algebra subroutines. They are often implemented within low level languages such as Fortran or assembler, but make their routines accessible to higher level languages. We use the "linear algebra pack" (LAPACK) library [167] with the OpenBLAS [168] implementation for the "basic linear algebra subroutines" (BLAS). Together these provide the routines necessary for linear algebra computations. To avoid a manual implementation handling the distributed memory via MPI, we use the "Portable, Extensible Toolkit for Scientific Computation" (PETSc) library [169], that abstracts the memory management and MPI calls. After specifying the details on which MPI process handles which data, it provides a simple interface to work with abstract matrix and vector objects using C or C++ [170]. The "Scalable Library for Eigenvalue Problem Computations" (SLEPc) [171] is an extension to PETSc, that provides various solvers for eigenvalue problems implemented via the corresponding PETSc objects.

Upon being started an MPI parallel program creates multiple processes, which can be distributed on different computational nodes or even machines. These processes usually referred to by their rank handle their own memory. They can send and receive data from other processes via the eponymous message passing interface (MPI), which is however much slower than local handling of the data. Since in linear algebra the most common operations are scalar products of vectors, matrix products and matrix-vector products, PETSc distributes the data of these objects among the processes according to their structure [172]. For a vector object each process knows the total dimensions of the vector, but only has local access to some of the rows of the vector depending on its rank within the MPI communicator (see Figure 4.4a). The same distribution also works for matrices, where each process carries the rows of the matrix corresponding to the rows it carries for vector objects. Matrices therefore have a block structure, where diagonal blocks are the ones where the same process is responsible for the corresponding rows and columns of the matrix. This is visualized in Figure 4.4b, where green blocks are the diagonal blocks and blue blocks are offdiagonal. The parallelization of

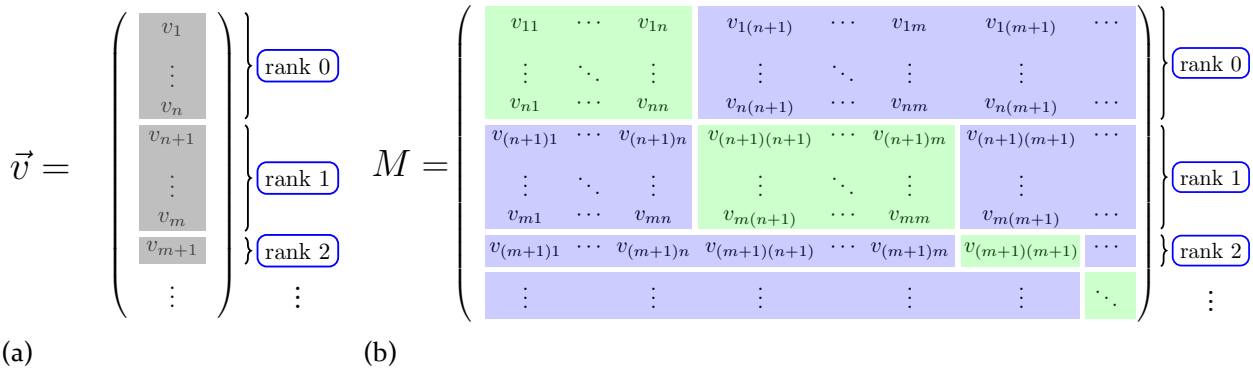

(a) (b)

Figure 4.4: Distribution of the data of a vector (a) and matrix (b) object among processes in PETSc. For the matrix in (b) the green shaded area indicates diagonal blocks, where row and column indices are treated by the same process. The blue shaded area are the offdiagonal blocks, where the matrix elements need communication via MPI with other processes for matrix-matrix or matrix-vector products.

matrix-matrix products and matrix-vector products is most efficient, if the matrices have as few entries in the offdiagonal blocks as possible, since these have to be passed from one process to another through the MPI communicator.

Since the Hamiltonian H_0 preserves orbital configuration we only have to implement it in certain orbital sectors. While in the orbiton free sector the Heisenberg coupling is dominated by antiferromagnetic interactions, in the presence of orbitons we also find strong ferromagnetic coupling (see Table 1). The cluster ground state in the presence of orbitons does therefore not necessarily minimize the total spin. We therefore implement the complete spin Hilbert space for a fixed orbital occupation. Similarly if we employ periodic boundary conditions, the total crystal momentum is conserved. From the matrix elements in Table 1 it is again unclear which momentum our starting state should have. A reduced basis leveraging these symmetries would be more efficient and be able to treat even larger clusters [173]. We instead implement the full cluster spin space with either no orbitons (2^N), one orbiton ($N \cdot 2^N$), two distinguishable orbitons ($N \cdot (N-1) \cdot 2^N$) or two indistinguishable orbitons ($N \cdot (N-1) \cdot 2^{N-1}$) as Hilbert spaces with their sizes for a N-site cluster indicated accordingly. We span it using the spin configuration in the z-basis and the position(s) of the orbital excitation as basis states.

Having decided on the Hilbert spaces, let us consider how to efficiently distribute their basis states among processes to minimize the need for sharing memory between processes. Since in each computation we only have to act once with the decay channel operator V_c, acting with H_0 is the biggest portion of our computational effort. We should therefore consider the different terms of H_0 and distribute basis states among processes such that it has the least possible amount of matrix elements in offdiagonal blocks. For simplicity we consider the number of appearing matrix elements for a two-dimensional cluster with periodic boundary conditions and limit our considerations to the orbital sector with one excitation.

The Hamiltonian H_0 (see equation (4.2)) has five terms. The crystal field contribution $H_{\text{i,crystal field}}$ is just a global offset in a fixed orbital configuration subspace. It is therefore save to drop it for all intermediate steps (i)-(iii). When evaluating the spectral function in step (iv), we just have to consider the difference in orbital energies to properly shift the spectral functions energy. The next term in the Hamiltonian is the orbital interaction H_{int}. It is diagonal in both orbital and spin configuration and therefore does not put any constraints on how we should distribute our basis. In the single excitation sector the dispersion of the orbital excitation H_{disp} maps to four other configurations amounting to the sites the orbital

excitation can move to. In contrast, the number of matrix elements the Heisenberg exchange H_{Hb} produces drastically varies depending on the spin configuration. For the fully polarized states it is fully diagonal, while for an antiferromagnetic Néel state its number of offdiagonal elements scales as the number of bonds in the cluster. The last term describes simultaneous hopping of an orbital excitation and Heisenberg exchange on the same bond $H_{\text{Hb-disp}}$. As with the dispersion term, there is a maximum of four sites to which the orbital excitation can move. Depending on the spins on those sites, it therefore leads to four to eight matrix elements. Four of these occupy the same spots in H_0 as the matrix elements of H_{disp} and therefore do not lead to additional matrix elements but just change the amplitude.

Since the orbital excitation only directly influences spin exchange in its immediate vicinity, the spin configuration of the cluster is dominantly antiferromagnetic and therefore has a small total spin. We therefore expect the Heisenberg exchange to have more offdiagonal matrix elements than both orbital dispersion contributions. In order to minimize the entries in the offdiagonal blocks of our distributed memory implementation, we distribute the Hilbert space in chunks of complete spin spaces. States differing only by their spin configuration will therefore always be handled by the same process. Depending on the cluster size and number of processes, multiple of these spin spaces with varying position(s) of the orbital excitation(s) may be handled by the same process. Since we want to allow for different cluster sizes, we perform this distribution at runtime on startup, when the information of the size of the cluster and number of processes is known. Since we keep the complete Hamiltonian in memory, memory limitations bottlenecks our computations for large cluster sizes. On high performance computational infrastructure we can distribute the processes among many nodes each with their own memory, which does however lead to a poor utilization of available resources.

We split the computation among the four steps outlined at the end of Section 4.3. Depending on the excitation we want to investigate, we generate H_0 distributed among all processes and diagonalize it using the SLEPc the Krylov-Schur solver [174], which produced the best convergence of the cluster ground state and first few excited states $\{|i\rangle\}$. Since the same set of converged states can be used for all decay channels, we write them and their energies $\{E_i\}$ to disk completing step (i).

Next we generate the decay channel V_c distributed among processes in the same manner as H_0. Since the number of orbital excitations can change through the decay in full decay or fission channels, V_c is in general not quadratic. The decayed Hilbert space thereby dictates how V_c is distributed among processes as it corresponds to the rows of V_c (see Figure 4.4). We evaluate the norm of the decayed states, normalize them and write the norms and the normalized states to disk, completing step (ii).

For step (iii), we have to generate H_0 in the decayed Hilbert space. This is the part of the computation with the most severe memory limitation, since both types of orbital excitations have fission channels, which lead to the large Hilbert space with two orbital excitations. Once it is generated spanning the Krylov space and obtaining the coefficients α and β is straightforwardly accomplished according to equations (4.14)-(4.17) using matrix-vector, vector-vector and scalar-vector products as well as vector addition. PETSc provides routines combining multiple of these steps into a single one.

Using the coefficients α, β, the norm of the decayed states, the starting states energy E_i and our broadening Γ, the evaluation of Fermi's golden rule as spectral function is then just the evaluation of the complex chain fraction shown in equation (4.20).

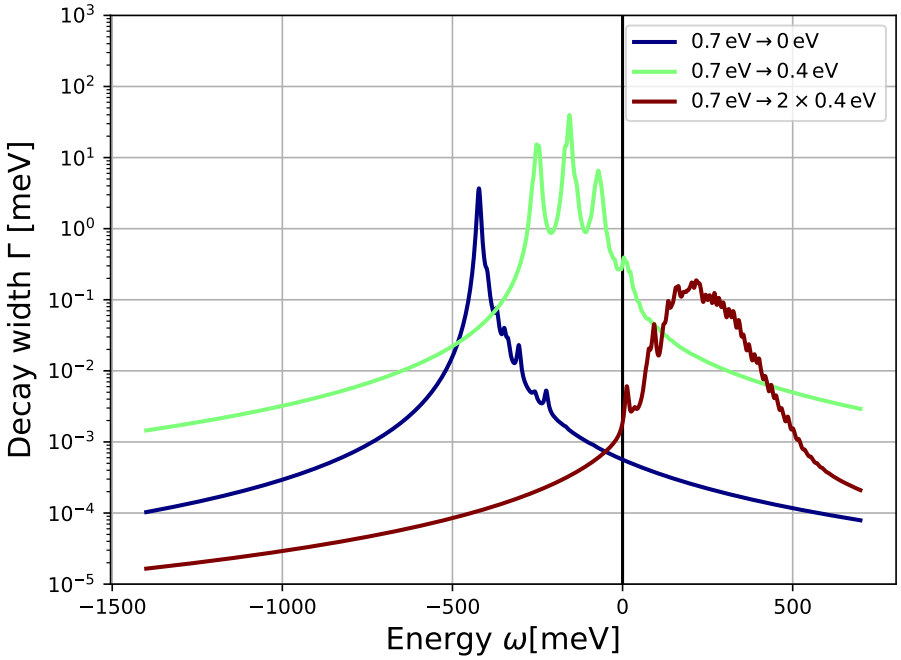

Figure 4.5: Spectral functions $\Gamma(\omega)$ of the decay operators for the three decay channels of the 0.7 eV-orbiton evaluated on the 6×3 site cluster. Other cluster sizes can be found in Appendix B Figure 4.5. We choose a broadening of 5 meV and compute $\Gamma(\omega)$ of the first five states in the undecayed subspace. The spectral weight for the full decay into magnons only (blue) is far removed from $\omega = 0$. For the intermediate decay process into magnons and a 0.4 eV-orbiton (green) and the fission process into magnons and two 0.4 eV-orbitons (red) this is not the case, such that they can significantly contribute to the decay. The intermediate fission process has enough spectral weight closeby to $\omega = 0$, that this decay process may be entirely responsible for the experimentally obtained lifetime $\Gamma_{0.7\,\mathrm{eV}} = 1.8\,\mathrm{meV}$.

4.5 Results

An exponential fit of the experimental non-linear signal $\Delta\Delta T/T_{\mathrm{avg}}(t_{\mathrm{pp}})$ finds time constants of the decay of this signal as $\tau_{0.7\,\mathrm{eV}} = 364\,\mathrm{fs}$ and $\tau_{1.5\,\mathrm{eV}} = 294\,\mathrm{fs}$, where the index denotes the first pump respectively. In terms of decay widths these correspond to

$$\Gamma_{0.7\,\mathrm{eV}} = \hbar/\tau_{0.7\,\mathrm{eV}} = 1.8\,\mathrm{meV} \tag{4.21}$$

$$\Gamma_{1.5\,\mathrm{eV}} = \hbar/\tau_{1.5\,\mathrm{eV}} = 2.2\,\mathrm{meV}\,. \tag{4.22}$$

The size of the Hamiltonians and states we load into memory differs for the decay channels. Using 500 GB of RAM we are able to compute the lifetime on clusters up to 22 sites for the full decay and single orbiton decay channels, while the fission channels are limited to 18 or 20 sites for distinguishable and indistinguishable orbitons in the decayed subspace. We therefore decided on using focusing our analysis on the 18-site cluster with 6 sites in the crystallographic b-direction, i.e., along the chains, and 3 sites in the a-direction. We choose this cluster since (i) three sites is the minimum necessary to employ periodic boundary conditions perpendicular to the chains and (ii) the longer the chains in the b-direction are the better the magnetic sector is captured. For 18 sites the 6×3 cluster is therefore the best choice. Comparing it to other cluster sizes and shapes (see Appendix B) we find it to be reasonably converged for a broadening of $\Gamma = 5\,\mathrm{meV}$.

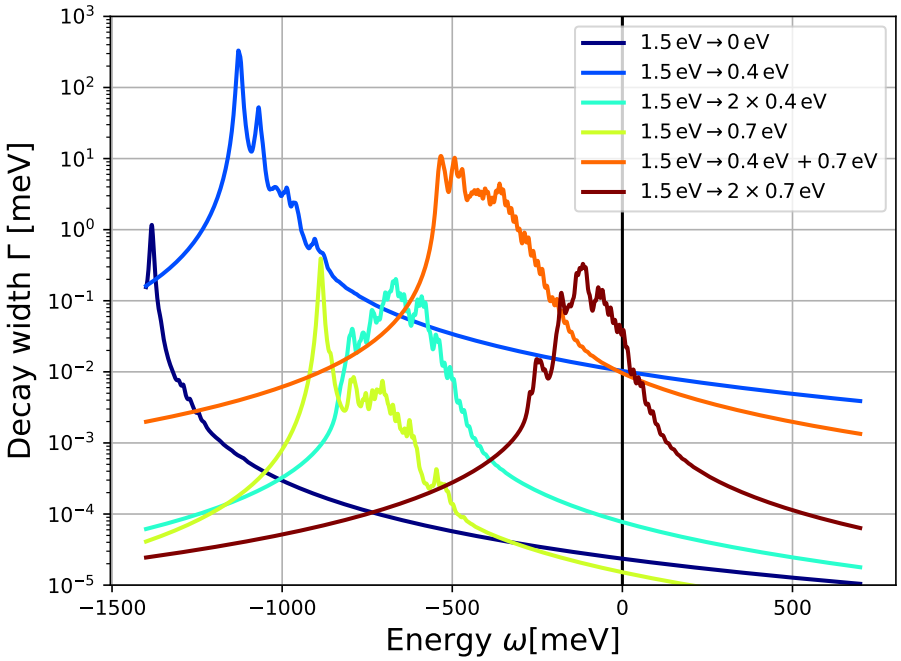

Figure 4.6: Spectral functions $\Gamma(\omega)$ of the decay operators for the three decay channels for the 1.5 eV-orbiton evaluated on the 6×3 site cluster. Other cluster sizes can be found in Appendix B Figure B.2. We choose a broadening of 5 meV and compute $\Gamma(\omega)$ as average using the cluster ground state and first four excited states as starting states. In contrast to the 0.7 eV-orbiton, here there is no decay channel strong enough in the vicinity of $\omega = 0$ to account for the experimental decay width $\Gamma_{1.5\,\mathrm{eV}} = 2.2$ meV.

Making use of multiple compute nodes using our MPI parallel implementation, evaluating the decay on larger clusters sizes would in principle be possible[8]. Since we additionally do not make use of the translational symmetry of the clusters or the conservation of total spin, pushing larger cluster sizes would lead to diminishing utilization of the computational resources as most of the matrix elements of the Hamiltonian loaded into memory are superfluous to the computation. For each decay channel we show the spectral function for varying cluster sizes and dimensions in Appendix B. Convergence is worst for the full decay channels into magnons only, as here the cluster size is limited by the undecayed one orbiton states. Since these are the ones with the largest gap, it is unlikely, that on larger clusters they meaningfully contribute to the decays of the 0.7 eV- and 1.5 eV-orbitons.

In the one orbiton sector of our undecayed subspace we achieve an energy resolution of few meV for the larger cluster sizes. We evaluate the spectral functions for the ground state and the first four excited states of each cluster size and average them. This avoids underestimating or overestimating the lifetime for a given cluster size if the ground state of a given cluster size is a particularly 'dark' or 'bright' state with respect to the decay operator V and its matrix element $\langle\psi_0| V^\dagger V |\psi_0\rangle$. In contrast to e.g. photodoped Mott-Hubbard excitations [163], where for a large Mott gap there can be a separation of energy and timescales between the relaxation dynamics of doublons and holes and their eventual recombination [149], for our orbitons it is less clear if there is indeed a similar separation and the analysis of the prethermalized orbiton ground state is sufficient[9]. On the largest cluster sizes we evaluate the lowest five eigenstates approximately

[8] Extrapolating the memory requirements shows a memory requirement of around 600 GB for the one orbiton sectors and around 14 TB for the distinguishable two orbiton sector on the 24-site cluster.

[9] Especially since we do not know anything about the coupling to phonons.

correspond to the thermally accessible energy scale as $k_B \cdot 10\,K \approx 0.9\,meV$. A rigorous analysis of the decaying state is left for future work. It could, e.g., be accomplished by explicitly modeling pumping of the initial orbiton-free thermal state and using an eigendecomposition similar to Section 3.5.2. The spectral functions for the five decaying states we evaluate are shown as faded lines in the plots in Appendix B.

4.5.1 Interpretation of the decay spectral functions

Before explicitly discussing both sets of decay spectral functions, we want to clarify how these can be interpreted. The most immediate and previously discussed property, that can be read of them, is the lifetime due to Fermi's golden rule by taking $\Gamma(\omega = 0)$.

Taking the full spectral function does, however, provide more information:
(i) It tells us about the convergence with respect to the cluster size and broadening. For finite clusters the spectral function is a sum of Lorentz curves (see equation (2.83)). These curves are centered on the eigenvalues of our cluster[10]. Far away from these eigenvalues the spectral function gets its weight only from the tails of these curves and is therefore strongly dependent on the broadening we employ. We can therefore check convergence with respect to cluster size by identifying frequency ranges dominated by overlapping peaks and those only composed of the tails of far away peaks. In the former ranges the spectral function, with an appropriately chosen broadening, approximates the infinite system, while in the latter regions larger clusters or extrapolations are necessary.

(ii) There are large uncertainties on the parameters of the model we set up to describe the spin-orbital dynamics in TiOCl. The spectral functions are very sensitive to these uncertainties, especially to the crystal field splitting. Small changes can therefore drastically change the value of $\Gamma(\omega = 0)$. One should therefore not put too much emphasis on this singular value, but consider all of $\Gamma(\omega)$ in the vicinity around $\omega = 0$.

(iii) The environment around $\omega = 0$ also allows us to estimate how additional degrees of freedom can influence the lifetime. Peaks at negative frequencies correspond to decay processes, that are forbidden by energy conservation as the decayed states have less energy than the decaying state. An additional degree of freedom, that can take on this energy, can therefore move this spectral weight and, even when associated with a small matrix element for the hybrid process, have a strong impact on the lifetime. In our computations special attention should therefore be paid to spectral weight at negative frequencies up to around 100 meV, since this weight could become accessible to few-phonon-assisted processes using the well documented phonons of TiOCl [106, 175]. The situation is reversed for spectral weight at small positive frequencies, which may be accessible to excited states in the undecayed subspace and could therefore contribute at high temperatures or when considering an eigendecomposition of the pumped state.

4.5.2 0.7 eV-orbiton

For the 0.7 eV-orbiton, there are three relevant decay channels (see Table 2): One for a decay into magnons only, one for a decay into magnons and an 0.4 eV-orbiton and one for the fission

[10] Since we do not fully diagonalize the decayed subspace and employ the Lehmann representation to compute the spectral function, they are not centered on the exact eigenvalues. Instead, the eigenvalues of the Krylov space we span determine their location. The larger we choose this space, the closer its eigenvalues approximate those of the full Hilbert space.

into two 0.4 eV-orbitons and magnons. We show the corresponding spectral functions $\Gamma(\omega)$ on the 6×3 site cluster in Figure 4.5 with a broadening of 5 meV.

The full decay into magnons (blue in Figure 4.5) has its spectral weight far removed from $\omega = 0$. It is the least converged of the three channels (see Appendix B). Extrapolating, we can nevertheless estimate this decay channel to contribute only of the order of μeV to the decay width of the 0.7 eV-orbiton.

The intermediate decay channel into an 0.4 eV-orbiton and magnons (green in Figure 4.5) has its spectral weight much closer to $\omega = 0$. This is the result of a much smaller crystal field gap of this decay channel (280 meV compared to 620 meV). Since this energy can be distributed in the magnetic degrees of freedom and dispersive degree of freedom of the orbiton, its spectral function is broader than that of the full decay. Its three peak structure is an artifact of the cluster size (compare Figure B.1b). Evaluating $\Gamma(0) = 0.32$ meV falls short of the experimentally measured lifetime $\Gamma_{0.7\,\mathrm{eV}} = 1.8$ meV. The abundance of spectral weight at small negative energies leads us to believe that points (ii) and (iii) of Section 4.5.1 could easily account for the missing factor of six, such that this decay process is the dominant decay channel for the 0.7 eV-orbiton.

The last decay channel is the fission process into two 0.4 eV-orbitons and magnons (red in Figure 4.5). Since its crystal field gap is –60 meV the majority of its spectral weight is at positive frequencies. Its decayed states contain two orbitons. Of the three decay channels it is therefore the broadest and due to its larger Hilbert space better converged. Its small matrix elements (see Table 2) and positioning at positive frequencies lead us to believe, that this decay channel does not significantly contribute to the lifetime of the 0.7 eV-orbiton. To computationally confirm this a better modeling of the pump is necessary. Excited contributions of the pumped 0.7 eV-orbiton can access the spectral weight at positive frequencies. The experiment furthermore found coherent phonons after the pump [67]. While unlikely due to their sparsity these could for a large phonon-orbiton scattering cross-section also increase the significance of this decay channel.

4.5.3 1.5 eV-orbiton

For the 1.5 eV-orbiton we have six decay channels (see Figure 4.6). We find the full decay into magnons only (dark blue), the decay into two 0.4 eV-orbitons and magnons (turquoise) and the decay into a 0.7 eV-orbiton and magnons (light green) not contributing significantly to the decay of the 1.5 eV-orbiton due to their small matrix elements and large crystal field gap.

The decay into one 0.4 eV-orbiton and magnons (medium blue) has a large matrix element but is separated by a large crystal field gap of 1130 meV. On its own it therefore also does not significantly contribute to the lifetime of the 1.5 eV-orbiton. It could however contribute as orbiton-magnon-assistance of a phonon-dominated decay process. We should additionally keep in mind, that all analysis within this chapter is based on a second order series expansion. A second order exchange processes with a large amplitude could be part of a fourth order exchange process with a still decently sized amplitude. As such it could e.g. be part of a fourth order three orbiton fission process that bridges the crystal field gap.

The two remaining decay channels are fission into an 0.4 eV-orbiton, an 0.7 eV-orbiton and magnons (orange) and to two 0.7 eV-orbitons and magnons (dark red). They have the smallest crystal field gap (520 meV and 240 meV respectively), which puts their spectral weight close to $\omega = 0$. Quantitatively speaking both of them cannot account for the experimentally obtained decay width of 2.2 meV as we find 9.6 μeV and 35 μeV respectively. In contrast to the decay of

the 0.7 eV-orbiton (see Section 4.5.2), here it is less clear how the uncertainties in our model parameters or phonons could lead to a better correspondence between our description and the experiment: The two 0.7 eV-orbiton fission channel is already at the correct energy but has too small of a matrix element. Multi-phonon process could shift some of the spectral weight from negative energies to $\omega = 0$ or the phonon-assisted fission process could have a much larger matrix element similar to dipole forbidden optical transitions. It is unclear weather or not this can explain the almost two orders of magnitude missing in the decay width. The decay channel into distinguishable orbitons (orange) has a much larger matrix element, but the majority of its spectral weight is below –300 meV. Whether or not phonons can bridge this gap remains as an open question for future work.

4.6 Conclusion and outlook

In this chapter we have computed the lifetime of orbital excitations in TiOCl due to decay into other orbital excitations and magnons. We accomplished this by evaluating Fermi's golden rule for an effective spin-orbital Hamiltonian. This allows us to exact diagonalization and Lanczos-based spectral functions on large clusters. We have compared the decay widths as obtained from the spectral functions of the different decay channels to an experimental estimate obtained as obtained from the nonlinear signal of a double-pump-probe spectroscopy experiment [67].

For the 0.7 eV-orbital excitation our calculations point towards it decaying into an 0.4 eV-orbiton and magnons. Within uncertainties in the parameters of our model or phonon assistance it may even be entirely responsible for the experimentally observed lifetime. In contrast, for the other orbital excitation pumped in the experiment at 1.5 eV we do not find any spin-orbital decay channel able to explain its shorter lifetime of the experimental nonlinear signal. There are orbital fission processes, but these alone cannot account for its quick decay.

This directly leads to the main open question for future work: Does the 1.5 eV excitation indeed decay this quickly and if so how does it decay?

There are multiple potential ways one could try and find an answer to this question. One approach would be measuring the decay using a different experimental setup more sensitive to the involved degrees of freedom. As outlined in Chapter 3, our cluster calculations are not able to sufficiently model the single-pump-probe spectroscopy to deduce orbtial occupancies. The spectral response of the double pump-probe spectroscopy is understood even less and our analysis based entirely on the presence or absence of the response linear in both pumps, but not as to how this response looks like. The orbiton lifetime is therein only one source for a pump-pump-delay (t_{pp}) dependence of the non-linear signal. Other sources, such as differing excitation efficiency of the pumps combined with differing envelopes, can similarly lead to a t_{pp} dependence of the nonlinear signal. Within our current model an analysis of these effects does however have too many free parameters to have any predictive power.

Two experiments with a more direct orbital sensitivity are x-ray absorbtion (XAS) and resonant inelastic x-ray scattering (RIXS). In both cases the spectra have to be time-resolved following an optical pump of the orbital excitations similar to the optical pump-probe experiment [66, 67]. Due to the large energy of intermediate core-hole states their dynamics remains local lending themselves to cluster calculations. For TiOCl in equilibrium there is already a good agreement between such cluster calculations and XAS on the titanium L-edge as well the RIXS spectra on this edge [100, 143]. Within RIXS it is even possible to obtain the dynamical spin-structure factor from the experimental energy-loss spectra [100]. By comparing the

distribution of spectral weight in non-equilibrium cluster calculations to the time-dependent spectra it should be possible to obtain the orbital occupation from shifts in the XAS-spectra. The linear dichroism of the L-edge may therein be more sensitive to the orbital occupancy than shifts in the L-edge positions. In time-resolved RIXS we expect shifts of spectral weight of the inelastic Stokes peaks as well as the appearance of anti-Stokes peaks, where the scattered x-ray photon gains energy [144]. On the phononic side, ultra-fast Raman-spectroscopy [176] may be able to uncover the role of phonons for these decay processes.

On the theoretical side we have already mentioned two shortcomings of our description of the decay processes: Phonons are absent and there is no explicit modeling of the pump. Including either of these significantly increases the computational effort necessary to compute lifetimes. They should therefore be combined with a more efficient implementation. Making use of the translational invariance of the cluster with periodic boundary conditions and the conservation of total spin should allow for the inclusion of additional phononic degree of freedom and the added computational effort of describing the pumped state. As an alternative to exact diagonalization, the system may also be suited to density-matrix renormalization-group approaches [177], since the clusters consist of weakly coupled one-dimensional chains. Series expansions are able to capture the magnetic spectra of dimerized one-dimensional chains in terms of triplon quasi-particles [112]. They map the Hamiltonian to an effective one for quasiparticles by means of a unitary transformation. Applying the same unitary to the decay channels may make it straightforward to evaluate Fermi's golden rule in this quasiparticle picture.

Our claim, that the decay of 0.7 eV-orbital excitation can be understood in terms of the decay channel to a 0.4 eV-orbiton and magnons (possibly assisted by few phonons), should be additionally verified. This is possible using the aforementioned x-ray experiments, but also using the existing optical double pump-probe spectroscopy setup: TiOBr is a compound isostructural to TiOCl [178]. Its one-dimensionality is however less pronounced and magnetic exchange processes weaker [179–181]. We could therefore check our claim by mirroring our computations for TiOBr and comparing the resulting lifetime prediction to the lifetime of the non-linear experimental signal of the double-pump-probe experiment on TiOBr.

Lastly, at the end of Chapter 3 we set out to find a description for the open dynamics of the decaying orbital excitations. This is possible by using the decay widths $\Gamma(\omega = 0)$ as coupling constants for orbiton heat baths. These describe the effective dynamic of the magnetic and orbital environment not explicitly captured in a cluster (see Chapter 3) or impurity [149] computation.

5 Cavity-mediated long-range interactions in the one-band Hubbard model

In this chapter we study the long-range interactions in a one-band Hubbard model induced through coupling it to an optical cavity. To this end we follow our publication on this subject [P2] in notation, terminology and phrasings and adapt parts of it with minor changes. It reports the authors findings, that were performed under the coauthors guidance. An early version of the code used for the exact diagonalization in this chapter was written by Jiajun Li.

5.1 Motivation

In the previous two chapters light played the role of a tool, that we use to probe the decoupled matter state or perturb it out of equilibrium. On the probing side, the linear response relation derived in Section 2.3.3 allowed us to neglect any light-matter hybridization, which would manifest as light-vertex corrections, in the computation of the optical conductivity [9]. If we want to utilize light in the field of material engineering [31, 33, 182–184] we want the light to modify matter properties allow for external control of their properties by means of the fields [178, 185–194].

Since it is usually not possible to track the non-equilibrium dynamics of a general light-matter coupled Hamiltonian, there are two settings of interest: Either we explicitly track the light-matter coupling on short timescales only or we treat light, which has to be particularly "well-behaved", such that the combined equations of motion can be described in an effective manner. In the former case, many interesting transient matter states can be created and controlled through e.g. photodoping charge excitations [195][1] or phonons [178, 189]. Time periodic driving fields fall in the second category since it is possible to derive an effective Hamiltonian for the stroboscopic time evolution using Floquet theory [32, 92, 196, 197] for a time-periodic external driving field or the harmonic field of an optical cavity. In this chapter we consider this setting.

In Floquet theory for a classical electromagnetic field there is no back-action of the matter on the field. As such separable matter systems will stay separable when coupled to the same Floquet drive. This is no longer the case when considering quantum electromagnetic fields allowing for light-mediated interactions. In free space this leads to dipole-dipole or van-der-Waals interactions [9], which can be enhanced by confining the electromagnetic field to the small mode volume of a cavity [198–200]. On the matter side they can be utilized to induce among others superradiant [201–204] and ferroelectric [205, 206] phase transitions or superconductivity [207, 208]. In these settings the electromagnetic field couples via a dipolar transition such that interactions are mediated by the exchange of a single photon. If g describes the amplitude of this coupling, these processes contribute terms of order g^2 to an expansion of the free/ground state energy or an effective Hamiltonian, which has the photons eliminated. For the free or ground state energy this sketched diagrammatically in Figure 5.1a.

Interactions mediated by nonlinear light-matter coupling of, e.g. diamagnetic coupling (see equation (2.144)), the Peierls phase (see equation (2.163)) or Raman processes require the exchange of two photons indicated for the free energy in Figure 5.1b. They therefore only contribute in order g^4, but have two major advantages:

[1] The non equilibrium optical conductivity of Chapter 3 falls into this category as well.

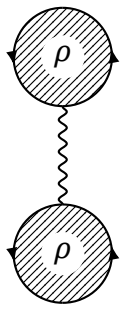

(a) Dipolar density-density interaction

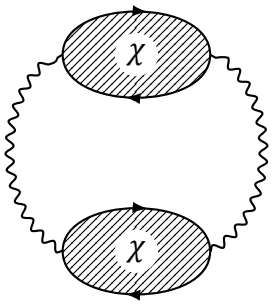

(b) van-der-Waals interactions

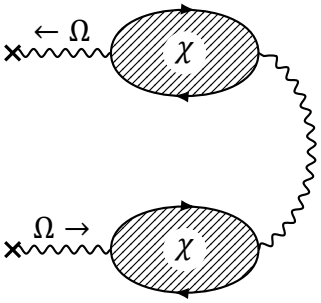

(c) driven van-der-Waals interactions

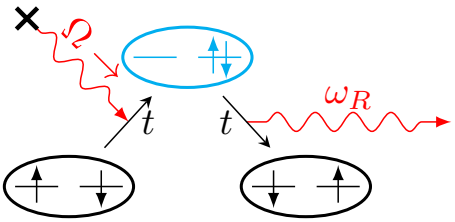

(d) Tracking the intermediate states of a scattering process

Figure 5.1: Diagrammatic expansion of the free or ground state energy in leading order of the light-matter coupling; (a) For dipoles the leading order diagram is a density-density interaction of order g^2 mediated by the exchange of one photon. (b) For non-polar but polarizable (parametrized by the susceptibility χ) systems the interaction requires the exchange of two photons and is therefore of order g^4. (c) In the driven case we can employ Floquet theory (see Section 2.6) and replace one of the exchanged photons by the external drive indicated as $\times$. (d) For expansions around the atomic limit, we utilize the Schrieffer-Wolff transformation, where instead of drawing diagrams, we sketch intermediate states. Indicated here is a Raman type process, where a photon of the drive is absorbed to create a charge excitation, whose breakup occupies a different mode. In contrast to the diagrammatic sketches of (a)-(c), this type of expansion does not allow for an understanding of effective processes as the combination of its subgraphs, but exchange processes have to be evaluated in their entirety.

(i) The nonlinear coupling can also account for local higher order effective processes, such as Raman scattering. This type of interaction can therefore also be mediated between degrees of freedom, that have no direct dipolar coupling such as spins [93] or orbitals [198, 209].
(ii) The two contributing photons can come from different modes. If we take one of these from an external drive[2], we can use it to control the mediated interaction through the drives frequency and amplitude (see Figure 5.1c). This control has proven invaluable in cold atom [210–212] or trapped ion settings [213]. In the condensed matter context previous works proposed for such interactions to produce quantum spin liquids [209] or superconductivity [214] via virtual band transitions, superconductivity via the diamagnetic coupling [215] or a renormalization of the electron-electron interaction in a semiconductor via excitonic resonances [216].

In this chapter we utilize these two properties to derive long-range cavity-mediated four-spin interactions in a Mott insulator coupled to a single-mode cavity tunable by an external drive. We describe it using the Hubbard model at half filling, which we map on an effective spin model using a series expansion around the atomic limit [25–27]. Depending on how the

[2] Taking both exchanged photons from the drive again leads to a factorization such that no interaction is mediated.

light-matter coupling is retained in this expansion one finds a photonically dressed effective spin-Hamiltonians [217–220] or a spin-photon Hamiltonian [93, 221].

An important aspect of this setting is that the strong coupling limit around which we expand has a quartic unperturbed Hamiltonian. A diagrammatic expansion is therefore no longer straightforward. Wick's theorem does not apply in this limit and diagrams cannot simply be understood in terms of their subgraphs. While it is still possible to formulate expansions accounting for this, in this thesis we use the Schrieffer-Wolff transformation, whose expansion is best understood in terms of virtual intermediate states instead of as diagrams. Extending a diagrammatic expansion around this limit, such as, e.g., the one proposed by W. Metzner [117], to account for light-matter coupling should be possible, but left for future work.

The quartic form of the unperturbed Hamiltonian also leads to a breakdown of successive series expansions, that first evaluate an effective vertex as $g_{\text{eff}}(a_1+a_1^\dagger)(a_2+a_2^\dagger)O$ for the bosons a_1, a_2 and the matter operator O and then uses this vertex to obtain a mediated interaction. This boson-vertex can also be obtained experimentally by e.g. Raman spectroscopy of matter system, where a_1, a_2 are the input and output fields. Characterizing the vertex this way does, as we will show, also not produce the proper mediated interaction inside a cavity. We will show that there is, however, a resonant regime, where these successive approaches are valid.

In synthetic quantum matter resonances can be engineered sharp enough for this not to be an issue [210, 212, 222]. In the condensed matter context it is usually not possible to rely on sharp resonances. Surface plasmons [194] and cavities [223, 224] are usually rather lossy and their excitations broad. Additionally, intermediate matter states are broadened by their dispersions and interactions. Near resonant driving can therefore lead to strong heating and suppression of the low temperature effects we want to observe [225].

We derive these interactions without relying on resonances using a fourth order series expansion. Our approach is able to capture the vacuum-mediated spin interactions. We compare it to the successive second-order approach based on the effective spin-photon vertex [93] and show how it becomes valid under resonant driving of the quantum mode. Finally, we estimate the magnitude of these interactions using the parameters for an organic one-band Mott-insulator [226, 227] and a split-ring resonator [223].

5.2 Model

5.2.1 Driven one-band Hubbard model in a single-mode cavity

In this chapter we want to consider a one-band Hubbard model, that is coupled to a single-mode cavity and an external Floquet-drive. In Section 2.2 we exhaustively discussed how we should couple light and matter fields and found that few-band models are best expressed in terms of the dipolar representation (see Section 2.4.3) [65, 73]. We therefore find

$$H = -t_0 \sum_{\langle i,j\rangle,\sigma} c_{i,\sigma}^\dagger c_{j,\sigma} e^{i\phi_{ij}} + U \sum_i n_{i\uparrow} n_{i\downarrow} + H_{\text{field}}\,, \tag{5.1}$$

where $c_{i,\sigma}$ is the fermionic annihilation operator of spin σ on site i, $n_{i\sigma} = c_{i\sigma}^\dagger c_{i\sigma}$ and t_0 the nearest neighbor hopping integral[3] and U is the onsite repulsion. ϕ_{ij} is the Peierl's phase [81]

$$\phi_{ij}(t) = q \int_{\mathbf{R}_i}^{\mathbf{R}_j} \mathbf{A}(\mathbf{r}, t) d\mathbf{r} \,. \tag{5.2}$$

Since we only consider one band there are no dipolar coupling $H_{\mathbf{E}\cdot\mathbf{P}}$ or self polarization $H_{\mathbf{P}\cdot\mathbf{P}}$ terms in our Hamiltonian. For the electromagnetic field we want to consider two settings: (i) the *isolated cavity*, where the field is that of a single cavity mode and (ii) the *driven cavity*, where there is the additional field of the external drive. Unless indicated otherwise, we use the term cavity field and quantum electromagnetic field in this chapter interchangeably.

We parametrize the external drive by its polarization $\mathbf{n}$, amplitude A_{cl} and frequency ω_{cl} as

$$\mathbf{A}_{\mathrm{cl}}(t) = \mathbf{n} A_{\mathrm{cl}} \cos(\omega_{\mathrm{cl}} t) \,. \tag{5.3}$$

The cavity field is obtained through a mode expansion (see Sections 2.4.1,2.4.2 or [64, 65]), where by construction we consider only a single mode. Its quantized field is therefore given as

$$\mathbf{A}_{\mathrm{qu}} = \mathbf{n} A_{\mathrm{qu}} \left(a + a^\dagger\right), \tag{5.4}$$

where we can express the amplitude of the field $A_{\mathrm{qu}} = \sqrt{1/(2\epsilon_0 \omega_{\mathrm{qu}} V)}$ via its frequency ω_{qu} and (effective) mode volume V.

The quantized field also contributes its free part to the Hamiltonian as

$$H_{\mathrm{field}} = \omega_{\mathrm{qu}} a^\dagger a \,. \tag{5.5}$$

While in terms of the time-dependent Schrödinger equation the classical field does not contribute a similar term to the Hamiltonian, we should discuss it within Floquet-theory (see Section 2.6). A Floquet state is represented in the extended Floquet Hilbert space, spanned by the matter Hilbert space and a discrete index $n \in \{0, \pm 1, \pm 2, \ldots\}$, which will be called the sideband index or Floquet index in the following [32, 95]. As such it is the temporal equivalent to the Bloch theorem for spatially translational invariant systems. In the extended space, the Floquet states are determined with a time-independent Schrödinger equation, where the extended Hamiltonian takes the blockmatrix form

$$H^{mn} = \delta_{mn} m\omega_{\mathrm{cl}} + \tilde{H}_{m-n} \,, \tag{5.6}$$

with the Fourier components

$$\tilde{H}_l = \frac{1}{T} \int_{t_0}^{t_0+T} dt H(t) e^{il\omega_{\mathrm{cl}} t} \tag{5.7}$$

of the T-periodic Hamiltonian ($T = 2\pi/\omega_{\mathrm{cl}}$). In these blocks we therefore find an energetic contribution proportional to ω_{cl}, that counts the sideband index. There is some ambiguity within the choice of t_0, which is usually referred to as Floquet-gauges. The spatial equivalent

[3] A generalization of the series expansions in this chapter to hopping elements beyond nearest-neighbor-hopping is straightforward.

to these gauges is the choice of unit-cell. Different choices are connected by a unitary transformation such that this choice can be used to find particularly simple formulations of the expanded Hamiltonian.

Lastly, we have to expand the Peierl's phases in terms of the fields. For the sake of simplicity, we use the dipole approximation on the level of the complete system. This amounts to choosing a uniform driving field and mode function throughout all of the matter system. This allows us to write

$$\phi_{ij} = \phi_{ij}^{\mathrm{qu}} + \phi_{ij}^{\mathrm{cl}} = \xi_{ij} g_{\mathrm{qu}} \left(a + a^\dagger\right) + \chi_{ij} g_{\mathrm{cl}} \cos(\omega_{\mathrm{cl}} t)\,, \tag{5.8}$$

where $g_{\mathrm{qu}} = qA_{\mathrm{qu}}|\mathbf{n}(\mathbf{R}_i - \mathbf{R}_j)|$ and $g_{\mathrm{cl}} = qA_{\mathrm{cl}}|\mathbf{n}(\mathbf{R}_i - \mathbf{R}_j)|$ are dimensionless coupling constants and $\xi_{ij}, \chi_{ij} = \pm 1$ encodes the direction of the bond.

A generalization beyond uniform bond polarization alignment and a constant mode function can straighforwardly be accomplished within the dipole approximation on the bond level by making the couplings bond dependent $g_{\mathrm{qu}} = g_{\mathrm{qu},ij}$, $g_{\mathrm{cl}} = g_{\mathrm{cl},ij}$ and performing the additional bookkeeping required by these dependencies throughout the derivation. There are systems, where our simplifications are directly applicable, such as split ring resonators [223]. We can furthermore already deduce, that within our simplifications mediated interactions can only be uniform and all-to-all.

For the evaluation in terms of a series expansion, it is helpful to expand the quantum Peierl's phase in terms of the cavity occupation number states $|\nu\rangle = (a^\dagger)^n/\sqrt{\nu!}\,|0\rangle$. To differentiate the occupation numbers from the Floquet sidebands, we will use greek indices for the cavity modes occupation and latin indices for the sidebands throughout this chapter. It is possible to evaluate the exponential of ladder operators as finite sum using a normal ordering [219]:

$$\langle\mu|\, e^{\mathrm{i}\phi_{ij}^{\mathrm{qu}}}\, |\nu\rangle = \mathrm{i}^{|\mu-\nu|} \xi_{ij}^{\mu-\nu} j_{\mu,\nu}(g_{\mathrm{qu}})\,, \tag{5.9}$$

where

$$j_{\mu,\nu}(g_{\mathrm{qu}}) = e^{-g_{\mathrm{qu}}^2/2} \sum_{k=0}^{\nu} \frac{(-1)^k g_{\mathrm{qu}}^{2k+|\mu-\nu|}}{k!(k+|\mu-\nu|)!} \frac{\sqrt{\mu!\nu!}}{(\nu-k)!} \tag{5.10}$$

for $\mu \geq \nu$ else the indices are swapped.

The classical Peierl's phase leads to a coupling between Floquet blocks as

$$\frac{1}{T}\int_{-T/2}^{T/2} dt e^{\mathrm{i}l\omega_{\mathrm{cl}}t} e^{\mathrm{i}\phi_{ij}^{\mathrm{cl}}} = \mathrm{i}^{|l|} \chi_{ij}^l J_{|l|}(g_{\mathrm{cl}})\,, \tag{5.11}$$

where

$$J_n(x) = \frac{1}{2\pi}\int_{-\pi}^{\pi} d\tau e^{\mathrm{i}n\tau + \mathrm{i}\sin(\tau)} = (-1)^n J_{-n}(x) \tag{5.12}$$

are Bessel functions.

For the isolated cavity setting, we therefore have to treat the Hamiltonian $H = \sum_{\mu\nu=0}^{\infty} H_{\mu\nu}\,|\mu\rangle\langle\nu|$ with

$$\begin{aligned} H_{\mu\nu} =& \delta_{\mu\nu}\left(U\sum_i n_{i\downarrow}n_{i\uparrow} + \mu\omega_{\mathrm{qu}}\right) \\ & -t_0 \mathrm{i}^{|\mu-\nu|} j_{\mu,\nu}(g_{\mathrm{qu}}) \sum_{\langle i,j\rangle,\sigma} \xi_{ij}^{\mu-\nu} c_{i\sigma}^\dagger c_{j\sigma}\,. \end{aligned} \tag{5.13}$$

In the driven case, we have to work with the Floquet-block Hamiltonian $H = \sum_{mn=-\infty}^{\infty} \sum_{\mu\nu=0}^{\infty} |m\mu\rangle \langle n\nu| H_{\mu\nu}^{mn}$:

$$\begin{aligned} H_{\mu\nu}^{mn} =& \delta_{mn}\delta_{\mu\nu}\left(U\sum_i n_{i\downarrow}n_{i\uparrow} + m\omega_{\mathrm{cl}} + \mu\omega_{\mathrm{qu}}\right) \\ & -t_0 \mathrm{i}^{|m-n|+|\mu-\nu|} J_{|m-n|}(g_{\mathrm{cl}}) j_{\mu,\nu}(g_{\mathrm{qu}}) \sum_{\langle i,j\rangle,\sigma} \chi_{ij}^{m-n} \xi_{ij}^{\mu-\nu} c_{i\sigma}^\dagger c_{j\sigma}\,. \end{aligned} \tag{5.14}$$

In this formulation the quantum and classical matrix elements of the Peierl's phase are very similar. It can be shown, that for $\nu \to \infty$ and a fixed amplitude $g_{\mathrm{qu}}\sqrt{\nu} = g_{\mathrm{cl}}$, the cavity case crosses over to the Floquet case [93].

5.2.2 Derivable light-dressed low-energy Hamiltonians

As in other cases earlier in this thesis, we want to consider the strong coupling limit $U \gg t_0$ at half filling. The expansion in this limit in second order without the inclusion of the transverse electromagnetic field again yields the spin 1/2-Heisenberg Hamiltonian

$$H_{\mathrm{Hb}} = J_{\mathrm{ex}} \sum_{\langle i,j\rangle} \vec{S}_i \cdot \vec{S}_j \tag{5.15}$$

with antiferromagnetic exchange interaction $J_{\mathrm{ex}} = 2t_0^2/U$. The purely laser-driven case ($g_{\mathrm{qu}} = 0, g_{\mathrm{cl}} > 0$) has been discussed extensively within Floquet theory: In the Floquet block-matrix structure an effective Floquet spin model is obtained by perturbatively eliminating both the charge fluctuations and the Floquet sidebands. The resulting low-energy Hamiltonian is a Heisenberg Hamiltonian with a dressed exchange interaction $J_{\mathrm{ex}}^F(\omega_{\mathrm{cl}}, g_{\mathrm{cl}})$ [92, 196, 217], which, depending on frequency and amplitude of the drive, can be positive (antiferromagnetic) and negative (ferromagnetic). The reversal of the exchange interaction has been confirmed in cold gas experiments [228]. Several generalizations have been discussed, including, e.g., effective models based on higher series expansions t_0/U [218], higher order exchange processes via ligand orbitals [229], orbital exchange processes [162], or doped states (t-J model) [230].

In the opposite case of a system only coupled to quantum photons, the Hamiltonian can be obtained likewise by a perturbative elimination of all charge and photon number fluctuations from some fixed cavity occupation ν. The resulting Hamiltonian can again be considered as a spin-1/2 Heisenberg Hamiltonian with dressed exchange interaction $J_{\mathrm{qu},\nu}$ for a cavity with ν photons [199]. The two important limits are the empty cavity ($\nu = 0$), which can be understood as a polaritonic dressing of the exchange interaction and $\nu \to \infty$ with fixed $g_{\mathrm{qu}}\sqrt{\nu} = g_{\mathrm{cl}}$. As outlined in the previous section, this limit recovers the Floquet exchange Hamiltonian [93]. Properties of the model, that rely on the quantumness of the electromagnetic field, should therefore be most pronounced for small cavity occupations. This can be understood in an intuitive frame: The Floquet-block matrix has an infinite ladder spectrum in the positive and negative direction. Matrix elements between blocks only depend on distance between blocks. The quantum harmonic oscillator, that describes the bare electromagnetic field, has a ladder spectrum, that extends to infinity only in the positive direction. Due to this boundedness from below, matrix elements between blocks depend on the absolute occupation numbers. When taking the Floquet-limit $\nu \to \infty$, this property washes out.

In real systems preparing stable multi-photon states $|\nu\rangle$ in the cavity are difficult to realize: Dissipative processes lead to a finite lifetime of excitations and a linewidth broadening of Γ. The effective Hamiltonian projected to a given occupation number can therefore in an undriven, open setting only describe the transient dynamics for $t \ll \Gamma^{-1}$. Alternatively, these Hamiltonians can be understood as effective description of a driven dissipative system, where an external drive of the cavity mode stabilizes a Fock state $|\nu\rangle$ using the non-linearity of the hybrid cavity-matter system [65]. In this work we will, however, neglect dissipative processes and focus mainly on the induced dynamics by the empty cavity and a drive fully described withing Floquet-theory.

5.2.3 Spin-photon Hamiltonian and Raman scattering

Alternative to eliminating both photonic and charge fluctuations, one can also eliminate only the latter. The resulting Hamiltonian is then defined on the subspace containing both spins and photons and can be considered as the effective spin-photon vertex in Figure 5.1 and will throughout this chapter be referred to as a spin-photon Hamiltonian. To second order in t_0/U, it was derived by Sentef *et al.* using a time-dependent Schrieffer-Wolff transformation in a rotating frame [93]:

$$H_{\mathrm{SP}} = J_{\mathrm{ex}} \sum_{\langle i,j \rangle} \mathcal{J}_{ij}(a^\dagger, a)\, P^S_{ij} + \omega_{\mathrm{qu}} a^\dagger a\,, \tag{5.16}$$

where the interaction operator

$$P^S_{ij} = \vec{S}_i \cdot \vec{S}_j - \frac{1}{4} \tag{5.17}$$

is the projector on a singlet on bond (ij), and the exchange interaction is replaced by the operator $\mathcal{J}_{ij}(a^\dagger, a)$. Since we again do not want to consider bond dependencies of the light matter coupling, we use $\mathcal{J}_{ij}(a^\dagger, a) = \mathcal{J}(a^\dagger, a)$. For the exact form of $\mathcal{J}$, see Ref. [93] and Appendix C.

We can understand the form of the matter interaction operator pictorially: In our model the fields couple nonlinearly to the dipole moment of electrons hopping between lattice sites. As there is only a single band, the kinetic degree of freedom is frozen out on bonds hosting a triplet configuration by the Pauli principle. For a first understanding, and for later reference, we quote the leading order of the operator in g_{qu} [93]

$$\mathcal{J}\left(a^\dagger, a\right) = \mathcal{J}_0\left(a^\dagger, a\right) + \left(\mathcal{J}_2\left(a^\dagger, a\right) a^2 + \mathrm{h.c.}\right)\,, \tag{5.18}$$

with

$$\mathcal{J}_0 = 1 - g^2_{\mathrm{qu}} \frac{\bar{\omega}_{\mathrm{qu}}}{1 + \bar{\omega}_{\mathrm{qu}}} + g^2_{\mathrm{qu}} a^\dagger a \frac{2\bar{\omega}^2_{\mathrm{qu}}}{1 - \bar{\omega}^2_{\mathrm{qu}}} + \mathcal{O}(g^4_{\mathrm{qu}})\,, \tag{5.19}$$

$$\mathcal{J}_2 = g^2_{\mathrm{qu}} \frac{\bar{\omega}^2_{\mathrm{qu}} + 2\bar{\omega}^4_{\mathrm{qu}}}{(1 - 4\bar{\omega}^2_{\mathrm{qu}})(1 - \bar{\omega}^2_{\mathrm{qu}})} + \mathcal{O}(g^4_{\mathrm{qu}})\,, \tag{5.20}$$

and $\bar{\omega}_{\mathrm{qu}} = \omega_{\mathrm{qu}}/U$. Taking matrix elements of $\mathcal{J}(a^\dagger, a)$ in a photon number state $|\nu\rangle$ would give the photon-dressed exchange interaction $J_{\mathrm{qu},\nu} = \langle \nu | \mathcal{J} | \nu \rangle$. The off-diagonal terms in the photon number describe processes such as a spin flip (due to the operator P^S_{ij}) together with a change in the photon number, i.e., photon-magnon scattering. For example, the two terms in the perturbative expression describe two photon absorption/emission ($\mathcal{J}_2$) as well as photon scattering ($\mathcal{J}_0$) on the spin system.

The time-dependent Schrieffer-Wolff transformation used in the derivation of equation (5.16) relies on time periodicity in a cavity co-rotating frame, i.e., one rotating with angular frequency ω_{qu}. A straightforward generalization of this derivation to the driven cavity setting is therefore difficult in the driven cavity setting, as for a general drive frequency ω_{cl}, the Hamiltonian is no longer time-periodic in the co-rotating frame.

We instead use the matrix elements obtained through the projection on the photon number states (see equation (5.14)), where we do not face this issue. Perturbatively eliminating charge excitations while keeping both cavity and sideband indices produces a mixed spin-photon-Floquet Hamiltonian. It is important to emphasize, that the series expansion in this case is not a two-block scheme as those described in Section 2.5 but a multiblock scheme. Equation (2.169) dictating the form of the generator and thereby the form of the effective Hamiltonian generalizes to the multiblock case with properly defined projectors P_0, P_1. For a well defined resolvent superoperator $\mathcal{L}$, this scheme does however require gaps between *all* blocks. We perform this expansion in the Appendix D. This gives a spin Hamiltonian in the extended Floquet/photon space, with the blockmatrix structure,

$$(H_{\mathrm{SP}})^{mn}_{\mu\nu} = \delta_{mn}\delta_{\mu\nu}(m\omega_{\mathrm{cl}} + \mu\omega_{\mathrm{qu}}) + J_{\mathrm{ex}} \sum_{\langle i,j \rangle} P^S_{ij} \mathcal{J}^{mn}_{\mu\nu}(g_{\mathrm{cl}}, g_{\mathrm{qu}})\,. \tag{5.21}$$

For the form of the matrix elements $\mathcal{J}^{mn}_{\mu\nu}$, see equation (D.12) in Appendix D. The matrix elements $\mathcal{J}^{mn}_{\mu\nu}$ describe the absorbtion/emission of $m-n$ photons from the classical drive under the absorbtion/emission of $\mu-\nu$ cavity photons from/into the cavity at occupation ν through second-order processes. For example, $\mathcal{J}^{01}_{10}$ describes scattering of a photon from the drive to the cavity (left half of Figure 5.7), while $\mathcal{J}^{10}_{01}$ describes the opposite scattering process (right half of Figure 5.7). In Appendix E we show that these terms are can quantitatively be understood as the matrix elements of resonant Raman scattering on the spin system [231].

5.3 Deriving the cavity-mediated interactions

We now turn to the central topic of this chapter, the derivation of cavity-induced long-range spin interactions. In general, to obtain a photon-dressed spin model, we work in a regime where driving and cavity frequencies are of the same order of U, such that U can be considered as a common high-energy scale, and t_0/U is treated as a small parameter[4]. Since we again want to map to an effective spin model, the effective spin Hamiltonian for the driven or undriven cavity is obtained by projecting the system to a subspace with no charge excitations, a given cavity occupation ν (such as $\nu = 0$), and the 0th Floquet sector while keeping virtual excitations to the other sectors perturbatively in t_0/U.

Since the spins couple indirectly to the fields, we have to go to fourth order in t_0/U. To this order, virtual tunneling processes lead to three different contributions in the effective Hamiltonian:
(i) Corrections to the nearest-neighbour exchange interaction beyond t_0^2/U,
(ii) short-range three-spin and four-spin interactions, which are restricted to connected clusters of the lattice, and

[4] If either of the frequcies $\omega_{\mathrm{qu}}, \omega_{\mathrm{cl}}$ become comparable to t_0, we run into issues with the convergence of our series expansion [91] as, similar to when we discussed the high-energy crystalfield excitations in Section 3.4, the two subspaces considered are no longer properly gapped with $\Delta \gg t_0$. This could again be overcome by choosing the subspaces $\mathcal{P}_0, \mathcal{P}_1$ accounting for this.

(iii) long-range cavity-mediated interactions between bonds (ij) and (kl) which are not connected by a hopping process.

Since a spin triplet state on a bond (ij) does not allow electron tunnelling and therefore does not couple to light, the long-range interaction between the bonds can involve only singlet states, and it can therefore be written in the form $P^S_{ij}P^S_{kl}$, with the singlet projectors (5.17). Hence, the effective Hamiltonian takes the general form

$$H_{\text{eff}} = \sum_{\langle i,j\rangle} J_{\text{Hb},ij} P^S_{ij} + \sum_{\langle i,j\rangle\langle k,l\rangle} K_{ij,kl} P^S_{ij} P^S_{kl} + \dots \,, \tag{5.22}$$

where the ellipsis ... refers to short-range three-spin and four-spin terms. They can give rise to interesting physics (see, e.g., Ref. [218] and [220]), but in this work we only focus only on the long-range interactions, which can have a significant qualitative effect on the behavior of the spin model.

To derive the interaction $K_{i_1 j_1, i_2 j_2}$ between disconnected bonds (i_1, j_1) and (i_2, j_2) on a lattice to fourth order in t_0/U, it is sufficient to consider two isolated dimers. This is because the interaction term $P^S_{i_1 j_1} P^S_{i_2 j_2}$ contains a spin-flip on both bonds, which already requires two hoppings per bond. Hence, to fourth order in t_0/U, no further virtual excited states can be generated on sites other than (i_1, j_1) and (i_2, j_2). We can therefore restrict our analysis to a 4-site system which only contains the two isolated dimers. In this setting the effective Hamiltonian takes the form

$$H_{\text{eff}} = 2J_{\text{Hb}}(P^S_{i_1 j_1} + P^S_{i_2 j_2}) + 8K P^S_{i_1 j_1} P^S_{i_2 j_2} \,, \tag{5.23}$$

where the additional prefactors come from the sum over sites in equation (5.22). The overall scale of the long-range interaction K will be $K_0 \equiv 2t_0^4/U^3$, with a dimensionless prefactor depending on the cavity occupation ν, the light-matter coupling g_{qu}, the laser driving strength g_{cl}, and the ratios $\bar{\omega}_{\text{qu}} = \omega_{\text{qu}}/U$ and $\bar{\omega}_{\text{cl}} = \omega_{\text{cl}}/U$,

$$K/K_0 \equiv \kappa^{(\nu)}(g_{\text{qu}}, g_{\text{cl}}, \bar{\omega}_{\text{qu}}, \bar{\omega}_{\text{qu}}) \,. \tag{5.24}$$

5.3.1 Extraction from exact diagonalization

The mediated-interaction leads to a non-additivity of the spectra of dimers in the cavity. Within the four site model, the interactions can be simply read off their spectra: The Hamiltonian has eigenenergies $E = 8K + 4J \equiv E_{SS}$ when both bonds host a singlet configuration, $E = 2J \equiv E_S$ when only one bonds hosts a singlet, and $E = 0$ when both bonds host triplets. Hence the interaction K is given by

$$8K = E_{\text{SS}} - 2E_{\text{S}} \,. \tag{5.25}$$

One can therefore numerically determine the amplitude of the interaction by solving the Hubbard model (equations (5.13) or (5.14)) for the two dimers as follows: First, we classify the eigenstates in terms of the number of singlets (which now includes the doubly occupied configurations) and triplets they contain. We define the energy $E^{\nu,m}_{\text{SS}}(g_{\text{qu}}, g_{\text{cl}}, t_0)$ as the energy of the state which is adiabatically connected to the state with zero charge excitations, two singlets, the mth Floquet sector, and ν photons at $g_{\text{qu}} = g_{\text{cl}} = t_0 = 0$. Similarly, the energy

$E_{\mathrm{S}}^{\nu,m}(g_{\mathrm{qu}}, g_{\mathrm{cl}}, t_0)$ is defined for one singlet. By comparing with (5.25), we obtain the effective interaction as the non-additive contribution of the singlet energies:

$$\Delta E^{\nu,0} = (E_{\mathrm{SS}}^{\nu,0} - \nu\omega_{\mathrm{qu}}) - 2(E_{\mathrm{S}}^{\nu,0} - \nu\omega_{\mathrm{qu}}). \tag{5.26}$$

Finally, the function (5.24) can be extracted by numerically taking the limit

$$\kappa^{(\nu)}(g_{\mathrm{qu}}, g_{\mathrm{cl}}, \bar{\omega}_{\mathrm{qu}}, \bar{\omega}_{\mathrm{qu}}) \overset{t_0 \to 0}{=} \frac{\Delta E^{\nu,0}(g_{\mathrm{qu}}, g_{\mathrm{cl}}, \bar{\omega}_{\mathrm{qu}}, \bar{\omega}_{\mathrm{qu}}, t_0)}{8 \cdot 2t_0^4/U^3}. \tag{5.27}$$

We have used this approach to benchmark the analytical perturbative expressions obtained below. In practice, we numerically diagonalize the Hamiltonian (5.13) (for the undriven cavity) or (5.14) (for the driven cavity), with a sufficiently high cutoff in the photon number and Floquet index to converge the result.

Since triplet states are exact eigenstates of both Hamiltonians, we can avoid performing the classification of eigenstates in terms of singlets and triplets by a priori using a basis spanned by the singlet and triplet configuration on the dimers. For the dimer $(1, 2)$ we use

$$\sqrt{2}\,|S\rangle = \left(c_{1\uparrow}^\dagger c_{2\downarrow}^\dagger - c_{1\downarrow}^\dagger c_{2\uparrow}^\dagger\right)|0\rangle \tag{5.28}$$

$$\sqrt{2}\,|T\rangle = \left(c_{1\uparrow}^\dagger c_{2\downarrow}^\dagger + c_{1\downarrow}^\dagger c_{2\uparrow}^\dagger\right)|0\rangle \tag{5.29}$$

$$\sqrt{2}\,|C^+\rangle = \left(c_{1\uparrow}^\dagger c_{1\downarrow}^\dagger + c_{2\uparrow}^\dagger c_{2\downarrow}^\dagger\right)|0\rangle \tag{5.30}$$

$$\sqrt{2}\,|C^-\rangle = \left(c_{1\uparrow}^\dagger c_{1\downarrow}^\dagger - c_{2\uparrow}^\dagger c_{2\downarrow}^\dagger\right)|0\rangle\,. \tag{5.31}$$

In this basis the Hamiltonian for this dimer coupled to the cavity becomes

$$\begin{aligned} H_{\mu\nu} = \delta_{\mu\nu}\Bigg(\mu\omega_{\mathrm{qu}} \sum_{\psi=S,T} |\psi\rangle\langle\psi| + \sum_{\psi=C^+,C^-} (U + \mu\omega_{\mathrm{qu}})\,|\psi\rangle\langle\psi|\Bigg) \\ - t_0 \mathrm{i}^{|\mu-\nu|} j_{\mu\nu}(g_{\mathrm{qu}}) \xi_{12}^{\mu-\nu}\Big((1 + (-1)^{\mu-\nu})\,|C^+\rangle\langle S| \\ + (1 - (-1)^{\mu-\nu})\,|C^-\rangle\langle S|\Big) + \mathrm{h.c.}\,, \end{aligned} \tag{5.32}$$

which is straightforwardly extended to the driven case.

From equation (5.32) we can furthermore read of, that it is only through the cavity coupling, that the odd charge excitation $|C^-\rangle$ couples to the singlet configuration. In the coupled setting, the symmetry of the coupling charge excitation is determined by whether an even or odd number of photons is exchanged during the hopping process. We can understand this by considering the symmetry of the states with respect to parity, which the Hamiltonian globally preserves: Due to the fermionic commutation relations $|S\rangle$ is even under the exchange of sites $1 \leftrightarrow 2$. Similarly $|C^+\rangle$ is even and $|C^-\rangle$ odd. Since we consider the electromagnetic field of the cavity to be described as a harmonic oscillator, it is even for even occupation numbers and odd for odd occupation numbers. Under the exchange of an even number of photons, both the dimer and the cavity preserve their parity, while under the exchange of an odd number of photons both dimer and field flip their parity only preserving it globally.

In this symmetrized basis the Hamiltonian therefore separates into parity blocks. We leverage this property for a better convergence of the eigenstates and for a reduced basis size, which allows us to push the truncations we impose on the cavity and Floquet space further. To obtain

the limit (5.27), we evaluate the spectrum for different t_0 and extract the series coefficient from a polynomial fit.

In the following subsections we derive the expressions for the interaction to leading order in t_0/U by means of two different series expansions. At first, we discuss a full fourth-order perturbation theory in t_0/U, which gives the exact result. Secondly, we describe the approach based on the spin-photon Hamiltonian introduced in Section 5.2.3, which describes photon-matter scattering with matrix elements $\propto t_0^2$ from which we eliminate the photons.

5.3.2 Fourth-order series expansion

We aim to derive the effective Hamiltonian in the subspace which contains no charge excitations (doubly occupied sites and holes), and a given photon number and Floquet index $m = 0$. All other states are energetically off-resonant and will be eliminated. Virtual transitions to the off-resonant states determine the effective Hamiltonian in the target energy space. The general procedure is to find a unitary transformation that decouples the target space and the off-resonant states up to a given perturbative order. In the rotated basis, we can then project out the off-resonant states, while the resulting Hamiltonian is the effective Hamiltonian in the target space. There are many different techniques for obtaining this transformation [25, 27, 84–86, 88, 232]. We follow the Schrieffer-Wolff transformation as defined by Loss *et al.* [91] and introduced in Section 2.5. For a given Hamiltonian

$$H = H_0 + \alpha V\,, \tag{5.33}$$

which we can separate in an unperturbed part H_0 and a perturbation V, it allows us to formulate the spectrum of H in terms of the eigenstates of H_0 as series in V. For a more detailed introduction, we refer to Section 2.5. In the formulation we use, it has the disadvantage of not obeying a linked-cluster property. For our setting this is irrelevant, since the cavity links all matter clusters.

Applied to a specific setting, it is helpful to understand the series expansion pictorially similar to the graphs of a diagrammatic expansion: Consider the eigenstates of H_0. Expanded in these, the perturbation maps between these as $V = \langle i|\, V\, |j\rangle \cdot |i\rangle\langle j|$. We can therefore interpret a series in V as successive steps through the eigenbasis of H_0. Evaluating the effective Hamiltonian in order n is therefore equivalent to summing over all paths through the eigenstates of H_0 we can take with n steps. Three such paths contributing to the fourth order expansion are sketched in Figure 5.2. Each path is then weighed using the resolvent operator applied according to how these steps move between H_0's target space $\mathcal{P}_0$ and its off-resonant complement $\mathcal{P}_1$ and a prefactor, that can be precomputed [91].

We again label the diagonal part of V as $V_\mathrm{d} = P_0VP_0 + P_1VP_1$ and its offdiagonal part as $V_\mathrm{od} = P_0VP_1 + P_1VP_0$. Before starting to evaluate these term, we can use the structure of our Hamiltonian to simplify the general structure of the fourth order series (equation (2.173)): In the charge excitation free subspace at half filling a hopping always creates a charge excitation. Hence $P_0V_\mathrm{d} = V_\mathrm{d}P_0 = 0$, and V_d vanishes in the low-energy subspace. Additionally, since we limit the geometry to two disconnected dimers, there are no processes with three hoppings connecting the charge excitation free target space with itself ($P_0V_\mathrm{od}V_\mathrm{d}V_\mathrm{od}P_0 = 0$), so that the third order is vanishing. In the Fermi-Hubbard model at half filling, this holds true for all odd orders of the perturbation theory for arbitrary lattices as long as they do not contain odd-sized loops. Furthermore, the unperturbed Hamiltonian H_0 acts trivially on states in our target spaces, i.e., $P_0H_0P_0 = E_0\mathbb{1}$. This property makes it possible to shift the superoperator $\mathcal{L}$

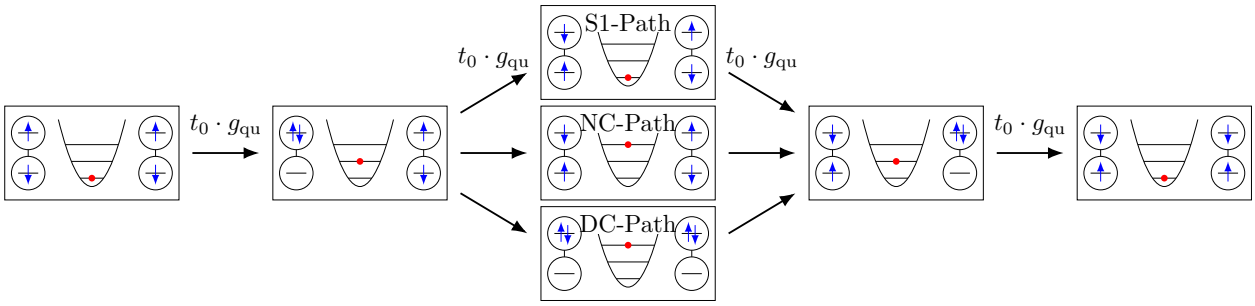

Figure 5.2: Different representative paths through the unperturbed Hilbert space in order $g_{qu}^4 t_0^4$. The intermediate state can be from the low-energy part of the unperturbed Hilbertspace (S1-path) or the high-energy part. In the latter case, we can either have a cavity excitation with no charge excitations (NC-path) or two charge excitations and arbitrary cavity occupation (DC-path). Figure reprinted from [P2] Copyright 2024 American Physical Society.

as $P_0\mathcal{L}(X)YP_0 = -P_0X\mathcal{L}(Y)P_0$ [91], which furthermore simplifies the general expression. Using these simplifications, up to fourth order we find

$$P_0H_{\text{eff}}P_0 = P_0H_0P_0 + P_0S_1V_{\text{od}}P_0 + \frac{1}{8}P_0[S_1,[S_1,[S_1,V_{\text{od}}]]]P_0 + P_0\mathcal{L}\left(S_1V_{\text{d}}\right)V_{\text{d}}S_1P_0\,. \tag{5.34}$$

This expression will now be evaluated explicitly for the isolated and undriven cavity, respectively. In the main text we will mainly summarize the resulting analytical expressions and their structure, while for the sake of brevity the derivations are shifted to the appendices.

5.3.2.1 Isolated cavity

Since the electronic part of the series expansion can is easiest understood in this case, let us first discuss the simplified setting of an isolated and empty cavity, i.e., we choose the low-energy part of the unperturbed Hilbert space with $\nu = 0$ photons as target space. This amounts to the projector

$$P_0 = \prod_i (1 - n_{i\uparrow}n_{i\downarrow}) \otimes |0\rangle\langle 0|\,. \tag{5.35}$$

Any hopping from the target space is part of V_{od}, since it has to create a charge excitation. For the diagonal part V_{d}, which only acts outside of the target space, there are two possibilities: (i) transitions between states with zero and one charge excitations but with the cavity in an excited state, or (ii) transitions between states with one and two charge excitations with arbitrary cavity occupations.

Using these processes/steps we distinguish between three different types of operator products/paths, which connect the target space with itself (see Figure 5.2): The first ones we label as *S1-paths*, since they are generated by the offdiagonal part of the perturbation V_{od} only and therefore described by the threefold nested commutator of S_1 and V_{od} in equation (5.34). For those also containing the diagonal part of the perturbation V_{d}, we distinguish between those with **N**o **C**harge excitations in the intermediate state as the *NC-paths* and those with a **D**ouble **C**harge excitation in the intermediate state as the *DC-paths*.

After some algebra (see Appendix F), we obtain the fourth-order terms of the Hamiltonian as a sum over the three contributions $H_{\mathrm{S1}}^{(0)} + H_{\mathrm{NC}}^{(0)} + H_{\mathrm{DC}}^{(0)}$,

$$H_{\mathrm{S1}}^{(0)} = 4K_0\big(P^S_{i_1j_1}+P^S_{i_2j_2}+2P^S_{i_1j_1}P^S_{i_2j_2}\big)\sum_{\alpha,\beta,\gamma=0}^{\infty} W_{\mathrm{S1}}^{0\alpha\beta\gamma0}, \tag{5.36}$$

$$H_{\mathrm{NC}}^{(0)} = 4K_0\big(P^S_{i_1j_1}+P^S_{i_2j_2}+2P^S_{i_1j_1}P^S_{i_2j_2}\big)\sum_{\alpha,\beta,\gamma=0}^{\infty} W_{\mathrm{NC}}^{0\alpha\beta\gamma0}, \tag{5.37}$$

$$H_{\mathrm{DC}}^{(0)} = 8K_0P^S_{i_1j_1}P^S_{i_2j_2}\sum_{\alpha,\beta,\gamma=0}^{\infty} W_{\mathrm{DC}}^{0\alpha\beta\gamma0}, \tag{5.38}$$

where $W_p^{0\alpha\beta\gamma0}$ sums the contribution from all path of type $p \in \{\mathrm{S1},\mathrm{NC},\mathrm{DC}\}$ with photon states $0 \to \gamma \to \beta \to \alpha \to 0$. Explicit expressions for the path contributions are given by

$$W_{\mathrm{S1}}^{0\alpha\beta\gamma0} = \mathcal{J}^{0\alpha\beta\gamma0}(g_{\mathrm{qu}})\frac{\delta_{\beta0}(-1)^{\alpha+\gamma}\left(2+(\gamma+\alpha)\bar{\omega}_{\mathrm{qu}}\right)}{\left(1+\alpha\bar{\omega}_{\mathrm{qu}}\right)^2\left(1+\gamma\bar{\omega}_{\mathrm{qu}}\right)^2} \tag{5.39}$$

$$W_{\mathrm{NC}}^{0\alpha\beta\gamma0} = -\mathcal{J}^{0\alpha\beta\gamma0}(g_{\mathrm{qu}})\frac{(1-\delta_{\beta0})(-1)^{\alpha+\beta+\gamma}(1+(-1)^{\beta})}{(1+\alpha\bar{\omega}_{\mathrm{qu}})(\beta\bar{\omega}_{\mathrm{qu}})(1+\gamma\bar{\omega}_{\mathrm{qu}})} \tag{5.40}$$

$$W_{\mathrm{DC}}^{0\alpha\beta\gamma0} = -\mathcal{J}^{0\alpha\beta\gamma0}(g_{\mathrm{qu}})\frac{(-1)^{\beta}\left(2+(-1)^{\alpha+\gamma}(1+(-1)^{\beta})\right)}{(1+\alpha\bar{\omega}_{\mathrm{qu}})(2+\beta\bar{\omega}_{\mathrm{qu}})(1+\gamma\bar{\omega}_{\mathrm{qu}})}, \tag{5.41}$$

where

$$\begin{aligned}\mathcal{J}^{\alpha\beta\gamma\delta\epsilon}(g_{\mathrm{qu}}) =& \mathrm{i}^{|\alpha-\beta|+|\beta-\gamma|+|\gamma-\delta|+|\delta-\epsilon|}\\ &\times\ j_{\alpha\beta}(g_{\mathrm{qu}})j_{\beta\gamma}(g_{\mathrm{qu}})j_{\gamma\delta}(g_{\mathrm{qu}})j_{\delta\epsilon}(g_{\mathrm{qu}}),\end{aligned}$$

and $K_0 = 2t_0^4/U^3$.

The extension of this scheme to arbitrary cavity number states $|\nu\rangle$ is straightforward. We shift the target space by using the projector

$$P_0^{(\nu)} = \prod_i \left(1 - n_{i\uparrow}n_{i\downarrow}\right) \otimes |\nu\rangle\langle\nu| \ . \tag{5.42}$$

instead of using equation (5.35). This has no influence on the allowed paths through the fermionic Hilbert space but changes their amplitudes, phases and resolvents. We find that this is accounted for by taking the results of the empty cavity and shifting the cavity occupation number indices $\alpha, \beta, \gamma \to \alpha - \nu, \beta - \nu, \gamma - \nu$ everywhere but in the coupling amplitudes $j_{\mu\nu}$. The generalized derivation can be found in Appendix G. We find equations (G.11)-(G.13) for the contributions $H_{\mathrm{S1}}^{(\nu)}$, $H_{\mathrm{NC}}^{(\nu)}$, and $H_{\mathrm{DC}}^{(\nu)}$, which generalize equations (5.36)-(5.38) to $\nu \neq 0$.

One can see that the fourth-order contribution contains both higher-order corrections to the exchange couplings (the terms proportional to $P^S_{i_1j_1} + P^S_{i_2j_2}$), and a mediated interaction (the terms proportional to the product $P^S_{i_1j_1}P^S_{i_2j_2}$). By comparing equations (5.36)-(5.38) (or

equations (G.11)-(G.13) for $\nu \neq 0$) to equation 5.23 one can therefore immediately read off the long-range interaction in the parametrization of equation (5.24). We write

$$\kappa^{(\nu)}(\bar{\omega}_{\mathrm{qu}}, g_{\mathrm{qu}}) \equiv \sum_{\mathrm{path}\in\{\mathrm{S1,NC,DC}\}} \kappa^{(\nu)}_{\mathrm{path}}(\bar{\omega}_{\mathrm{qu}}, g_{\mathrm{qu}})\,, \tag{5.43}$$

where $\kappa^{(\nu)}_{\mathrm{path}}(\bar{\omega}_{\mathrm{qu}}, g_{\mathrm{qu}}) = \sum_{\alpha,\beta,\gamma} W^{\nu\alpha\beta\gamma\nu}_{\mathrm{path}}$ is the prefactor of the product $P^S_{i_1 j_1} P^S_{i_2 j_2}$ in the Hamiltonian $H^{(\nu)}_{\mathrm{path}}$. We evaluate the sums over intermediate photon numbers α, β, γ numerically, which necessitates introducing an upper cutoff $\nu_{\max}$ for the cavity occupation. The result quickly converges with increasing $\nu_{\max}$ [219]. The three contributions $\kappa^{(\nu)}_{\mathrm{S1}}$, $\kappa^{(\nu)}_{\mathrm{NC}}$, and $\kappa^{(\nu)}_{\mathrm{DC}}$ will also be analyzed separately below.

For $\nu \neq 0$, these interactions come with an additional caveat: Close to resonances ($\mu\bar{\omega}_{\mathrm{qu}} \approx 1$ for any $\mu \leq \nu$) the gap between the target space and the rest of the unperturbed Hilbert space vanishes. To ensure convergence of the perturbative series, this may limit the range of t_0/U we can investigate [91]. Luckily the contribution of high-order resonances requires many photon number transitions, and the convergence of the series is therefore controlled not only by t_0/U, but also by g_{qu}, which in experimentally realizable settings usually is $g_{\mathrm{qu}} \ll 1$ (see Section 5.5).

The fact, that the Schrieffer-Wolff transformation is not a linked-cluster expansion is furthermore directly reflected in our results: For $g_{\mathrm{qu}} = 0$ we recover two uncoupled Hubbard dimers. The effective Hamiltonian therefore has to separate into the sum over both dimers effective Hamiltonians, i.e., the terms $\propto P^S_{i_1 j_1} P^S_{i_2 j_2}$ have to vanish. In this limit the expansions common prefactor becomes $\mathcal{J}^{0\alpha\beta\gamma 0}(0) = \delta_{0\alpha}\delta_{0\beta}\delta_{0\gamma}$. The NC-paths contribution directly vanish, while the S1 and DC paths still individually contribute an interaction $\propto P^S_{i_1 j_1} P^S_{i_2 j_2}$. It is only when they are taken jointly that these contributions cancel and the linked-cluster property of the effective Hamiltonian is recovered. This is visible even more clearly, when considering the leading order of all contributions in g_{qu}, which we show in the Appendix F.2.

5.3.2.2 Driven Cavity

In order to extend our series expansion to the driven case we have to extend the projectors. The target space is now defined by the doublon-free sector, a given cavity occupation ν, and the zeroth Floquet sector:

$$P^{\nu}_0 = \prod_i (1 - n_{i\uparrow} n_{i\downarrow}) \otimes |\nu_{\mathrm{qu}}\rangle\langle\nu_{\mathrm{qu}}| \otimes |0_{\mathrm{cl}}\rangle\langle 0_{\mathrm{cl}}|\,. \tag{5.44}$$

Because of the translational invariance between sidebands in Floquet space, the effective Hamiltonian obtained by projection to Floquet sector m is independent of m, and we choose $m = 0$ without loss of generality. The fermionic operator part of the resulting series expansion is again unchanged, such that in the derivation of the interactions only the sums, amplitudes and resolvents of the resulting terms have to be adapted. We show this in Appendix G. Analogous to equation (5.43), the interaction can again be written as a sum of the contributions of S1-, NC- and DC-paths,

$$\kappa^{(\nu)}(\bar{\omega}_{\mathrm{qu}}, g_{\mathrm{qu}}, \bar{\omega}_{\mathrm{cl}}, g_{\mathrm{cl}}) \equiv \sum_{\mathrm{path}\in\{\mathrm{S1,NC,DC}\}} \kappa^{(\nu)}_{\mathrm{path}}(\bar{\omega}_{\mathrm{qu}}, g_{\mathrm{qu}}, \bar{\omega}_{\mathrm{cl}}, g_{\mathrm{cl}})\,, \tag{5.45}$$

where

$$\kappa^{(\nu)}_{\text{path}}(\bar{\omega}_{\text{qu}}, g_{\text{qu}}, \bar{\omega}_{\text{cl}}, g_{\text{cl}}) = \sum_{a,b,c=-\infty}^{\infty} \sum_{\alpha,\beta,\gamma=0}^{\infty} W^{\nu\alpha\beta\gamma\nu;abc}_{\text{path}} \tag{5.46}$$

now sums over all path in the photon number and Floquet space. We show the analytic forms of the weights $W^{\nu\alpha\beta\gamma\nu;abc}_{\text{path}}$ for a path with through the unperturbed Hilbert space along the photon numbers and Floquet indices $(\nu, 0) \rightarrow (\gamma, c) \rightarrow (\beta, b) \rightarrow (\alpha, a) \rightarrow (\nu, 0)$ in equations (G.14)-(G.16) in the appendix.

5.3.3 Spin-photon Hamiltonian approach

Alternative to the derivation presented in the previous section, one could try to start from the spin-photon Hamiltonian (5.16) (or spin-photon-Floquet Hamiltonian (5.21)), from which charge excitations have already been eliminated for an effective spin-photon scattering vertex. From these vertices as second step one can subsequently eliminate the photon excitations. We will refer to this approach as the "spin-photon" approach. The resulting effective Hamiltonian will be called $H_{\text{eff-SP}}$ with its corresponding interaction κ_{SP} (using again the parametrization (5.24)). While this is an intuitive procedure, its validity is restricted to certain limits, as will be discussed in the result section.

5.3.3.1 Isolated cavity

Starting from the spin-photon Hamiltonian (5.16), we focus on a fixed photon number sector ν and eliminate all photon number off-diagonal matrix elements. This corresponds to a more standard second-order perturbation theory, where $H_{\text{eff-SP}}$ is given by the first two terms in equation 5.34 only, and the off-diagonal matrix elements correspond to the matrix elements $\mathcal{J}$ for m-photon emission and absorption. This gives an interaction $K^{(\nu)}_{\text{SP}} = K_0 \kappa^{(\nu)}_{\text{SP}}(\bar{\omega}_{\text{qu}}, g_{\text{qu}})$, with

$$\begin{aligned}\kappa^{(\nu)}_{\text{SP}} = &-2 \sum_{n=1}^{\infty} \langle \nu | \, \mathcal{J}_{2n} a^{2n} \frac{1}{2n\omega_{\text{qu}}} (a^\dagger)^{2n} \mathcal{J}_{2n} \, | \nu \rangle \\ &+2 \sum_{n=1}^{\infty} \langle \nu | \, (a^\dagger)^{2n} \mathcal{J}_{2n} \frac{1}{2n\omega_{\text{qu}}} \mathcal{J}_{2n} a^{2n} \, | \nu \rangle \, .\end{aligned} \tag{5.47}$$

The two summands describe virtual photon emission and absorption respectively, where the latter term vanishes for $2n > \nu$.

5.3.3.2 Driven cavity

In the driven case, an initial elimination of charge excitations produces the spin-photon-Floquet matrix elements of equation (5.21). Eliminating both cavity and sideband fluctuation in second order from this effective Hamiltonian (see Appendix H), we obtain equation (H.3)-(H.5).

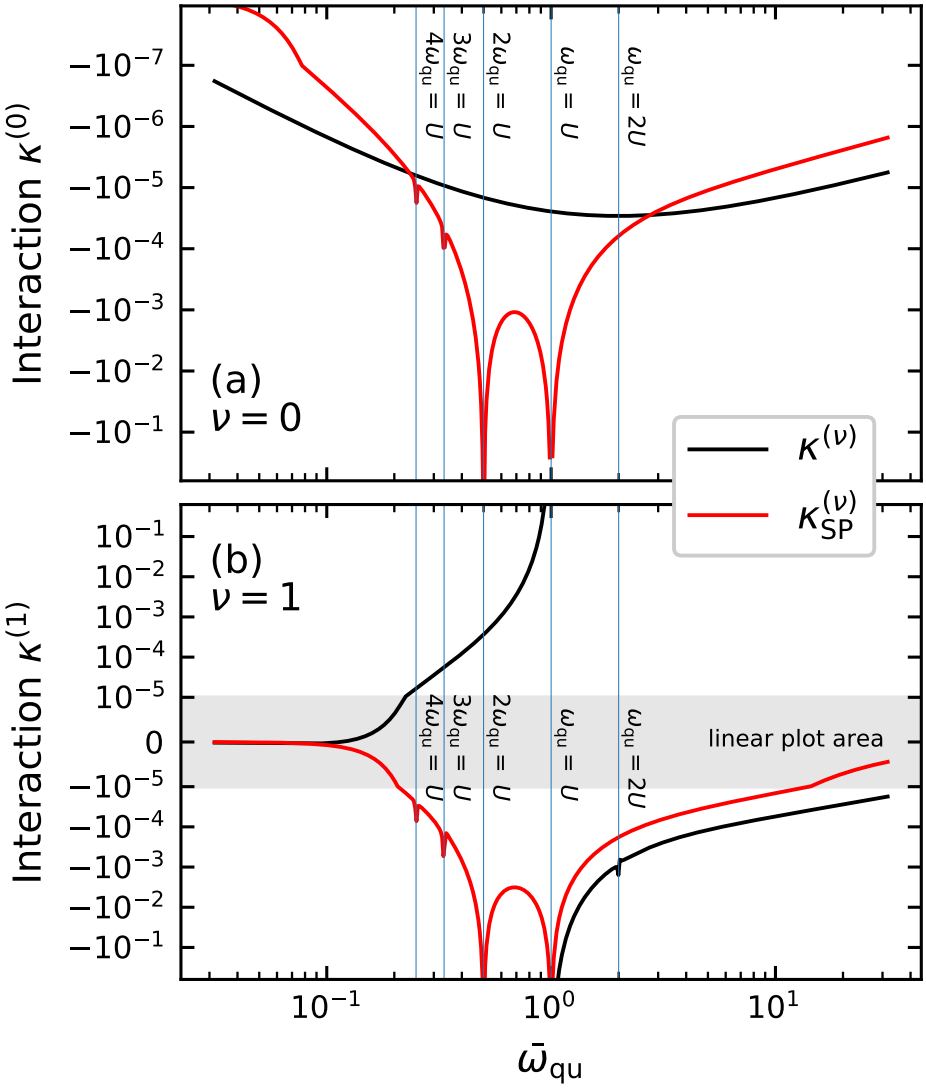

Figure 5.3: Cavity induced singlet-singlet interaction for $g_{qu} = 0.1$. (a) Empty cavity ($\nu = 0$). (b) Cavity with one photon ($\nu = 1$). The black lines indicate the interaction κ^{ν} (see equation (5.43)), while the red lines show the interaction $\kappa^{(\nu)}_{SP}$ obtained from the spin-photon approach (see equation (5.47)). In (b) the vertical axis is linear in the shaded area, otherwise it is logarithmic. Figure reprinted from [P2] Copyright 2024 American Physical Society.

5.4 Results

5.4.1 Closed cavity

We start by discussing the induced interactions for the isolated single-mode cavity. In addition to a general discussion we explicitly compare the full fourth-order expansion and the interaction obtained from the simpler spin-photon approach.

The black lines in Figure 5.3 show the long-range interaction $\kappa^{(\nu)}$ (see equation (5.43)) as a function of the cavity frequency $\bar{\omega}_{\mathrm{qu}} = \omega_{\mathrm{qu}}/U$. Note that this result, like all other results shown below, is obtained from the analytical expressions of Section 5.3.2 and benchmarked with the numerical approach outlined in Section 5.3.1. The interaction $\kappa^{(0)}$ for an empty cavity shows a weak dependence on frequency (see Figure 5.3(a)) without any singular behavior at the resonances $n\omega_{\mathrm{qu}} = U$ ($\bar{\omega}_{\mathrm{qu}} = 1/n$). The interaction induced by vacuum fluctuations between two individual dimers is much weaker than the direct spin exchange, unless one reaches the ultra-strong light matter coupling regime ($g_{\mathrm{qu}} \gtrsim 1$). This is understood because the leading order in the long-range interaction is $\mathcal{O}(g_{\mathrm{qu}}^4)$. In Figure 5.3(b) we also show the result for the isolated cavity with one photon. In this case, one observes a resonant enhancement of the interaction close to $\bar{\omega}_{\mathrm{qu}} = 1$. This resonant behavior comes from an intermediate state with one charge excitation, which is created through virtual absorption of a photon from the cavity, and therefore acquires the energy resolvent $1/(U - \omega_{\mathrm{qu}})$. The small resonance at $\omega_{\mathrm{qu}} = 2U$ can similarly be understood as a resonant enhancement of the intermediate states in the DC-paths.

The red lines in Figure 5.3 show the result $\kappa_{\mathrm{SP}}^{(\nu)}$ obtained from the spin-photon approach. One can see that for the undriven cavity with few photons, the spin-photon approach generally gives an incorrect result: For $\bar{\omega}_{\mathrm{qu}} \gg 1$ we find $\kappa_{\mathrm{SP}}^{(\nu)} \cong \kappa^{(\nu)}/4$ (see discussion below for the factor $1/4$), while at smaller frequencies the prediction based on the spin-photon Hamiltonian is also qualitatively wrong. In particular, the spin-photon approach predicts a resonant enhancement of the interaction at integer fractions $\bar{\omega}_{\mathrm{qu}} = 1/n$ even for the empty cavity. These divergences arise from the divergence of the photon number off-diagonal matrix elements $\mathcal{J}_{2n}$ in the spin-photon Hamiltonian (5.16), or, in more physical terms, the resonant enhancement of the optical non-linearity. In contrast, it is clear that there should be no resonant enhancement of the induced interaction for the empty cavity, because all intermediate states which contribute to the correlated super-exchange are gapped from the ground state.

While the deviation between the approaches is not too surprising from a formal standpoint, it is nevertheless of physical importance: In order to understand the cavity-mediated interactions, one in general cannot use a phenomenological approach that would use the spin-photon Hamiltonian with matrix elements that are obtained from nonlinear optical measurements (see comments at the end of Section 5.2.3).

5.4.2 Understanding the differences between the approaches

We can understand the deviation between the spin-photon approach and the exact result, if we take a closer look at how they are derived within a series expansion. Writing out the transformations, the two effective Hamiltonians are given as

$$H_{\mathrm{eff}} = P_0^{c,U} e^{S_{c,U}} H e^{-S_{c,U}} P_0^{c,U}\,, \tag{5.48}$$

$$H_{\mathrm{eff-SP}} = P_0^{c} e^{S_c} P_0^{U} e^{S_U} H e^{-S_U} P_0^{U} e^{-S_c} P_0^{c}\,, \tag{5.49}$$

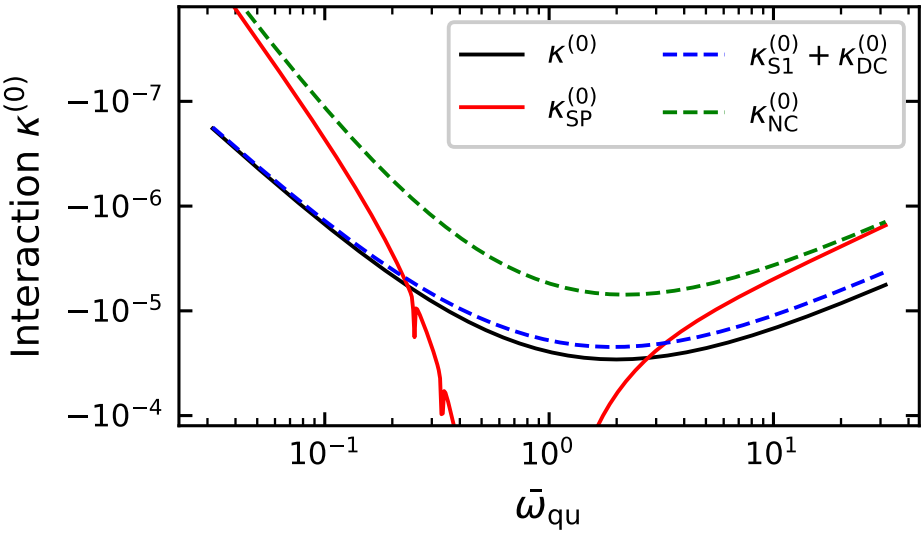

Figure 5.4: Different contributions (dashed) to the total interaction $\kappa^{(0)}$ (black) in the ground state of the quantum field. For $\omega_{\mathrm{qu}} \gg U$, the spin-photon based interaction $\kappa^{(0)}_{\mathrm{SP}}$ (red) converges to $\kappa^{(0)}_{\mathrm{NC}} = \kappa^{(0)}/4$. Figure reprinted from [P2] Copyright 2024 American Physical Society.

where H_{eff} is the effective Hamiltonian obtained from simultaneous elimination of charge (U) and cavity (c) excitations, while $H_{\mathrm{eff-SP}}$ is obtained from the spin-photon Hamiltonians, i.e., from the successive elimination of both degrees of freedom (Sec. 5.3.3). Here $S_{c,U}$, S_c, S_U are the generators of the unitary transformations and $P_0^{c,U}$, P_0^c, P_0^U the corresponding projectors to the target subspace. For the spin-photon approach, one first constructs the spin-photon Hamiltonian $H_{\mathrm{SP}} = P_0^U e^{S_U} H e^{-S_U} P_0^U$ in the doublon free subspace, and then eliminates the photons.

One deviation which can be directly read of from the definition is caused by the position of the projector P_0^U: The first unitary transformation (e^{S_U}) applied to H in equation (5.49) removes the leading-order coupling between the doublon free subspace and the rest of the Hilbert space. Subsequently projecting to the doublon free subspace removes the contribution of intermediate states with more than one double occupation. The projection to the doublon free subspace therefore cuts out all contributions of the DC-paths from the perturbation theory. Furthermore, since the interaction is only mediated by the photon number offdiagonal parts of H_{SP}, the contributions from the S1-paths (or rather the imbalance between the DC- and S1-path) are not captured either. This is easiest seen in equation (5.47), where the series expansion does not provide a contribution for $n = 0$.

To support this discussion, it is illustrative to individually compare the contributions $\kappa^{(\nu)}_{\mathrm{NC}}$ and $\kappa^{(\nu)}_{\mathrm{S1}} + \kappa^{(\nu)}_{\mathrm{DC}}$ [5] to the interaction $\kappa^{(\nu)}_{\mathrm{SP}}$ obtained from the spin-photon approach (see Figure 5.4). In the far-off resonant limit $\omega_{\mathrm{qu}} \gg U$ one finds that $\kappa^{(\nu)}_{\mathrm{SP}}$ approaches the contribution $\kappa^{(\nu)}_{\mathrm{NC}}$. This not surprising, because the NC-paths have the same structure as that imposed by the spin-photon approach. Moreover, in this limit the NC-paths contribute precisely 1/4 of the interaction. It is illustrating to confirm these observations from the analytical expressions to

[5] As argued earlier, $\kappa^{(\nu)}_{\mathrm{S1}}$ and $\kappa^{(\nu)}_{\mathrm{DC}}$ individually describing a mediated interaction is an artifact of Schrieffer-Wolff transformation not being a linked cluster expansion. We therefore only consider them combined.

leading order in g_{qu}: Expanding equations (5.36)-(5.38) (with (5.39)-(5.41)) in the light-matter coupling g_{qu} (see Appendix F.2), we find

$$\kappa^{(0)} = -2g_{\mathrm{qu}}^4 \frac{\bar{\omega}_{\mathrm{qu}}^2}{(1+\bar{\omega}_{\mathrm{qu}})^3} + \mathcal{O}(g_{\mathrm{qu}}^6)\,, \tag{5.50}$$

$$\kappa_{\mathrm{NC}}^{(0)} = -2g_{\mathrm{qu}}^4 \frac{\bar{\omega}_{\mathrm{qu}}^3}{(1+\bar{\omega}_{\mathrm{qu}})^2(1+2\bar{\omega}_{\mathrm{qu}})^2} + \mathcal{O}(g_{\mathrm{qu}}^6)\,, \tag{5.51}$$

while the spin-photon approach gives

$$\kappa_{\mathrm{SP}}^{(0)} = -2\frac{|\langle 0|\,\mathcal{J}_2\,|0\rangle|^2}{\bar{\omega}_{\mathrm{qu}}} + \mathcal{O}(g_{\mathrm{qu}}^6)\,, \tag{5.52}$$

with $\mathcal{J}_2$ given by equation (5.20). For $\bar{\omega}_{\mathrm{qu}} \gg 1$, one can now see that $\kappa_{\mathrm{SP}}^{(0)} = \kappa_{\mathrm{NC}}^{(0)} = \kappa^{(0)}/4$.

The divergences of κ_{SP} at the resonances between the cavity frequency ω_{qu} and the onsite interaction U have a different origin. Since the first elimination in the derivation of $H_{\mathrm{eff-SP}}$ is a multi-block orthogonalization scheme, where each cavity occupation number defines a block, it relies on proper energy gaps between all of these blocks in the unperturbed Hamiltonian. Close to resonance between charge and photon excitations, the condition $|n\omega_{\mathrm{qu}} - U| \gg t_0$ necessary for a convergent series expansion is no longer fulfilled for some integer n, which leads to artificial resonances in the spin-photon based perturbation theory at $\bar{\omega}_{\mathrm{qu}} = 1/n$. These therefore do not indicate any physical behavior, but only a breakdown of the expansion. Similar to the elimination of charge excitations in TiOCl, that we describe in Section 3.4, this breakdown does not effect all parts of the effective Hamiltonian equally. In particular, the second-order photon number diagonal contributions of the spin-photon Hamiltonian discussed in [93] in terms of the dressed magnetic exchange are unaffected by this breakdown, as long as the considered occupation number is not the one causing the breakdown. In contrast, the offdiagonal elements, that we need for the derivation of the mediated interaction, are not converged.

To leading order g_{qu}^4, we find these resonances at $\bar{\omega}_{\mathrm{qu}} = 1$ and $1/2$, where $\mathcal{J}_2$ (equation (5.20)) diverges. Higher orders produce additional divergences at higher ratios. The fourth-order approach, in contrast, is a two-block scheme. It therefore only requires the target sector to be sufficiently gapped to the rest of the Hilbert space, which is always fulfilled for $t_0 \ll \omega_{\mathrm{qu}}, U$.

The spin-photon approach is therefore expected to properly describe the interactions only if the result is dominated by the NC-paths and they themselves are properly contained. We find regimes where both holds in the driven setting, when the classical drive is near resonant to the cavity.

5.4.3 Driven cavity

In this section, we proceed to the discussion of the driven cavity. Probably the experimentally most relevant setting is a situation where the coupling to the quantum field is weak, and an external drive is used to boost and control the interaction. For example, the cavity field can correspond to surface plasmon mode, and a laser is used to "activate" the exchange of virtual plasmons, which then mediate the interaction (see also discussion in Section 5.5). We therefore restrict the discussion of the driven cavity to results which are leading order in the coupling g_{qu}, but of arbitrary order in the laser amplitude g_{cl}. Moreover, all results for the

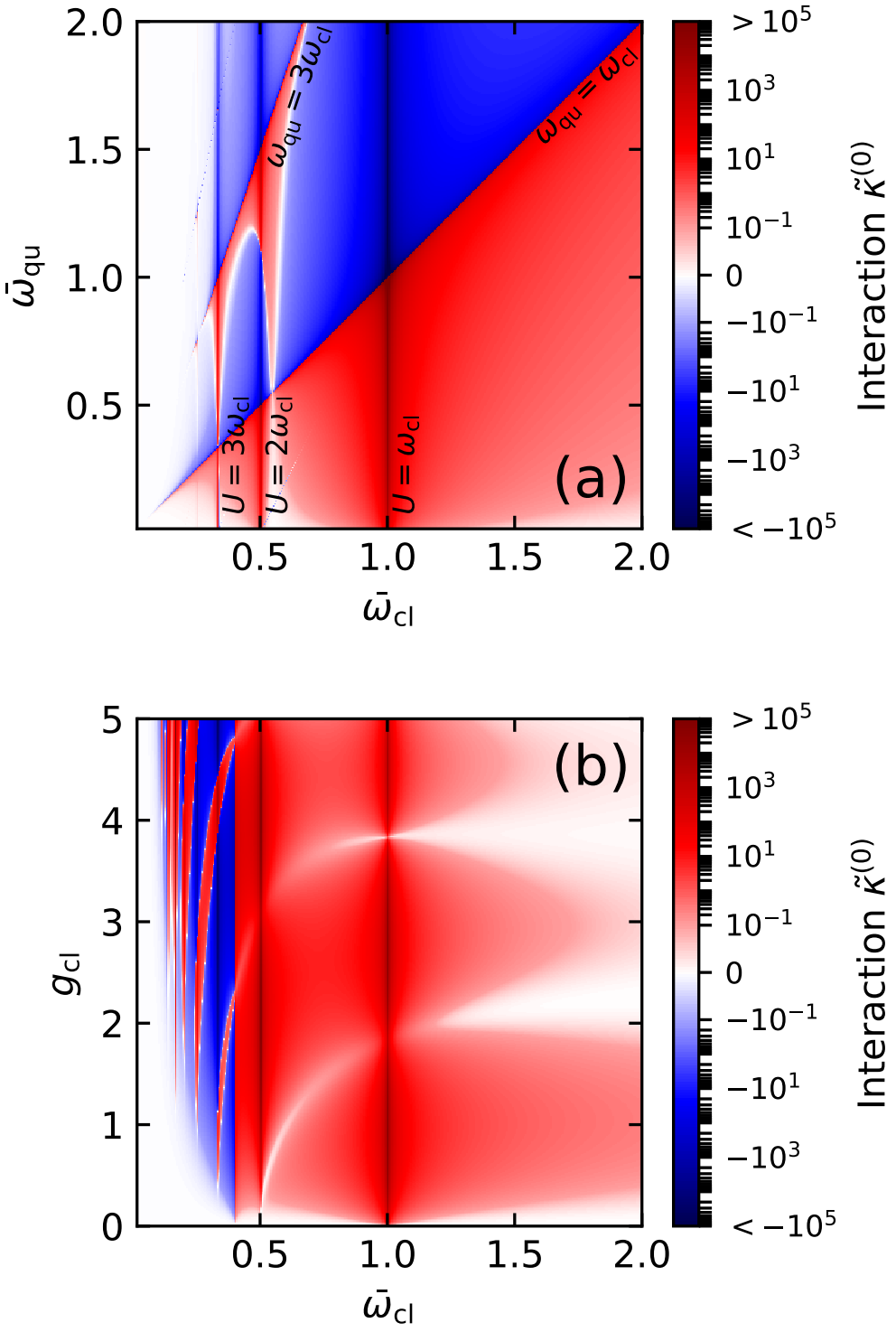

Figure 5.5: (a) Induced long-range interaction $\tilde{\kappa}$ (equation (5.53)) as function of the classical and the cavity frequency for $g_{cl} = 0.7$; (b) Interaction as function of the classical frequency ω_{cl} and driving strength g_{qu}, for $\bar{\omega}_{qu} = 0.4$. For both plots the logarithmic scale of the colomap is interrupted by a linear scale between -10^{-1} to 10^{-1}. Figure reprinted from [P2] Copyright 2024 American Physical Society.

driven case will be restricted to $\nu = 0$, and we therefore omit the index ν in the following. The interaction (5.24) is therefore written as

$$\kappa(\bar{\omega}_{\mathrm{qu}}, \bar{\omega}_{\mathrm{cl}}, g_{\mathrm{cl}}, g_{\mathrm{qu}}) \equiv g_{\mathrm{qu}}^2 \tilde{\kappa}(\bar{\omega}_{\mathrm{qu}}, \bar{\omega}_{\mathrm{cl}}, g_{\mathrm{cl}}) + \mathcal{O}(g_{\mathrm{qu}}^4)\,, \tag{5.53}$$

and we will analyze the result $\tilde{\kappa}$, and the corresponding expression $\tilde{\kappa}_{\mathrm{SP}}$ from the spin-photon approach.

Figure 5.5(a) shows the interaction $\tilde{\kappa}$ for fixed driving strength g_{cl} as function of ω_{qu} and ω_{cl}. As before, the data are obtained with the full fourth-order approach and benchmarked against exact diagonalization. From the color plot, we can see that it is possible to enhance the long-range interactions using two different types of near-resonant driving: One option is driving the Mott gap resonantly, taking

$$|\bar{\Delta}_U| \equiv |\bar{\omega}_{\mathrm{cl}} - 1| \ll 1\,. \tag{5.54}$$

This amounts to the vertical strip around $\bar{\omega}_{\mathrm{cl}} = 1$ in the figure, where the interaction diverges evenly as $\bar{\Delta}_U^{-2}$. Alternatively, we can resonantly drive the quantum field as $|\omega_{\mathrm{qu}} - \omega_{\mathrm{cl}}| \ll t_0$, i.e.,

$$|\bar{\Delta}_{\mathrm{qu}}| \equiv |\bar{\omega}_{\mathrm{qu}} - \bar{\omega}_{\mathrm{cl}}| \ll 1\,. \tag{5.55}$$

This amounts to the diagonal line $\bar{\omega}_{\mathrm{qu}} = \bar{\omega}_{\mathrm{cl}}$ in the color plot, where we find an odd divergence of the interaction scaling as $\bar{\Delta}_{\mathrm{qu}}^{-1}$. At sufficiently large driving strengths g_{cl}, there are also singularities at the multi-photon resonances, such as $n\omega_{\mathrm{cl}} = U$, or $n\omega_{\mathrm{cl}} = \omega_{\mathrm{qu}}$.[6] Figure 5.5(b) shows the dependence of the interaction on the driving strength g_{cl}. One observes a rich behavior with many zeros and sign changes. These are associated with the zeros of the Bessel functions in the Floquet Hubbard model (5.14), corresponding to dynamical localization of the electrons.

To assess the validity of the spin-photon approach, we compare the interactions $\tilde{\kappa}$ and $\tilde{\kappa}_{\mathrm{SP}}$ along a cut of constant $\bar{\omega}_{\mathrm{qu}}$ in Figure 5.5(a) shown in Figure 5.6. One finds that the leading resonance at $\omega_{\mathrm{qu}} = \omega_{\mathrm{cl}}$ is captured by both approaches (dashed line), while away from this resonance the two approaches deviate. The spin-photon approach again features additional divergences, and it has an opposite sign in some regimes.

The fact that the leading resonance in $\bar{\Delta}_{\mathrm{qu}}$ is captured by the spin-photon approach can be explained as follows: For $\bar{\Delta}_{\mathrm{qu}} \ll 1$ the interaction is dominated by an intermediate state without electronic excitations, but only the exchange of a photon from the drive to the cavity. This corresponds to an exchange path such as shown in Figure 5.7, in which the processes on the two dimers, i.e., Raman-type processes leading to a spin flip upon exchange of a photon between laser and cavity, can be understood as successive. This successive picture is precisely contained in the spin-photon approach.

Mathematically we can also explicitly show this within our series expansion by expanding the long-range interaction in the detuning $\bar{\Delta}_{\mathrm{qu}}$ [7]. We find that the leading contribution $\propto 1/\Delta_{\mathrm{qu}}$ from the NC-paths and the driven spin-photon Hamiltonian agree (see Appendix H, equation H.7). In this region the interaction is therefore properly captured and the phenomenological ansatz valid.

[6] Similar resonance appear in the lower right half for $\omega_{\mathrm{cl}} = n\omega_{\mathrm{qu}}$, if we go beyond second order in g_{qu}.

[7] Since the interaction diverges at this resonance, the leading order will be $\bar{\Delta}_{\mathrm{qu}}^{-1}$.

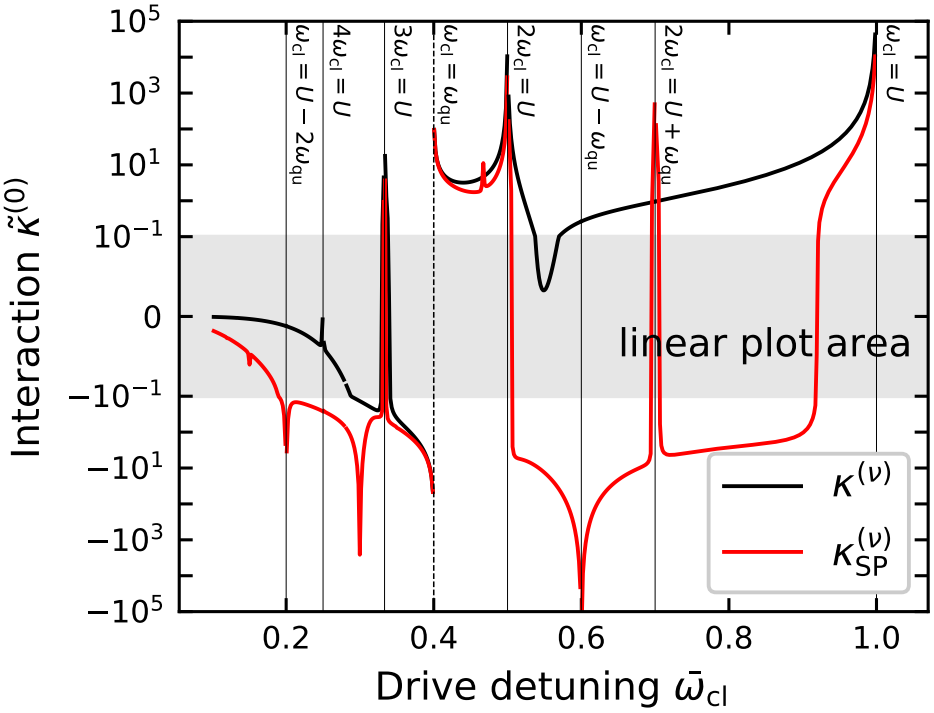

Figure 5.6: Horizontal cross-section of the data in Figure 5.5(a) at $\bar{\omega}_{\mathrm{qu}} = 0.4$, compared to the interaction $\tilde{\kappa}_{\mathrm{SP}}$ obtained from the spin-photon-Floquet Hamiltonian; As with the undriven case, the spin-photon based approach has additional resonances, but matches the proper approach at $\bar{\Delta}_{\mathrm{qu}} \ll 1$ (dashed line). In the grey-shaded area, the scale of the plot is again linear. Figure reprinted from [P2] Copyright 2024 American Physical Society.

If we instead choose $\bar{\Delta}_U$ small, i.e., near resonant driving of charge excitations, the scalings of the three paths become $H_{S1} \propto \Delta_U^{-3}$, $H_{NC} \propto \Delta_U^{-2}$ and $H_{DC} \propto \Delta_U^{-3}$, such that the resonant S1/DC-paths dominate and the leading order is not correctly captured by the spin-photon approach.

5.5 Discussion for realistic parameters

5.5.1 Single mode cavity setting

In this section, we illustrate the previous results for a realistic set of parameters. For the matter we assume a lattice constant $d = 1\,\mathrm{nm}$, Hubbard interaction $U = 0.8\,\mathrm{eV}$, and hopping $t_0 = 50\,\mathrm{meV}$. These parameters are close to the ones of the organic Mott insulator ET-F_2TCNQ [226, 227], but can be taken in general as representative for a good Mott insulator with a small ratio t_0/U.

Note that ET-F_2TCNQ should be modeled as an extended Hubbard model with a nearest-neighbor interaction $V \sum_{\langle i,j\rangle,\sigma\sigma'} n_{i\sigma} n_{j\sigma'}$. Including this term in our unperturbed Hamiltonian H_0 of the series expansion does not introduce any new types of processes. In fact, the only the intermediate energy of the virtual charge excitation is modified. Since our derivation only contained charge excitations, where the double occupation and hole are neighboring, this change is fully accounted for by using an effective screened onsite interaction $U_{\mathrm{eff}} = U - V$. In this particular system both t_0 and V can furthermore be tuned by applying static pressure over some range [227].

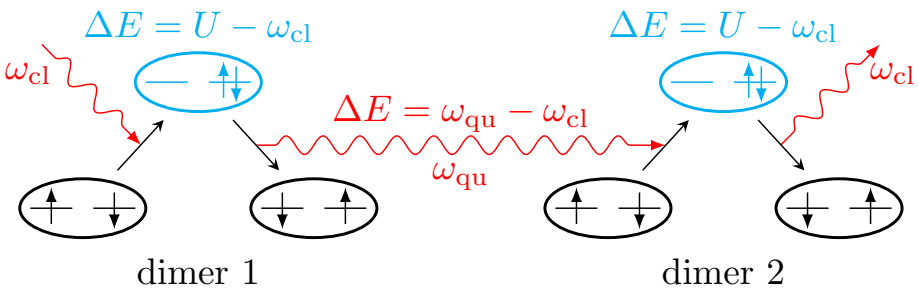

Figure 5.7: Contribution to the resonant enhancement of the interaction at $\bar{\Delta}_{\mathrm{qu}} \ll 1$, with two successive two-step processes: (i) A Raman process on dimer 1: The system absorbs a photon from the classical drive during the first hopping on dimer 1, leading to an intermediate virtual state with energy $U - \omega_{\mathrm{cl}}$, followed by a decay of the charge excitation under the emission of a cavity photon. (ii) The reverse Raman process on dimer 2. The intermediate state energy between (i) and (ii) is $\Delta_{\mathrm{qu}} = \omega_{\mathrm{qu}} - \omega_{\mathrm{cl}}$. Note that if the laser drive is not resonant to U, also paths contribute to the leading order $1/\bar{\Delta}_{\mathrm{qu}}$, where the sequence of processes *within* the same dimer is reversed (such as cavity photon emission before the laser photon absorption), but nevertheless the spin flips on the two dimers are successive. Figure reprinted from [P2] Copyright 2024 American Physical Society.

The material TiOCl we discussed in Chapters 3, 4 could serve as exemplary system as well having $t_0 \approx 300\,\mathrm{meV}$ to $350\,\mathrm{meV}$ for the lowest orbital and $U \approx 2.5\,\mathrm{eV}$. Driving this system at higher frequencies will, however, most likely melt the low-temperature orbital order. Driving at low frequencies also leads to complications as there are multiple phonons, that are either infrared or Raman active [106, 175, 233]. In contrast for ET-F_2TCNQ there is comparatively little coupling between the electrons and phonons and no additional orbital transitions [227]. A description within the one-band Hubbard model is therefore still possible for this material in the driven case.

The cavity is modeled as a single mode resonator, where the electric field is confined in a mode volume L^3 with a homogeneous mode function. This can be taken as an ideal description of a split-ring resonator [223]. The assumption of a cubic volume and a homogeneous mode function is of course rather simplistic, but it gives the correct order of magnitude for the light-matter coupling. Realistic settings allow for resonance frequencies $f_{\mathrm{qu}} = \omega_{\mathrm{qu}}/2\pi$ in the THz regime, and a µm-sized cavity, which corresponds to a large compression of the mode volume (L^3) below the free space value $\lambda_{\mathrm{qu}}^3 = (c/f_{\mathrm{qu}})^3$.

We will exemplarily consider a cavity frequency $f_{\mathrm{q}} = \omega_{\mathrm{q}}/2\pi = 6\,\mathrm{THz}$. In this case $\hbar\omega_{\mathrm{qu}}$ is sufficiently small compared to the charge gap U ($\bar{\omega}_{\mathrm{qu}} \approx 0.0341$), such that electronic excitations due to (multi)-photon absorption are strongly suppressed for driving with an external laser at a frequency ω_{cl} close to ω_{qu}. For further illustration, we will also consider larger frequencies (such as $f_{\mathrm{q}} = \omega_{\mathrm{q}}/2\pi = 60\,\mathrm{THz}$, $\bar{\omega}_{\mathrm{qu}} \approx 0.341$) for which cavities may be more difficult to design, but which is still sufficiently detuned from the charge gap.

For a single mode with electric field confined in the volume L^3, standard quantization gives the vacuum field strength (see equation 2.143) $A_{\mathrm{qu}} = \sqrt{\hbar/(2\epsilon_0\omega_{\mathrm{qu}}L^3)}$. (We restore factors $\hbar$ in this section.) With the Peierls phase (5.8), the dimensionless coupling $g_{\mathrm{qu}} = A_0 dq/\hbar$ becomes

$$g_{\mathrm{qu}} = \sqrt{\frac{e^2d^2}{2\epsilon_0 L^3\hbar\omega_{\mathrm{qu}}}} \approx \frac{46.8}{\sqrt{f_{\mathrm{qu}}[\mathrm{THz}]}}\sqrt{\frac{d^3}{L^3}}\,. \tag{5.56}$$

For this setting, we will now compute the cavity-induced long-range interaction, and compare it to the other relevant scale, the short-range exchange J. For this, a few comments are in order:

(i) In the (driven) cavity, also the direct exchange J will be modified with respect to the free space value $J_0 = 2t_0^2/U$. However, because we are mainly interested in quantifying the strength of the induced long-range interactions, we compare the long-range interaction to the same scale (J_0) for all parameters.

(ii) The effect of the long-range interaction on the material depends, in addition to the strength of the interaction, on the geometry. For example, one can imagine a 2D geometry, where the direction of the cavity polarization implies that long-range interactions are induced only along one direction. An interaction $K < 0$ would therefore favor the bonds along that direction to be in a singlet state, in competition with the isotropic Heisenberg exchange. In this paper we focus on the strength of the induced interactions (and how to compute them), while the discussion of possible phase transitions due to such interactions is left for future work. We will therefore evaluate a relevant overall scale of the interaction, defined as follows:

(iii) For the single-mode cavity, the induced interaction is an all-to-all interaction. Hence, the short range exchange should not be compared to the interaction K between individual dimers, but to the mean-field interaction $K_{\mathrm{mf}} = NK$ of one given dimer with all (N) others[8]. For simplicity, we assume that the complete mode volume of the cavity is filled with the material, so that $N = (L/d)^3$, and analyze the ratio

$$\frac{K_{\mathrm{mf}}}{J_0} = \frac{8K_0}{J_0}\frac{L^3}{d^3}\kappa^{(\nu)}(g_{\mathrm{cl}}, g_{\mathrm{qu}}, \bar{\omega}_{\mathrm{cl}}, \bar{\omega}_{\mathrm{q}})\,, \tag{5.57}$$

where κ is computed as in the previous sections. For $K_{\mathrm{mf}}/J_0 \gtrsim 1$, one can expect the cavity-induced long-range interactions to become a relevant or even dominant correction to the short-range Heisenberg exchange.

5.5.2 Undriven cavity

Figure 5.8 shows the ratio K_{mf}/J_0 for the undriven cavity. One can see that a strong long-range interaction can be reached only for relatively small cavities, while the effect of the interaction vanishes for large L. This can be understood as follows: For large L, the coupling decreases with increasing mode volume like $g_{\mathrm{qu}} \sim L^{-3/2}$, and the induced interaction can therefore eventually be approximated by the leading order in g_{qu}, i.e., $K \sim g_{\mathrm{qu}}^4 \sim L^{-6}$. In the thermodynamic limit (being defined as $L \to \infty$, $g_{\mathrm{qu}} \sim L^{-3/2}$, and $N \sim L^3$), interactions which are induced by the vacuum fluctuations of a single mode therefore scale like $K_{\mathrm{mf}} = KN \sim L^{-3}$ and become irrelevant. The scaling should hold similarly for other interactions which are induced by nonlinear processes. This finding is in line with general arguments which imply that the change of the energy of an extended material ($\sim N$ atoms) due to the coupling to a *single* cavity mode is $\mathcal{O}(N^0)$ (sub-extensive) in the thermodynamic limit, and therefore irrelevant for the static properties of the material [234–236].

[8] A computation of resulting phase diagrams would have to replace the factor N by the self-consistently determined singlet expectation value $\sum_{\langle i,j\rangle}\left\langle P_{ij}^S\right\rangle$.

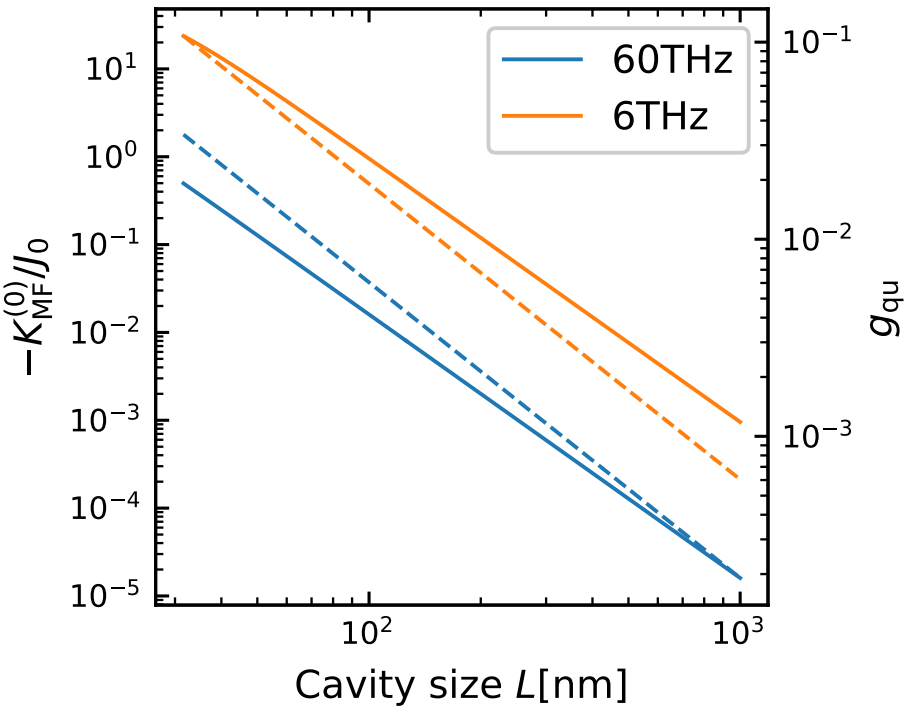

Figure 5.8: Ratio K_{mf}/J_0 (solid curves, left axis) for the empty cavity, where the size of the cavity is changed in order to control the light-matter coupling g_{qu} (dashed curves, right axis). Parameters are $U = 0.8\,\mathrm{eV}$, $t_0 = 50\,\mathrm{meV}$, $d = 1\,\mathrm{nm}$, and cavity frequencies $f_{\mathrm{qu}} = 6\,\mathrm{THz}$ ($\bar{\omega}_{\mathrm{qu}} \approx 0.0341$) and $f_{\mathrm{qu}} = 60\,\mathrm{THz}$ ($\bar{\omega}_{\mathrm{qu}} \approx 0.341$) as indicated. Figure reprinted from [P2] Copyright 2024 American Physical Society.

On the other hand, the quantitative analysis in Figure 5.8 shows that a ratio of $K_{\mathrm{mf}} \approx J_0$, where the long-range interactions become comparable or even dominant over the short-range interactions, can be obtained already for cavities which are still large enough to host a quasi macroscopic number of atoms (e.g., for $f_{\mathrm{qu}} = 6\,\mathrm{THz}$, $K_{\mathrm{mf}}/J_0 \approx 1$ for $L \approx 100\,\mathrm{nm}$, corresponding to $N \sim 10^6$ unit cells). Hence, collective many-body effects due to vacuum-induced long-range interactions may indeed be accessible under realistic conditions. At the same time, one should note that in this parameter regime the single particle coupling g_{qu} is still considerably smaller than one. Because the cavity effect on the short-range Heisenberg exchange interactions is directly controlled by g_{qu} without an additional factor N (see, e.g., equation (5.19)), long-range interactions constitute the main effect of the cavity on the material in this regime. For even smaller cavities, long-range interactions dominate over the short-range Heisenberg exchange (until the system is too small to be considered as macroscopic, such as in a nano-plasmonic cavity). This shows that in general long-range interactions should be kept in mind whenever single-mode cavity settings are proposed to engineer spin or other type of exchange interactions [93, 199, 200, 220].

As a side remark, note that the vanishing of the interaction in the thermodynamic limit naturally implies the absence of any phase transition induced by the empty single-mode cavity, at least in the strict mathematical sense. In particular, this applies to a hypothetical phase transition where due to the induced long-range interaction a macroscopic number of dimers would "condense". This condensation would induce a macroscopic squeezing of the cavity mode ($\langle a^2 \rangle \sim N$, $\langle a \rangle = 0$), in analogy to the equilibrium superradiant phase with $\langle a \rangle \sim N$ [202, 203, 237]. The superradiant phase is absent for the single mode case when linear terms $\propto A$ and quadratic (diamagnetic) terms $\propto A^2$ of the light matter interaction are treated consistently [238, 239], and a similar argument should hold for the hypothetical macroscopic

squeezing transition with respect to the nonlinear light-matter interactions contained in the Peierls phase.

5.5.3 Driven cavity

We now proceed to the driven case. As explained in Section 5.4.3, a near-resonant laser drive $\omega_{\mathrm{cl}} \approx \omega_{\mathrm{q}}$ is favorable condition to enhance the interaction without heating the material. Because real cavities in condensed matter setting usually have relatively low quality factors Q (such as a $Q \approx 10$ [223, 224]), the detuning should not be chosen too small, as otherwise the drive would occupy the cavity and the number states no longer be a suitable basis. We therefore analyze a laser frequency with $\pm 10\%$ detuning, e.g., $f_{\mathrm{cl}} = 0.9 \cdot \omega_{\mathrm{qu}}/2\pi = 5.4\,\mathrm{THz}$ for the red detuned case with respect to $f_{\mathrm{qu}} = 6\,\mathrm{THz}$. The laser coupling strength is $g_{\mathrm{cl}} = deE_0/(\hbar\omega_{\mathrm{cl}})$, with the electric field amplitude E_0. For $d = 1\,\mathrm{nm}$, g_{cl} can be written as

$$g_{\mathrm{cl}} \approx 242\,\frac{E_0[\mathrm{V\,nm^{-1}}]}{f_{\mathrm{cl}}[\mathrm{THz}]}\,. \tag{5.58}$$

Hence, non-perturbative couplings $g_{\mathrm{cl}} \gtrsim 1$ can be reached with field strength of the order $0.1\,\mathrm{V\,nm^{-1}}$. This should be experimentally accessible, in particular taking into account near-field enhancement effects.

Although the formalism provided in the main text also applies when both g_{cl} and g_{qu} are strong, the driven case is most interesting in the regime where the interaction induced by vacuum fluctuations is weak. This is the case for large L, where the vacuum-induced interaction scales like $K_{\mathrm{mf}} \sim N g_{\mathrm{qu}}^4 \sim L^{-3}$. In contrast, in the driven case the interaction between individual dimers scales like $g_{\mathrm{qu}}^2 \sim L^{-3}$ (see equation (5.53)), so that $K_{\mathrm{mf}} \sim L^3 g_{\mathrm{qu}}^2$ remains finite in the thermodynamic limit. In Figure 5.9 we therefore show the large L limit of the induced interaction, $K_{\mathrm{mf}}/J_0 = K_0/J_0(N g_{\mathrm{qu}}^2)\tilde{\kappa}(\bar{\omega}_{\mathrm{qu}}, \bar{\omega}_{\mathrm{cl}}, g_{\mathrm{cl}})$, where the factor $N g_{\mathrm{qu}}^2 \approx (46.8)^2/f_{\mathrm{qu}}[\mathrm{THz}]$ is independent of L (equation (5.56)).

Figure 5.9 shows the interaction ratio as a function of the laser driving g_{cl} (or E_0), for several values of f_{qu}, and fixed detunings $f_{\mathrm{cl}} = (1 \pm 0.1) f_{\mathrm{qu}}$. One finds that with sufficiently large drivings, interactions ratios K_{mf}/J_0 of order 1 can be induced, even for drivings which are sufficiently off-resonant for low Q factors. At the same time, the comparison with the result obtained from the spin-photon Hamiltonian (dashed line) can deviate qualitatively from the full prediction. This clearly shows that in general, to discuss laser-induced long-range spin interactions in solids, a correct treatment of the off-resonant terms, as done by the full fourth-order theory provided in this work, is necessary. This should hold similarly for other interactions which are induced by nonlinear processes.

5.6 Conclusion and outlook

In this chapter we have investigated cavity-mediated long-range interactions within a Mott insulator, as described by the Hubbard model. These interactions correspond to correlated spin-flips at distant sites, and originate from the nonlinear interplay between spins and photons, such as Raman scattering and multi-photon absorption/emission. We have explored these interactions in two scenarios: (i) In the undriven cavity, where interactions emerge through the exchange of virtual photons, and (ii), in a laser-driven cavity, which opens the potential for Floquet engineering of long-range interactions.

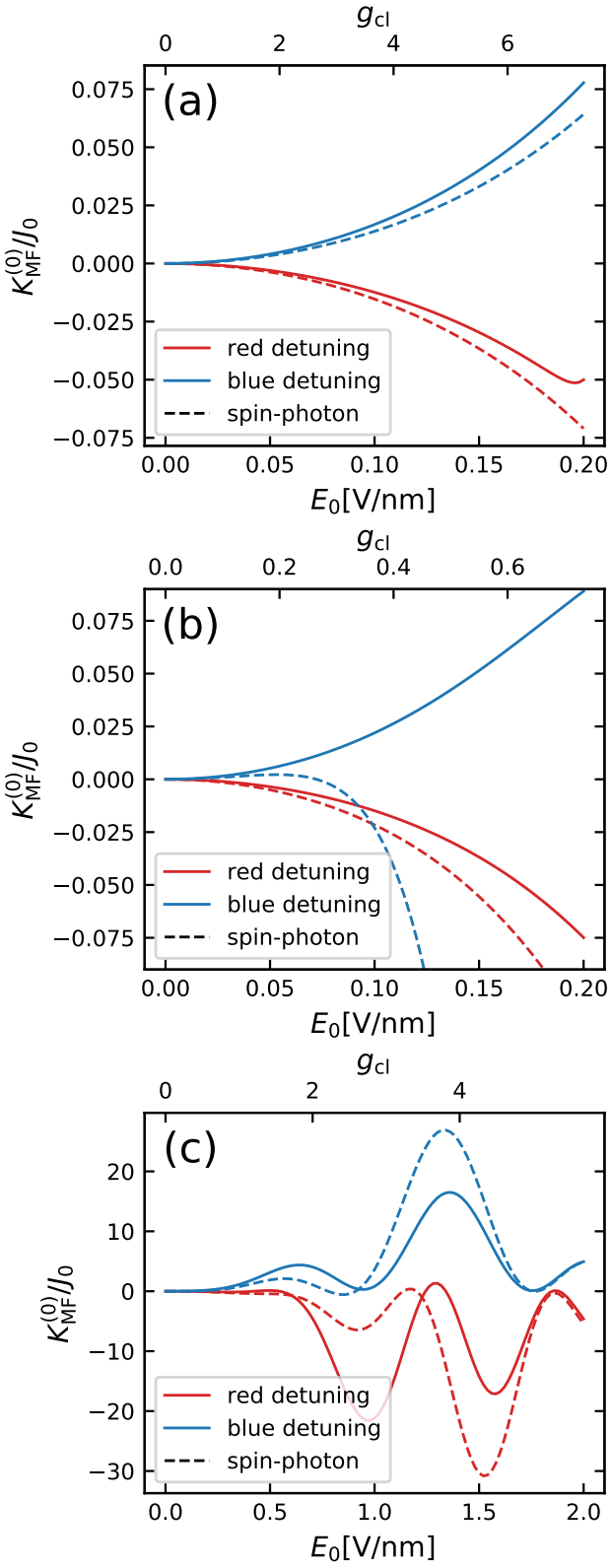

Figure 5.9: Ratio K_{mf}/J_0 for the driven cavity in the large L limit where red and blue detuning denote a relative detuning $\mp 10\%$ of the driving frequency with respect to the cavity frequency. The three cases displayed are (a) $f_{qu} = 6\,\text{THz}$, (b) $f_{qu} = 60\,\text{THz}$, (c) $f_{qu} = 77.4\,\text{THz}$. The latter amounts to the parameters of Fig. 5.5(b) and can be understood as vertical cuts left and right of the resonance $\omega_{cl} = \omega_{qu}$. In all plots, the solid lines indicate the interaction as obtained by the fourth-order approach, the dashed lines are obtained by the spin-photon approach. Figure reprinted from [P2] Copyright 2024 American Physical Society.

In the derivation of these long-range interactions, a simple approach would be to start from an effective Hamiltonian which describes the nonlinear interaction of photons and spins. At first sight, this "spin-photon" approach seems intuitive. Vacuum mediated interactions would e.g. be obtained to second order in the effective light-matter interaction, with virtual two-photon emission and absorption at two different lattice sites. Moreover, it would allow for a simple phenomenological determination of the relevant matrix parameters by optical measurements in free space (such as Raman scattering). However, we show that the spin-photon approach has its limitations. It can be used only within narrow parameter regimes, particularly when the laser is in close resonance with the cavity resonance. In typical condensed matter systems, these resonance conditions may not be easy to meet, e.g., when cavities of low Q factor are used and when the material itself has broad absorption bands. Moreover, the spin-photon approach gives a qualitatively wrong prediction of the vacuum-mediated interactions. Instead, we have provided a comprehensive derivation of the interactions, starting from the underlying electronic model (a Hubbard model), using a fourth-order perturbation theory in the parameter t_0/U.

We have evaluated these interactions for a single mode resonator, such as a split-ring cavity. While one can see that in this case the effect of long-range interactions eventually becomes negligible in the thermodynamic limit (because the light-matter coupling decreases like $\sim 1/\sqrt{V}$ with the mode volume), one finds that the light-induced interactions can remain highly relevant and even dominate over the short-range Heisenberg interactions up to cavity sizes which still host an almost macroscopic ensemble of atoms. This motivates future studies of the nonlinear response of correlated electron systems in mesoscopic settings such as small split-ring resonators.

This work can naturally be extended in several directions:
(i) The long-range interactions are rather unconventional, as they do not correspond to long-range Heisenberg interactions, but to correlated spin flips at distant sites (i.e., four-spin processes). It will be interesting to study whether these interactions can lead to exotic magnetic orders by competing with the short range Heisenberg interactions. The long-range (all-to-all) property of the interaction necessitates techniques, that are capable of treating them properly, such as self-consistent mean-field theories, quantum Monte-Carlo approaches [240, 241] or high-order series expansions with Monte-Carlo embedding [241, 242]. While a direct probe of the magnetic structure using neutron or X-ray scattering may be difficult (depending on the cavity geometry), a sufficiently strong change of the magnetic order can be probed by standard thermodynamic or transport probes, which are still available in a cavity. Moreover, optical measurements can be done in a frequency window where the cavity is transparent [224]. Another, more exotic possibility, is to use nonlinear optical measurements to probe the nonclassical nature of the light resulting from a strong light matter hybridization.
(ii) The analysis is not limited to spin systems but can encompass all degrees of freedom that nonlinearly couple to light. Systems with orbital order, which often show frustration of the short-range interaction, represent an interesting material class in this regards.
(iii) Thusfar the role of dissipation has been completely neglected in our description. The broadening of excitations should already be possible to capture through extending the series expansion to a non-Hermitian unperturbed Hamiltonian H_0 [243]. It is, however, a priori unclear whether or not general open dynamics can lead to additional effects such as, e.g., the emergence of a spatial structure through retardation effects.
(iv) The derivation can straightforwardly be extended to the multi-mode case, where a single cavity mode is replaced by a continuum of modes, such as coplanar waveguides, Fabry-Perot cavities, or surface plasmons [71, 200, 206, 208, 209, 244]. This is in particular relevant for

the laser-driven scheme: A photon can be scattered from the laser to the dispersive cavity mode and back into the laser, and thus mediate an interaction $K(\mathbf{r}, \mathbf{r}')$ between scattering centers at sites $\mathbf{r}$ and $\mathbf{r}'$, where the dependence on distance $\mathbf{r} - \mathbf{r}'$ is set by the dispersion of the cavity mode, and the limit $c \to \infty$ recovers the all-to-all case. As long as the interaction to the quantum mode is treated to leading order in the coupling (see equation (5.53)), the results of our work should be generalizable by replacing g_{qu}^2 by the space dependent couplings $g_{\mathbf{q}}(\mathbf{r}) g_{\mathbf{q}}(\mathbf{r}')^*$ for a mode with wave vector $\mathbf{q}$, and then summing over all modes $\mathbf{q}$. In a recent work Svendsen et al. [245] suggested a resummation of a continuum of modes into a single effective mode for Fabry-Perot cavities. It would be particularly interesting to investigate weather or not this approach is valid for the computation of vacuum-mediated interactions or it is necessary to perform the resummation after the series expansion.

6 Conclusion and outlook

In this thesis we have investigated how the coupling between light and matter can be used to measure and manipulate the properties of correlated electrons. Chapter 2 served as introduction to concepts necessary for this, such as linear response theory or the dipolar representation of light-matter coupling.

In Chapter 3 we have computed the time-dependent optical conductivity of the spin-Peierls compound TiOCl following a pump resonant to one of its two optically active orbital excitations. We accomplished this by first deriving an ab-initio tight-binding Hamiltonian for this compound using density functional theory and a fit of the remaining free parameters to the magnetic properties via a series expansion. We evaluated the time-dependent optical conductivity on small clusters using an instantaneous phenomenological description of the pump in the crystal field basis. The time-dependent spectral function required an eigendecomposition for which we developed a spectral function based iterative eigendecomposition scheme. There were however two issues associated with this approach:
(i) the cluster sizes computationally achievable are too small to fully converge the spectra for a quantitative agreement between the experimentally measured and computed spectra. On a qualitative level we did, however, find spectral weight that lends credence to the notion, that the non-thermal redshift of the Mott-gap found in the experiment [67, P1] is sensitive to orbital occupancy.
(ii) the only type of time-evolution our approach can capture is unitary on the small cluster, whereas in the experiment a return to equilibrium is clearly visible.
There are two ways forward to improve the correspondence between the computed and measured spectra: Either an alternative experimental platform, that probes the dynamics more locally than optical spectroscopy, should be considered. Two possibilities for such experiments are x-ray absorption (XAS) on the titanium L-edge [100, 143] or resonant inelastic x-ray scattering (RIXS) [100] on the same edge. Both of these approaches have already been successfully employed in equilibrium, where cluster calculations gave a good fit. Or for a better correspondence of the theoretical description to the optical experiment larger clusters using more sophisticated cluster techniques [145–147] should be evaluated or lattice embedding techniques used. This could be accomplished either using a phenomenological master equation to include the leading order open dynamics or by using non-equilibrium dynamical mean-field theory. For the latter it may be too difficult to converge an explicit description of all relevant degrees of freedom, i.e., multiple bands for the pump, the magnetic degree of freedom and potentially even phonons for the proper open dynamics, within a cluster extension [94]. A prior analysis determining the minimal necessary degrees of freedom is therefore likely necessary. While we leave this analysis for future work for the case of phonons, orbital and charge degrees of freedom, in Chapter 4 we analyze the open dynamics of orbital excitations due to coupling between spin and orbital degrees of freedom.

We accomplished this analysis by evaluating Fermi's golden rule as spectral function on clusters large enough to facilitate the decay of orbital excitations into magnons and differing orbital excitation. The ratio between the crystal field gaps and the magnetic exchange therein determines the cluster size necessary for the corresponding decay spectral functions to converge. For most of them an 18 site cluster is sufficient. This is too large for an implementation within our tight-binding model but feasible for the effective spin-orbital Hamiltonian we derived in Chapter 3. Within this effective description we find orbital decay and orbital fission channels, which allows orbital excitations to decay into magnons and one or more additional orbital

excitations. There is furthermore an additional coupling between the magnetic exchange and present orbital excitations. The excitations of the system are therefore not of bare orbital character but hybrid orbital-magnetic-quasiparticles we call orbitons. These can be understood as an orbital excitation surrounded by a bound cloud of magnons. Since this cloud differs between orbitons, it can lead to additional free magnons during a decay process, which helps bridging the crystal field gaps. We compared the resulting decay widths quantitatively to the lifetimes obtained from the nonlinear signal in a double-pump-probe spectroscopy experiment. Within the uncertainties of our model and potential phonon-assistance of the decay, we found the lifetime of the orbital excitation at 0.7 eV to be sufficiently described as a decay into a lower lying orbiton at 0.4 eV and magnons. In contrast, for the 1.5 eV orbital excitation we did not find any decay channel within our model, that can sufficiently describe the even shorter lifetime. Building upon our work, there are therefore three ways forward:
(i) The unexplained short lifetime of the 1.5 eV excitation requires further theoretical and experimental investigation. One step towards this goal is obtaining a better understanding of the spectral response of the double-pump-probe spectroscopy. The footprints of the decay process are likely hidden in the shape of the nonlinear signal, but the lack of a theoretical sufficient understanding of the involved processes and dynamics makes them currently inaccessible. Improving our description of these through the techniques outlined in the previous paragraph may be able to uncover them. Furthermore, the x-ray measurements suggested in the previous paragraph (XAS and RIXS) may also be suited for this task due to their more direct orbital and magnetic sensitivities [100]. On the theoretical side the inclusion of phonons in our description is a promising next step. Making full use of the currently unused symmetries of the cluster should keep the combined spin-phonon-orbital Hilbert space still evaluable for large cluster sizes. The pumping process also requires further analysis. Optical d-d-transitions create orbital excitation without the proper magnon cloud (and potentially an additional phonon cloud) of the associated orbiton. As such an eigendecomposition similar to the one we performed for the non-equilibrium optical conductivity in Chapter 3 can produce the full ensemble of decaying orbiton-magnon states for which the lifetime should be evaluated.
(ii) Our claim, that our model can explain the lifetime of the 0.7 eV-orbiton, should be put to the test. This can again be accomplished by the aforementioned x-ray experiments, but there is also a possibility of confirming this within the optical setup: TiOBr is an isostructural compound with qualitatively similar dynamics. Applying the computational steps we did for the chloride to the bromide all the way from the ab-initio calculation to the decay spectral functions, we should therefore be able to predict quantitative differences in the corresponding bromide orbiton lifetime.
(iii) Lastly, for the 0.7 eV-orbital excitation our results allows setting up an effective open description. The magnon-orbiton coupling could e.g. be included as effective bath degree of freedom in a non-equilibrium dynamical mean-field theory [149] using our decay spectral functions to quantify the hybridization with this bath.

In the last part of this thesis, we investigated long-range cavity-mediated spin-interactions in the Mott-insulating cavity-coupled Hubbard model. These can be understood as a type of magnetic van-der-Waals interaction. A perturbative elimination of the charge excitations, which form the virtual intermediate polarized states, leads to magnetic interactions as the magnetic configuration influences the polarizability. We have shown that in order to compute these interactions it is not sufficient to quantify this polarizability in the form of an effective spin-photon description either theoretically by a second order series expansion [93] or experimentally through (hyper-) Raman-scattering [P2, 231]. Instead a fourth order series expansion within the underlying electronic tight-binding model is necessary. We have furthermore shown that an additional time-periodic optical drive describable within Floquet-theory can

be used to control the sign and amplitude of these mediated interactions through hybrid cavity-drive processes. Finally, we investigated the strength of these interactions for material realistic parameters, where we found that interactions mediated by an isolated cavity can collectively be relevant up to mesoscopic systems sizes while in the driven case they can collectively contribute even in the thermodynamic limit making this setting an interesting platform for the field of Floquet engineering. Building upon the work presented in this thesis, there are multiple ways forward: One way is to go to more elaborate descriptions of both the light and the matter. On the matter side our derivation can be generalized to other degrees of freedom indirectly coupled to the electromagnetic field. Consider e.g. orbitons, such as the ones discussed in Chapter 3 for TiOCl. They can also couple to the electromagnetic field via the Mott-gap allowing for long-range orbital interactions, that in certain systems may be able to influence equilibrium orbital order or non-equilibrium orbiton lifetimes. The most interesting generalization in terms of cavity material engineering is however a description of the quantized light in terms of a mode continuum. This not only applies to many more systems such as Fabry-Perot cavities, waveguides or plasmon modes, but also allows for the engineering of the spatial dependence of the mediated interaction through the modes dispersion. The opposite setting compared to the single-mode case we investigated in the main part resulting in all-to-all interaction is, e.g., obtained for a multimode degenerate cavity [246]. We are currently planing to explicitly consider plasmonic modes [206], since they are likely able to achieve the strong coupling case in a condensed matter setting [71, 194]. Within our current setting we have furthermore only shown, that long-range singlet-singlet interactions exist. The types of phases these can induce in extended systems is also an interesting subject for future research. There exist Monte-Carlo approaches capable of dealing with such long-range interactions [240–242], but to our knowledge none of these have yet considered the particular four-spin interactions we found. Lastly, the impact of dissipation on both the light and matter sides of our model should be considered. Dissipation in the optical mode combined with retardation effects can potentially introduce a spatial dependence to the interactions even in the single mode case. Dissipation can furthermore limit the resonant enhancement possible before finite linewidths cause heating of the cavity field or the coupled matter and is therefore very relevant for experimental implementations.

Summing up, our work has shown that light-matter coupling can induce and unveil intricate dynamics of correlated electron systems. We were able to treat these using exact diagonalization and series expansions. These have the advantage of usually being universally applicable. More specialized techniques tailored to this setting have the potential to push our understanding of these systems further. Our findings hopefully provide a good starting point for these studies on both the theoretical and experimental side.

Appendix

In accordance to the disclaimers in the beginning of Chapters 3, 5, 5 the Appendix also reproduces parts already reported in our publications [P1, P2]. Sections A and B reproduce the results of the currently unpublished work [P1] and is therefore in large parts identical in notation, terminology and phrasings. Sections C-H are adapted from [P2] with minor changes.

A More details on the implementation of the non equilibrium spectral function

In Chapter 3 we compute the time-dependent optical conductivity of optically pumped TiOCl. We accomplish this via an iterative eigendecomposition using the spectral function of the pumped state. We show these spectral functions for the iterative decomposition steps in Figure A.1 for the two-site cluster and Figure A.2 for the four-site cluster.

For the two-site cluster it is furthermore indicative to analyze the optical conductivity for all four differing clusters and magnetic state combinations. We show these in Figure A.3.

B Convergence of the spectral functions for the lifetime computation of orbitons in TiOCl

In order to check the convergence of the spectral functions computed on the finite clusters with a broadening $\Gamma = 5\,\mathrm{meV}$, we evaluate it for different cluster shapes and sizes. We are memory limited to 22 site clusters for the single orbiton sectors and 20 site clusters for the two orbiton sector.

For the 0.7 eV-orbiton we show the spectral functions for different cluster sizes in Figure B.1. The only decay channel with a significant deviation between clusters is the full decay into magnons only (see Figure B.1a). We can understand this in terms of the Hilbert space sizes. Since we first have to diagonalize the undecayed subspace, its single orbiton Hilbert space dictates the maximal cluster size due to memory limitation. For the intermediate decay (see Figure B.1b) and the orbital fission (see Figure B.1c) the decayed Hilbert space is just as large ($N \cdot 2^N$) or bigger ($N \cdot (N-1) \cdot 2^{N-1}$) than the undecayed Hilbert space ($N \cdot 2^N$) for a given cluster size with N sites. For the full decay it is much smaller (2^N), which leads to a slower convergence of the spectral functions. Due to the large orbital gap of 620 meV the spectral weight that we do find for the evaluable cluster sizes is far removed from $\omega = 0$. It is therefore not likely, that for larger cluster sizes, where the spectral function is fully converged, there is significant spectral weight at $\omega = 0$ and this decay channel influences the lifetime of the 0.7 eV-orbiton much.

The same situation repeats for the 1.5 eV-orbiton, since the orbiton free subspace again has the smallest Hilbert space for a given cluster size (see Figure B.2a). There are furthermore multiple outliers and systematic differences deserving a short discussion:

Multiple decay channels have significant matrix elements along the crystallographic a-direction, i.e., perpendicular to the one-dimensional Heisenberg chains (see Table 3). For chains or ladder-shaped clusters, these matrix elements are underrepresented, since we use open boundary conditions until a direction has at least three sites. This leads to a clear difference

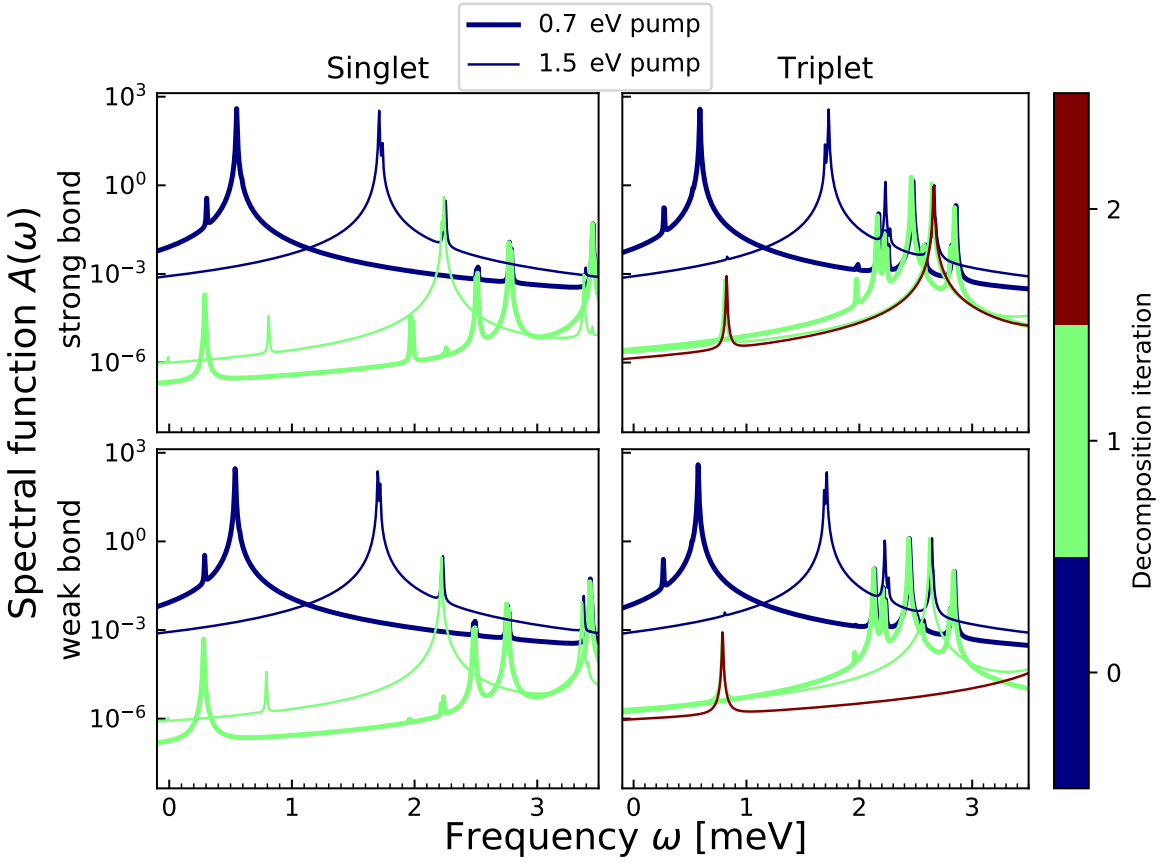

Figure A.1: Spectral function of the two site eigendecomposition through the iterative process; the spectral functions are the negative imaginary part of the projected pumped states propagator, such that their integrals correspond not yet decomposed remainder. The frequency denotes the detuning with respect to the ground state.

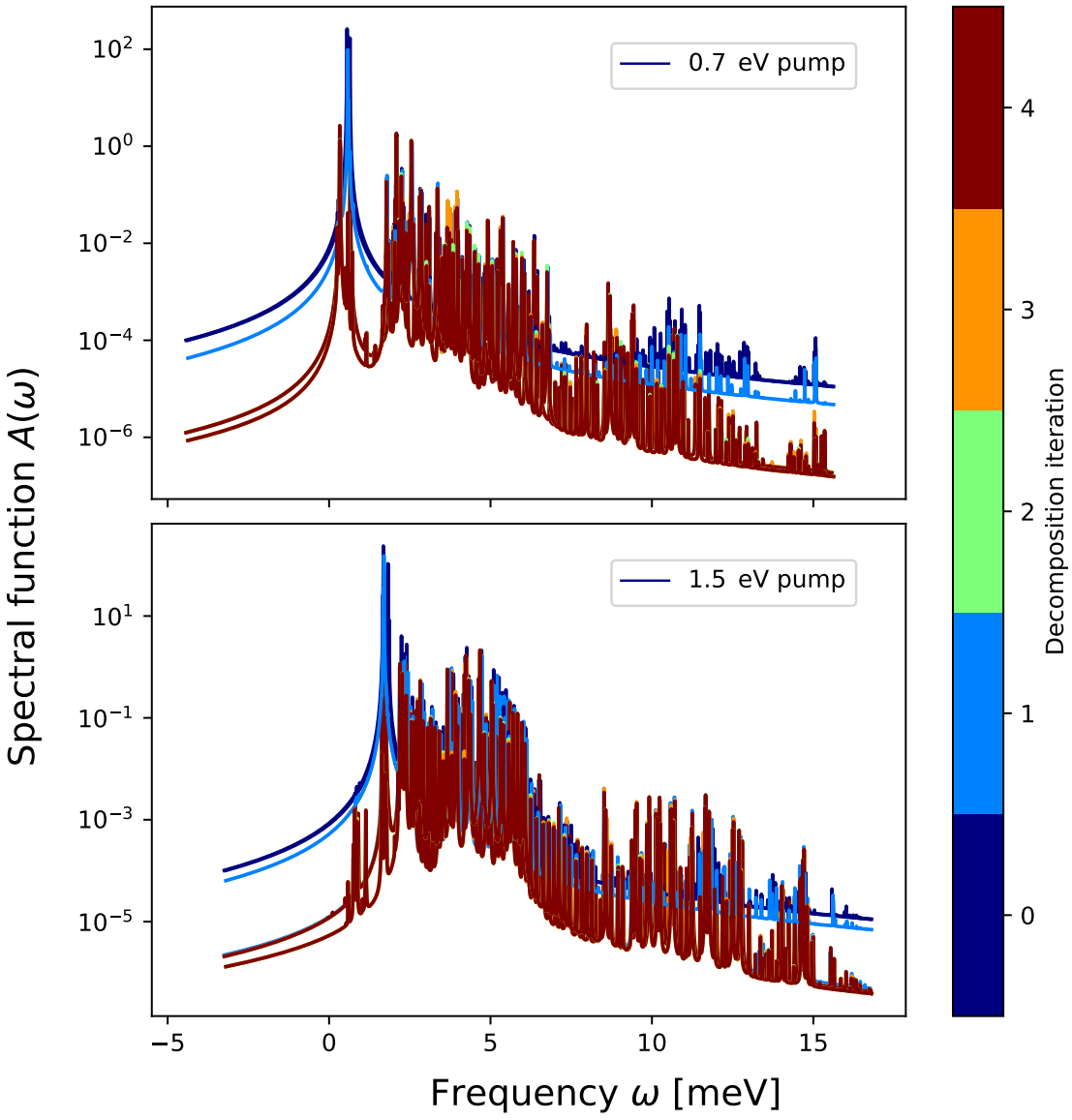

Figure A.2: Spectral function of the four site eigendecomposition through the iterative process; the spectral functions are the negative imaginary part of the projected pumped states propagator, such that their integrals correspond not yet decomposed remainder. The frequency denotes the detuning with respect to the ground state. Compared to Figure A.1, there are more eigenstates still not accounted for by the decomposition. Since the scale of the plot is logarithmic, these account for little combined weight.

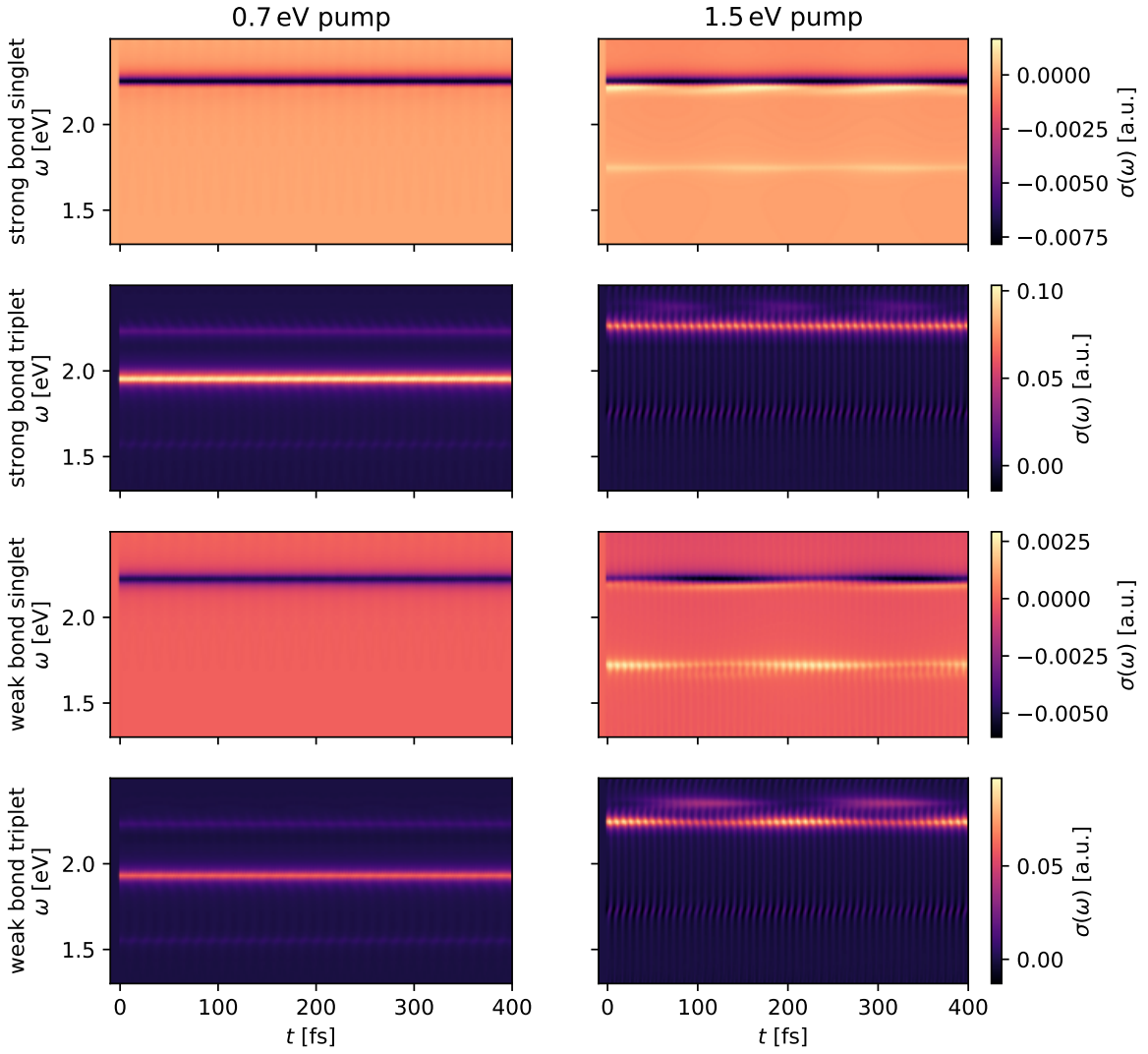

Figure A.3: Conductivity difference $\Delta\sigma(\omega, t)$ evaluated on the two site cluster. Figure 3.7a shows the four clusters combined into a single conductivity neglecting the dimerization of the lattice.

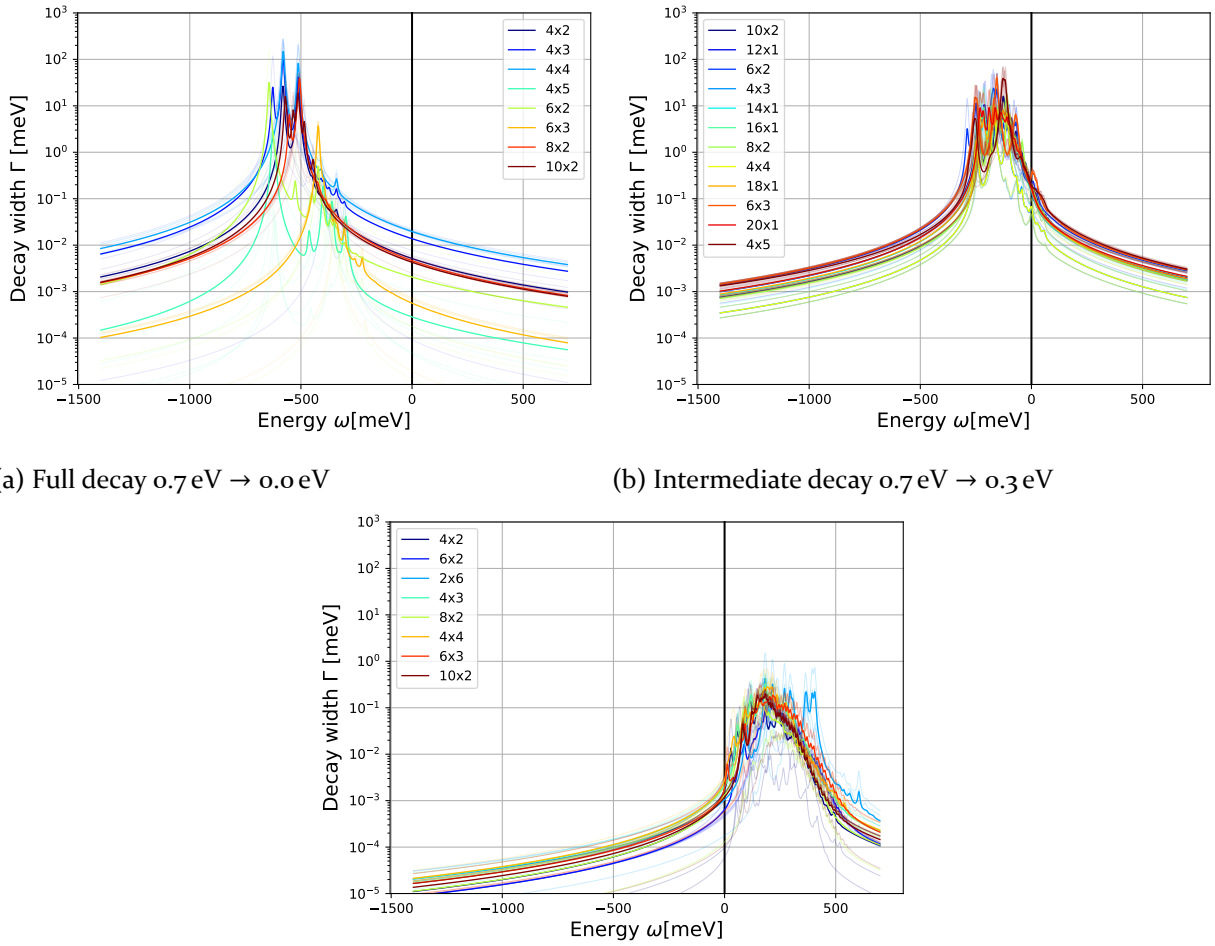

(a) Full decay 0.7 eV → 0.0 eV

(b) Intermediate decay 0.7 eV → 0.3 eV

(c) Fission 0.7 eV → 2 × 0.3 eV

Figure B.1: Spectral functions of the decay operator for the 0.7 eV-orbiton. The shaded lines are spectral functions for the five lowest eigenstates in the undecayed subspace and the thick lines their averages as indicated in the main text. For the full decay there is no decay matrix element on the one dimensional chain (see Table 2). We employ open boundary conditions along directions with one or two sites. For more sites we use periodic boundary conditions.

between these and the clusters with three or more sites in the a-direction for the intermediate decay channels (see Figure B.2b and Figure B.2c) and the 0.3 eV + 0.7 eV fission channel (see Figure B.2e).

It is however not helpful to increase the cluster dimensions too much perpendicular to the chains, since within all subspaces the Hamiltonian is dominated by the ground state Heisenberg exchange. The more bonds our cluster contains in the crystallographic b-direction, the better this exchange is captured. In Figure B.2c and Figure B.2f this is visible best visible for the 4×5 site cluster. Since the chains in the b-direction approximately factorize, five four-site chains are less well converged than fewer but longer chains. This leads to the spiky structure of the spectral function we see in those figures. The distinguishable two orbiton subspace is the most memory intensive to evaluate. For the 20×1 cluster the Hamiltonian and states barely fit within the 500 GB memory. The other 20 site clusters we want to evaluate have overall more bonds and therefore require more memory, since we keep the Hamiltonian as sparse matrix in memory.

Comparing all clusters for all decay channels among each other, the 6×3 cluster appears to be the best compromise between convergence of the spectra of the Heisenberg chains and enough sites in the a-direction to allow for periodic boundary conditions. The results we present in the main part of this thesis are therefore those of the 6×3 cluster. Making better use of symmetries or using more memory to push clusters to 24 sites would however be ideal, since it would allow for the 8×3 and 6×4 clusters. In some settings, it is furthermore beneficial to evaluate non-rectangular clusters [132, 163] for Lanczos techniques. This could additionally be checked.

C Explicit for of the spin-photon Hamiltonian

In Section 5.2.2 we refer to the effective spin-photon coupling derived by Sentef et al. [93] through a second-order time-dependent Schrieffer-Wolff transformation the cavity-coupled Hubbard model. For the sake of completeness we want to paraphrase the explicit form of the therein obtained Hamiltonian and its effective coupling:

$$H = J_{\text{ex}} \sum_{\langle i,j \rangle} \left(\vec{S}_i \vec{S}_j - \frac{1}{4} \right) \mathcal{J}[a^\dagger, a] + \omega_{\text{qu}} a^\dagger a \tag{C.1}$$

$$\mathcal{J}[a, a^\dagger] = \mathcal{J}_0[a^\dagger, a] + \sum_{m=1}^{\infty} \left(\left(a^\dagger\right)^{2m} \mathcal{J}_{2m}[a, a^\dagger] + \text{h.c.} \right) \tag{C.2}$$

$$\mathcal{J}_{2m}[a, a^\dagger] = \sum_{c=0}^{\infty} g_{\text{qu}}^{2c+2m} \left(a^\dagger\right)^c a^c \mathcal{L}_{c,m}(g_{\text{qu}}, \bar{\omega}) \tag{C.3}$$

$$\mathcal{L}_{c,m}(\bar{\omega}, g_{\text{qu}}) = \frac{1}{2(2c+2m)!c!} \sum_{p=0}^{2(c+m)} (-1)^p \binom{2(c+m)}{p} \cdot \left(L_{p-c}(\bar{\omega}, g_{\text{qu}}) + L_{p-c-2m}(\bar{\omega}, g_{\text{qu}}) \right) \tag{C.4}$$

$$L_p(\bar{\omega}, g_{\text{qu}}) = e^{-g_{\text{qu}}^2} \sum_{r=0}^{\infty} \frac{g_{\text{qu}}^{2r}}{r!} \frac{1}{1 + (r+p)\bar{\omega}} \tag{C.5}$$

with $J_{\text{ex}} = 4t_0^2/U$ and $\bar{\omega} = \omega_{\text{qu}}/U$.

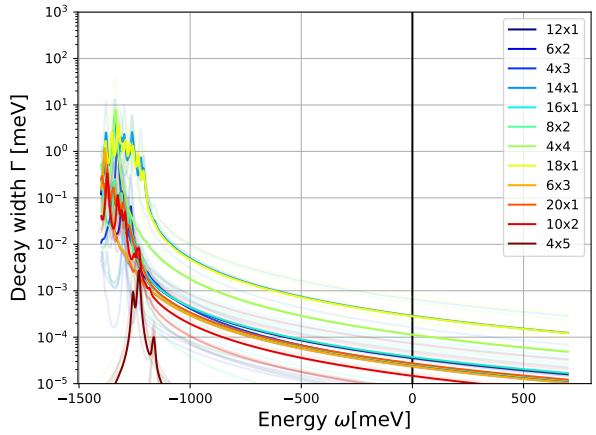

(a) Full decay 1.5 eV → 0.0 eV

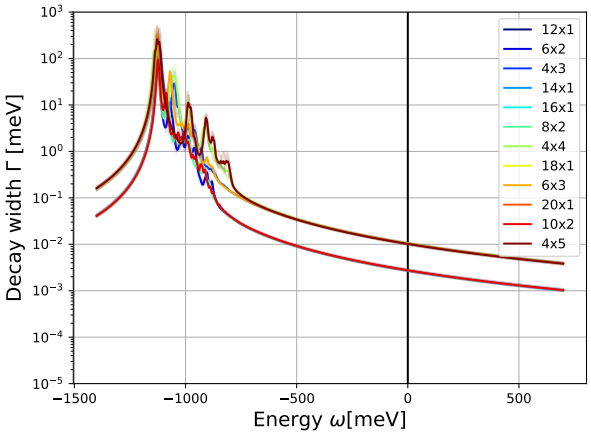

(b) Intermediate decay 1.5 eV → 0.3 eV

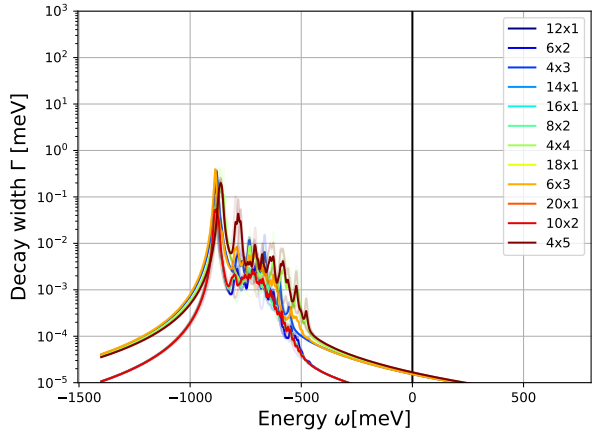

(c) Intermediate decay 1.5 eV → 0.7 eV

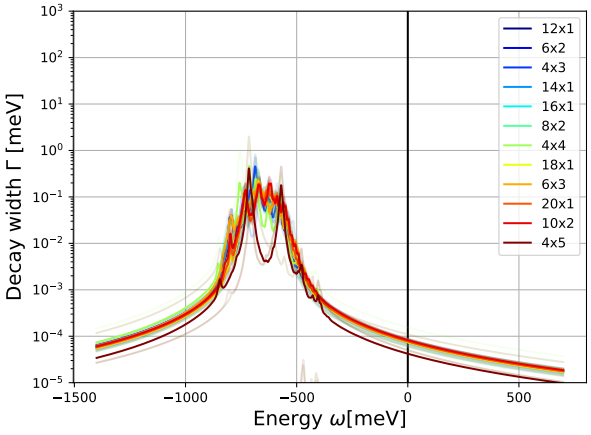

(d) Fission 1.5 eV → 2 × 0.3 eV

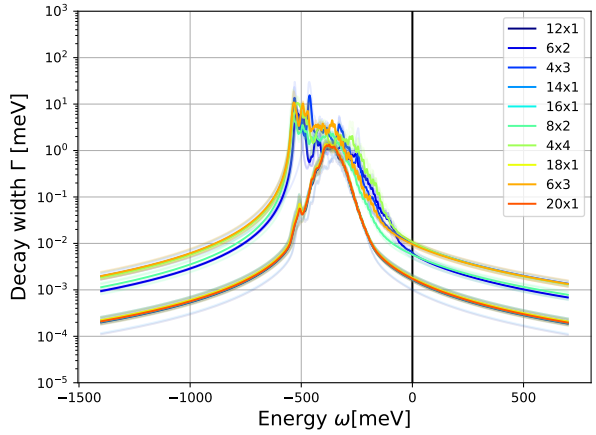

(e) Fission 1.5 eV → 0.3 eV + 0.7 eV

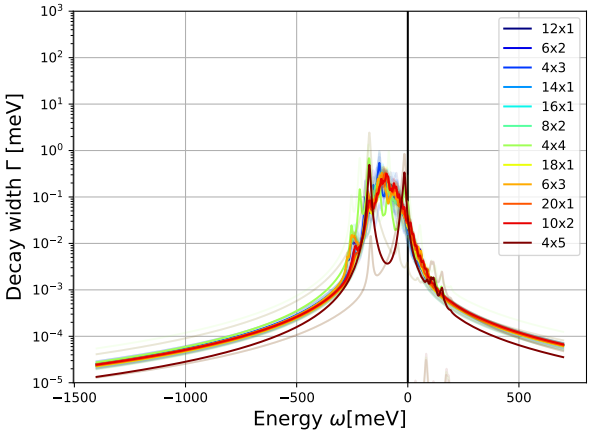

(f) Fission 1.5 eV → 2 × 0.7 eV

Figure B.2: Spectral functions of the decay operator for the 1.5 eV-orbiton. The shaded lines are spectral functions for the five lowest eigenstates in the undecayed subspace and the thick lines their averages as indicated in the main text. We employ open boundary conditions along directions with one or two sites. For more sites we use periodic boundary conditions.

D Derivation of the driven spin-photon Hamiltonian

In this section, we perform the second order Schrieffer Wolff transformation to eliminate double occupancies from the driven cavity coupled Hamiltonian (5.14) using a second order series expansion within a multiblock formulation of the Schrieffer-Wolff transformation described in Section 2.5. The low energy target space $\mathcal{P}_0$ is the doublon free sector. The projector to this subspace P_0 is given by

$$P_0 = \prod_i (1 - n_{i\uparrow} n_{i\downarrow}) \,. \tag{D.1}$$

To leading order, the generator (2.170) of the Schrieffer Wolff transformation is

$$\begin{aligned} P_0 S_1 P_1 &= \sum_{i\in\mathcal{P}_0, j\in\mathcal{P}_1} \frac{|i\rangle\langle i| V |j\rangle\langle j|}{E_i - E_j} \\ &= \sum_{m,l=-\infty}^{\infty} \sum_{\mu,\lambda=0}^{\infty} \frac{P_0 V_{\mu\lambda}^{ml} P_1 \,|m,\mu\rangle\langle l,\lambda|}{0 + m\omega_{\mathrm{cl}} + \mu\omega_{\mathrm{qu}} - (U + l\omega_{\mathrm{cl}} + \lambda\omega_{\mathrm{qu}})} \,, \end{aligned} \tag{D.2}$$

where V is the hopping part of the Hamiltonian. In the second equality, we represent the operator in a combined Floquet-photon basis $|m,\mu\rangle$, and $V_{\mu\nu}^{mn}$ is the corresponding electronic part of the operator elements, as implicitly defined in equation (5.14), i.e.,

$$V_{\mu\nu}^{mn} = -t_0 \, \mathrm{i}^{|m-n|+|\mu-\nu|} J_{|m-n|}(g_{\mathrm{cl}}) j_{\mu,\nu}(g_{\mathrm{qu}}) \sum_{\langle i,j\rangle\sigma} \chi_{ij}^{m-n} \xi_{ij}^{\mu-\nu} \, c_{i\sigma}^\dagger c_{j\sigma} \,. \tag{D.3}$$

Analogous to equation (D.2), we have

$$P_1 S_1 P_0 = \sum_{l,n=-\infty}^{\infty} \sum_{\lambda,\nu=0}^{\infty} \frac{P_1 V_{\lambda\nu}^{ln} P_0 \,|l,\lambda\rangle\langle n,\nu|}{U + l\omega_{\mathrm{cl}} + \lambda\omega_{\mathrm{qu}} - (n\omega_{\mathrm{cl}} + \nu\omega_{\mathrm{qu}})} \,. \tag{D.4}$$

Taking its matrix elements with respect to the cavity occupation and Floquet sidebands, we obtain the second order effective spin-photon-Floquet Hamiltonian

$$\tilde{H}_{\mu\nu}^{mn} = \langle \mu, m| \, P_0 \left(H_0 + \frac{1}{2}[S_1, V_{\mathrm{od}}] \right) P_0 \, |\nu, n\rangle \tag{D.5}$$

$$= \delta_{mn}\delta_{\mu\nu} \left(m\omega_{\mathrm{cl}} + \mu\omega_{\mathrm{qu}} \right) \tag{D.6}$$

$$\begin{aligned} &+ \frac{1}{2} \sum_{l=-\infty}^{\infty} \sum_{\lambda=0}^{\infty} \Big(\frac{P_0 V_{\mu\lambda}^{ml} P_1}{0 + m\omega_{\mathrm{cl}} + \mu\omega_{\mathrm{qu}} - (U + l\omega_{\mathrm{cl}} + \lambda\omega_{\mathrm{qu}})} V_{\lambda\nu}^{ln} P_0 \\ &\qquad - P_0 V_{\mu\lambda}^{ml} \frac{P_1 V_{\lambda\nu}^{ln} P_0}{U + l\omega_{\mathrm{cl}} + \lambda\omega_{\mathrm{qu}} - (n\omega_{\mathrm{cl}} + \nu\omega_{\mathrm{qu}})} \Big) \\ &= \delta_{mn}\delta_{\mu\nu} \left(m\omega_{\mathrm{cl}} + \mu\omega_{\mathrm{qu}} \right) \\ &- \frac{1}{2} \sum_{l=-\infty}^{\infty} \sum_{\lambda=0}^{\infty} \Big(\frac{P_0 V_{\mu\lambda}^{ml} P_1 V_{\lambda\nu}^{ln} P_0}{U + (l-m)\omega_{\mathrm{cl}} + (\lambda-\mu)\omega_{\mathrm{qu}}} \\ &\qquad + \frac{P_0 V_{\mu\lambda}^{ml} P_1 V_{\lambda\nu}^{ln} P_0}{U + (l-n)\omega_{\mathrm{cl}} + (\lambda-\nu)\omega_{\mathrm{qu}}} \Big) . \end{aligned} \tag{D.7}$$

Inserting the expression (D.3) for V, we further find

$$\begin{aligned}
&P_0 V^{ml}_{\mu\lambda} P_1 V^{ln}_{\lambda\nu} P_0 \\
=&P_0 \sum_{\langle i,j\rangle\sigma} (-t_0)\mathrm{i}^{|m-l|+|\mu-\lambda|} J_{|m-l|}(g_l) j_{\mu,\lambda}(g_c) \chi_{ij}^{m-l} \xi_{ij}^{\mu-\lambda} c^\dagger_{i\sigma} c_{j\sigma} P_1 \\
\cdot\ &P_1 \sum_{\langle k,l\rangle\sigma'} (-t_0)\mathrm{i}^{|l-n|+|\lambda-\nu|} J_{|l-n|}(g_l) j_{\lambda,\nu}(g_c) \chi_{kl}^{l-n} \xi_{kl}^{\lambda-\nu} c^\dagger_{k\sigma'} c_{l\sigma'} P_0 \qquad \text{(D.8)} \\
=&t_0^2 \mathrm{i}^{|m-l|+|\mu-\lambda|+|l-n|+|\lambda-\nu|} J_{|m-l|}(g_l) j_{\mu,\lambda}(g_c) J_{|l-n|}(g_l) j_{\lambda,\nu}(g_c) \\
&\sum_{\langle i,j\rangle} \chi_{ij}^{m-l} \xi_{ij}^{\mu-\lambda} \chi_{ji}^{l-n} \xi_{ji}^{\lambda-\nu} \sum_{\sigma,\sigma'} P_0 c^\dagger_{i\sigma} c_{j\sigma} c^\dagger_{j\sigma'} c_{i\sigma'} P_0 \,. \qquad \text{(D.9)}
\end{aligned}$$

The last term is identified as the singlet projector, $\sum_{\sigma,\sigma'} P_0 c^\dagger_{i\sigma} c_{j\sigma} c^\dagger_{j\sigma'} c_{i\sigma'} P_0 = 2P^S_{ij}$. Moreover, in the sum $\sum_{\langle i,j\rangle}$ over nearest neighbors each bond appears twice, once with $\chi_{ij} = \xi_{ij} = 1$ and once with $\chi_{ij} = \xi_{ij} = -1$. Using this fact, and the symmetry $\chi_{ij} = -\chi_{ji}$, $\xi_{ij} = -\xi_{ji}$, the sum can be rewritten as

$$\sum_{\langle i,j\rangle} \chi_{ij}^{m-l} \xi_{ij}^{\mu-\lambda} \chi_{ji}^{l-n} \xi_{ji}^{\lambda-\nu} 2P^S_{ij} = (-1)^{l-n+\lambda-\nu} \sum_{\langle i,j\rangle} \left(1 + (-1)^{m-n+\mu-\nu}\right) P^S_{ij}. \qquad \text{(D.10)}$$

In summary, the right hand side of equation (D.9) becomes

$$\begin{aligned}
&t_0^2 \mathrm{i}^{|m-l|+|\mu-\lambda|+|l-n|+|\lambda-\nu|} (-1)^{l-n+\lambda-\nu} J_{|m-l|}(g_l) j_{\mu,\lambda}(g_c) J_{|l-n|}(g_l) j_{\lambda,\nu}(g_c) \\
&\cdot \left(1 + (-1)^{m-n+\mu-\nu}\right) \sum_{\langle i,j\rangle} P^S_{ij} \,. \qquad \text{(D.11)}
\end{aligned}$$

Inserting this back into equation (D.7), and defining

$$\begin{aligned}
\mathcal{J}^{mn}_{\mu\nu} = -J_{\mathrm{ex}} \frac{1}{2} \sum_{l=-\infty}^{\infty} \sum_{\lambda=0}^{\infty} &\mathrm{i}^{|m-l|+|\mu-\lambda|+|l-n|+|\lambda-\nu|} (-1)^{l-n+\lambda-\nu} \\
&\cdot J_{|m-l|}(g_l) j_{\mu,\lambda}(g_c) J_{|l-n|}(g_l) j_{\lambda,\nu}(g_c) \left(1 + (-1)^{m-n+\mu-\nu}\right) \\
&\cdot \Big(\frac{1}{1 + (l-m)\bar{\omega}_{\mathrm{cl}} + (\lambda-\mu)\bar{\omega}_{\mathrm{qu}}} + \frac{1}{1 + (l-n)\bar{\omega}_{\mathrm{cl}} + (\lambda-\nu)\bar{\omega}_{\mathrm{qu}}} \Big), \qquad \text{(D.12)}
\end{aligned}$$

we arrive at equation (5.21).

E Connection between the Floquet-spin-photon Hamiltonian and resonant Raman-scattering

In this section we explain the connection between the Floquet-spin-photon Hamiltonian and the matrix elements of resonant Raman scattering.

Although the light matter Hamiltonian via the Peierls phase includes higher order nonlinear terms, a photon scattering with initial state $|i\rangle$ and final state $|f\rangle$ to the low-energy part of the Hilbert space can only occur via an intermediate state $|m\rangle$ with a charge excitation. This is because the light-matter coupling only appears in the hopping term, which at half filling creates charge excitations in $|m\rangle$ when acting on any $|i\rangle$. The Raman matrix elements can therefore be computed using time-dependent perturbation theory [247] up to second

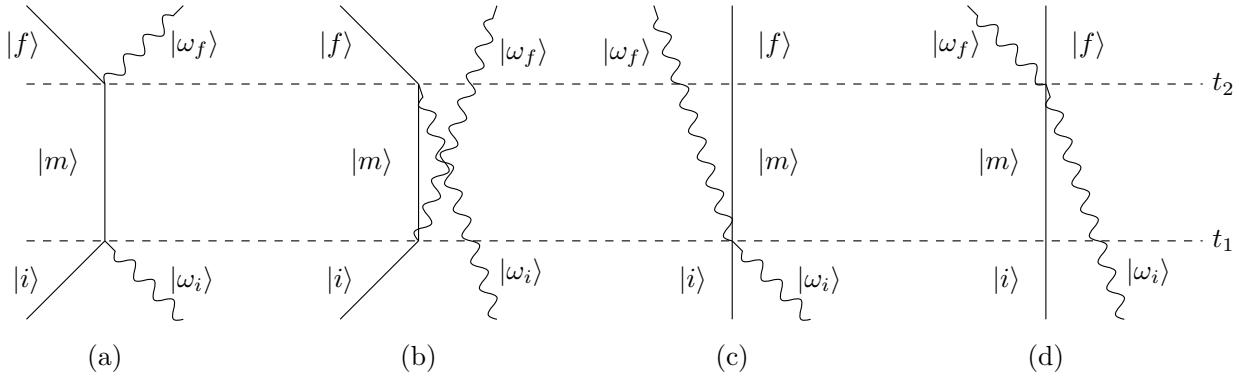

Figure E.1: Sketches of the scattering processes from many particle state $|i\rangle \otimes |\omega_i\rangle$ to $|f\rangle \otimes |\omega_f\rangle$ for the time-dependent perturbation theory, which schematically representing Eqs. (E.1)-(E.4) for time-dependent perturbation theory [247]. Since we are interested in second-order processes in t_0, the hopping operator H_t acts twice at times t_1 and t_2, which changes the both the state of the solid and the state $|\omega_{i/f}\rangle$ of the field. Figure reprinted from [P2] Copyright 2024 American Physical Society.

order in t_0. Within the second order time-dependent perturbation theory, the tunnelling operator H_t acts twice and there are four distinct contributions $c_{(a)}$-$c_{(d)}$ to the amplitude $c(t) = c_{(a)} + c_{(b)} + c_{(c)} + c_{(d)}$ for the transition from $|i, \omega_i\rangle$ to $|f, \omega_f\rangle$ within the time t; the structure of these contribution is sketched in Fig. E.1, and the algebraic expressions are given by

$$c_{(a)}(t) = \int_0^t dt_2 \int_0^{t_2} dt_1 \sum_m \langle f, \omega_f | H_t | m \rangle e^{i(\epsilon_f - \epsilon_m + \omega_f)t_2} \langle m | H_t | i, \omega_i \rangle e^{i(\epsilon_m - (\epsilon_i + \omega_i))t_1} \tag{E.1}$$

$$c_{(b)}(t) = \int_0^t dt_2 \int_0^{t_2} dt_1 \sum_m \langle f, \omega_f | H_t | m, \omega_f + \omega_i \rangle e^{i(\epsilon_f - \epsilon_m - \omega_i)t_2} \langle m, \omega_f + \omega_i | H_t | i, \omega_i \rangle e^{i(\epsilon_m + \omega_f - \epsilon_i)t_1} \tag{E.2}$$

$$c_{(c)}(t) = \int_0^t dt_2 \int_0^{t_2} dt_1 \sum_m \langle f, \omega_f | H_t | m, \omega_f \rangle e^{i(\epsilon_f - \epsilon_m)t_2} \langle m, \omega_f | H_t | i, \omega_i \rangle e^{i(\epsilon_m + \omega_f - \epsilon_i - \omega_i)t_1} \tag{E.3}$$

$$c_{(d)}(t) = \int_0^t dt_2 \int_0^{t_2} dt_1 \sum_m \langle f, \omega_f | H_t | m, \omega_i \rangle e^{i(\epsilon_f + \omega_f - \epsilon_m - \omega_i)t_2} \langle m, \omega_i | H_t | i, \omega_i \rangle e^{i(\epsilon_m - \epsilon_i)t_1} . \tag{E.4}$$

In all expressions, we can perform the t_1 integral in the form $\int_0^{t_2} dt_1 e^{ixt_1} \to -ie^{ixt_2}/x$, where we have neglect the contribution from the lower boundary of the t_1 integral, as it provides a contribution dependent on the turn-on of the interaction at $t = 0$ [247]. For the sum $c(t) = c_{(a)} + c_{(b)} + c_{(c)} + c_{(d)}$, this gives

$$c(t) = -i \int_0^t dt_2 \sum_m \tilde{M}(m) e^{i(\epsilon_f + \omega_f - (\epsilon_i + \omega_i))t_2} , \tag{E.5}$$

where matrix elements and resolvents are summarized into

$$\begin{aligned}\tilde{M}(m) = &\frac{\langle f,\omega_f|\, H_t\,|m\rangle\,\langle m|\, H_t\,|i,\omega_i\rangle}{\epsilon_m-(\epsilon_i+\omega_i)}\\ &+\frac{\langle f,\omega_f|\, H_t\,|m,\omega_f+\omega_i\rangle\,\langle m,\omega_f+\omega_i|\, H_t\,|i,\omega_i\rangle}{\epsilon_m+\omega_f-\epsilon_i}\\ &+\frac{\langle f,\omega_f|\, H_t\,|m,\omega_f\rangle\,\langle m,\omega_f|\, H_t\,|i,\omega_i\rangle}{\epsilon_m+\omega_f-\epsilon_i-\omega_i}\\ &+\frac{\langle f,\omega_f|\, H_t\,|m,\omega_i\rangle\,\langle m,\omega_i|\, H_t\,|i,\omega_i\rangle}{\epsilon_m-\epsilon_i}\,. \end{aligned} \tag{E.6}$$

Evaluating the remaining integral and some algebra gives

$$\begin{aligned}|c(t)|^2/t &= \sum_{m,m'}\tilde{M}(m)\tilde{M}(m')^*\frac{\sin((\epsilon_f+\omega_f-(\epsilon_i+\omega_i))/2\cdot t)^2}{t\left[(\epsilon_f+\omega_f-(\epsilon_i+\omega_i))/2\right]^2}\\ &\to \pi\sum_{m,m'}\tilde{M}(m)\tilde{M}(m')^*\delta(\epsilon_f+\omega_f-(\epsilon_i+\omega_i))\,, \end{aligned} \tag{E.7}$$

where in the second equation we have used the limit $\lim_{t\to\infty}\frac{\sin(xt)^2}{x^2t}=\pi\delta(x)$. Imposing on shell condition for the energy, $\epsilon_f+\omega_f-\epsilon_i-\omega_i=0$, one can rewrite the matrix element $\tilde{M}$ in the form

$$\begin{aligned}2\tilde{M} = &\langle f,\omega_f|\, H_t\,|m\rangle\,\langle m|\,\frac{H_t}{\epsilon_m-(\epsilon_i+\omega_i)}\,|i,\omega_i\rangle\\ &-\langle f,\omega_f|\,\frac{H_t}{\epsilon_f+\omega_f-\epsilon_m}\,|m\rangle\,\langle m|\, H_t\,|i,\omega_i\rangle\\ &+\langle f,\omega_f|\, H_t\,|m,\omega_f+\omega_i\rangle\,\langle m,\omega_f+\omega_i|\,\frac{H_t}{\epsilon_m+\omega_f-\epsilon_i}\,|i,\omega_i\rangle\\ &-\langle f,\omega_f|\,\frac{H_t}{\epsilon_f-\epsilon_m-\omega_i}\,|m,\omega_f+\omega_i\rangle\,\langle m,\omega_f+\omega_i|\, H_t\,|i,\omega_i\rangle\\ &+\langle f,\omega_f|\, H_t\,|m,\omega_f\rangle\,\langle m,\omega_f|\,\frac{H_t}{\epsilon_m+\omega_f-(\epsilon_i+\omega_i)}\,|i,\omega_i\rangle\\ &-\langle f,\omega_f|\,\frac{H_t}{\epsilon_f+\omega_f-(\epsilon_m+\omega_f)}\,|m,\omega_f\rangle\,\langle m,\omega_f|\, H_t\,|i,\omega_i\rangle\\ &+\langle f,\omega_f|\, H_t\,|m,\omega_i\rangle\,\langle m,\omega_i|\,\frac{H_t}{\epsilon_m-\epsilon_i}\,|i,\omega_i\rangle\\ &-\langle f,\omega_f|\,\frac{H_t}{\epsilon_f+\omega_f-(\epsilon_m+\omega_i)}\,|m,\omega_i\rangle\,\langle m,\omega_i|\, H_t\,|i,\omega_i\rangle\,. \end{aligned} \tag{E.8}$$

With the expression for the resolvent superoperator $\mathcal{L}(X)$ of the Schrieffer-Wolff transformation (see equation (2.171)) and the partition of unity in the upper Hubbard band $I = \sum_m (|m\rangle\langle m| + |m,\omega_i\rangle\langle m,\omega_i| + |m,\omega_f\rangle\langle m,\omega_f| + |m,\omega_i+\omega_f\rangle\langle m,\omega_i+\omega_f|)$, we can identify

$$\begin{aligned}\sum_m \tilde{M} &= \frac{1}{2}\langle f,\omega_f| H_t\mathcal{L}(H_t)\,|i,\omega_i\rangle - \frac{1}{2}\langle f,\omega_f|\,\mathcal{L}(H_t)H_t\,|i,\omega_i\rangle \\ &= \frac{1}{2}\langle f,\omega_f|\,[H_t,\mathcal{L}(H_t)]\,|i,\omega_i\rangle\ . \end{aligned} \tag{E.9}$$

With equations (D.5) and (2.170), the last term is identified as a matrix element of the (Floquet-) spin-photon Hamiltonian

$$\sum_m \tilde{M} = \langle f,\omega_f|\,\tilde{H}_{\mathrm{SP}}\,|i,\omega_i\rangle\ . \tag{E.10}$$

The matrix element $\tilde{M}$ of resonant scattering on the energy shell in the low-energy sector is therefore exactly the same as that of the multi-block second-order effective low-energy Hamiltonian.
For the two modes present in the driven spin-photon Hamiltonian, we can therefore give a scattering interpretation to the matrix elements: e.g., $\mathcal{J}^{01,10}\delta(\omega_{\mathrm{qu}}-\omega_{\mathrm{cl}})/\mathcal{J}^{10,01}\delta(\omega_{\mathrm{qu}}-\omega_{\mathrm{cl}})$ is the Raman scattering matrix element from the classical mode to the quantum mode or vice versa, $\mathcal{J}^{0n,10}\delta(\omega_{\mathrm{qu}-n\omega_{\mathrm{cl}}})$ are Hyper-Raman matrix elements and $\mathcal{J}^{11,\nu\nu}$ describes the dressed propagation of classical light through the sample.

F Derivation of the fourth-order effective Hamiltonian

F.1 Full expressions

Using equation (5.34) as starting point, we can evaluate the fourth order effective Hamiltonian (see Section 2.5 or reference [91]) first for the simplest choice of low-energy subspace, i.e., with no charge excitations and the quantum mode unoccupied (see equation (5.35)).
The zeroth order vanishes, while the second order gives

$$\begin{aligned} H_2 &= J_{\mathrm{ex}}\sum_{\mu=0}^{\infty}\frac{j_{0,\mu}(g_{\mathrm{qu}})^2}{1+\mu\bar{\omega}_{\mathrm{qu}}}\sum_{\langle i,j\rangle}\left(\vec{S}_i\vec{S}_j-\frac{1}{4}\right) \\ &= -J_{\mathrm{ex}}\sum_{\mu=0}^{\infty}\frac{j_{0,\mu}(g_{\mathrm{qu}})j_{\mu,0}(g_{\mathrm{qu}})}{1+\mu\bar{\omega}}\sum_{\langle i,j\rangle}P_{ij}^{S}, \end{aligned} \tag{F.1}$$

where we have used the usual form of the spin operators $S^+ = c_\uparrow^\dagger c_\downarrow, S^- = c_\downarrow^\dagger c_\uparrow, S^z = (n_\uparrow - n_\downarrow)/2$ and the projector P_{ij}^S on the singlet state on bond ij.

Let us next evaluate the three appearing fourth-order paths through the Hilbert space from Figure 5.2. To abbreviate the notation, we split the contributions into a product of three factors: the scalar contributions of the matrix elements $\mathcal{A}$ of the perturbation V, the energy

resolvents $\mathcal{R}$ from the superoperator $\mathcal{L}$ and the electronic operator contribution $\hat{O}$. We start with the S1-path. For the operator contribution, we obtain

$$\begin{aligned}\hat{O}_{\mathrm{S1}} &= \sum_{\sigma_1,\sigma_2,\sigma_3,\sigma_4} P_0 c^\dagger_{i_1\sigma_1} c_{j_1\sigma_1} c^\dagger_{j_1\sigma_2} c_{i_1\sigma_2} P_0 c^\dagger_{i_2\sigma_3} c_{j_2\sigma_3} c^\dagger_{j_2\sigma_4} c_{i_2\sigma_4} P_0 \\ &= 4 P_{i_1 j_1} P_{i_2 j_2},\end{aligned} \tag{F.2}$$

where we have used that the intermediate projectors P_0 constrain the position of the second and fourth hopping. After expanding the nested commutator in equation (5.34), which gives the S1-path contribution, the matrix elements $\mathcal{A}$ and operator contributions $\hat{O}$ turn out to be the identical for all eight terms, and their resolvents can be summed up a single contribution

$$\mathcal{R}_{\mathrm{S1}} = \frac{1}{U^3} \frac{8 + 4(\gamma+\alpha)\bar{\omega}_{\mathrm{qu}}}{(1+\alpha\bar{\omega}_{\mathrm{qu}})^2 (1+\gamma\bar{\omega}_{\mathrm{qu}})^2}. \tag{F.3}$$

Lastly, using the definition

$$\mathcal{J}^{\alpha\beta\gamma\delta\epsilon}(g_{\mathrm{qu}}) = j_{\alpha\beta} j_{\beta\gamma} j_{\gamma\delta} j_{\delta\epsilon} i^{|\alpha-\beta|} i^{|\beta-\gamma|} i^{|\gamma-\delta|} i^{|\delta-\epsilon|}, \tag{F.4}$$

the matrix elements are given by

$$\mathcal{A}_{\mathrm{S1}} = t_0^4 j_{0\alpha}(g_{\mathrm{qu}}) j_{\alpha 0}(g_{\mathrm{qu}}) j_{0\gamma}(g_{\mathrm{qu}}) j_{\gamma 0}(g_{\mathrm{qu}}) = t_0^4 (-1)^{\alpha+\gamma} \mathcal{J}^{0\alpha 0\gamma 0}. \tag{F.5}$$

Combining the expressions for $\mathcal{A}_{\mathrm{S1}}$, O_{S1}, and $\mathcal{R}_{\mathrm{S1}}$, we obtain

$$H_{\mathrm{S1}} = \frac{1}{8} \sum_{\substack{\langle i_1 j_1\rangle \\ \langle i_2 j_2\rangle}} \sum_{\alpha,\gamma=0}^{\infty} \mathcal{A}_{S1} \mathcal{R}_{S1} \hat{O}_{S1} \tag{F.6}$$

$$= K_0 \sum_{\alpha,\gamma=0}^{\infty} \mathcal{J}^{0\alpha 0\gamma 0} \frac{(-1)^{\alpha+\gamma}(2+(\gamma+\alpha)\bar{\omega}_{\mathrm{qu}})}{(1+\alpha\bar{\omega}_{\mathrm{qu}})^2(1+\gamma\bar{\omega}_{\mathrm{qu}})^2} \sum_{\substack{\langle i_1 j_1\rangle \\ \langle i_2 j_2\rangle}} P_{i_1 j_1} P_{i_2 j_2}, \tag{F.7}$$

with $K_0 = 2t_0^4/U^3$, which gives equation (5.36).

The other two contributions describe processes with hopping inside the high-energy sector. In H_{NC} we combine all processes with no intermediate charge excitation after two hoppings. These paths therefore trace the identical path in the fermionic Hilbert space as those contained in H_{S1}, but the sums over the photonic Hilbert space and the resolvents are changed:

$$\begin{aligned}\hat{O}_{\mathrm{NC}} &= \sum_{\sigma_1,\sigma_2,\sigma_3,\sigma_4} P_0 c^\dagger_{i_1\sigma_1} c_{j_1\sigma_1} c^\dagger_{j_1\sigma_2} c_{i_1\sigma_2} P_0 c^\dagger_{i_2\sigma_3} c_{j_2\sigma_3} c^\dagger_{j_2\sigma_4} c_{i_2\sigma_4} P_0 \\ &= 4 P_{i_1 j_1} P_{i_2 j_2}\end{aligned} \tag{F.8}$$

$$\mathcal{R}_{\mathrm{NC}} = -\frac{1}{U^3} \frac{1}{(1+\alpha\bar{\omega}_{\mathrm{qu}})(\beta\bar{\omega}_{\mathrm{qu}})(1+\gamma\bar{\omega}_{\mathrm{qu}})}, \tag{F.9}$$

$$\mathcal{A}_{\mathrm{NC}} = t_0^4 \mathcal{J}^{0\alpha\beta\gamma 0} \xi^{0-\alpha}_{i_1 j_1} \xi^{\alpha-\beta}_{j_1 i_1} \xi^{\beta-\gamma}_{i_2 j_2} \xi^{\gamma-0}_{j_2 i_2} = t_0^4 \mathcal{J}^{0\alpha\beta\gamma 0} (-1)^{\alpha+\gamma+\beta} \xi^{\beta}_{i_1 j_1} \xi^{\beta}_{i_2 j_2}, \tag{F.10}$$

where in the last step we have used the symmetry $\xi_{ij} = -\xi_{ji}$. When combining all terms

$$H_{\mathrm{NC}} = \sum_{\langle i_1 j_1\rangle} \sum_{\langle i_2 j_2\rangle} \sum_{\alpha,\beta,\gamma=0}^{\infty} (1-\delta_{\beta 0}) \mathcal{A}_{\mathrm{NC}} \mathcal{R}_{\mathrm{NC}} \hat{O}_{\mathrm{NC}}, \tag{F.11}$$

the expression contains the lattice sums $\sum_{\langle i_1,j_1\rangle} P_{i_1 j_1} \xi^{\beta}_{i_1 j_1}$ (and similarly for i_2, j_2). Because $\xi_{i_1 j_1}$ is antisymmetric under exchange of i_1 and j_1, $P_{i_1 j_1}$ is symmetric, and each bond $\langle i_1, j_1\rangle$ appears once in each direction, the sum contributes only for even β, where $\xi^{\beta}_{i_1 j_1} = 1$. Hence the expression for H_{NC} gives,

$$H_{\mathrm{NC}} = -K_0 \sum_{\alpha,\beta,\gamma=0}^{\infty} \mathcal{J}^{0\alpha\beta\gamma 0} \frac{(1-\delta_{\beta 0})(-1)^{\alpha+\beta+\gamma}(1+(-1)^{\beta})}{(1+\alpha\bar{\omega}_{\mathrm{qu}})(\beta\bar{\omega}_{\mathrm{qu}})(1+\gamma\bar{\omega}_{\mathrm{qu}})} \sum_{\substack{\langle i_1 j_1\rangle \\ \langle i_2 j_2\rangle}} P_{i_1 j_1} P_{i_2 j_2}, \tag{F.12}$$

where a factor $(1+(-1)^{\beta})/2$ has been introduced to select the even β.

Finally, we derive the contribution from the DC path, which contain two intermediate charge excitations. This requires the involvement of two separate bonds and is possible with two separate operator sequences: The double occupation which is created first (on site i_4 in the expression below) can be the first (δ_1) or the last one (δ_2) to be broken up,

$$\begin{aligned}\hat{O}_{\mathrm{DC}} &= \sum_{\sigma_1,\sigma_2,\sigma_3,\sigma_4} P_0 c^{\dagger}_{i_1\sigma_1} c_{j_1\sigma_1} c^{\dagger}_{i_2\sigma_2} c_{j_2\sigma_2} (\overbrace{\delta_{i_1 j_3}\delta_{i_2 j_4}\delta_{i_3 j_1}\delta_{i_4 j_2}}^{\delta_1} + \overbrace{\delta_{i_1 j_4}\delta_{i_2 j_3}\delta_{i_3 j_2}\delta_{i_4 j_1}}^{\delta_2}) c^{\dagger}_{i_3\sigma_3} c_{j_3\sigma_3} c^{\dagger}_{i_4\sigma_4} c_{j_4\sigma_4} P_0 \\ &= 4(\delta_1+\delta_2) P_{i_1 j_1} P_{i_2 j_2}\end{aligned} \tag{F.13}$$

In the regular Hubbard model, these path contribute equally, but the cavity coupling introduces a phase which depends on the order of the hoppings. The resolvents for both types of path are given by

$$\mathcal{R}_{\mathrm{DC}} = -\frac{1}{U^3} \frac{1}{(1+\alpha\bar{\omega}_{\mathrm{qu}})(2+\beta\bar{\omega}_{\mathrm{qu}})(1+\gamma\bar{\omega}_{\mathrm{qu}})}. \tag{F.14}$$

Including the constraints δ_1 and δ_2 for the evaluation of the matrix elements based amplitude gives

$$\begin{aligned}&(\delta_1+\delta_2)\mathcal{A}_{\mathrm{DC}} \\ =&t_0^4 \mathcal{J}^{0\alpha\beta\gamma 0} \xi^{0-\alpha}_{i_1 j_1} \xi^{\alpha-\beta}_{i_2 j_2} (\delta_1+\delta_2) \xi^{\beta-\gamma}_{i_3 j_3} \xi^{\gamma-0}_{i_4 j_4} && \text{(F.15)} \\ =&t_0^4 \mathcal{J}^{0\alpha\beta\gamma 0} \Big(\delta_1 \xi^{0-\alpha}_{i_1 j_1} \xi^{\alpha-\beta}_{i_2 j_2} \xi^{\beta-\gamma}_{j_1 i_1} \xi^{\gamma-0}_{j_2 i_2} + \delta_2 \xi^{0-\alpha}_{i_1 j_1} \xi^{\alpha-\beta}_{i_2 j_2} \xi^{\beta-\gamma}_{j_2 i_2} \xi^{\gamma-0}_{j_1 i_1}\Big) && \text{(F.16)} \\ =&t_0^4 \mathcal{J}^{0\alpha\beta\gamma 0} (-1)^{\beta} \Big(\delta_1 \xi^{\beta-\alpha-\gamma}_{i_1 j_1} \xi^{\alpha+\gamma-\beta}_{i_2 j_2} + \delta_2 \xi^{\gamma-\alpha}_{i_1 j_1} \xi^{\alpha-\gamma}_{i_2 j_2}\Big), && \text{(F.17)}\end{aligned}$$

where in equation (F.16) we have replaced the indices i_3, j_3, i_4, j_4 by i_1, j_1, i_2, j_2 according to the constraints δ_1 and δ_2, and in equation (F.17) we have used the symmetry $\xi_{ij} = -\xi_{ji}$. Following a similar argument as the one below equation (F.11), under the lattice sums $\sum_{\langle i_1 j_1\rangle,\langle i_2,j_2\rangle}$ the

term $\sim \delta_1$ and $\sim \delta_2$ contribute only if $(\alpha+\gamma-\beta)$ or $(\alpha-\gamma)$ are even, respectively. Hence, under the lattice sum we can replace the matrix elements by

$$\begin{aligned}&(\delta_1+\delta_2)\mathcal{A}_{\mathrm{DC}}\\&\to t_0^4\mathcal{J}^{0\alpha\beta\gamma 0}(-1)^{\beta}\left(\delta_1\frac{1+(-1)^{\alpha+\beta+\gamma}}{2}+\delta_2\frac{1+(-1)^{\alpha+\gamma}}{2}\right).\end{aligned}\tag{F.18}$$

Since summing over all bonds $\langle i_3 j_3\rangle, \langle i_4 j_4\rangle$ fulfills the conditions imposed by δ_1, δ_2 exactly one time each if $\langle i_1 j_1\rangle \neq \langle i_2 j_2\rangle$, the combination of all terms gives equation (5.38) of the main text,

$$\begin{aligned}H_{\mathrm{DC}} &= \sum_{\substack{\langle i_1 j_1\rangle\\ \neq\langle i_2 j_2\rangle}}\sum_{\alpha,\beta,\gamma=0}^{\infty}\mathcal{A}_{\mathrm{DC}}\mathcal{R}_{\mathrm{DC}}\hat{O}_{\mathrm{DC}}\\&= -K_0\sum_{\alpha,\beta,\gamma=0}^{\infty}\mathcal{J}^{0\alpha\beta\gamma 0}(-1)^{\beta}\frac{2+(-1)^{\alpha+\gamma}(1+(-1)^{\beta})}{(1+\alpha\bar{\omega}_{\mathrm{qu}})(2+\beta\bar{\omega}_{\mathrm{qu}})(1+\gamma\bar{\omega}_{\mathrm{qu}})}\\&\cdot\sum_{\substack{\langle i_1 j_1\rangle\\ \neq\langle i_2 j_2\rangle}}P_{i_1 j_1}P_{i_2 j_2}.\end{aligned}\tag{F.19}$$

F.2 Leading order in g_{qu}

For further illustration, let us take these terms and expand in g_{qu} up to the fourth order.

$$\begin{aligned}H_{\mathrm{S1}} = \quad & 2K_0\Big(1-g_{\mathrm{qu}}^2\frac{\bar{\omega}_{\mathrm{qu}}(3+2\bar{\omega}_{\mathrm{qu}})}{(1+\bar{\omega}_{\mathrm{qu}})^2}+g_{\mathrm{qu}}^4\frac{\bar{\omega}_{\mathrm{qu}}^2(6+22\bar{\omega}_{\mathrm{qu}}+25\bar{\omega}_{\mathrm{qu}}^2+8\bar{\omega}_{\mathrm{qu}}^3)}{(1+\bar{\omega}_{\mathrm{qu}})^3(1+2\bar{\omega}_{\mathrm{qu}})^2}\Big)\\&\cdot\sum_{\substack{\langle i_1 j_1\rangle\\ \langle i_2 j_2\rangle}}P_{i_1 j_1}P_{i_2 j_2}\end{aligned}\tag{F.20}$$

$$\begin{aligned}H_{\mathrm{DC}} = -2K_0\Big(1-g_{\mathrm{qu}}^2\frac{\bar{\omega}_{\mathrm{qu}}(3+2\bar{\omega}_{\mathrm{qu}})}{(1+\bar{\omega}_{\mathrm{qu}})^2}+g_{\mathrm{qu}}^4\frac{\bar{\omega}_{\mathrm{qu}}^2(7+25\bar{\omega}_{\mathrm{qu}}+28\bar{\omega}_{\mathrm{qu}}^2+8\bar{\omega}_{\mathrm{qu}}^3)}{(1+\bar{\omega}_{\mathrm{qu}})^3(1+2\bar{\omega}_{\mathrm{qu}})^2}\Big)\\\cdot\sum_{\substack{\langle i_1 j_1\rangle\\ \neq\langle i_2 j_2\rangle}}P_{i_1 j_1}P_{i_2 j_2}\end{aligned}\tag{F.21}$$

$$H_{\mathrm{NC}} = -2K_0 g_{\mathrm{qu}}^4\frac{\bar{\omega}_{\mathrm{qu}}^3}{(1+\bar{\omega}_{\mathrm{qu}})^2(1+2\bar{\omega}_{\mathrm{qu}})^2}\sum_{\substack{\langle i_1 j_1\rangle\\ \langle i_2 j_2\rangle}}P_{i_1 j_1}P_{i_2 j_2}\tag{F.22}$$

By constraining $\langle i_2, j_2\rangle$ to either the same bond or different bonds, we obtain the local fourth-order corrections to the Heisenberg exchange or the long-range mediated interactions:

$$J_{\text{loc}} = 2K_0\left(1 - g_{\text{qu}}^2\frac{\bar{\omega}_{\text{qu}}(3+2\bar{\omega}_{\text{qu}})}{(1+\bar{\omega}_{\text{qu}})^2} + g_{\text{qu}}^4\frac{\bar{\omega}_{\text{qu}}^2(6+21\bar{\omega}_{\text{qu}}+24\bar{\omega}_{\text{qu}}^2+8\bar{\omega}_{\text{qu}}^3)}{(1+\bar{\omega}_{\text{qu}})^3(1+2\bar{\omega}_{\text{qu}})^2}\right) \tag{F.23}$$

$$K = 2K_0 g_{\text{qu}}^4\left(\underbrace{-\frac{\bar{\omega}_{\text{qu}}^2(1+3\bar{\omega}_{\text{qu}}+3\bar{\omega}_{\text{qu}}^2)}{(1+\bar{\omega}_{\text{qu}})^3(1+2\bar{\omega}_{\text{qu}})^2}}_{\kappa_{\text{S1}}/2+\kappa_{\text{DC}}/2}\underbrace{-\frac{\bar{\omega}_{\text{qu}}^2(\bar{\omega}_{\text{qu}}+\bar{\omega}_{\text{qu}}^2)}{(1+\bar{\omega}_{\text{qu}})^3(1+2\bar{\omega}_{\text{qu}})^2}}_{\kappa_{\text{NC}}/2}\right) \tag{F.24}$$

$$= -2K_0 g_{\text{qu}}^4\frac{\bar{\omega}_{\text{qu}}^2}{(1+\bar{\omega}_{\text{qu}})^3}. \tag{F.25}$$

Note that to orders g_{qu}^0 and g_{qu}^2 the terms H_{S1} and H_{DC} have contributions even when $\langle i_1, j_1\rangle$ and $\langle i_2, j_2\rangle$ are on different bonds. As outlined in the main part of this thesis, this is due to the lack of a linked-cluster property of our expansion. When all terms are summed up the contributions of order g_{qu}^0 and g_{qu}^2 to the interaction contributions cancel, so that leading contribution to the interaction is $\mathcal{O}(g_{\text{qu}}^4)$.

G Generalization of the derivation of the interaction for cavity occupation and classical driving

As outlined in the main text, we can accomplish this by amending the expansion shown in Section F to account for occupation of the quantum mode and classical drive by amending the energy resolvents and the amplitude terms. Since the Floquet-block Hamiltonian (equation (5.14)) and any effective Floquet Hamiltonian derived from it are translationally invariant under a global shift of the sideband index, it is sufficient to compute the effective Floquet Hamiltonian for one sideband only, $n = 0$.

Close to resonance the convergence radius of the perturbative series grows rapidly. Higher order processes can therefore contribute more strongly, which formally limits our truncated scheme to small values of t_0 [91]. In our setting, it is, however, not only t_0, which controls the coupling to these potentially resonant blocks, but also the light-matter coupling constants $g_{\text{qu}}, g_{\text{cl}}$. Furthermore in physical systems, the frequencies $\omega_{\text{qu}}, \omega_{\text{cl}}$ have a finite linewidth. It is therefore reasonable to ignore resonances outside of the large cutoff we apply for the numerical evaluation of the interaction strength.

In second order we find

$$H_{2,\nu} = J_{\text{ex}}\sum_{m=-\infty}^{\infty}\sum_{\mu=0}^{\infty}\frac{j_{\nu,\mu}(g_{\text{qu}})^2 J_{|m|}(g_{\text{cl}})^2}{1+(\mu-\nu)\bar{\omega}_{\text{qu}}+m\bar{\omega}_{\text{cl}}}\sum_{\langle i,j\rangle}\left(\vec{S}_i\vec{S}_j - \frac{1}{4}\right). \tag{G.1}$$

To get the fourth-order terms, we extend the amplitude prefactor (equation (F.4)) and use

$$\begin{aligned}\mathcal{J}_{abcde}^{\alpha\beta\gamma\delta\epsilon}(g_{\text{qu}}, g_{\text{cl}}) =& j_{\alpha\beta}(g_{\text{qu}})j_{\beta\gamma}(g_{\text{qu}})j_{\gamma\delta}(g_{\text{qu}})j_{\delta\epsilon}(g_{\text{qu}})\\ &\cdot J_{|a-b|}(g_{\text{cl}})J_{|b-c|}(g_{\text{cl}})J_{|c-d|}(g_{\text{cl}})J_{|d-e|}(g_{\text{cl}})\\ &\cdot i^{|\alpha-\beta|+|\beta-\gamma|+|\gamma-\delta|+|\delta-\epsilon|}\cdot i^{|a-b|+|b-c|+|c-d|+|d-e|}.\end{aligned} \tag{G.2}$$

The operator contribution $\hat{O}_{\mathrm{S1}}$, $\hat{O}_{\mathrm{NC}}$ and $\hat{O}_{\mathrm{DC}}$ to the three types of path is the same as for the empty cavity (equations (F.2), (F.8), and (F.13)). The resolvent of the S1-term becomes

$$\mathcal{R}_{\mathrm{S1}} = \frac{1}{U^3}\frac{8 + 4(\alpha+\gamma-2\nu)\bar{\omega}_{\mathrm{qu}} + 4(a+c)\bar{\omega}_{\mathrm{cl}}}{\left(1 + (\alpha-\nu)\bar{\omega}_{\mathrm{qu}} + a\bar{\omega}_{\mathrm{cl}}\right)^2\left(1 + (\gamma-\nu)\bar{\omega}_{\mathrm{qu}} + c\bar{\omega}_{\mathrm{cl}}\right)^2} \tag{G.3}$$

and its amplitude

$$\mathcal{A}_{\mathrm{S1}} = t_0^4 \mathcal{J}_{0a0c0}^{\nu\alpha\nu\gamma\nu}(g_{\mathrm{qu}}, g_{\mathrm{cl}})(-1)^{\alpha+\gamma}(-1)^{a+c}. \tag{G.4}$$

Since the target space from which we eliminate fluctuations has the cavity in the number state $|\nu\rangle$, the S1-paths have to return to this state after two hoppings.

For the NC-term we find

$$\mathcal{R}_{\mathrm{NC}} = \frac{1}{U^3}\Big[\left(1 + (\alpha-\nu)\bar{\omega}_{\mathrm{qu}} + a\bar{\omega}_{\mathrm{cl}}\right) \cdot \left((\beta-\nu)\bar{\omega}_{\mathrm{qu}} + b\bar{\omega}_{\mathrm{cl}}\right)\left(1 + (\gamma-\nu)\bar{\omega}_{\mathrm{qu}} + c\bar{\omega}_{\mathrm{cl}}\right)\Big]^{-1} \tag{G.5}$$

and

$$\mathcal{A}_{\mathrm{NC}} = t_0^4 \mathcal{J}_{0abc0}^{\nu\alpha\beta\gamma\nu}(g_{\mathrm{qu}}, g_{\mathrm{cl}})(-1)^{\alpha+(\beta-\nu)+\gamma}(\xi_{i_1j_1}\xi_{i_2j_2})^{\beta-\nu}(-1)^{a+b+c}(\chi_{i_1j_1}\chi_{i_2j_2})^b \tag{G.6}$$

$$\to \frac{1}{2}t_0^4 \mathcal{J}_{0abc0}^{\nu\alpha\beta\gamma\nu}(g_{\mathrm{qu}}, g_{\mathrm{cl}})(-1)^{\alpha+(\beta-\nu)+\gamma}(-1)^{a+b+c}(1 + (-1)^{\beta-\nu+b}), \tag{G.7}$$

where the second equality hold only under the lattice sums, and we have used that the signs of the projected polarization can only either be aligned or anti-aligned for all bonds (see analogous to the arguments below equation (F.11)). Finally, the DC-term becomes

$$\mathcal{R}_{\mathrm{DC}} = \frac{1}{U^3}\Big[\left(1 + (\alpha-\nu)\bar{\omega}_{\mathrm{qu}} + a\bar{\omega}_{\mathrm{cl}}\right) \cdot \left(2 + (\beta-\nu)\bar{\omega}_{\mathrm{qu}} + b\bar{\omega}_{\mathrm{cl}}\right)\left(1 + (\gamma-\nu)\bar{\omega}_{\mathrm{qu}} + c\bar{\omega}_{\mathrm{cl}}\right)\Big]^{-1} \tag{G.8}$$

and the matrix elements are (generalizing equation (F.18)),

$$(\delta_1+\delta_2)\mathcal{A}_{\mathrm{DC}} = t_0^4 \mathcal{J}_{0abc0}^{\nu\alpha\beta\gamma\nu}(g_{\mathrm{qu}}, g_{\mathrm{cl}})(\delta_1+\delta_2)\xi_{i_1j_1}^{\nu-\alpha}\xi_{i_2j_2}^{\alpha-\beta}\xi_{i_3j_3}^{\beta-\gamma}\xi_{i_4j_4}^{\gamma-\nu}\chi_{i_1j_1}^{0-a}\chi_{i_2j_2}^{a-b}\chi_{i_3j_3}^{b-c}\chi_{i_4j_4}^{c-0} \tag{G.9}$$

$$\to \frac{1}{2}t_0^4 \mathcal{J}_{0abc0}^{\nu\alpha\beta\gamma\nu}(g_{\mathrm{qu}}, g_{\mathrm{cl}})(-1)^{\beta-\nu+b}(2 + (-1)^{\alpha+\gamma+a+c}(1 + (-1)^{(\beta-\nu)+b})), \tag{G.10}$$

where again the second equality holds under the lattice sums. Combining all terms, we can write the effective Hamiltonian in the notation of the main text (equations (5.36) to (5.38)), with modified matrix elements (5.39) to (5.41). For the undriven cavity $g_{\mathrm{cl}} = 0$ at nonzero cavity occupation ν we have

$$W_{\mathrm{S_I}}^{\nu\alpha\beta\gamma\nu}(g_{\mathrm{cl}},\bar{\omega}_{\mathrm{qu}}) = \mathcal{J}^{\nu\alpha\beta\gamma\nu}(g_{\mathrm{qu}})\delta_{\beta,\nu}\frac{(-1)^{\alpha+\gamma}\left(2+(\alpha+\gamma-2\nu)\bar{\omega}_{\mathrm{qu}}\right)}{\left(1+(\alpha-\nu)\bar{\omega}_{\mathrm{qu}}\right)^2\left(1+(\gamma-\nu)\bar{\omega}_{\mathrm{qu}}\right)^2}, \tag{G.11}$$

$$W_{\mathrm{NC}}^{\nu\alpha\beta\gamma\nu}(g_{\mathrm{cl}},\bar{\omega}_{\mathrm{qu}}) = \mathcal{J}^{\nu\alpha\beta\gamma\nu}(g_{\mathrm{qu}})(1-\delta_{\beta,\nu})\frac{(-1)^{\alpha+(\beta-\nu)+\gamma}(1+(-1)^{\beta-\nu})}{\left(1+(\alpha-\nu)\bar{\omega}_{\mathrm{qu}}\right)\left((\beta-\nu)\bar{\omega}_{\mathrm{qu}}\right)\left(1+(\gamma-\nu)\bar{\omega}_{\mathrm{qu}}\right)}, \tag{G.12}$$

$$W_{\mathrm{DC}}^{\nu\alpha\beta\gamma\nu}(g_{\mathrm{cl}},\bar{\omega}_{\mathrm{qu}}) = \mathcal{J}^{\nu\alpha\beta\gamma\nu}(g_{\mathrm{qu}})\frac{(-1)^{\beta-\nu}(2+(-1)^{\alpha+\gamma}(1+(-1)^{(\beta-\nu)}))}{\left(1+(\alpha-\nu)\bar{\omega}_{\mathrm{qu}}\right)\left(2+(\beta-\nu)\bar{\omega}_{\mathrm{qu}}\right)\left(1+(\gamma-\nu)\bar{\omega}_{\mathrm{qu}}\right)}, \tag{G.13}$$

while for the most general case of a driven cavity one has

$$W_{\mathrm{S_I}}^{\nu\alpha\beta\gamma\nu;abc} = \mathcal{J}_{0abc0}^{\nu\alpha\beta\gamma\nu}(g_{\mathrm{qu}},g_{\mathrm{cl}})\delta_{\beta,0}\delta_{b,0}\frac{(-1)^{\alpha+\gamma}(-1)^{a+c}\left(2+(\alpha+\gamma-2\nu)\bar{\omega}_{\mathrm{qu}}+(a+c)\bar{\omega}_{\mathrm{cl}}\right)}{\left(1+(\alpha-\nu)\bar{\omega}_{\mathrm{qu}}+a\bar{\omega}_{\mathrm{cl}}\right)^2\left(1+(\gamma-\nu)\bar{\omega}_{\mathrm{qu}}+c\bar{\omega}_{\mathrm{cl}}\right)^2}, \tag{G.14}$$

$$W_{\mathrm{NC}}^{\nu\alpha\beta\gamma\nu;abc} = \mathcal{J}_{0abc0}^{\nu\alpha\beta\gamma\nu}(g_{\mathrm{qu}},g_{\mathrm{cl}})(1-\delta_{\beta,\nu}\delta_{b,0})\frac{(-1)^{\alpha+(\beta-\nu)+\gamma+a+b+c}(1+(-1)^{\beta-\nu+b})}{\left(1+(\alpha-\nu)\bar{\omega}_{\mathrm{qu}}+a\bar{\omega}_{\mathrm{cl}}\right)\left((\beta-\nu)\bar{\omega}_{\mathrm{qu}}+b\bar{\omega}_{\mathrm{cl}}\right)\left(1+(\gamma-\nu)\bar{\omega}_{\mathrm{qu}}+c\bar{\omega}_{\mathrm{cl}}\right)}, \tag{G.15}$$

$$W_{\mathrm{DC}}^{\nu\alpha\beta\gamma\nu;abc} = \mathcal{J}_{0abc0}^{\nu\alpha\beta\gamma\nu}(g_{\mathrm{qu}},g_{\mathrm{cl}})\frac{(-1)^{\beta-\nu+b}(2+(-1)^{\alpha+\gamma+a+c}(1+(-1)^{(\beta-\nu)+b}))}{\left(1+(\alpha-\nu)\bar{\omega}_{\mathrm{qu}}+a\bar{\omega}_{\mathrm{cl}}\right)\left(2+(\beta-\nu)\bar{\omega}_{\mathrm{qu}}+b\bar{\omega}_{\mathrm{cl}}\right)\left(1+(\gamma-\nu)\bar{\omega}_{\mathrm{qu}}+c\bar{\omega}_{\mathrm{cl}}\right)}. \tag{G.16}$$

H Interaction in the spin-photon-Floquet approach

To eliminate cavity and sideband fluctuations from an arbitrary cavity occupation, we can use a second order Schrieffer-Wolff transformation (see equation (2.172)). Here our unperturbed Hamiltonian is the cavity occupation and sideband index $(H_0)^{mn}_{\mu\nu} = \delta_{mn}\delta_{\mu\nu}(m\omega_{\mathrm{cl}} + \mu\omega_{\mathrm{qu}})$, the spin-photon-drive scattering term $H_{\mathrm{SP}} - H_0$ acts as perturbation and we choose the target space using the projector

$$P_0 = |\nu_{\mathrm{qu}}\rangle\langle\nu_{\mathrm{qu}}| \otimes |0_{\mathrm{cl}}\rangle\langle 0_{\mathrm{cl}}|\,. \tag{H.1}$$

The perturbation therefore has a diagonal and an offdiagonal contribution. Further using $P_0 H_0 P_0 = \nu\omega_{\mathrm{qu}}\mathbb{1}$, we can simplify to

$$H^{\nu}_{\mathrm{SP}} = (H_{\mathrm{SP}})^{00}_{\nu\nu} - \sum_{b=-\infty}^{\infty}\sum_{\beta=0}^{\infty} \tilde{H}^{0b,\nu\beta}\frac{(1-\delta_{b0}\delta_{\nu,\beta})}{b\omega_{\mathrm{cl}} + (\beta-\nu)\omega_{\mathrm{qu}}} H^{b0,\beta\nu}. \tag{H.2}$$

Again splitting up the result of in an operator part $\hat{O}_{\mathrm{SP}}$, an amplitude $\mathcal{A}_{\mathrm{SP}}$ and a resolvent $\mathcal{R}_{\mathrm{SP}}$, we obtain

$$\hat{O}_{\mathrm{SP}} = P_{i_1 j_1} P_{i_2 j_2} \tag{H.3}$$

$$\begin{aligned}\mathcal{A}_{\mathrm{SP}} &= 2t_0^4 \mathcal{J}^{\nu\alpha\beta\gamma\nu}_{0abc0}(g_{\mathrm{qu}}, g_{\mathrm{cl}}) \\ &\quad\cdot(-1)^{a+b+c+(\alpha-\nu)+(\beta-\nu)+(\gamma-\nu)}(1+(-1)^{(\beta-\nu)+b})\end{aligned} \tag{H.4}$$

$$\begin{aligned}&U^3((\beta-\nu)\bar{\omega}_{\mathrm{qu}} + b\bar{\omega}_{\mathrm{cl}})\cdot\mathcal{R}_{\mathrm{SP}} = \\ &\quad[(1+(\alpha-\nu)\bar{\omega}_{\mathrm{qu}} + a\bar{\omega}_{\mathrm{cl}})(1+(\gamma-\nu)\bar{\omega}_{\mathrm{qu}} + c\bar{\omega}_{\mathrm{cl}})]^{-1} \\ &+ [(1+(\alpha-\nu)\bar{\omega}_{\mathrm{qu}} + a\bar{\omega}_{\mathrm{cl}})(1+(\gamma-\beta)\bar{\omega}_{\mathrm{qu}} + (c-b)\bar{\omega}_{\mathrm{cl}})]^{-1} \\ &+ [(1+(\alpha-\beta)\bar{\omega}_{\mathrm{qu}} + (a-b)\bar{\omega}_{\mathrm{cl}})(1+(\gamma-\beta)\bar{\omega}_{\mathrm{qu}} + (c-b)\bar{\omega}_{\mathrm{cl}})]^{-1} \\ &+ [(1+(\alpha-\beta)\bar{\omega}_{\mathrm{qu}} + (a-b)\bar{\omega}_{\mathrm{cl}})(1+(\gamma-\nu)\bar{\omega}_{\mathrm{qu}} + c\bar{\omega}_{\mathrm{cl}})]^{-1}.\end{aligned} \tag{H.5}$$

Comparing this result to the fourth-order expansion, we find that this result almost resembles the contribution of the NC-path (equation (G.15)). The amplitude is missing a factor of four, while the resolvent has the correct term (the second line of equation (H.5)) and three additional contributions.

In a setting, where scattering of b photons from the drive to the cavity, bringing it from ν photons to β photons, is resonant, we can expand $\mathcal{R}_{\mathrm{SP}}$ in the detuning $\bar{\Delta} = (\beta-\nu)\omega_{\mathrm{qu}} + b\bar{\omega}_{\mathrm{cl}} \ll 1$:

$$\begin{aligned}&U^3\bar{\Delta}\cdot\mathcal{R}_{\mathrm{SP}} = \\ &\quad[(1+(\alpha-\nu)\bar{\omega}_{\mathrm{qu}} + a\bar{\omega}_{\mathrm{cl}})(1+(\gamma-\nu)\bar{\omega}_{\mathrm{qu}} + c\bar{\omega}_{\mathrm{cl}})]^{-1} \\ &+ [(1+(\alpha-\nu)\bar{\omega}_{\mathrm{qu}} + a\bar{\omega}_{\mathrm{cl}})(1+(\gamma-\nu)\bar{\omega}_{\mathrm{qu}} + c\bar{\omega}_{\mathrm{cl}} - \bar{\Delta})]^{-1} \\ &+ [(1+(\alpha-\nu)\bar{\omega}_{\mathrm{qu}} + a\bar{\omega}_{\mathrm{cl}} - \bar{\Delta})(1+(\gamma-\nu)\bar{\omega}_{\mathrm{qu}} + c\bar{\omega}_{\mathrm{cl}} - \bar{\Delta})]^{-1} \\ &+ [(1+(\alpha-\nu)\bar{\omega}_{\mathrm{qu}} + a\bar{\omega}_{\mathrm{cl}} - \bar{\Delta})(1+(\gamma-\nu)\bar{\omega}_{\mathrm{qu}} + c\bar{\omega}_{\mathrm{cl}})]^{-1}\end{aligned} \tag{H.6}$$

$$\begin{aligned}&= \frac{4}{(1+(\alpha-\nu)\bar{\omega}_{\mathrm{qu}} + a\bar{\omega}_{\mathrm{cl}})(1+(\gamma-\nu)\bar{\omega}_{\mathrm{qu}} + c\bar{\omega}_{\mathrm{cl}})} \\ &+ 2\frac{2+(\alpha+\gamma-2\nu)\bar{\omega}_{\mathrm{qu}} + (a+c)\bar{\omega}_{\mathrm{cl}}}{(1+(\alpha-\nu)\bar{\omega}_{\mathrm{qu}} + a\bar{\omega}_{\mathrm{cl}})^2(1+(\gamma-\nu)\bar{\omega}_{\mathrm{qu}} + c\bar{\omega}_{\mathrm{cl}})^2}\bar{\Delta} + \mathcal{O}(\bar{\Delta}^2)\end{aligned} \tag{H.7}$$

Since under this resonance condition the NC-paths contributions dominate over the S1- and DC-paths contributions, we can therefore the validity of the spin-photon Hamiltonian approach by choosing a small detuning $\Delta \ll U$ under the assumption, that the drive does not introduce any additional charge-cavity-Floquet resonances.

Bibliography

[1] Hohenberg, P.; Kohn, W.: Inhomogeneous Electron Gas. In: *Physical Review* 136.3B (1964), B864–B871.

[2] Kohn, W.; Sham, L. J.: Self-Consistent Equations Including Exchange and Correlation Effects. In: *Physical Review* 140.4A (1965), A1133–A1138.

[3] Kohn, W.: Nobel Lecture: Electronic structure of matter—wave functions and density functionals. In: *Reviews of Modern Physics* 71.5 (1999), 1253–1266.

[4] Anderson, P. W.: New Approach to the Theory of Superexchange Interactions. In: *Physical Review* 115.1 (1959), 2–13.

[5] Kanamori, J.: Electron Correlation and Ferromagnetism of Transition Metals. In: *Progress of Theoretical Physics* 30.3 (1963), 275–289.

[6] Bardeen, J.; Cooper, L. N.; Schrieffer, J. R.: Theory of Superconductivity. In: *Physical Review* 108.5 (1957), 1175–1204.

[7] Landau, L. D.: On the theory of the Fermi liquid. In: *Sov. Phys. JETP* 8.1 (1959), 70.

[8] Abrikosov, A. A.; Khalatnikov, I. M.: The theory of a fermi liquid (the properties of liquid 3He at low temperatures). In: *Reports on Progress in Physics* 22.1 (1959), 329–367.

[9] Abrikosov, A.; Gorkov, L.; Dzyaloshinski, I.; Silverman, R.: *Methods of Quantum Field Theory in Statistical Physics*. Dover Books on Physics. Dover Publications, 1975.

[10] Mott, N. F.: The Basis of the Electron Theory of Metals, with Special Reference to the Transition Metals. In: *Proceedings of the Physical Society. Section A* 62.7 (1949), 416–422.

[11] Bednorz, J. G.; Müller, K. A.: Possible high T-c superconductivity in the Ba-La-Cu-O system. In: *Zeitschrift für Physik B Condensed Matter* 64.2 (1986), 189–193.

[12] Emery, V. J.: Theory of high-T_c superconductivity in oxides. In: *Physical Review Letters* 58.26 (1987), 2794–2797.

[13] Zhang, F. C.; Rice, T. M.: Effective Hamiltonian for the superconducting Cu oxides. In: *Physical Review B* 37.7 (1988), 3759–3761.

[14] Seidel, A.; Marianetti, C. A.; Chou, F. C.; Ceder, G.; Lee, P. A.: S=1/2 chains and spin-Peierls transition in TiOCl. In: *Physical Review B* 67.2 (2003).

[15] Zhang, Y.-Z.; Jeschke, H. O.; Valentí, R.: Microscopic model for transitions from Mott to spin-Peierls insulator in TiOCl. In: *Physical Review B* 78.20 (2008).

[16] Rückamp, R. et al.: Optical study of orbital excitations in transition-metal oxides. In: *New Journal of Physics* 7 (2005), 144–144.

[17] Hubbard, J. In: *Proceedings of the Royal Society of London. Series A. Mathematical and Physical Sciences* 276.1365 (1963), 238–257.

[18] Gutzwiller, M. C.: Effect of Correlation on the Ferromagnetism of Transition Metals. In: *Physical Review Letters* 10.5 (1963), 159–162.

[19] Lieb, E. H.; Wu, F. Y.: Absence of Mott Transition in an Exact Solution of the Short-Range, One-Band Model in One Dimension. In: *Physical Review Letters* 20.25 (1968), 1445–1448.

[20] Metzner, W.; Vollhardt, D.: Correlated Lattice Fermions in $d = \infty$ Dimensions. In: *Physical Review Letters* 62.3 (1989), 324–327.

[21] Georges, A.; Kotliar, G.: Hubbard model in infinite dimensions. In: *Physical Review B* 45.12 (1992), 6479–6483.

[22] Toschi, A.; Katanin, A. A.; Held, K.: Dynamical vertex approximation: A step beyond dynamical mean-field theory. In: *Physical Review B* 75.4 (2007).

[23] Rubtsov, A. N.; Katsnelson, M. I.; Lichtenstein, A. I.: Dual fermion approach to nonlocal correlations in the Hubbard model. In: *Physical Review B* 77.3 (2008).

[24] Freericks, J. K.; Turkowski, V. M.; Zlatić, V.: Nonequilibrium Dynamical Mean-Field Theory. In: *Physical Review Letters* 97.26 (2006).

[25] Takahashi, M.: Half-filled Hubbard model at low temperature. In: *Journal of Physics C: Solid State Physics* 10.8 (1977), 1289–7301.

[26] Chao, K. A.; Spałek, J.; Oleś, A. M.: Canonical perturbation expansion of the Hubbard model. In: *Physical Review B* 18.7 (1978), 3453–3464.

[27] MacDonald, A. H.; Girvin, S. M.; Yoshioka, D.: t/U expansion for the Hubbard model. In: *Physical Review B* 37.16 (1988), 9753–9756.

[28] White, S. R.: Density matrix formulation for quantum renormalization groups. In: *Physical Review Letters* 69.19 (1992), 2863–2866.

[29] Zewail, A. H.: Femtochemistry: Atomic-Scale Dynamics of the Chemical Bond. In: *The Journal of Physical Chemistry A* 104.24 (2000), 5660–5694.

[30] Giannetti, C.; Capone, M.; Fausti, D.; Fabrizio, M.; Parmigiani, F.; Mihailovic, D.: Ultrafast optical spectroscopy of strongly correlated materials and high-temperature superconductors: a non-equilibrium approach. In: *Advances in Physics* 65.2 (2016), 58–238.

[31] Basov, D. N.; Averitt, R. D.; Hsieh, D.: Towards properties on demand in quantum materials. In: *Nature Materials* 16.11 (2017), 1077–1088.

[32] Bukov, M.; D'Alessio, L.; Polkovnikov, A.: Universal high-frequency behavior of periodically driven systems: from dynamical stabilization to Floquet engineering. In: *Advances in Physics* 64.2 (2015), 139–226.

[33] Schlawin, F.; Kennes, D. M.; Sentef, M. A.: Cavity quantum materials. In: *Applied Physics Reviews* 9.1 (2022).

[34] Czycholl, G.: *Theoretische Festkörperphysik*. Springer Berlin Heidelberg, 2008.

[35] Czycholl, G.: *Solid State Theory, Volume 2: Applications: Non-equilibrium, Behavior in External Fields, Collective Phenomena*. Springer Berlin Heidelberg, 2023.

[36] Arovas, D. P.; Berg, E.; Kivelson, S. A.; Raghu, S.: The Hubbard Model. In: *Annual Review of Condensed Matter Physics* 13.1 (2022), 239–274.

[37] Qin, M.; Schäfer, T.; Andergassen, S.; Corboz, P.; Gull, E.: The Hubbard Model: A Computational Perspective. In: *Annual Review of Condensed Matter Physics* 13.1 (2022), 275–302.

[38] Schäfer, T. et al.: Tracking the Footprints of Spin Fluctuations: A MultiMethod, Multi-Messenger Study of the Two-Dimensional Hubbard Model. In: *Physical Review X* 11.1 (2021).

[39] Essler, F. H. L.; Korepin, V. E.; Schoutens, K.: Complete solution of the one-dimensional Hubbard model. In: *Physical Review Letters* 67.27 (1991), 3848–3851.

[40] Liu, L.; Yao, H.; Berg, E.; White, S. R.; Kivelson, S. A.: Phases of the Infinite *U* Hubbard Model on Square Lattices. In: *Physical Review Letters* 108.12 (2012).

[41] Bonča, J.; Prelovšek, P.: Thermodynamics of the planar Hubbard model. In: *Physical Review B* 67.8 (2003).

[42] Harl, J.; Schimka, L.; Kresse, G.: Assessing the quality of the random phase approximation for lattice constants and atomization energies of solids. In: *Physical Review B* 81.11 (2010).

[43] Slater, J. C.: The Theory of Complex Spectra. In: *Physical Review* 34.10 (1929), 1293–1322.

[44] Haverkort, M.: Spin and orbital degrees of freedom in transition metal oxides and oxide thin films studied by soft x-ray absorption spectroscopy. PhD thesis. Universität zu Köln, 2005.

[45] Hund, F.: Zur Deutung verwickelter Spektren, insbesondere der Elemente Scandium bis Nickel. In: *Zeitschrift für Physik* 33.1 (1925), 345–371.

[46] Altland, A.; Simons, B. D.: *Condensed Matter Field Theory*. Cambridge University Press, 2010.

[47] Cohen-Tannoudji, C.; etc.; Dupont-Roc, J.; Grynberg, G.: *Photons and atoms*. en. Nashville, TN: John Wiley & Sons, 1989.

[48] Năstase, H.: *Classical Field Theory*. Cambridge University Press, 2019.

[49] Srednicki, M.: *Quantum Field Theory*. Cambridge University Press, 2007.

[50] Jackson, J. D.: *Classical Electrodynamics*. en. 3rd ed. Nashville, TN: John Wiley & Sons, 1998.

[51] Russakoff, G.: A Derivation of the Macroscopic Maxwell Equations. In: *American Journal of Physics* 38.10 (1970), 1188–1195.

[52] Bañados, M.; Reyes, I.: A short review on Noether's theorems, gauge symmetries and boundary terms. In: *International Journal of Modern Physics D* 25.10 (2016), 1630021.

[53] Kleinert, H.: *Multivalued Fields: In Condensed Matter, Electromagnetism, and Gravitation*. WORLD SCIENTIFIC, 2008.

[54] Noether, E.: Invariante Variationsprobleme. ger. In: *Nachrichten von der Gesellschaft der Wissenschaften zu Göttingen, Mathematisch-Physikalische Klasse* 1918 (1918), 235–257.

[55] Avery, S. G.; Schwab, B. U. W.: Noether's second theorem and Ward identities for gauge symmetries. In: *Journal of High Energy Physics* 2016.2 (2016).

[56] Brown, L. S.: *Quantum Field Theory*. Cambridge University Press, 1992.

[57] Weinberg, S.: *The Quantum Theory of Fields*. Cambridge University Press, 1995.

[58] Peskin, M. E.: *An Introduction To Quantum Field Theory*. CRC Press, 2018.

[59] Schäfer, C.; Ruggenthaler, M.; Rokaj, V.; Rubio, A.: Relevance of the Quadratic Diamagnetic and Self-Polarization Terms in Cavity Quantum Electrodynamics. In: *ACS Photonics* 7.4 (2020), 975–990.

[60] Kobe, D. H.: Gauge-invariant classical Hamiltonian formulation of the electrodynamics of nonrelativistic particles. In: *American Journal of Physics* 49.6 (1981), 581–588.

[61] Casimir, H. B. G.; Polder, D.: The Influence of Retardation on the London-van der Waals Forces. In: *Physical Review* 73.4 (1948), 360–372.

[62] Raja, A. et al.: Coulomb engineering of the bandgap and excitons in two-dimensional materials. In: *Nature Communications* 8.1 (2017).

[63] Loon, E. G. C. P. van; Schüler, M.; Springer, D.; Sangiovanni, G.; Tomczak, J. M.; Wehling, T. O.: Coulomb engineering of two-dimensional Mott materials. In: *npj 2D Materials and Applications* 7.1 (2023).

[64] Glauber, R. J.; Lewenstein, M.: Quantum optics of dielectric media. In: *Physical Review A* 43.1 (1991), 467–491.

[65] Li, J.; Golez, D.; Mazza, G.; Millis, A. J.; Georges, A.; Eckstein, M.: Electromagnetic coupling in tight-binding models for strongly correlated light and matter. In: *Physical Review B* 101.20 (2020).

[66] Montanaro, A.; Giusti, F.; Colja, M.; Brajnik, G.; Marciniak, A. M. A.; Sergo, R.; De Angelis, D.; Glerean, F.; Sparapassi, G.; Jarc, G.; Carrato, S.; Cautero, G.; Fausti, D.: Visible pump–mid infrared pump–broadband probe: Development and characterization of a three-pulse setup for single-shot ultrafast spectroscopy at 50 kHz. In: *Review of Scientific Instruments* 91.7 (2020).

[67] Montanaro, A.: Non-equilibrium response of quantum materials to resonant low-energy electronic photo-excitations. Available at https://hdl.handle.net/11368/3030498. PhD thesis. Trieste, Italy: Università degli Studi di Trieste, 2022.

[68] Zagoskin, A.: *Quantum Theory of Many-Body Systems: Techniques and Applications*. Springer International Publishing, 2014.

[69] Kubo, R.: Statistical-Mechanical Theory of Irreversible Processes. I. General Theory and Simple Applications to Magnetic and Conduction Problems. In: *Journal of the Physical Society of Japan* 12.6 (1957), 570–586.

[70] Casimir, H. B.: *On the attraction between two perfectly conducting plates*. In: *Proc. Kon. Ned. Akad. Wet.* Vol. 51. 1948, 793.

[71] Eckhardt, C. J.; Grankin, A.; Kennes, D. M.; Ruggenthaler, M.; Rubio, A.; Sentef, M. A.; Hafezi, M.; Michael, M. H.: Surface-mediated ultra-strong cavity coupling of two-dimensional itinerant electrons. 2024.

[72] Mortensen, N. A.: Mesoscopic electrodynamics at metal surfaces: — From quantum-corrected hydrodynamics to microscopic surface-response formalism. In: *Nanophotonics* 10.10 (2021), 2563–2616.

[73] Dmytruk, O.; Schiró, M.: Gauge fixing for strongly correlated electrons coupled to quantum light. In: *Physical Review B* 103.7 (2021).

[74] Power, E. A.; Zienau, S.: On the radiative contributions to the Van der Waals force. In: *Il Nuovo Cimento* 6.1 (1957), 7–17.

[75] Power, E. A.; Zienau, S.: Coulomb gauge in non-relativistic quantum electro-dynamics and the shape of spectral lines. In: *Philosophical Transactions of the Royal Society of London. Series A, Mathematical and Physical Sciences* 251.999 (1959), 427–454.

[76] Atkins, P. W.; Woolley, R. G.: The interaction of molecular multipoles with the electromagnetic field in the canonical formulation of non-covariant quantum electrodynamics. In: *Proceedings of the Royal Society of London. A. Mathematical and Physical Sciences* 319.1539 (1970), 549–563.

[77] Rabi, I. I.: Space Quantization in a Gyrating Magnetic Field. In: *Physical Review* 51.8 (1937), 652–654.

[78] Jaynes, E.; Cummings, F.: Comparison of quantum and semiclassical radiation theories with application to the beam maser. In: *Proceedings of the IEEE* 51.1 (1963), 89–109.

[79] Dicke, R. H.: Coherence in Spontaneous Radiation Processes. In: *Physical Review* 93.1 (1954), 99–110.

[80] Tavis, M.; Cummings, F. W.: Exact Solution for an N-Molecule—Radiation-Field Hamiltonian. In: *Physical Review* 170.2 (1968), 379–384.

[81] Peierls, R.: Zur Theorie des Diamagnetismus von Leitungselektronen. In: *Zeitschrift für Physik* 80.11–12 (1933), 763–791.

[82] Luttinger, J. M.: The Effect of a Magnetic Field on Electrons in a Periodic Potential. In: *Physical Review* 84.4 (1951), 814–817.

[83] Löwdin, P.-O.: Studies in Perturbation Theory. IV. Solution of Eigenvalue Problem by Projection Operator Formalism. In: *Journal of Mathematical Physics* 3.5 (1962), 969–982.

[84] Schrieffer, J. R.; Wolff, P. A.: Relation between the Anderson and Kondo Hamiltonians. In: *Physical Review* 149.2 (1966), 491–492.

[85] Shavitt, I.; Redmon, L. T.: Quasidegenerate perturbation theories. A canonical van Vleck formalism and its relationship to other approaches. In: *The Journal of Chemical Physics* 73.11 (1980), 5711–5717.

[86] Knetter, C.; Uhrig, G.: Perturbation theory by flow equations: dimerized and frustrated S = 1/2 chain. In: *The European Physical Journal B - Condensed Matter and Complex Systems* 13.2 (2000), 209–225.

[87] Krull, H.; Drescher, N. A.; Uhrig, G. S.: Enhanced perturbative continuous unitary transformations. In: *Physical Review B* 86.12 (2012).

[88] Hörmann, M.; Schmidt, K. P.: Projective cluster-additive transformation for quantum lattice models. In: *SciPost Physics* 15.3 (2023).

[89] Wick, G. C.: The Evaluation of the Collision Matrix. In: *Physical Review* 80.2 (1950), 268–272.

[90] Oitmaa, J.; Hamer, C.; Zheng, W.: *Series Expansion Methods for Strongly Interacting Lattice Models*. Cambridge University Press, 2006.

[91] Bravyi, S.; DiVincenzo, D. P.; Loss, D.: Schrieffer–Wolff transformation for quantum many-body systems. In: *Annals of Physics* 326.10 (2011), 2793–2826.

[92] Bukov, M.; Kolodrubetz, M.; Polkovnikov, A.: Schrieffer-Wolff Transformation for Periodically Driven Systems: Strongly Correlated Systems with Artificial Gauge Fields. In: *Physical Review Letters* 116.12 (2016).

[93] Sentef, M. A.; Li, J.; Künzel, F.; Eckstein, M.: Quantum to classical crossover of Floquet engineering in correlated quantum systems. In: *Physical Review Research* 2.3 (2020).

[94] Tsuji, N.; Barmettler, P.; Aoki, H.; Werner, P.: Nonequilibrium dynamical cluster theory. In: *Physical Review B* 90.7 (2014).

[95] Eckardt, A.: Colloquium: Atomic quantum gases in periodically driven optical lattices. In: *Reviews of Modern Physics* 89.1 (2017).

[96] Tsuji, N.; Oka, T.; Aoki, H.: Correlated electron systems periodically driven out of equilibrium: Floquet+DMFT formalism. In: *Physical Review B* 78.23 (2008).

[97] Ito, S.; Schüler, M.; Meierhofer, M.; Schlauderer, S.; Freudenstein, J.; Reimann, J.; Afanasiev, D.; Kokh, K. A.; Tereshchenko, O. E.; Güdde, J.; Sentef, M. A.; Höfer, U.; Huber, R.: Build-up and dephasing of Floquet–Bloch bands on subcycle timescales. In: *Nature* 616.7958 (2023), 696–701.

[98] Tokura, Y.; Nagaosa, N.: Orbital Physics in Transition-Metal Oxides. In: *Science* 288.5465 (2000), 462–468.

[99] Ahn, C.; Cavalleri, A.; Georges, A.; Ismail-Beigi, S.; Millis, A. J.; Triscone, J.-M.: Designing and controlling the properties of transition metal oxide quantum materials. In: *Nature Materials* 20.11 (2021), 1462–1468.

[100] Glawion, S.; Heidler, J.; Haverkort, M. W.; Duda, L. C.; Schmitt, T.; Strocov, V. N.; Monney, C.; Zhou, K. J.; Ruff, A.; Sing, M.; Claessen, R.: Two-Spinon and Orbital Excitations of the Spin-Peierls System TiOCl. In: *Physical Review Letters* 107.10 (2011).

[101] Schäfer, H.; Wartenpfuhl, F.; Weise, E.: Über Titanchloride. V. Titan(III)-oxychlorid. In: *Zeitschrift für anorganische und allgemeine Chemie* 295.3–4 (1958), 268–280.

[102] Saha-Dasgupta, T.; Valentí, R.; Rosner, H.; Gros, C.: TiOCl, an orbital-ordered system? In: *Europhysics Letters (EPL)* 67.1 (2004), 63–69.

[103] Beynon, R. J.; Wilson, J. A.: TiOCl, TiOBr-are these RVB d1, S=1/2 materials? The results of scandium substitution set in the context of other S=1/2 systems of current interest for high-temperature superconductivity and the metal-insulator transition. In: *Journal of Physics: Condensed Matter* 5.13 (1993), 1983–2000.

[104] Hemberger, J.; Hoinkis, M.; Klemm, M.; Sing, M.; Claessen, R.; Horn, S.; Loidl, A.: Heat capacity of the quantum magnet TiOCl. In: *Physical Review B* 72.1 (2005).

[105] Rückamp, R.; Baier, J.; Kriener, M.; Haverkort, M. W.; Lorenz, T.; Uhrig, G. S.; Jongen, L.; Möller, A.; Meyer, G.; Grüninger, M.: Zero-Field Incommensurate Spin-Peierls Phase with Interchain Frustration in TiOCl. In: *Physical Review Letters* 95.9 (2005).

[106] Fausti, D.; Lummen, T. T. A.; Angelescu, C.; Macovez, R.; Luzon, J.; Broer, R.; Rudolf, P.; Loosdrecht, P. H. M. van; Tristan, N.; Büchner, B.; Smaalen, S. van; Möller, A.; Meyer, G.; Taetz, T.: Symmetry disquisition on the TiOX phase diagram (X=Br,Cl). In: *Physical Review B* 75.24 (2007).

[107] Kataev, V.; Baier, J.; Möller, A.; Jongen, L.; Meyer, G.; Freimuth, A.: Orbital order in the low-dimensional quantum spin system TiOCl probed by ESR. In: *Physical Review B* 68.14 (2003).

[108] Caimi, G.; Degiorgi, L.; Kovaleva, N. N.; Lemmens, P.; Chou, F. C.: Infrared optical properties of the spin-1/2 quantum magnet TiOCl. In: *Physical Review B* 69.12 (2004).

[109] Schönleber, A.; Smaalen, S. van; Palatinus, L.: Structure of the incommensurate phase of the quantum magnet TiOCl. In: *Physical Review B* 73.21 (2006).

[110] Pytte, E.: Peierls instability in Heisenberg chains. In: *Physical Review B* 10.11 (1974), 4637–4642.

[111] Imai, T.; Chou, F. C.: Novel Spin-Gap Behavior in Layered S=1/2 Quantum Spin System TiOCl. 2003.

[112] Schmidt, K. P.; Knetter, C.; Uhrig, G. S.: Spectral properties of the dimerized and frustrated S=1/2 chain. In: *Physical Review B* 69.10 (2004).

[113] Shaz, M.; Smaalen, S. van; Palatinus, L.; Hoinkis, M.; Klemm, M.; Horn, S.; Claessen, R.: Spin-Peierls transition in TiOCl. In: *Physical Review B* 71.10 (2005).

[114] Polli, D.; Brida, D.; Mukamel, S.; Lanzani, G.; Cerullo, G.: Effective temporal resolution in pump-probe spectroscopy with strongly chirped pulses. In: *Physical Review A* 82.5 (2010).

[115] Aichhorn, M.; Saha-Dasgupta, T.; Valentí, R.; Glawion, S.; Sing, M.; Claessen, R.: Momentum-resolved single-particle spectral function for TiOCl from a combination of density functional and variational cluster calculations. In: *Physical Review B* 80.11 (2009).

[116] Saha-Dasgupta, T.; Lichtenstein, A.; Valentí, R.: Correlation effects on the electronic structure of TiOCl: A NTMO+DMFT study. In: *Physical Review B* 71.15 (2005).

[117] Metzner, W.: Linked-cluster expansion around the atomic limit of the Hubbard model. In: *Physical Review B* 43.10 (1991), 8549–8563.

[118] Koepernik, K.; Eschrig, H.: Full-potential nonorthogonal local-orbital minimum-basis band-structure scheme. In: *Physical Review B* 59.3 (1999), 1743–1757.

[119] Opahle, I.; Koepernik, K.; Eschrig, H.: Full-potential band-structure calculation of iron pyrite. In: *Physical Review B* 60.20 (1999), 14035–14041.

[120] Eschrig, H.; Koepernik, K.; Chaplygin, I.: Density functional application to strongly correlated electron systems. In: *Journal of Solid State Chemistry* 176.2 (2003), 482–495.

[121] Perdew, J. P.; Burke, K.; Ernzerhof, M.: Generalized Gradient Approximation Made Simple. In: *Physical Review Letters* 77.18 (1996), 3865–3868.

[122] Koepernik, K.; Janson, O.; Sun, Y.; Brink, J. van den: Symmetry-conserving maximally projected Wannier functions. In: *Physical Review B* 107.23 (2023).

[123] Shih, B.-C.; Zhang, Y.; Zhang, W.; Zhang, P.: Screened Coulomb interaction of localized electrons in solids from first principles. In: *Physical Review B* 85.4 (2012).

[124] Vaugier, L.; Jiang, H.; Biermann, S.: Hubbard U and Hund exchange J in transition metal oxides: Screening versus localization trends from constrained random phase approximation. In: *Physical Review B* 86.16 (2012).

[125] Haverkort, M.: Quanty Website. 2024. URL: https://quanty.org/ (visited on 11/04/2024).

[126] Haverkort, M. W.; Zwierzycki, M.; Andersen, O. K.: Multiplet ligand-field theory using Wannier orbitals. In: *Physical Review B* 85.16 (2012).

[127] Lu, Y.; Höppner, M.; Gunnarsson, O.; Haverkort, M. W.: Efficient real-frequency solver for dynamical mean-field theory. In: *Physical Review B* 90.8 (2014).

[128] Wang, Y.; Fabbris, G.; Dean, M.; Kotliar, G.: EDRIXS: An open source toolkit for simulating spectra of resonant inelastic x-ray scattering. In: *Computer Physics Communications* 243 (2019), 151–165.

[129] Eckstein, M.; Werner, P.: Simulation of time-dependent resonant inelastic x-ray scattering using nonequilibrium dynamical mean-field theory. In: *Physical Review B* 103.11 (2021).

[130] Werner, P.; Johnston, S.; Eckstein, M.: Nonequilibrium-DMFT based RIXS investigation of the two-orbital Hubbard model. In: *Europhysics Letters* 133.5 (2021), 57005.

[131] Shao, C.; Tohyama, T.; Luo, H.-G.; Lu, H.: Numerical method to compute optical conductivity based on pump-probe simulations. In: *Physical Review B* 93.19 (2016).

[132] Prelovšek, P.; Bonča, J.: Ground State and Finite Temperature Lanczos Methods. In: *Strongly Correlated Systems*. Springer Berlin Heidelberg, 2013, 1–30.

[133] Koch, E.: The Lanczos Method. In: *Many-body physics: From Kondo to Hubbard*. Ed. by Pavarini, E.; Koch, E.; Coleman, P. Schriften des Forschungszentrums Jülich Reihe Modeling and Simulation. Forschungszentrum Jülich, 2015, 313–342.

[134] Prelovšek, P.: The Finite Temperature Lanczos Method and its Applications. In: *The physics of correlated insulators, metals, and superconductors*. Ed. by Pavarini, E.; Koch, E.; Scalettar, R.; Martin, R. Schriften des Forschungszentrums Jülich Reihe Modeling and Simulation. Forschungszentrum Jülich, 2017, 175–197.

[135] Ericsson, T.; Ruhe, A.: The spectral transformation Lanczos method for the numerical solution of large sparse generalized symmetric eigenvalue problems. In: *Mathematics of Computation* 35.152 (1980), 1251–1268.

[136] Meerbergen, K.; Spence, A.; Roose, D.: Shift-invert and Cayley transforms for detection of rightmost eigenvalues of nonsymmetric matrices. In: *BIT* 34.3 (1994), 409–423.

[137] Lehoucq, R. B.; Salinger, A. G.: Large-scale eigenvalue calculations for stability analysis of steady flows on massively parallel computers. In: *International Journal for Numerical Methods in Fluids* 36.3 (2001), 309–327.

[138] Sachdev, S.; Bhatt, R. N.: Bond-operator representation of quantum spins: Mean-field theory of frustrated quantum Heisenberg antiferromagnets. In: *Physical Review B* 41.13 (1990), 9323–9329.

[139] Bethe, H.: Zur Theorie der Metalle: I. Eigenwerte und Eigenfunktionen der linearen Atomkette. In: *Zeitschrift für Physik* 71.3–4 (1931), 205–226.

[140] Mattis, D. C.: *The theory of magnetism I: Statics and Dynamics*. Springer Series in Solid-State Sciences. Berlin, Germany: Springer, 1987.

[141] Spronken, G.; Fourcade, B.; Lépine, Y.: Finite-size study of the one-dimensional spin-(1/2) dimerized Heisenberg chain. In: *Physical Review B* 33.3 (1986), 1886–1903.

[142] Hansmann, P.; Haverkort, M. W.; Toschi, A.; Sangiovanni, G.; Rodolakis, F.; Rueff, J. P.; Marsi, M.; Held, K.: Atomic and itinerant effects at the transition-metal x-ray absorption K pre-edge exemplified in the case of V_2O_3. In: *Physical Review B* 85.11 (2012).

[143] Glawion, S.; Haverkort, M. W.; Berner, G.; Hoinkis, M.; Gavrila, G.; Kraus, R.; Knupfer, M.; Sing, M.; Claessen, R.: Unoccupied electronic structure of TiOCl studied using x-ray absorption near-edge spectroscopy. In: *Journal of Physics: Condensed Matter* 24.25 (2012), 255602.

[144] Kunnus, K. et al.: Anti-Stokes resonant x-ray Raman scattering for atom specific and excited state selective dynamics. In: *New Journal of Physics* 18.10 (2016), 103011.

[145] Bilous, P.; Thirion, L.; Menke, H.; Haverkort, M. W.; Pálffy, A.; Hansmann, P.: Neural-network-supported basis optimizer for the configuration interaction problem in quantum many-body clusters: Feasibility study and numerical proof. 2024.

[146] Thirion, L.; Hansmann, P.; Bilous, P.: SOLAX: A Python solver for fermionic quantum systems with neural network support. 2024.

[147] Schmerwitz, Y. L. A.; Thirion, L.; Levi, G.; Jónsson, E. Ö.; Bilous, P.; Jónsson, H.; Hansmann, P.: Revisiting N_2 with Neural-Network-Supported CI. 2024.

[148] Georges, A.; Kotliar, G.; Krauth, W.; Rozenberg, M. J.: Dynamical mean-field theory of strongly correlated fermion systems and the limit of infinite dimensions. In: *Reviews of Modern Physics* 68.1 (1996), 13–125.

[149] Aoki, H.; Tsuji, N.; Eckstein, M.; Kollar, M.; Oka, T.; Werner, P.: Nonequilibrium dynamical mean-field theory and its applications. In: *Reviews of Modern Physics* 86.2 (2014), 779–837.

[150] Breuer, H.-P.; Petruccione, F.: *The Theory of Open Quantum Systems*. Oxford University PressOxford, 2007.

[151] Alicki, R.: The Markov master equations and the Fermi golden rule. In: *International Journal of Theoretical Physics* 16.5 (1977), 351–355.

[152] Maier, T.; Jarrell, M.; Pruschke, T.; Hettler, M. H.: Quantum cluster theories. In: *Reviews of Modern Physics* 77.3 (2005), 1027–1080.

[153] Lichtenstein, A. I.; Katsnelson, M. I.: Antiferromagnetism and d-wave superconductivity in cuprates: A cluster dynamical mean-field theory. In: *Physical Review B* 62.14 (2000), R9283–R9286.

[154] Kotliar, G.; Savrasov, S. Y.; Pálsson, G.; Biroli, G.: Cellular Dynamical Mean Field Approach to Strongly Correlated Systems. In: *Physical Review Letters* 87.18 (2001).

[155] Parcollet, O.; Biroli, G.; Kotliar, G.: Cluster Dynamical Mean Field Analysis of the Mott Transition. In: *Physical Review Letters* 92.22 (2004).

[156] Park, H.; Haule, K.; Kotliar, G.: Cluster Dynamical Mean Field Theory of the Mott Transition. In: *Physical Review Letters* 101.18 (2008).

[157] Keldysh, L. V.: Diagram technique for nonequilibrium processes. In: *SOVIET PHYSICS JETP* 20.4 (1965).

[158] Herrmann, A. J.; Tsuji, N.; Eckstein, M.; Werner, P.: Nonequilibrium dynamical cluster approximation study of the Falicov-Kimball model. In: *Physical Review B* 94.24 (2016).

[159] Fermi, E.: *Nuclear physics*. Univ. of Chicago Press, 1953, 142.

[160] Kosloff, R.: Quantum thermodynamics and open-systems modeling. In: *The Journal of Chemical Physics* 150.20 (2019).

[161] Kugel', K. I.; Khomskiĭ, D. I.: The Jahn-Teller effect and magnetism: transition metal compounds. In: *Soviet Physics Uspekhi* 25.4 (1982), 231–256.

[162] Müller, A.; Grandi, F.; Eckstein, M.: Ultrafast control of spin-orbital separation probed with time-resolved resonant inelastic x-ray scattering. In: *Physical Review B* 106.12 (2022).

[163] Lenarčič, Z.; Prelovšek, P.: Ultrafast Charge Recombination in a Photoexcited Mott-Hubbard Insulator. In: *Physical Review Letters* 111.1 (2013).

[164] Prelovšek, P.; Bonča, J.: Ground State and Finite Temperature Lanczos Methods. In: *Strongly Correlated Systems*. Ed. by Avella, A.; Mancini, F. Springer Berlin Heidelberg, 2013, 1–30.

[165] Lanczos, C.: An iteration method for the solution of the eigenvalue problem of linear differential and integral operators. In: *Journal of Research of the National Bureau of Standards* 45.4 (1950), 255.

[166] Demmel, J. W.: *Applied Numerical Linear Algebra*. Society for Industrial and Applied Mathematics, 1997.

[167] Anderson, E.; Bai, Z.; Bischof, C.; Blackford, L. S.; Demmel, J.; Dongarra, J.; Du Croz, J.; Greenbaum, A.; Hammarling, S.; McKenney, A.; Sorensen, D.: *LAPACK Users' Guide*. Society for Industrial and Applied Mathematics, 1999.

[168] OpenBLAS Website. 2024. URL: http://www.openblas.net/ (visited on 11/25/2024).

[169] Balay, S. et al.: PETSc Web page. https://petsc.org/. 2024.

[170] Balay, S. et al.: *PETSc/TAO Users Manual*. Tech. rep. ANL-21/39 - Revision 3.22. Argonne National Laboratory, 2024.

[171] Hernandez, V.; Roman, J. E.; Vidal, V.: SLEPc: A scalable and flexible toolkit for the solution of eigenvalue problems. In: *ACM Transactions on Mathematical Software* 31.3 (2005), 351–362.

[172] Zhang, J.; Brown, J.; Balay, S.; Faibussowitsch, J.; Knepley, M.; Marin, O.; Mills, R. T.; Munson, T.; Smith, B. F.; Zampini, S.: The PetscSF Scalable Communication Layer. In: *IEEE Transactions on Parallel and Distributed Systems* 33.4 (2022), 842–853.

[173] Wietek, A.; Läuchli, A. M.: Sublattice coding algorithm and distributed memory parallelization for large-scale exact diagonalizations of quantum many-body systems. In: *Physical Review E* 98.3 (2018).

[174] Hernandez, V.; Roman, J. E.; Tomas, A.; Vidal, V.: *A survey of software for sparse eigenvalue problems*. Tech. rep. STR-7. Available at https://slepc.upv.es. Universitat Politècnica de València, 2009.

[175] Pisani, L.; Valentí, R.; Montanari, B.; Harrison, N. M.: Density functional study of the electronic and vibrational properties of TiOCl. In: *Physical Review B* 76.23 (2007).

[176] Kukura, P.; McCamant, D. W.; Mathies, R. A.: Femtosecond Stimulated Raman Spectroscopy. In: *Annual Review of Physical Chemistry* 58.1 (2007), 461–488.

[177] Chitra, R.; Pati, S.; Krishnamurthy, H. R.; Sen, D.; Ramasesha, S.: Density-matrix renormalization-group studies of the spin-1/2 Heisenberg system with dimerization and frustration. In: *Physical Review B* 52.9 (1995), 6581–6587.

[178] Fausti, D.; Tobey, R. I.; Dean, N.; Kaiser, S.; Dienst, A.; Hoffmann, M. C.; Pyon, S.; Takayama, T.; Takagi, H.; Cavalleri, A.: Light-Induced Superconductivity in a Stripe-Ordered Cuprate. In: *Science* 331.6014 (2011), 189–191.

[179] Lemmens, P.; Choi, K. Y.; Valentí, R.; Saha-Dasgupta, T.; Abel, E.; Lee, Y. S.; Chou, F. C.: Spin gap formation in the quantum spin systems TiOX, X=Cl and Br. In: *New Journal of Physics* 7 (2005), 74–74.

[180] Macovez, R.; Luzon, J.; Schiessling, J.; Sadoc, A.; Kjeldgaard, L.; Smaalen, S. van; Fausti, D.; Loosdrecht, P. H. M. van; Broer, R.; Rudolf, P.: Hybridization, superexchange, and competing magnetoelastic interactions in TiOBr. In: *Physical Review B* 76.20 (2007).

[181] Hoinkis, M.; Sing, M.; Glawion, S.; Pisani, L.; Valentí, R.; Smaalen, S. van; Klemm, M.; Horn, S.; Claessen, R.: One-dimensional versus two-dimensional correlation effects in the oxyhalides TiOCl and TiOBr. In: *Physical Review B* 75.24 (2007).

[182] Torre, A. de la; Kennes, D. M.; Claassen, M.; Gerber, S.; McIver, J. W.; Sentef, M. A.: Colloquium: Nonthermal pathways to ultrafast control in quantum materials. In: *Reviews of Modern Physics* 93.4 (2021).

[183] Garcia-Vidal, F. J.; Ciuti, C.; Ebbesen, T. W.: Manipulating matter by strong coupling to vacuum fields. In: *Science* 373.6551 (2021).

[184] Bloch, J.; Cavalleri, A.; Galitski, V.; Hafezi, M.; Rubio, A.: Strongly correlated electron–photon systems. In: *Nature* 606.7912 (2022), 41–48.

[185] Schiffrin, A. et al.: Optical-field-induced current in dielectrics. In: *Nature* 493.7430 (2012), 70–74.

[186] Wang, Y. H.; Steinberg, H.; Jarillo-Herrero, P.; Gedik, N.: Observation of Floquet-Bloch States on the Surface of a Topological Insulator. In: *Science* 342.6157 (2013), 453–457.

[187] Sentef, M.; Claassen, M.; Kemper, A.; Moritz, B.; Oka, T.; Freericks, J.; Devereaux, T.: Theory of Floquet band formation and local pseudospin textures in pump-probe photoemission of graphene. In: *Nature Communications* 6.1 (2015).

[188] Mahmood, F.; Chan, C.-K.; Alpichshev, Z.; Gardner, D.; Lee, Y.; Lee, P. A.; Gedik, N.: Selective scattering between Floquet–Bloch and Volkov states in a topological insulator. In: *Nature Physics* 12.4 (2016), 306–310.

[189] Mitrano, M.; Cantaluppi, A.; Nicoletti, D.; Kaiser, S.; Perucchi, A.; Lupi, S.; Di Pietro, P.; Pontiroli, D.; Riccò, M.; Clark, S. R.; Jaksch, D.; Cavalleri, A.: Possible light-induced superconductivity in K3C60 at high temperature. In: *Nature* 530.7591 (2016), 461–464.

[190] Bretscher, H. M.; Andrich, P.; Telang, P.; Singh, A.; Harnagea, L.; Sood, A. K.; Rao, A.: Ultrafast melting and recovery of collective order in the excitonic insulator Ta2NiSe5. In: *Nature Communications* 12.1 (2021).

[191] Marciniak, A.; Marcantoni, S.; Giusti, F.; Glerean, F.; Sparapassi, G.; Nova, T.; Cartella, A.; Latini, S.; Valiera, F.; Rubio, A.; Brink, J. van den; Benatti, F.; Fausti, D.: Vibrational coherent control of localized d–d electronic excitation. In: *Nature Physics* 17.3 (2021), 368–373.

[192] Montanaro, A.; Giusti, F.; Zanfrognini, M.; Di Pietro, P.; Glerean, F.; Jarc, G.; Rigoni, E. M.; Mathengattil, S. Y.; Varsano, D.; Rontani, M.; Perucchi, A.; Molinari, E.; Fausti, D.: Anomalous non-equilibrium response in black phosphorus to sub-gap mid-infrared excitation. In: *Nature Communications* 13.1 (2022).

[193] Jarc, G.; Mathengattil, S. Y.; Montanaro, A.; Giusti, F.; Rigoni, E. M.; Sergo, R.; Fassioli, F.; Winnerl, S.; Dal Zilio, S.; Mihailovic, D.; Prelovšek, P.; Eckstein, M.; Fausti, D.: Cavity-mediated thermal control of metal-to-insulator transition in 1T-TaS2. In: *Nature* 622.7983 (2023), 487–492.

[194] Kipp, G. et al.: Cavity electrodynamics of van der Waals heterostructures. 2024.

[195] Afanasiev, D.; Gatilova, A.; Groenendijk, D. J.; Ivanov, B. A.; Gibert, M.; Gariglio, S.; Mentink, J.; Li, J.; Dasari, N.; Eckstein, M.; Rasing, T.; Caviglia, A. D.; Kimel, A. V.: Ultrafast Spin Dynamics in Photodoped Spin-Orbit Mott Insulator Sr_2IrO_4. In: *Physical Review X* 9.2 (2019).

[196] Itin, A. P.; Katsnelson, M. I.: Effective Hamiltonians for Rapidly Driven Many-Body Lattice Systems: Induced Exchange Interactions and Density-Dependent Hoppings. In: *Physical Review Letters* 115.7 (2015).

[197] Oka, T.; Kitamura, S.: Floquet Engineering of Quantum Materials. In: *Annual Review of Condensed Matter Physics* 10.1 (2019), 387–408.

[198] Petrosyan, D.; Fleischhauer, M.: Quantum Information Processing with Single Photons and Atomic Ensembles in Microwave Coplanar Waveguide Resonators. In: *Physical Review Letters* 100.17 (2008).

[199] Kiffner, M.; Coulthard, J. R.; Schlawin, F.; Ardavan, A.; Jaksch, D.: Manipulating quantum materials with quantum light. In: *Physical Review B* 99.8 (2019).

[200] Li, J.; Schamriß, L.; Eckstein, M.: Effective theory of lattice electrons strongly coupled to quantum electromagnetic fields. In: *Physical Review B* 105.16 (2022).

[201] Wang, Y. K.; Hioe, F. T.: Phase Transition in the Dicke Model of Superradiance. In: *Physical Review A* 7.3 (1973), 831–836.

[202] Hepp, K.; Lieb, E. H.: On the superradiant phase transition for molecules in a quantized radiation field: the dicke maser model. In: *Annals of Physics* 76.2 (1973), 360–404.

[203] Mazza, G.; Georges, A.: Superradiant Quantum Materials. In: *Physical Review Letters* 122.1 (2019).

[204] Schellenberger, A.; Schmidt, K. P.: (Almost) everything is a Dicke model - Mapping non-superradiant correlated light-matter systems to the exactly solvable Dicke model. In: *SciPost Physics Core* 7.3 (2024).

[205] Ashida, Y.; İmamoğlu, A.; Faist, J.; Jaksch, D.; Cavalleri, A.; Demler, E.: Quantum Electrodynamic Control of Matter: Cavity-Enhanced Ferroelectric Phase Transition. In: *Physical Review X* 10.4 (2020).

[206] Lenk, K.; Li, J.; Werner, P.; Eckstein, M.: Dynamical mean-field study of a photon-mediated ferroelectric phase transition. In: *Physical Review B* 106.24 (2022).

[207] Sentef, M. A.; Ruggenthaler, M.; Rubio, A.: Cavity quantum-electrodynamical polaritonically enhanced electron-phonon coupling and its influence on superconductivity. In: *Science Advances* 4.11 (2018).

[208] Schlawin, F.; Cavalleri, A.; Jaksch, D.: Cavity-Mediated Electron-Photon Superconductivity. In: *Physical Review Letters* 122.13 (2019).

[209] Chiocchetta, A.; Kiese, D.; Zelle, C. P.; Piazza, F.; Diehl, S.: Cavity-induced quantum spin liquids. In: *Nature Communications* 12.1 (2021).

[210] Mottl, R.; Brennecke, F.; Baumann, K.; Landig, R.; Donner, T.; Esslinger, T.: Roton-Type Mode Softening in a Quantum Gas with Cavity-Mediated Long-Range Interactions. In: *Science* 336.6088 (2012), 1570–1573.

[211] Klinder, J.; Keßler, H.; Bakhtiari, M. R.; Thorwart, M.; Hemmerich, A.: Observation of a Superradiant Mott Insulator in the Dicke-Hubbard Model. In: *Physical Review Letters* 115.23 (2015).

[212] Landig, R.; Hruby, L.; Dogra, N.; Landini, M.; Mottl, R.; Donner, T.; Esslinger, T.: Quantum phases from competing short- and long-range interactions in an optical lattice. In: *Nature* 532.7600 (2016), 476–479.

[213] Kapale, K. T.; Agarwal, G. S.; Scully, M. O.: Cavity-mediated long-range interaction for fast multiqubit quantum logic operations. In: *Physical Review A* 72.5 (2005).

[214] Eckhardt, C. J.; Chattopadhyay, S.; Kennes, D. M.; Demler, E. A.; Sentef, M. A.; Michael, M. H.: Theory of resonantly enhanced photo-induced superconductivity. In: *Nature Communications* 15.1 (2024).

[215] Gao, H.; Schlawin, F.; Buzzi, M.; Cavalleri, A.; Jaksch, D.: Photoinduced Electron Pairing in a Driven Cavity. In: *Physical Review Letters* 125.5 (2020).

[216] Wang, X.; Jaksch, D.; Schlawin, F.: Excitonic enhancement of cavity-mediated interactions in a two-band Hubbard model. In: *Physical Review B* 109.11 (2024).

[217] Mentink, J. H.; Balzer, K.; Eckstein, M.: Ultrafast and reversible control of the exchange interaction in Mott insulators. In: *Nature Communications* 6.1 (2015).

[218] Claassen, M.; Jiang, H.-C.; Moritz, B.; Devereaux, T. P.: Dynamical time-reversal symmetry breaking and photo-induced chiral spin liquids in frustrated Mott insulators. In: *Nature Communications* 8.1 (2017).

[219] Li, J.; Eckstein, M.: Manipulating Intertwined Orders in Solids with Quantum Light. In: *Physical Review Letters* 125.21 (2020).

[220] Viñas Boström, E.; Sriram, A.; Claassen, M.; Rubio, A.: Controlling the magnetic state of the proximate quantum spin liquid α-RuCl3 with an optical cavity. In: *npj Computational Materials* 9.1 (2023).

[221] Grunwald, L.; Boström, E. V.; Svendsen, M. K.; Kennes, D. M.; Rubio, A.: Cavity Spectroscopy for Strongly Correlated Systems. 2024.

[222] Maschler, C.; Ritsch, H.: Cold Atom Dynamics in a Quantum Optical Lattice Potential. In: *Physical Review Letters* 95.26 (2005).

[223] Maissen, C.; Scalari, G.; Valmorra, F.; Beck, M.; Faist, J.; Cibella, S.; Leoni, R.; Reichl, C.; Charpentier, C.; Wegscheider, W.: Ultrastrong coupling in the near field of complementary split-ring resonators. In: *Physical Review B* 90.20 (2014).

[224] Jarc, G.; Mathengattil, S. Y.; Giusti, F.; Barnaba, M.; Singh, A.; Montanaro, A.; Glerean, F.; Rigoni, E. M.; Zilio, S. D.; Winnerl, S.; Fausti, D.: Tunable cryogenic terahertz cavity for strong light–matter coupling in complex materials. In: *Review of Scientific Instruments* 93.3 (2022).

[225] Murakami, Y.; Tsuji, N.; Eckstein, M.; Werner, P.: Nonequilibrium steady states and transient dynamics of conventional superconductors under phonon driving. In: *Physical Review B* 96.4 (2017).

[226] Hasegawa, T.; Kagoshima, S.; Mochida, T.; Sugiura, S.; Iwasa, Y.: Electronic states and anti-ferromagnetic order in mixed-stack charge-transfer compound (BEDT-TTF)(F2TCNQ). In: *Solid State Communications* 103.8 (1997), 489–493.

[227] Mitrano, M.; Cotugno, G.; Clark, S. R.; Singla, R.; Kaiser, S.; Stähler, J.; Beyer, R.; Dressel, M.; Baldassarre, L.; Nicoletti, D.; Perucchi, A.; Hasegawa, T.; Okamoto, H.; Jaksch, D.; Cavalleri, A.: Pressure-Dependent Relaxation in the Photoexcited Mott Insulator ET-F_2TCNQ influence of Hopping and Correlations on Quasiparticle Recombination Rates. In: *Physical Review Letters* 112.11 (2014).

[228] Desbuquois, R.; Messer, M.; Görg, F.; Sandholzer, K.; Jotzu, G.; Esslinger, T.: Controlling the Floquet state population and observing micromotion in a periodically driven two-body quantum system. In: *Physical Review A* 96.5 (2017).

[229] Chaudhary, S.; Hsieh, D.; Refael, G.: Orbital Floquet engineering of exchange interactions in magnetic materials. In: *Physical Review B* 100.22 (2019).

[230] Gao, H.; Coulthard, J. R.; Jaksch, D.; Mur-Petit, J.: Anomalous Spin-Charge Separation in a Driven Hubbard System. In: *Physical Review Letters* 125.19 (2020).

[231] Shastry, B. S.; Shraiman, B. I.: Theory of Raman scattering in Mott-Hubbard systems. In: *Physical Review Letters* 65.8 (1990), 1068–1071.

[232] Löwdin, P.-O.: Studies in Perturbation Theory. IV. Solution of Eigenvalue Problem by Projection Operator Formalism. In: *Journal of Mathematical Physics* 3.5 (1962), 969–982.

[233] Lemmens, P.; Choi, K. Y.; Caimi, G.; Degiorgi, L.; Kovaleva, N. N.; Seidel, A.; Chou, F. C.: Giant phonon softening in the pseudogap phase of the quantum spin system TiOCl. In: *Physical Review B* 70.13 (2004).

[234] Pilar, P.; De Bernardis, D.; Rabl, P.: Thermodynamics of ultrastrongly coupled light-matter systems. In: *Quantum* 4 (2020), 335.

[235] Lenk, K.; Li, J.; Werner, P.; Eckstein, M.: Collective theory for an interacting solid in a single-mode cavity. 2022.

[236] De Bernardis, D.; Jaako, T.; Rabl, P.: Cavity quantum electrodynamics in the nonperturbative regime. In: *Physical Review A* 97.4 (2018).

[237] Latini, S.; Shin, D.; Sato, S. A.; Schäfer, C.; De Giovannini, U.; Hübener, H.; Rubio, A.: The ferroelectric photo ground state of SrTiO 3 ?: Cavity materials engineering. In: *Proceedings of the National Academy of Sciences* 118.31 (2021).

[238] Andolina, G. M.; Pellegrino, F. M. D.; Giovannetti, V.; MacDonald, A. H.; Polini, M.: Cavity quantum electrodynamics of strongly correlated electron systems: A no-go theorem for photon condensation. In: *Physical Review B* 100.12 (2019).

[239] Andolina, G. M.; Pellegrino, F. M. D.; Giovannetti, V.; MacDonald, A. H.; Polini, M.: Theory of photon condensation in a spatially varying electromagnetic field. In: *Physical Review B* 102.12 (2020).

[240] Yang, L.; Weinberg, P.; Feiguin, A.: Topological to magnetically ordered quantum phase transition in antiferromagnetic spin ladders with long-range interactions. In: *SciPost Physics* 13.3 (2022).

[241] Adelhardt, P.; Koziol, J. A.; Langheld, A.; Schmidt, K. P.: Monte Carlo Based Techniques for Quantum Magnets with Long-Range Interactions. In: *Entropy* 26.5 (2024), 401.

[242] Adelhardt, P.; Schmidt, K. P.: Continuously varying critical exponents in long-range quantum spin ladders. In: *SciPost Physics* 15.3 (2023).

[243] Starkov, G. A.; Fistul, M. V.; Eremin, I. M.: Schrieffer-Wolff transformation for non-Hermitian systems: Application for PT-symmetric circuit QED. In: *Physical Review B* 108.23 (2023).

[244] Ashida, Y.; Yokota, T.; İmamoğlu, A.; Demler, E.: Nonperturbative waveguide quantum electrodynamics. In: *Physical Review Research* 4.2 (2022).

[245] Svendsen, M. K.; Ruggenthaler, M.; Hübener, H.; Schäfer, C.; Eckstein, M.; Rubio, A.; Latini, S.: Theory of Quantum Light-Matter Interaction in Cavities: Extended Systems and the Long Wavelength Approximation. 2023.

[246] Arnaud, J. A.: Degenerate Optical Cavities. In: *Applied Optics* 8.1 (1969), 189.

[247] Sakurai, J. J.; Freedman, D. Z.: Advanced Quantum Mechanics. In: *American Journal of Physics* 36.5 (1968), 465–466.

Own publications referring to this work

[P1] Montanaro, A.; Fadler, P.; Rigoni, E. M.; Glerean, F.; Hansmann, P.; Schmidt, K. P.; Eckstein, M.; Fausti, D.: Inter-orbital scattering dynamics in a low-dimensional antiferromagnet. 2025.

[P2] Fadler, P.; Schmidt, K. P.; Li, J.; Eckstein, M.: Engineering photon-mediated long-range spin interactions in Mott insulators. In: *Physical Review B* 109.8 (2024).

Acknowledgements

A friend and colleague of mine once compared writing a thesis to running a marathon. Similar to a marathon, it has indeed been a long and arduous journey with many ups and down. Since one usually has to do the running part of a marathon alone, in my opinion, this analogy does not do the support and assistance I received on the way justice. I therefore want to use this last page to thank the people, who helped me on the way.

Most importantly of which, I want to thank my supervisors Martin and Kai. Both of them gave me the space to explore, learn, fail, grow and succeed on my journey, while always being available for helpful advise on the way. Therein Martin not only managed to hand me advise on correlated out-of-equilibrium systems, but also some of his passion for working in that field. I am also thankful to him for moving me to the TiOCl project, that became Chapters 3 and 4 of this thesis. Starting this new project and the collaboration with Angela, Daniele and Philipp brought some fresh wind into my PhD at a time, where it felt like this was exactly needed. Without Kai this thesis would also not have been possible. His talks and lectures were what originally drew me to starting my PhD in condensed matter physics. Despite his filled schedule it was always possible to find time to discuss with him. It was great to work within Qucolima and one could definitely feel, that he was one of the driving forces behind making it that way.

I also want to thank Philipp for always taking the time to answer my many questions on real materials to me at a time, when I barely understood toy models. I am grateful to Angela and Daniele for allowing me to use their experimental data in my thesis. Their patience allowed me to gain some insights in to the experimental side of condensed matter physics and has lasted all the way through the feature creep, that became half of this thesis.

The support of Niklas and Patrick and the extra work they did on my behalf also deserves a special mention: Niklas performed an additional DFT calculation with cRPA for TiOCl and his crystallographic expertise helped in creating some of the figures in Chapter 3. Patrick revived the old series expansions of Kai's thesis on the dimerized Heisenberg model. I am also thankful to Jiajun for his work prior to me starting my thesis and his assistance during its beginning.

I want to thank Henri, Benedikt, Matthias 1, Matthias 2, Robert and Christopher for their C++-, Linux- and general IT-support. I also want to thank the current and former members of the chairs for theoretical condensed matter physics, theory 1, theory 5 and the AGMM for the enjoyable social environment, which persisted even virtually during the pandemic. I hope that once I am an alumni these groups new advocates for coffee breaks can be found (although I think Louis and Viktor are up to the task).

A special thanks also goes to Andreas, Angela, Anja, Antonio, Benedikt, Janna, Matthias 1 and Philipp for proof reading small and large parts of this thesis.

Last but not least, I want to thank Ursula and Ingrid for their endless patience with my ability to fail and forget filling out various forms.